Kinetic Study of Microwave Start-up in Tokamak Plasmas

Erasmus Johannes du Toit

Doctor of Philosophy

University of York

Physics

September 2017

Abstract

Spherical tokamaks (STs) have a particular need for non-inductive start-up methods, due to the limited space for a shielded inboard solenoid. Plasma current start-up assisted by electron Bernstein waves (EBW) has been demonstrated successfully in a number of experiments. The dynamic start-up phase involves a change in field topology, as the initially open magnetic field lines form closed flux surfaces (CFS) under the initiation of a plasma current. This change in field topology will bring about a change in the current drive (CD) mechanism, and, although various mechanisms have been proposed to explain the formation of CFS, no detailed theoretical studies have previously been undertaken.

This thesis reports on the development of a kinetic start-up model for EBW-assisted plasma current start-up in MAST. In order to ensure the model is tractable and computationally manageable, the time evolution of the electron distribution function is studied in zero spatial and two momentum dimensions under several effects thought to be important during start-up.

In order to obtain numerical solutions to the time evolution of the distribution function, a positivity-preserving solution to two-dimensional advection-diffusion equations including mixed derivative terms are required. A numerical scheme for solving these equations is presented, and shown to improve the accuracy of lower-order finite difference schemes.

It is shown that the open magnetic field line configuration allows electrons to freely stream out of the plasma, but that the addition of a small vertical magnetic field leads to the preferential confinement of a selection of electrons and the generation of a plasma current. Collisions then act to "feed" this loss mechanism by increasing the parallel momentum of electrons through pitch-angle scattering, leading to greater losses and a greater plasma current. This CD mechanism is shown to be consistent with several experimentally observed effects, providing a theoretical understanding of these effects, while comparisons between simulation and experiment is good.

This work has applications for future STs, as it builds on our current, theoretical understanding of non-inductive plasma current start-up.

Contents

List of Figures

Acknowledgements

This thesis would not have been possible without the support of certain people. I would like to thank my supervisors, Roddy Vann and Martin O'Brien, for their guidance, encouragement and support. Our conversations have broadened my mind and helped me on my path to completing this work, teaching me several valuable lessons along the way.

I gratefully acknowledge the support from the University of York, the WW Smith Fund, the Golden Key International Honour Society, and Culham Centre for Fusion Energy, in particular for the financial support without which this work would not have been possible.

My friends and colleagues who have made my time in York so enjoyable, thank you very much. Without you this endeavour would have been a lot more stressful.

Lastly, a special word of thanks to my parents, who have supported me throughout this endeavour, and have always been there to encourage me. Without your support I would not have been able to complete this work.

Declaration

I declare that this thesis has not previously been accepted in substance for any degree and is not being concurrently submitted in candidature for any degree other than Doctor of Philosophy of the University of York. This thesis is the result of my own investigations, except where otherwise stated. Other sources are acknowledged by explicit references.

Parts of the work presented in this thesis have been published in:

E.J. du Toit, M.R. O'Brien and R.G.L. Vann, "*A kinetic study of microwave start-up of tokamak plasmas*", EPJ Web of Conferences **147**, 01002 (2017).

The contents of Chapter 5 have also been submitted to:

E.J. du Toit, M.R. O'Brien and R.G.L. Vann, "*Positivity-preserving scheme for two-dimensional advection-diffusion equations including mixed derivatives*", Computer Physics Communications (submitted).

Parts of this work have also been presented at several conferences, both as oral presentations:

19$^{\text{th}}$ Workshop on Electron Cyclotron Emission and Electron Cyclotron Resonance Heating, India (April, 2016)

19$^{\text{th}}$ International Spherical Torus Workshop, South Korea (September, 2017)

and as poster presentations:

43$^{\text{rd}}$ IOP Plasma Physics Conference, UK (May, 2016)

44^{th} EPS Conference on Plasma Physics, UK (June, 2017)

Finally, parts of the work presented in Appendix A is the result of work conducted by Alexey Arefiev in collaboration with Alf Köhn, Eberhard Holzhauer, Vladimir Shevchenko, Roddy Vann, and myself. My contribution to the collaboration is discussed in Appendix A, and is published as part of the greater work:

A.V. Arefiev, E.J. du Toit, A. Köhn, E. Holzhauer, V.F. Shevchenko and R.G.L. Vann, "*Kinetic simulations of X-B and O-X-B mode conversion*", AIP Conference Proceedings **1689**, 090003 (2015).

A.V. Arefiev, I.Y. Dodin, A. Köhn, E.J. du Toit, E. Holzhauer, V.F. Shevchenko and R.G.L. Vann, "*Kinetic simulations of X-B and O-X-B mode conversion and its deterioration at high input power*", Nuclear Fusion **57**, 116024 (2017).

Signed ..... Date .....

Chapter 1

Introduction

Nuclear fusion is the process that powers the sun and is responsible for life on Earth. What we see as light and feel as warmth is the result of a nuclear reaction in the core of our Sun, the result of hydrogen atoms colliding, and fusing, to form heavier helium atoms, and releasing tremendous amounts of energy in the process. Naturally, we had to ask ourselves: can we replicate this process on Earth?

The first fusion experiments were conducted in the 1940s, and, following their early promise, fusion physics laboratories were established in nearly every industrialized nation, with fusion machines operating in the Soviet Union, the United Kingdom, the United States, France, Germany, and Japan, since the mid-1950s. Through years of experiments, our understanding of the fusion process was gradually refined, leading to the development of improved machines in order to achieve the ultimate goal: ignition, where the energy obtained from fusion is greater than the energy required to power it [1].

One of the most successful approaches to fusion has been the development of magnetic confinement fusion (MCF) devices, such as the tokamak. In order to generate the high temperatures required for fusion, hydrogen fuel is ionised to form a plasma, and confined using strong magnetic fields. A plasma current is generated to, along with external coils, create the required magnetic fields for confinement.

In tokamaks, a central solenoid is used to generate a plasma current inductively, while in the more compact, spherical tokamaks (STs), the limited space for a shielded inboard solenoid precipitates the need for non-inductive methods, such as radiofrequency (RF) beams, to both heat the plasma and generate a current.

In this chapter, the concept of fusion is introduced, followed by a short description of

current fusion devices. The success of non-inductive start-up is touched upon, and a brief overview of our current understanding of plasma current generation is presented, before the aims of this thesis are outlined.

1.1 Magnetic confinement fusion

The nuclear fusion reaction, the process which powers our Sun, has been a topic of research for more than 60 years. The majority of research has focused on the D-T reaction between deuterium and tritium, due to its relatively high cross-section. In this reaction, deuterium and tritium, isotopes of hydrogen, are fused together to form helium [2],

$$ {}^{2}_{1}\mathrm{D} + {}^{3}_{1}\mathrm{T} \rightarrow {}^{4}_{2}\mathrm{He}\,(3.5\,\mathrm{MeV}) + {}^{1}_{0}\mathrm{n}\,(14.1\,\mathrm{MeV}) \tag{1.1} $$

as well as a high-energy neutron. The energy of the neutron can be used to generate heat to ultimately drive a generator and produce electricity.

The goal of ignition is achieved when this reaction becomes self-sustaining: when α particles provide the heating required to maintain the temperature required for the fusion process, and external heating is no longer required. This will occur when the Lawson criterion [3],

$$ nT\tau_E > 3 \times 10^{21}\,\mathrm{m}^{-3}\,\mathrm{keV.s} \tag{1.2} $$

is satisfied, where n is the number density, T the temperature, and τ_E the energy confinement time.

In MCF, the D-T fuel is heated to $T \sim 10\,\mathrm{keV}$[1], at which point it is fully ionised and forms a plasma. No solid material is capable of withstanding such high temperatures, so strong magnetic fields are used to confine the plasma and achieve the necessary confinement time τ_E. Although ignition has not yet been achieved in this way, continued advances in device design, engineering, materials science, diagnostics and theoretical understanding have seen incremental progress made towards this goal. The ITER device, currently under construction, is expected to achieve $Q = 10$; that is, an output power ten times greater than the input power, an important step towards ignition.

[1] 10 keV equals about 100 million degrees Celsius, approximately six times hotter than the Sun's core

1.1.1 The tokamak

The tokamak is a device that uses magnetic fields in order to confine a plasma in the shape of a torus. In a tokamak, a current is passed through a central solenoid, which acts as the primary circuit in a transformer. This creates a change in magnetic flux through the torus, inducing a toroidal current through the plasma within the tokamak vessel, which leads to ohmic heating, while the plasma current generates a poloidal magnetic field.

External poloidal field coils are used to add an additional poloidal magnetic field component for greater control over the position and shaping of the plasma. Along with external toroidal field coils, which are used to create a toroidal magnetic field component, the resultant magnetic field lines are helical, shown schematically in figure 1.1. This confines the plasma while avoiding the consequences of fundamental particle drifts which had reduced plasma confinement in earlier devices.

In a purely toroidal field, due to the field gradient in the radial direction, electrons and ions experience a ∇B drift in opposite vertical directions [2], creating a vertical electric field $\vec{E}$ which results in an $\vec{E} \times \vec{B}$ drift in the radial direction. This results in a large net loss of particles radially outwards from the device, but can be avoided with a helical field. As the top and bottom of the plasma are connected by field lines, particles will flow along them to balance any vertical ∇B drift and prevent an electric field being established.

The poloidal field created by the sum of the magnetic fields produced by the external coils and the plasma current is necessary for the formation of helical field lines. Projecting these field lines onto the poloidal field, they form closed loops, called closed flux surfaces (CFS), along which electrons and ions can travel without being lost. The generation of a plasma current is therefore a vital necessity in the formation of CFS and the confinement of the plasma.

1.1.2 The spherical tokamak

Conventional tokamaks typically have aspect ratios > 2.5 (that is the ratio of the major to the minor radii of the torus), while alternative tokamak designs have been produced with aspect ratios of half this. The outboard last CFS of the plasma therefore approaches the shape of a sphere, giving these designs the name of spherical tokamaks (STs).

These low aspect ratio designs allow operation at a higher plasma β, or ratio of plasma

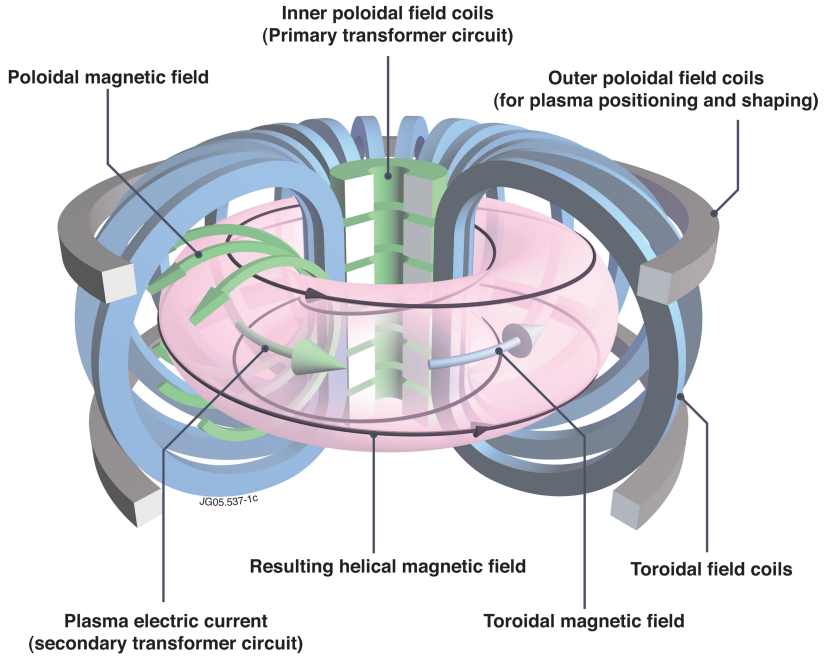

(a)

Figure 1.1: Schematic of the electromagnetic fields and coils of the JET tokamak, showing the resultant helical magnetic field. Image taken from [4].

to magnetic pressure,

$$\beta = \frac{nk_BT}{(B^2/2\mu_0)} \tag{1.3}$$

where n is the number density, T the temperature and B the magnetic field strength. The consequence of higher β is that a given temperature and pressure can be achieved using a significantly smaller magnetic field, making such a device more economical to build and operate. In addition, the compact structure is cheaper to construct and the spherical geometry provides inherent suppression of certain instabilities.

The ST was first proposed in the 1980s by Peng and Strickler [5], and a number have been constructed globally, including START at Culham Centre for Fusion Energy (CCFE) in the UK, superseded by MAST, the Mega-Amp Spherical Tokamak, in 1999, depicted in figure 1.2. MAST, presently undergoing a major upgrade, achieves toroidal $\beta \sim 3$ times those in conventional aspect ratio tokamaks, with a relatively low magnetic field, high flow shear and strong variation in toroidal field across the minor radius. This has allowed the testing of theories in new operational regimes and provided new insight into tokamak physics [7].

A fundamental problem with STs is the limited space for a shielded central solenoid, due to its compact design. This introduces the need for non-inductive plasma current start-up,

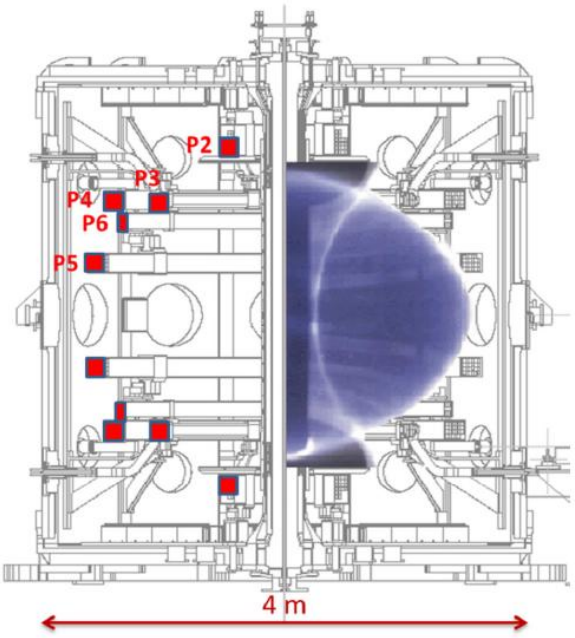

(a)

Figure 1.2: Schematic of the poloidal field coil locations in MAST (left) and a typical plasma cross-section (right). Image taken from [6].

such as neutral beam injection (NBI) or RF beams. The relatively low density during start-up, however, limits the usefulness of NBI, such that RF beams are the only viable candidate for plasma current start-up in STs.

1.2 Tokamak start-up

Tokamak start-up consists of three phases: the plasma breakdown phase, during which the hydrogen gas is ionised to form a plasma; the plasma burn-through phase, during which a plasma current is initiated and the magnetic field line topology changes from an open field line configuration to the formation of CFS; and the subsequent ramp-up process of plasma current I_P until it arrives at a flat-top state [8].

1.2.1 Plasma breakdown

The plasma breakdown phase involves the ionisation of the neutral hydrogen gas in forming a plasma, and can be explained by the Townsend avalanche theory. In this theory, free electrons are accelerated by an electric field, collide with gas molecules, and consequently free additional electrons which will be accelerated to free more electrons. The result is the

ionisation of the gas and the formation of a plasma [9].

Similar to the use of a central solenoid, the electric field of an injected RF beam also accelerates electrons, which leads to the ionization of neutral atoms and the freeing of additional electrons. In ITER, for example, a combination of the central solenoid and RF beams will be used to ensure reliable breakdown and start-up [8].

1.2.2 Plasma burn-through phase and the formation of closed flux surfaces

The initiation and subsequent ramp-up of a plasma current is a necessity for the formation of helical field lines or CFS. The poloidal field coils create a vertical and small radial magnetic field, but with the addition of a plasma current, the poloidal projection of the magnetic field form CFS, as illustrated in figure 1.3. The formation of CFS greatly improves confinement, as electrons can no longer freely stream out of the plasma along the open magnetic field lines.

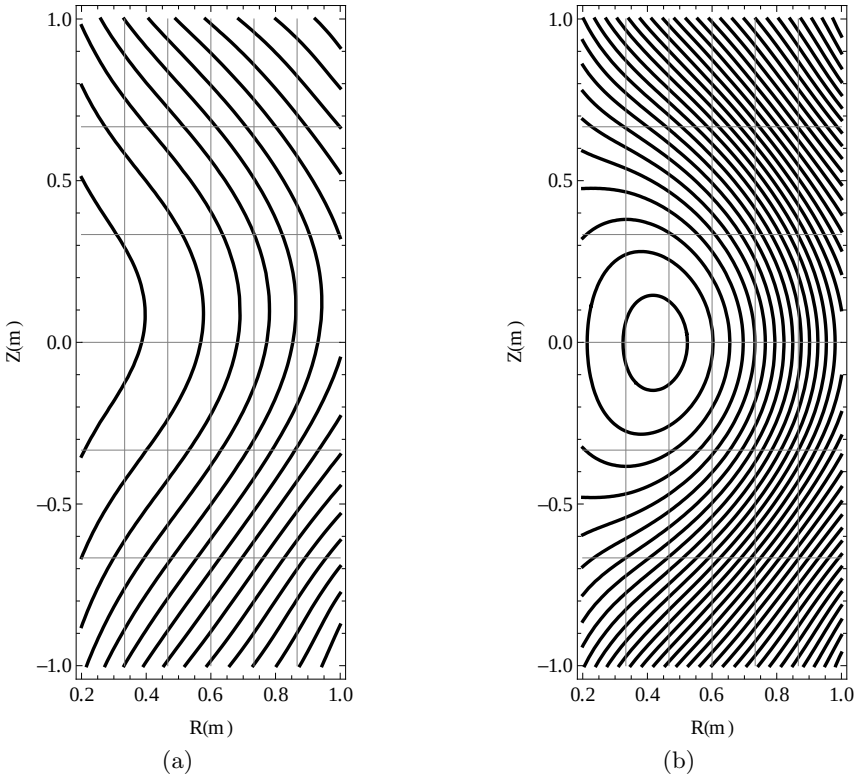

Figure 1.3: Lines of constant magnetic field in the poloidal plane for (a) initial times, when the field lines are open, and (b) upon the initiation of a sufficiently strong plasma current for CFS to form.

The formation of CFS is governed by the initiation of a plasma current. In conventional

tokamaks, electrons are accelerated along the electric field created by the central solenoid, generating a plasma current through ohmic current drive. After the formation of CFS, the bootstrap current, resulting from collisions between trapped and passing electrons, is typically responsible for a large portion of the observed current [10].

The continued use of the central solenoid will lead to an increase in the plasma current, and, as CFS have been formed, the increase in density will lead to a further increase in current, until flat-top is reached.

For non-inductive start-up, however, the initiation of a plasma current is not as well understood, and several current drive (CD) mechanisms have been proposed to describe the experimentally observed formation of CFS under ECRH [6, 10–16].

1.3 Non-inductive plasma current start-up

The use of RF waves for non-inductive start-up has been demonstrated in a number of experiments [6, 10, 11, 17, 18]. These experiments have mostly relied on the injection of RF waves in the electron cyclotron (EC) frequency range, and have demonstrated the generation of a plasma current in the absence of an external electric field. Several CD mechanisms have been proposed for this observation, of which only a few will be highlighted here.

Fisch and Boozer [19] proposed a CD mechanism by which the preferential heating of electrons moving in one direction creates an anisotropic plasma resistivity, generating a plasma current. An EC wave is used to transfer momentum to electrons, increasing the perpendicular energy of electrons moving in a particular direction along the magnetic field lines. These electrons undergo fewer collisions which lead to an anisotropic plasma resistivity, and manifests itself as a plasma current [20].

Another possible CD mechanism relies on the preferential confinement of electrons in an open magnetic field line configuration [21]. During start-up, the toroidal magnetic field is typically at least two orders of magnitude greater than the poloidal magnetic field at the major radius. In this scenario, electrons will experience ∇B and curvature drifts in the same direction, but by adding a small vertical magnetic field, the parallel drift of a selection of electrons along this vertical field can cancel the ∇B and curvature drifts, leading to the confinement of these electrons. This leads to the preferential confinement of co- or counter-moving electrons, generating a plasma current.

Other CD mechanisms include the Pfirsch-Schlüter current [10], which relies on the formation of a pressure gradient, with a current generated through force balance ($\vec{J} \times \vec{B} = \nabla p$), and the Bootstrap current, which is generated by collisions between passing and trapped particles, and is an effect of the density gradient.

Several attempts have been made in order to model non-inductive start-up in order to help understand experimental observations and predict future start-up requirements for STs. These models typically rely on the reconstruction of magnetic fields and pressure profiles from experimentally measured observables in support of pressure-driven currents [10, 22]. The reliance on experimental data, however, is undesirable, while these methods only provide qualitative information of the CD mechanism.

A more successful method relied on the study of single particle orbits for studying the formation of CFS [12, 17, 18]. These approaches showed the importance of the preferential confinement of electrons in the open field line configuration found during start-up, and, along with a pressure-driven current, demonstrated the formation of CFS.

The study of single particle orbits for the initiation of CFS may have been successful, but, unless the orbit of every electron is studied, the electron distribution function is needed in order to calculate a generated plasma current. This approach was used before [12], but failed to model the time evolution of observables such as the plasma current, temperature and density, and was therefore unable to resolve several experimentally observed effects which is currently not well understood.

The electron distribution function has successfully been employed to study electron cyclotron current drive (ECCD) after the formation of CFS [23]. A study of the distribution function allows the separation of effects believed to have an influence on start-up, such as orbital losses due to the open magnetic field line configuration, collisions, and RF heating, in order to gain a better understanding of microwave start-up.

The development of such a model, however, does not come without challenges. Due to the open magnetic field line configuration electrons can freely stream out of the plasma, but such a loss mechanism depends on the magnetic field structure, while studying the plasma-wave interaction resulting from the injected RF beam depends on the spatially varying magnetic field. In order to accurately capture all these effects thought to be important during start-up, the electron distribution function will have to be studied in both space and velocity dimensions.

In this thesis, however, the assumption is made that the important physics can be captured in a model that depends on zero spatial and two momentum dimensions. In order to account for the 0D nature of the model appropriate volume averages and approximations are taken to accurately capture the spatially dependent effects.

1.4 Developing a kinetic start-up model

Although several attempts at simulating non-inductive start-up have been made in the past, models typically fail in simulating the time evolution of plasma parameters such as the current, density and temperature, and rather focused on the initiation of CFS and the CD mechanism responsible for it. The aim of this thesis is to develop a model for studying non-inductive start-up, in particular the CD mechanism responsible for the generation of a plasma current, and to provide explanations for experimentally observed effects not understood before.

There are two main approaches to studying the evolution of plasmas, either through a fluid or kinetic approach. For studying non-inductive plasma current start-up, which is dependent on the plasma-wave interaction resulting from the injected RF beam, a kinetic model is necessary, as the motion and velocity of electrons are of interest.

Motivated by the success of experiments conducted on MAST, of which an overview is given in Chapter 2, the development of a kinetic start-up model is discussed in Chapter 3. The developed model studies the electron distribution function under several effects, including electron losses along the open magnetic field lines, discussed in detail in Chapter 4, and the plasma-wave interaction with the injected RF beam.

The numerical approximation to the electron distribution function is discussed in Chapter 5, with the results of start-up simulations given in Chapter 6. In particular, explanations of the CD mechanism, as well as explanations for observed experimental effects not understood before, are provided, with simulations comparing favourably to experimentally measured observables. Finally, Chapter 7 summarizes the findings and looks ahead to future work.

Chapter 2

Microwave start-up in spherical tokamaks

The compact size of STs precipitate the need to minimise or eliminate their reliance on inductive heating and current drive (CD), due to a lack of space for a shielded central solenoid. The low densities encountered during start-up exclude the use of neutral beams, and the only remaining option is the use of RF beams.

The advantage of RF beams lies in its ability to provide localised, directional heating. The Fisch-Boozer mechanism, based on the preferential heating of electrons to create an anisotropic plasma resistivity, is a very attractive concept for CD using EC waves. For typical plasma parameters, however, the core appears inaccessible for conventional EM modes in the range of frequencies corresponding to the first few EC resonances [24, 25].

Electron Bernstein waves (EBWs), on the other hand, have been shown to provide localized, highly efficient heating and CD in STs, both theoretically [13, 26] and experimentally [6, 11, 27–29]. The advantages of EBWs are that, unlike the ordinary (O) and extraordinary (X) modes, they are strongly absorbed at nearly all harmonics of the cyclotron resonance, even in relatively cold plasmas. EBWs also do not have any density cut-offs inside the plasma and can therefore access plasmas of arbitrary densities [25, 28].

EBW assisted start-up on MAST was used to generate significant plasma current giving the prospect of a fully solenoid-free plasma start-up. These experiments relied on a double mode conversion (MC) for EBW excitation, consisting of an O-mode, launched from the low field side, being reflected off a mirror-polariser on the central rod as X-mode. The X-mode

propagates from the high field side through the ECR and experiences a subsequent X to EBW MC near the UHR, which is then totally absorbed. Plasma currents as high as 73 kA were achieved with up to 100 kW of injected RF power [6, 11, 29].

In this chapter, the theory of RF waves in a plasma, which leads to localised heating, is briefly discussed, before the design and execution of experiments on MAST is reviewed. A brief discussion on EBW CD introduces the need for the development of a theoretical model to simulate EBW start-up.

2.1 Waves in a hot plasma

In the presence of a static magnetic field, the trajectories of charged particles become helices, spiralling around the magnetic field lines. This leads to the coupling of particle motion to external electric fields of, for example, injected RF beams, with the response to a perpendicular electric field being totally different from the response to a parallel field. In order to understand this response, Maxwell's equations, describing the propagation of an EM field, must be coupled to the collisionless Boltzmann, or Vlasov, equation, describing the motion of particles in the presence of electric and magnetic fields. The result is the plasma dispersion relation, derived in Appendix A [30].

The solution to the plasma dispersion relation is obtained from the wave equation,

$$\hat{\varepsilon} \cdot \vec{E} + \vec{N} \times (\vec{N} \times \vec{E}) = 0 \tag{2.1}$$

where the vector $\vec{N}$ is in the same direction as the wave vector $\vec{k}$ and its magnitude is the refractive index. The dielectric tensor $\hat{\varepsilon}$ contains integrals of the distribution function and plasma parameters, such as the plasma and cyclotron frequency.

The dispersion relation is derived under the assumption that deviations on the order of a gyro-orbit do not occur, and damping is weak. This implies that the magnetic and electric fields of the EM wave can be written as perturbations to the background, equilibrium quantities. The hot plasma dispersion relation has two major consequences: firstly, the resonance condition leads to cyclotron damping at all harmonics of the resonance; and secondly, multiple modes for the EM wave, including electrostatic modes such as EBWs, exist.

2.1.1 Cyclotron damping

The plasma dispersion relation contains integrals of the form

$$\int \mathrm{d}^3 p \, \frac{g(f_0, \omega_p, \omega_c)}{\omega - k_\parallel v_\parallel - n\omega_c}$$

where $g(f_0, \omega_p, \omega_c)$ is some function depending on the distribution function f_0 and the plasma and cyclotron frequencies. These integrals have singularities where the resonance condition,

$$\omega - k_\parallel v_\parallel - n\omega_c = 0 \tag{2.2}$$

is satisfied, which leads to cyclotron damping. It is termed cyclotron damping due to there being a resonance at all the multiples of the cyclotron frequency, the strongest of these occurring at the fundamental ($n = 1$) cyclotron frequency. The Doppler shift, due to non-zero $k_\parallel$, allows for a broadening of the resonance, while the relativistic cyclotron frequency $\omega_c = \omega_{c0}/\gamma$, where γ is the Lorentz factor, leads to a relativistic mass shift of the resonance, depending on the temperature of the distribution.

A physical picture of cyclotron damping is very similar to that of Landau damping [31], where there is no background magnetic field (or $n = 0$) and the resonance condition is simply given by

$$\omega - k_\parallel v_\parallel = 0.$$

The common picture used to describe Landau damping is that of a surfer on a wave [32] - an electron "sees" the electric field of the incoming wave, and, if it has a velocity slightly slower than the wave, it will be accelerated by it, while if it has a velocity slightly faster than the wave, the wave will gain energy and the electron will lose energy, as illustrated in figure 2.1. The velocity of the wave is known as the phase velocity, and there will normally be fewer electrons moving faster than the wave than there are electrons moving slower than the wave, such that, overall, energy is given from the wave to the distribution of electrons (figure 2.2), leading to damping.

Cyclotron damping differs from Landau damping in two important aspects. The first is that damping occurs when an electron "sees" the electric field at its cyclotron frequency, rather than at zero frequency, and secondly, acceleration is perpendicular to the particle's free-streaming motion [30].

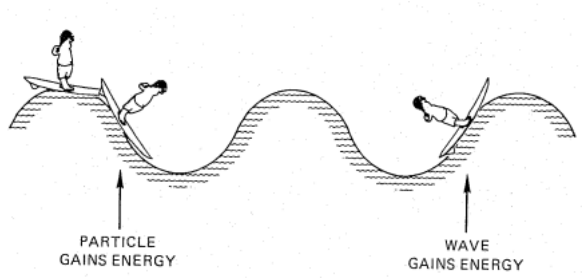

Figure 2.1: Physical picture of Landau damping [32].

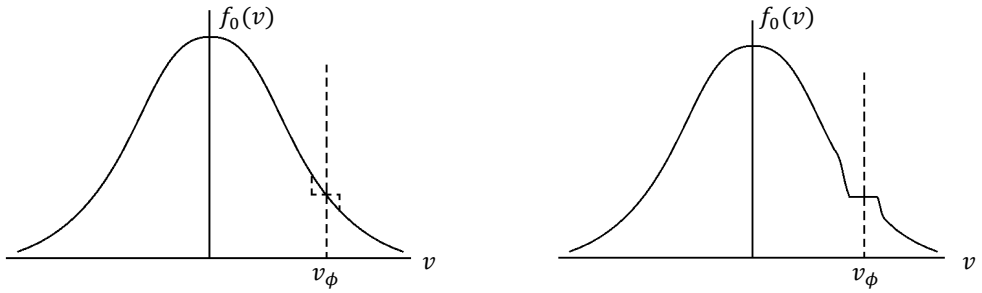

Figure 2.2: (a) The location of heating on a Maxwellian distribution function leads to (b) the acceleration of electrons in the vicinity of the phase-velocity.

An injected RF wave will be damped due to oscillations in both time and space in which there exists a component of the electric field $\vec{E}$ that is perpendicular to the background magnetic field $\vec{B}_0$. Electrons streaming along magnetic field lines will see the oscillations of the electric field at different frequencies due to the Doppler effect, while the relativistic mass shift also gives a broadening of the cyclotron resonance.

The advantage of cyclotron damping from EM modes is that the location of absorption can be determined by changing either the injected frequency of the RF wave ω or the magnetic field $\vec{B}_0$. In a ST, where the magnetic field varies like $B \sim B_0/R$, changing the value of B_0 will change the radial location of the cyclotron resonance, while similarly the frequency of the wave ω can be tuned to change the radial location where the cyclotron resonance condition (2.2) is satisfied.

The drawback with EM modes is that density cut-offs exist, beyond which the waves cannot propagate, while absorption is typically weak during start-up when the temperature and density are low. The two EM modes typically encountered are the ordinary (O) and extraordinary (X) modes, for which the cold plasma dispersion relation, for perpendicular

propagation, is given by

$$N^2 = 1 - \frac{\omega_p^2}{\omega^2} \tag{2.3}$$

for the O-mode and

$$N^2 = 1 - \frac{\omega_p^2}{\omega^2}\frac{\omega - \omega_p^2}{\omega^2 - \omega_p^2 - \omega_c^2} \tag{2.4}$$

for the X-mode. The O-mode has a density cut-off where $\omega_p^2 = \omega^2$ and can therefore not propagate through plasmas above a certain density. These plasmas are known as overdense.

The X-mode, on the other hand, has two density cut-offs, while it becomes evanescent at the UHR,

$$\omega^2 = \omega_p^2 + \omega_c^2 \tag{2.5}$$

where it can couple to electrostatic modes.

2.1.2 Electron Bernstein waves

At the UHR the cold-plasma dispersion relation predicts a singularity for the X-mode. At this point, the EBW can be excited via a linear mode conversion from the incident X-mode [33], where the EM mode couples with an electrostatic mode. Electrostatic waves are short wavelength modes that are obtained by replacing the vector electric field $\vec{E}$ by a potential gradient $-\nabla\phi$, such that the electrostatic dispersion relation is given by [30, 35, 36, 38]

$$\vec{k} \cdot \hat{\varepsilon} \cdot \vec{k} = 0 \tag{2.6}$$

under the assumption that $N^2 \gg |\varepsilon_{ij}|$ for all i, j, while the electric field is determined from the usual wave equation (2.1).

EBWs are typically approximated as electrostatic waves, as their polarization is close to electrostatic and they do not propagate in a vacuum. EBWs were first discovered in 1958 [34] and generalized in the years following (see, for example [35]). They were identified as being a promising candidate for microwave plasma heating and CD in STs, as they have no density cut-off for propagation, while absorption is strong as a result of the electrostatic nature of the waves [13, 36, 37].

The excitation, propagation and absorption of EBWs is a topic that has been intensively discussed [33, 36–39] due to its favourable properties for plasma heating and CD. In typical ST plasmas, the UHR and ECR are located very close to each other during start-up, due to

the low densities. The excitation of EBWs at the UHR is related to the singularity in the cold plasma dispersion relation, where the cold plasma EM modes are converted to the hot plasma Bernstein modes via a linear mode conversion [33]. The electrostatic approximation is quite accurate for EBWs [35] as the parallel refractive index $N_{\parallel} \leq 1$ while the perpendicular refractive index $N_{\perp}$ becomes very large in the vicinity of the ECR [38]. This allows for localised, efficient current drive, as the parallel refractive index $N_{\parallel}$ for EBWs is determined by the local magnetic field and will be non-zero for absorption above or below the midplane of the torus. This provides a directionality with respect to the background magnetic field, and as the absorption is strong, a net current can be generated [13].

2.2 Electron Bernstein wave start-up experiments on MAST

EBW assisted start-up on MAST was used to generate significant plasma current giving the prospect of a fully solenoid-free plasma start-up. These experiments relied on a double mode conversion (MC) for EBW excitation, consisting of an O-mode beam, launched from the low field side (LFS), being reflected off a mirror-polariser on the central rod as X-mode. The X-mode propagates from the high field side (HFS), through the ECR and experiences a subsequent X to EBW MC near the UHR, which is then totally absorbed. Plasma currents as high as 73 kA were achieved with up to 100 kW of injected RF power [6, 11, 29].

2.2.1 Experimental setup and design

EBW start-up using a 28 GHz gyrotron capable of delivering 100 kW of power for up to 0.5 s was demonstrated on MAST [6, 11, 29]. MAST had 5 pairs of poloidal field coils inside the vacuum vessel as shown in figure 2.3(a). Upper and lower parts of P2 - P5 coils carry current in the same direction and generate the vertical magnetic field required for plasma shaping and equilibrium, while the upper and lower parts of the P6 coils carry current in opposite directions and generate a radial magnetic field providing vertical control of the plasma.

The optimal frequency for ECRH and ECCD is in the range of the fundamental EC resonance. The central rod current therefore generates a current of 2 MA in order to create a toroidal magnetic field B_{ϕ}, giving the radial location of the ECR for 28 GHz at 0.4 m [11].

Conventional ECRH and ECCD methods typically cannot be used in STs because of the

specific plasma parameters. Usually the plasma is overdense, such that the core is inaccessible for conventional EM modes in the range of frequencies corresponding to the first few EC harmonics. EBWs, however, are predominantly electrostatic waves, which cannot propagate in a vacuum, but can be coupled to the vacuum EM waves through MC mechanisms. This allows EBWs to be excited within the plasma with externally launched X- or O-modes [25].

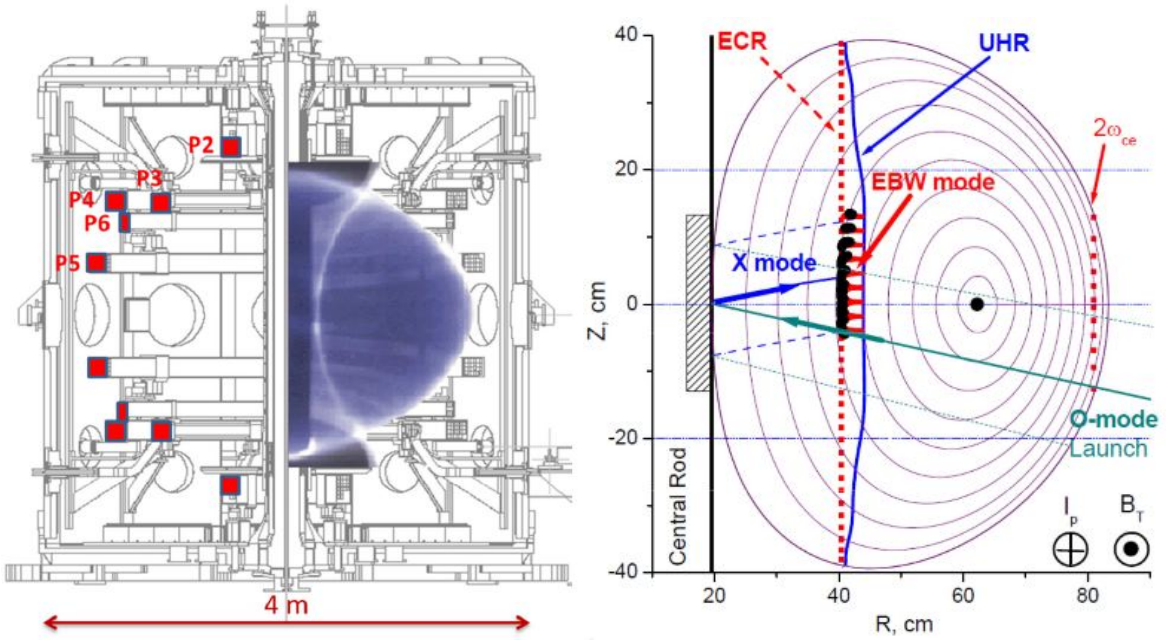

(a) (b)

Figure 2.3: (a) Location of poloidal field coils in MAST (left) and a typical plasma cross-section (right), (b) EBW assisted plasma start-up schematic, showing a poloidal projection of EBW ray-tracing based on plasma equilibrium reconstructed from experimental data [11].

There are a number of methods for exciting EBWs from externally launched EM waves using different MC mechanisms. For instance, the slow X-mode launched from the HFS of the tokamak converts totally into the EBW-mode at the UHR. This is the most effective mechanism of EBW excitation [40], and has been shown to generate significant plasma currents on COMPASS-D [28].

Another method, based on the O-X-B MC from the LFS, relies on the conversion of the O-mode into the slow X-mode near the O-mode cutoff, and then the slow X-mode is totally converted into the EBW-mode at the UHR. The O-X stage is the most demanding part of this process because it requires the O-mode cutoff and the slow X-mode cutoff to be coincident. Whereas the O-mode cutoff only depends on the local plasma density, the slow X-mode cutoff depends on the local plasma density, magnetic field, and parallel component

$N_{\|}$ of the refractive index [25].

EBWs may also be excited with the X-mode launched from the LFS. In this case the fast X-mode tunnels through the evanescent layer between the right-hand cutoff and the UHR and then couples to the slow X-mode, which is mode converted into the EBW-mode at the UHR [25].

The EBW start-up method employed on MAST was first proposed in [24,25], and is also discussed in [41]. This start-up method consists of three sequential stages:

1. First, the ordinary polarized RF beam launched from the LFS passes through the vessel and reflects from a grooved mirror-polariser incorporated into a graphite tile on the central rod. The launched Gaussian beam was tilted to the midplane at 10° and hit the central rod at the midplane, as illustrated in figure 2.3(b). The polarization of the reflected beam is converted into the X-mode polarization.

2. Second, the X-mode produces intensive ionisation near the UHR and quickly builds up electron pressure.

3. Third, as electron temperature rises, collisional absorption at the UHR is weakened and cyclotron absorption becomes dominant. From that moment, the X-mode is completely converted into the EBW-mode at the UHR, which propagates back to the ECR. EBWs are absorbed by electrons at the Doppler shifted resonance and can generate significant plasma current if the absorption is localised above or below the midplane [13, 28].

2.2.2 O-X-B mode conversion and absorption

The described EBW start-up method [6, 11, 24, 25, 41], has natural limitations. Firstly, the plasma must be transparent for the O-mode. This implies the plasma must be well underdense for the RF frequency injected into the plasma, i.e

$$\omega_{\mathrm{RF}}^2 \gg \omega_p^2$$

or, equivalently,

$$n_e \ll 9.7 \times 10^{18}\,\mathrm{m}^{-3}$$

for the 28 GHz RF frequency considered here.

The second limit comes from the lower density case. If the inequality,

$$\frac{\omega_p^2}{\omega_{\mathrm{RF}}^2} < \frac{T_e}{m_e c^2} \tag{2.7}$$

where T_e is an electron temperature and m_e is an electron mass, is valid at the UHR, the X-B MC does not take place and the X mode passes through the plasma [40]. During the RF breakdown phase this low density limit is quickly exceeded and the gas puff needs to be controlled to avoid the plasma reaching over dense conditions.

A plasma is created through the ionisation of a neutral gas. Breakdown occurs if the ionisation rate exceeds the losses, i.e. [9],

$$\frac{\mathrm{d}n_e}{\mathrm{d}t} = n_e \left(\frac{1}{\tau_{\mathrm{ion}}} - \frac{1}{\tau_{\mathrm{loss}}} \right) \tag{2.8}$$

where the losses are primarily determined by the gas pressure p and characteristic connection length L_f. This leads to the Townsend criterion, the minimum electric field needed for plasma breakdown,

$$E(\mathrm{V\,m^{-1}}) \geq \frac{1.25 \times 10^4\, p(\mathrm{Torr})}{\log\left[510\, p(\mathrm{Torr}) L_f(\mathrm{m})\right]} \tag{2.9}$$

.

In RF breakdown, however, it is known that the breakdown voltage increases with increasing RF frequency, as the amplitude of electron oscillations becomes smaller and electrons gain a smaller amount of energy from the EM field of higher frequency. This leads to an effective electric field required for RF breakdown, for example, for deuterium [41],

$$E_{\mathrm{eff}} \approx \frac{p\lambda}{55.6} E \tag{2.10}$$

where E is an RF electric field, p is the gas pressure in torr and λ is the vacuum wavelength in centimetres. At high RF frequencies, the minimum electric field required for RF breakdown does not depend on the connection length L_f, in contrast to Ohmic plasma breakdown. Figure 2.4 shows the RF power required for breakdown in MAST. For 28 GHz, about 100 kW of power is required for breakdown.

For effective breakdown, the RF beam must be extraordinarily polarized, with power in excess of 100 kW. However, RF beams below this power are able to increase the density of free electrons around the ECR layer, enabling EBW excitation at the UHR. The electric

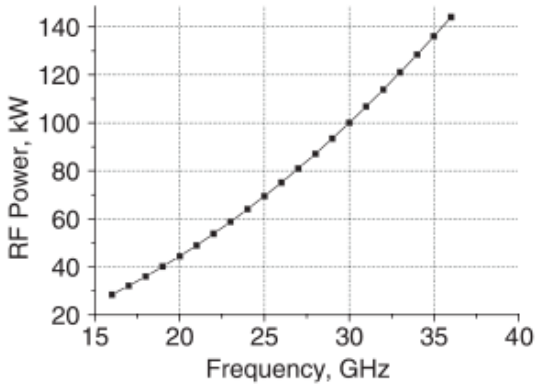

(a)

Figure 2.4: RF power required for breakdown in MAST for different RF frequencies, calculated theoretically. Image taken from [41].

field of the EBW mode experiences strong (typically a factor ~ 10) amplification near the UHR which is sufficient for the production of well sustained breakdown at RF power levels much lower than 100 kW [29].

An increase in the plasma density and temperature leads to a reduction in collisional absorption at the UHR, such that the EBW is excited by the X-mode. The excited EBW mode propagates back towards the ECR, but is totally absorbed before it reaches it, due to the Doppler shifted resonance. Modelling showed that only a small fraction of injected RF power ($\sim 2\%$) is typically absorbed from the O- and X-modes in start-up plasmas, while the main part is converted into, and absorbed from, the EBW mode [6, 11]. The absorption of EBW remains high even in cold plasmas, and can be estimated using a simple analytical formula obtained within a global wave-dynamical treatment of MC processes. It gives good agreement with numerical simulation within the range of parameters typical for start-up plasmas [40],

$$\tau = \frac{\pi}{2} R\, k\, \frac{\omega_p^2}{\omega_c^2}$$

where τ is an optical thickness, R is a major radius of the plasma, $k = \omega/c$ is the wave vector, and ω_p and ω_c are the plasma and cyclotron frequencies, respectively. For MAST start-up parameters it can be simplified even further [29],

$$\tau = 120\, n_e^{18} \tag{2.11}$$

where n_e^{18} is an electron density in units of $10^{18}\,\mathrm{m}^{-3}$. The absorption coefficient A can be

estimated as usual [40],

$$A = 1 - e^{-\tau} \tag{2.12}$$

such that absorption is very close to 100% for a wide range of densities and is independent of plasma temperature.

Absorption occurs for electrons which satisfy the relativistic resonance condition,

$$\omega - k_{\parallel} v_{\parallel} - \omega_{c0}/\gamma = 0 \tag{2.13}$$

near the fundamental EC resonance, where $k_{\parallel}$ is the component of the wave vector k parallel to the magnetic field B. EBWs can develop very large $k_{\parallel}$, such that the Doppler downshift of the ECR is important even in cold plasmas.

The EBW wave vector is essentially perpendicular to the UHR layer, so the perpendicular part of the refractive index $N_{\perp}$ dominates the parallel part $N_{\parallel}$ by about two orders of magnitude. The sign of $N_{\parallel}$ determines whether EBW interacts with electrons moving along or opposite the magnetic field, from equation (2.13). The sign of $N_{\parallel}$ is given by the projection of the wave vector k on the local magnetic field near the UHR where the EBW originated. Usually the toroidal field is much greater than the poloidal field, $B_{\phi} \gg B_{\theta}$, during start-up, and therefore $k_{\parallel} \approx k_{\phi} + k_{\theta}\, B_{\theta}/B$, where k_{ϕ} and k_{θ} are the toroidal and poloidal components respectively. At their origin, the k vector is almost perpendicular to the UHR layer resulting in $k_{\theta}\, B_{\theta}/B \gg k_{\phi}$, except for in the vicinity of the midplane. The sign of $k_{\parallel}$ is therefore mainly determined by the sign of $k_{\theta}\, B_{\theta}/B$, and, as the radial magnetic field B_R has different signs above and below the midplane (see figure 4.4 for example), this results in a different sign for $k_{\parallel}$ above and below the midplane [28, 29].

EBW rays propagating close to the midplane undergo oscillations around $N_{\parallel} = 0$, destroying the directionality of the wave and resulting in no net effect to the generated current [13,39], as these EBWs deposit energy above and below the midplane, generating plasma current in opposite directions [28]. However, if the absorption is localised predominantly above or below the midplane, to gain a directionality with respect to the magnetic field, significant plasma current can be generated, giving the prospect of a fully non-inductive plasma start-up [28].

2.2.3 EBW start-up experiments

An important part of any start-up scenario is a transition from an open magnetic field line configuration to the formation of CFS. A spontaneous formation of CFS has been observed in a number of RF assisted start-up experiments [10,14,17], and although different mechanisms driving CFS formation have been proposed, it is governed mainly by EBW CD.

Initial EBW start-up experiments conducted on MAST were reported in [11], under a constant vertical poloidal field of $B_V = -2.3\,\mathrm{mT}$ near the ECR located at $R = 0.41\,\mathrm{m}$. The vessel was pre-filled with deuterium prior to RF injection, leading to an increase in plasma density near the midplane. The line integrated density, shown in figure 2.5, shows the initial increase in density, accompanied by an increase in plasma current for the first $20 - 30\,\mathrm{ms}$, before it gradually decays to zero. The maximum current achieved, over a range of experiments with B_V ramped up and down in time, was about $10\,\mathrm{kA}$, but it could not be sustained for longer than $50\,\mathrm{ms}$, and no CFS was formed.

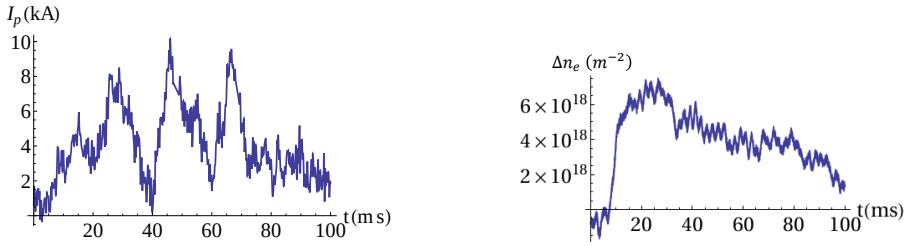

Figure 2.5: The time evolution of (a) the plasma current and (b) the change in line integrated density for MAST shot #16837.

The importance of using single particle orbits to analyse the start-up scenario was first noted in [14]. By studying the current generated from confined electrons originating from the UHR, where an interaction with the excited EBW produces a kick in electron energy, the current generated can be explained. Electrons are subjected to a parallel motion along magnetic field lines, and a vertical drift due to the curvature and inhomogeneity of the magnetic field, such that the guiding centre approximation for an electron's velocity in the vertical direction is given by (Appendix D),

$$V_Z = \frac{B_Z}{B} v_\parallel + \frac{m_e}{q_e\, B\, R}\left(v_\parallel^2 + \frac{v_\perp^2}{2}\right) \tag{2.14}$$

which, for $B_Z < 0$ only equals zero for electrons with $v_\parallel > 0$. The selective confinement

of these electrons carry a positive current, which modifies the curvature of the poloidal magnetic field, allowing for the existence of electrons carrying negative current, and the decay in plasma current seen in initial experiments.

The refractive index of the EBW parallel to the magnetic field $N_{\parallel}$ does not change sign along the EBW trajectory except for propagation near the midplane [39]. Around the midplane, the value of $N_{\parallel}$ oscillates around $N_{\parallel} = 0$, accelerating electrons with both $v_{\parallel} > 0$ and $v_{\parallel} < 0$, sustaining the negative current generation. The sign of $N_{\parallel}$ can be controlled by changing the local curvature of the vacuum poloidal field B_V, for example, by shifting the B_V minimum upwards providing favourable $N_{\parallel}$ in the MC zone [11].

In MAST, because $B_V < 0$, $N_{\parallel} < 0$ above the midplane and $N_{\parallel} > 0$ below the midplane. To generate a positive current, $N_{\parallel} > 0$ is required in the region of absorption to generate electrons with $v_{\parallel} > 0$ which carries a positive current. This can be achieved by shifting the plasma upwards, such that $N_{\parallel} > 0$ in the region of absorption.

A vertical shift of the magnetic field can be created with a radial field, through the P6 coils on MAST. Experiments were conducted on MAST to investigate this effect, by providing a vertical shift of about 20 cm throughout the shot, creating $N_{\parallel} > 0$ in the MC zone. In this case, the negative current was suppressed by an expanding positive current, leading to the formation of CFS formation near the midplane. After the formation of CFS, the vertical magnetic field changes its sign in the MC zone, leading to $N_{\parallel} < 0$, and electrons with $v_{\parallel} < 0$, carrying a negative current, are heated. The measured plasma current, shown in figure 2.6, shows the initial increase in I_P, until CFS start to form, followed by a steady decrease. The current carried by the P6 coils remain constant, such that, once CFS forms, the poloidal magnetic field in the region of absorption changes sign and $N_{\parallel} < 0$, generating a negative current.

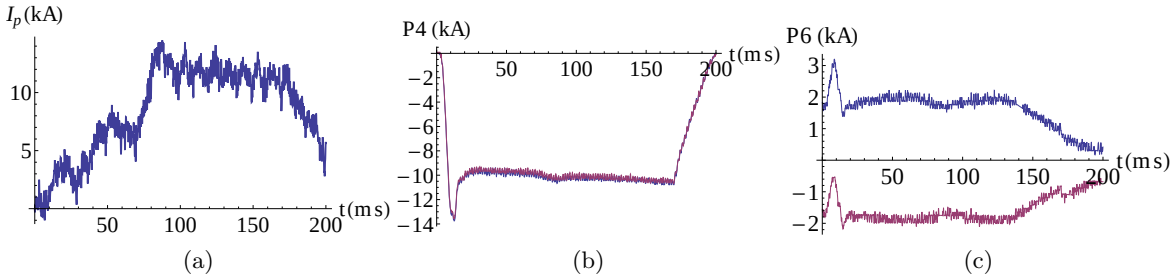

Figure 2.6: The time evolution of (a) the plasma current, (b) the current in the P4 coils and (c) the current in the P6 coils for MAST shot #17299. The P4 coils create a vertical magnetic field, while the P6 coils create a radial magnetic field.

To counter the reversal of $N_{\|}$, the plasma must be down-shifted back to the machine midplane after CFS formation, in order to ensure $N_{\|} > 0$ in the MC zone. Plasma currents up to 33 kA were achieved with constant B_V and RF power alone, and with an optimal up/down shift of the plasma [11]. The resultant plasma current, along with the currents in the P4 and P6 coils, are shown in figure 2.7. CFS starts to form around 70 ms, at which point the current in the P6 coils are switched off to ensure $N_{\|} > 0$ in the region of absorption. This allows a further increase in the plasma current until the vertical magnetic field created by the P4 coils is switched off around 200 ms.

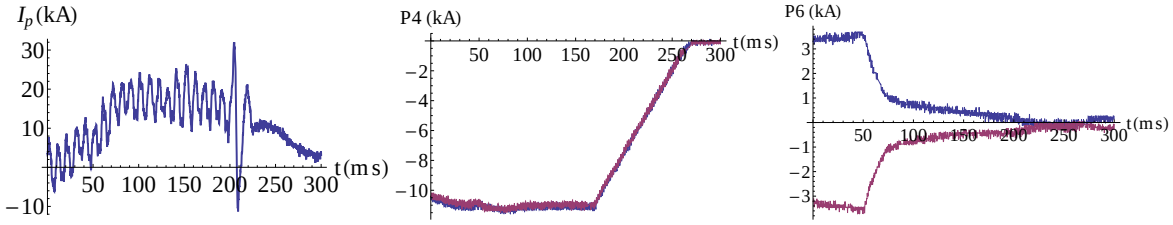

(a) (b) (c)

Figure 2.7: The time evolution of (a) the plasma current, (b) the current in the P4 coils and (c) the current in the P6 coils for MAST shot #18158. The P4 coils create a vertical magnetic field, while the P6 coils create a radial magnetic field.

Experiments showed that the most efficient way to achieve higher plasma current and keep the plasma in equilibrium is to apply a B_V ramp-up. It showed that a vertical shift of the B_V minimum helps to form CFS, and by ramping up the vacuum poloidal field strength B_V larger plasma currents can be achieved [6, 29]. The measured plasma current, as well as the current in the P2 and P4 coils, which creates the vertical poloidal field B_V, are shown in figure 2.8, and show an increase in the plasma current for an increasing B_V field.

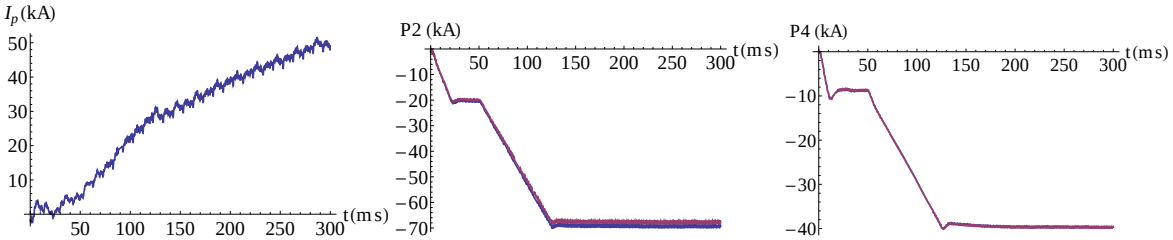

(a) (b) (c)

Figure 2.8: The time evolution of (a) the plasma current, (b) the current in the P2 coils and (c) the current in the P4 coils for MAST shot #28941. Both the P2 and P4 coils generate a vertical magnetic field.

The duration of the RF pulse also plays a role in the generated plasma current. Exper-

iments were conducted, with similar vacuum magnetic fields, by injecting RF power of the same level for 320 ms, 400 ms and 440 ms, to show that the longer the RF pulse, the larger the generated plasma current [29]. Figure 2.9 shows the generated plasma current for these three cases. As the vacuum magnetic fields are similar for each shot, the initial increase in I_P is similar, with the current decaying once the RF power is switched off.

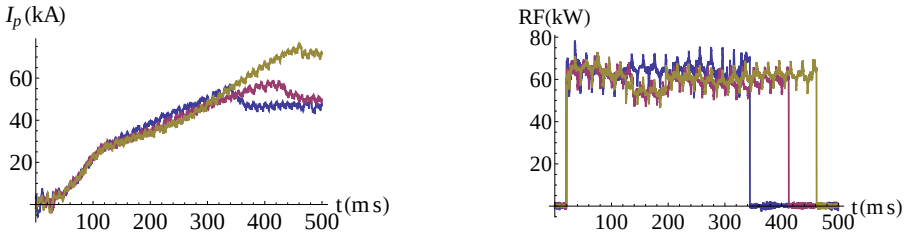

Figure 2.9: The time evolution of (a) the plasma current and (b) the RF power for successive MAST shots #28947 (blue), #28953 (red) and #28954 (yellow) of increasing RF power duration.

A record current of 73 kA was generated with 60 kW of injected RF power for 440 ms, using optimised B_V ramp-up. If the RF pulse had been available for a longer time, a larger plasma current would most likely have been reached, but even so a current drive efficiency of 1.2 A/W was achieved. In order to compare the current drive efficiency of different experiments, the generated plasma currents at a given time after CFS have formed are compared and shown in figure 2.10. Interestingly, all experimental points fit a linear dependence of generated plasma current versus RF power injected into the plasma, with a current drive efficiency of ~ 1 A/W [6, 29].

Experiments showed that the plasma current decays slowly after the end of the RF pulse, but can be shortened by additional gas puffing. This suggests that the current is carried predominantly by suprathermal electrons, which are almost collisionless in the plasma, such that they do not slow down after the RF drive is switched off [11, 29]. Detailed studies of electron cyclotron emission (ECE) data showed that the current is predominantly carried by a fast electron tail with energy of $25 - 50$ keV. The total current can be explained as due to a population of energetic electrons less than 5% of the total number of electrons [29].

Detailed measurements of electron temperature and density profiles were not possible, as the plasma density was below the Thomson scattering sensitivity limit, but, where measurements were possible, it suggested plasma densities of about $3 \times 10^{17}\,\mathrm{m}^{-3}$, as estimated

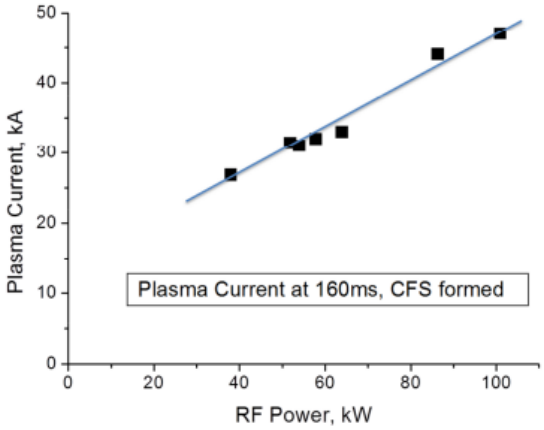

Figure 2.10: Scaling of start-up current measured after closed flux surfaces formation against injected RF power [29].

from interferometric measurements, and electron temperatures ranging from 200 eV to about 400 eV. These parameters were used for ray-tracing and Fokker-Planck modelling, to show that EBWs develop $N_{\|}$ within the range of $0.3 - 0.5$ as they approach the ECR, with about 98% of power absorbed from the EBW mode. The difference between power absorbed by electrons with positive and negative $v_{\|}$ was found to be responsible for the net generated current, with Fokker-Planck modelling predicting currents about a factor 2 larger than the experimentally measured plasma current [29], however, as explained in the next section, Fokker-Planck calculations of current drive are not valid in this plasma regime.

2.3 Modeling EBW start-up

EBW start-up experiments conducted on MAST relied on a double MC for EBW excitation. It showed that a fully non-inductive start-up scheme is possible with RF waves in the range of the fundamental EC frequency, with record plasma current of up to 73 kA generated. Experiments qualitatively proved the EBW CD mechanism, but by developing a model for studying EBW start-up, greater understanding of the start-up scenario can be obtained.

Experiments drew a number of conclusions, some of which are well understood, while others are less well understood:

1. Ray-tracing and Fokker-Planck modelling confirmed that the injected RF power undergoes a double MC for the excitation and absorption of EBW. A large amount of power ($\sim 98\%$) is absorbed from the EBW, with the value of the wave vector parallel

to the magnetic field $k_{\parallel}$ determined by the local magnetic field at the UHR. Modelling predicted that the CD mechanism responsible is the difference in power absorbed between electrons with $v_{\parallel} > 0$ and $v_{\parallel} < 0$, with the predicted plasma current generated about a factor 2 greater than experimentally measured. The problem is that models for studying ECCD assume the formation of CFS [23, 42, 43], which is not the case during start-up. These models are therefore not valid for studying the early phase of RF start-up, and so the development of a start-up model is needed to understand the influence of various parameters during this early phase [6, 11].

2. Experiments concluded that the majority of the plasma current is carried by energetic electrons with energies above 25 keV, as measured from the time it takes for the plasma current to decay after RF power is switched off, and from ECE measurements. EBW generates a large value for the wave vector parallel to the magnetic field $k_{\parallel}$, even though the wave is almost perpendicular to the magnetic field. This allows electrons at high energies to still interact with the wave, leading to the creation of energetic electrons [6, 11].

3. Shifting the plasma up or down helps the formation of CFS. By definition, a positive current is carried by electrons with $v_{\parallel} > 0$, due to the toroidal field in MAST $\vec{B}_{\phi} = -B_{\phi}\hat{\phi}$. In order to heat electrons with $v_{\parallel} > 0$, an EBW with $N_{\parallel} > 0$ must be created at the UHR, but this can only be done below the midplane. As the majority of the EBW is deposited just above the midplane, shifting the magnetic axis upward will create favourable $N_{\parallel}$ in the MC zone. After CFS form, the vertical magnetic field changes sign in the MC zone, and the magnetic axis must be shifted back downwards to ensure $N_{\parallel} > 0$ in the MC zone [6, 11].

4. Experiments showed that the most efficient way of generating a large plasma current is by increasing the vacuum poloidal field strength, with no explanation given for this phenomena [6, 11, 16].

5. Experiments showed that there exists a linear relationship between the injected RF power and generated plasma current. From Fokker-Planck modelling a stronger than linear dependence is expected, but might only be observed at higher power [6]. Unfortunately, the RF power available in experiments was limited to 100 kW, but, as the

Fokker-Planck models used to predict plasma current are not valid for start-up scenarios, an EBW start-up model should give a better understanding of the relationship between injected RF power and generated plasma current [6].

Experiments showed that a fully non-inductive start-up scheme is possible with RF waves, even though some aspects with regards to the generation of a plasma current, in particular, are not well understood. For instance, experiments concluded that the current is carried by energetic electrons. As these electrons undergo very few collisions, typical CD mechanisms, such as the Fisch-Boozer mechanism [19], have to be excluded. Other notable studies into CD mechanisms have included pressure driven currents [14], and the study of single particle orbits [12, 14, 15]. These models, however, rely on the reconstruction of magnetic equilibria from experimentally measured quantities, and are therefore unable to provide quantitative insight into how plasma observables evolve during start-up.

In order to gain a better understanding of RF start-up, a new model must be developed in order to provide explanations and make predictions for EBW start-up. Although models exist for studying RF CD, these are only valid after CFS have formed, while the most interesting phase during RF start-up is the formation of CFS. The effect of the open magnetic field line configuration is therefore expected to be important during start-up, as well as the plasma-wave interaction. The aim of this thesis then is to develop a model capable of simulating EBW start-up and provide explanations for experimentally observed effects, especially the CD mechanism and the role of the vacuum poloidal field.

Chapter 3

Development of a kinetic plasma start-up model

EBW-assisted start-up experiments conducted on MAST showed the feasibility of fully non-inductive start-up, with currents up to 73 kA achieved noninductively with up to 100 kW of input power [6]. An important aspect of the start-up phase is the transition from an open magnetic field line configuration to the formation of closed flux surfaces (CFS). The formation of CFS drastically affects the plasma equilibrium and confinement, and therefore also the current drive (CD) mechanism. An investigation of the start-up process and development of reliable start-up models are therefore not only important for gaining an understanding of successful start-up in tokamaks, but also for predicting performance and start-up requirements for present and future STs.

The plasma-wave interaction and its use for CD have long been studied [19], but modelling has mainly focused on the flat-top or current ramp-up phase, after the formation of CFS [23, 43], and is therefore not valid for start-up studies. Start-up models have been developed for simulating inductive start-up, but only consider the heating from RF power, and neglect any CD resulting from its use [8, 9, 44, 45], while non-inductive start-up has been studied qualitatively using single particle orbits as a means of understanding the CD mechanism, rather than simulating the start-up process, such that several experimentally observed phenomena remain unexplained.

In this chapter, the development of a new start-up model is described. In order to be computationally manageable, the model needs to be tractable, while covering the important

physics to provide sufficient insight into non-inductive start-up. This will lead to the inclusion of the effects thought to be most important during start-up, while other effects will be neglected.

The challenges in developing a model for simulating non-inductive start-up are first discussed, followed by the approximations and assumptions which led to the creation of a 0D model for studying the electron distribution function in two momentum dimensions. This model forms the cornerstone of this thesis, with the solution and results discussed in the following chapters.

3.1 Simulating microwave start-up

The development of models is crucial for both understanding and predicting start-up requirements. Although plasma-wave interactions for the means of CD have been studied for decades, it has mainly focused on the flat-top or current ramp-up phase, after the formation of CFS [23, 42, 43]. These models are therefore not valid during the start-up phase, when the magnetic field line configuration is open.

Existing start-up models, on the other hand, model inductive start-up, and only consider the heating resulting from the use of RF power, while neglecting its contribution to the CD [8, 9, 44, 45]. These models can therefore not be used when studying non-inductive start-up where the generated current results from the use of RF power.

The use of RF power for the generation of a plasma current has mainly been modelled through the use of single particle orbits, particularly as a means to explain the formation of CFS under RF power alone [12, 14, 15, 46]. These models, although useful in providing insight into the CD mechanism, are unable to simulate the entire start-up scenario or study the various dependences and relationships between different start-up variables. Therefore the development of new models is necessary to conduct more detailed studies in order to quantitatively simulate the start-up process and study the various dependences and relationships between observables.

There are many effects to take into consideration for any start-up scenario, amongst the most important the effect of the open magnetic field line configuration during start-up and the effect of RF heating. These two effects greatly complicate the study of any start-up scenario for two reasons:

1. The formation of CFS confines the motion of electrons to these closed field lines, as particle drifts cancel around the particle orbit, and orbital losses of electrons are greatly reduced. This effect has been used to simplify the study of ECCD after the formation of CFS as electron orbits can be averaged over [23, 42], but cannot be used during start-up. In the open magnetic field line geometry, electron orbits depend on both the origin and the electron's momentum $\vec{p}$, in addition to the magnetic field line structure, which rapidly changes as a plasma current is generated. Taking an average over the particle orbits, as can be done after the formation of CFS, is therefore not possible, as each electron has a unique orbit. The motion of electrons in real space, including the orbital losses of electrons, therefore complicates the study of single particle orbits, while the rapid change of the magnetic field topology adds to this problem.

2. The plasma-wave interaction depends on both momentum and position, through the magnetic field. The size of the beam is finite, but the location in the plasma where an electron interacts with it will determine the amount of energy an electron can gain. Such an interaction will change the electron's momentum, and by extension also its orbit.

The only way of including all effects, and accurately studying the effect of the open magnetic field line configuration and plasma-wave interaction, will be to solve the full problem, by solving the path and interactions of each electron in 3D. Such a model is of course computationally impossible, as a typical plasma has of the order of $10^{18} - 10^{20}$ electrons and ions, and reasonable approximations and assumptions will have to be made to simplify the problem while maintaining most of the important physics.

3.2 Development of a 0D2V kinetic model

Non-inductive start-up can be studied either through the particle approach, by simulating the movement and interactions of groups of particles and the injected RF wave, which is computationally very expensive, or by studying the time evolution of the electron distribution function, as has been done for RF heating after the formation of CFS [23, 42, 43].

The distribution function,

$$f = f(\vec{r}, \vec{p}, t)$$

can be used to calculate the parallel current density,

$$J_{\parallel}(\vec{r},t) = q_e \int v_{\parallel} f(\vec{r},\vec{p},t)\,\mathrm{d}^3p \tag{3.1}$$

electron density,

$$n_e(\vec{r},t) = \int f(\vec{r},\vec{p},t)\,\mathrm{d}^3p \tag{3.2}$$

the power absorbed,

$$P_d(\vec{r},t) = \frac{1}{2}m_e \int \mathrm{d}V \int v^2 \left(\frac{\partial f}{\partial t}\right)_{\text{RF heating}} \mathrm{d}^3p \tag{3.3}$$

and the thermal velocity,

$$\frac{3}{2}\left(m_e v_t(\vec{r},t)\right)^2 = \frac{1}{n_e}\int p^2 f(\vec{r},\vec{p},t)\,\mathrm{d}^3p \tag{3.4}$$

from which the temperature,

$$T_e(\vec{r},t) = \frac{1}{2}m_e\left(v_t(\vec{r},t)\right)^2 \tag{3.5}$$

can be found. This makes the distribution function a useful tool in studying non-inductive start-up. Note that the temperature is merely a measure of the average energy of a distribution, which allows the comparison of average energy between different, (non)-Maxwellian, distributions.

To completely describe the problem, without any assumptions or averages, the full $3+3$ dimensional distribution function must be solved as a function of time. This does not, however, particularly simplify the problem - as electron orbits are momentum dependent, electrons are not confined to fixed orbits, and it's still necessary to trace out the orbit of each electron in order to describe their motion in space. Added to this is the position and momentum dependent plasma-wave interaction, and it is clear that creating a $3+3$ dimensional distribution function would be nearly impossible, and a number of simplifications must be made.

Firstly, for simplicity, and to allow for rapid calculations, the distribution function is assumed to have zero spatial dependences, based off the success of other 0D start-up models [8,9,44,45]. This assumption implies that the distribution function is homogeneous in space, which it will not be during start-up due to the momentum dependence of electron orbits and

the localised RF heating, but in order to ensure the model is tractable, such a simplification must be made. In order to account for the spatial dependences of some effects, such as the plasma-wave interaction, appropriate volume averages will have to be taken when calculating the 0D approximations of these terms.

Secondly, a strong magnetic field results in a large gyrofrequency. If the gyrofrequency exceeds all other frequencies of interest, the gyrophase can be averaged over to eliminate one dimension. This is similar to assuming that deviations on the order of a gyro-orbit does not occur, such that only two momentum dimensions need to be retained, and the distribution function can be studied in either cylindrical $(p_\parallel, p_\perp)$ or spherical (p, θ) coordinates.

The choice between the two coordinate systems depend on the effects impacting the distribution. For example, collisions are best described in spherical coordinates, while the natural coordinate system for describing RF heating is cylindrical coordinates. As experiments concluded that the majority of the generated current is carried by energetic electrons [6, 11], which undergo very few collisions, and the typical collision times during start-up is long due to the low densities (Appendix E), collisions are not expected to be dominant. In comparison, RF heating is expected to dominate, and therefore the electron distribution function

$$f = f(p_\parallel, p_\perp, t)$$

is studied in cylindrical coordinates and depends on only two momentum dimensions (0D2V), as well as time.

If the distribution function is known, all quantities of interest during start-up can be studied. Of course, in general, the distribution function will be both position and momentum dependent, with its shape determined by a wide variety of effects, such as ionisation, orbital drifts, collisions, plasma-wave interactions, electric fields, radiation, and recombination, amongst others, and including all effects is difficult.

A further simplification is therefore made by separating the problem into three parts, studying the wave propagation and absorption, the electron density evolution, and the plasma current generation separately. The wave propagation and absorption can be studied with ray-tracing models, by solving the dispersion relation (Appendix A). However, it has been showed that the majority of the injected power ($\sim 95\%$) is converted to and absorbed from the EBW in MAST [6, 11], and the assumption is therefore made that all injected power is

absorbed from the EBW.

The time evolution of the electron density can be obtained from particle and power balance models, and depends on ionisation, recombination, equilibration and impurity effects [8, 44]. These effects are dominated by collisions, and, as experiments concluded that the majority of the plasma current is carried by energetic electrons, which undergo very few collisions, the effects of density evolution and current generation can be separated into effects dominated by thermal and energetic electrons, respectively. In this work, the time evolution of the electron density is assumed known, while ionisation effects are neglected in modelling the generation of a plasma current.

The electron distribution function therefore mainly models the energetic electrons and their effect on the generated plasma current. Ionisation effects, such as recombination, equilibration, radiation and impurity effects are therefore neglected, as they mainly influence the electron density and not the current drive. However, a source term is included in order to ensure the distribution function has the correct density. In order to make predictions for future STs, these effects will have to be included in order to accurately model the time evolution of the electron density, but this is neglected for now.

The time evolution of the electron distribution function is then described by the following effects only,

$$\frac{\partial f(p_\parallel, p_\perp, t)}{\partial t} = \text{source} + \text{loss} + \text{RF heating} + \text{induction} + \text{collisions} \tag{3.6}$$

where the source term describes cold electrons entering the system, resulting mainly from ionisations, the loss term models electrons streaming out of the plasma volume along the open magnetic field lines, the RF heating term models the interaction between the electrons and injected RF power, the induction term describes the response of the plasma to a varying plasma current, and the collision term describes electron-electron and electron-ion Coulomb collisions.

These terms will all impact the distribution function in different areas of momentum space, as illustrated in figure 3.1. In order to study the time evolution of the distribution function under the effect of these terms, mathematical expressions for each term must be formulated.

The distribution function $f = f(p_\parallel, p_\perp, t)$ is then represented in cylindrical coordinates,

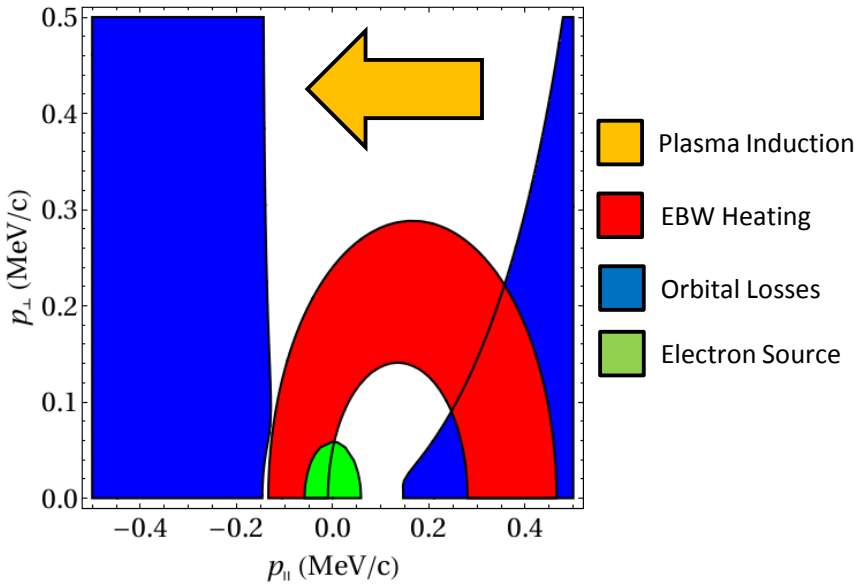

(a)

Figure 3.1: The typical locations where the various terms have an effect on the distribution function in momentum space.

where $p_\parallel$ is the momentum component parallel to the magnetic field and $p_\perp$ is the momentum component perpendicular to the magnetic field. As the toroidal magnetic field is typically about two orders of magnitude greater than the poloidal magnetic field in the plasma core during start-up, $p_\parallel$ is taken to be in the toroidal direction, and small fluctuations in the orientation of $p_\parallel$ and $p_\perp$ can be neglected. The choice of coordinate system is determined by the RF heating and collision terms; RF heating is best described in cylindrical coordinates, while collisions are best described in spherical coordinates. As experiments have suggested that the current is carried by energetic electrons, which undergo very few collisions, and the measured densities are relatively low, collision times are long compared to RF frequencies (Appendix E). As the natural coordinate system for describing RF heating is cylindrical coordinates, the distribution function is described in cylindrical coordinates $(p_\parallel, p_\perp)$. The numerical solution of the distribution function will be discussed in Chapter 5.

3.3 Electron sources

An important aspect of start-up is the increase in electron density, as collisions between free electrons and neutral atoms lead to ionisations, resulting in additional free electrons. Under the assumption that the ionised electrons are isotropic in momentum and have the same

characteristic temperature, the source term, modelling the addition of cold electrons to the plasma, can be represented with a Maxwellian,

$$\left(\frac{\partial f}{\partial t}\right)_{\text{source}} = \frac{S_0}{\pi^{3/2} p_0^3} \exp\left[-\frac{p_\parallel^2 + p_\perp^2}{p_0^2}\right] \tag{3.7}$$

where S_0 is the rate at which they are added. The value of p_0 is determined from the thermal velocity of a 2 eV Maxwellian distribution.

The value of S_0 is determined in such a way to maintain the time dependence of the density calculated from the distribution function compared to some known density, providing consistency. In general, the value of S_0 depends on the ionisation rate, which depends on the electron temperature and density, as well as the exact shape of the distribution function. However, as the majority of the plasma current is carried by energetic electrons which undergo very few collisions, thermal electrons are responsible for ionisations, while not contributing to the current drive. The effect of ionisation is therefore neglected, and the time evolution of the electron density assumed known.

In order to make predictions for future STs, the time evolution of the electron density has to be modelled. This can be done by solving particle and energy balance [8, 9], and by including the additional effects of ionisation and recombination, amongst others. In this work, however, the density is assumed known.

3.4 Loop voltage and plasma induction

The generation of a plasma current creates a changing magnetic field, which, according to Faraday's law, generates an electric field. According to Lenz's law, the current induced by this electric field will be in a direction opposing the current that created it, i.e.

$$\varepsilon = -\frac{d\Phi_B}{dt}$$

where Φ_B is the magnetic flux created by the plasma current I_P and ε is the induced voltage.

In terms of self-induction, Lenz's law can be written as a circuit equation,

$$V_L = -L_P \frac{dI_P}{dt} \tag{3.8}$$

where V_L is the loop voltage generated by a change in plasma current, and the minus sign indicates that it opposes the direction of the current I_P. The self-inductance of the plasma L_P can be calculated with [47],

$$\frac{1}{2}L_P I_P^2 = \int_V \frac{B_\theta^2}{2\mu_0}\mathrm{d}^3 r$$

where the integral has to be done over the plasma volume and B_θ is the poloidal magnetic field. It is also given by [44],

$$L_P = \mu_0 R_0 \left(\log \frac{8R_0}{a} + \frac{\ell_i}{2} - 2 \right)$$

where R_0 and a is the major and minor radii, respectively, and the internal inductance is given by [2]

$$\ell_i = \frac{2\int_0^a B_\theta^2 r \mathrm{d}r}{a^2 B_{\theta a}^2} \approx 0.5$$

for a flat I_P profile. This leads to a value for the self-inductance of $L_P \approx 6.5 \times 10^{-7}\,\mathrm{H}$ for a typical MAST plasma, used throughout this work. Although the value for L_P will not be constant during start-up, it is assumed to be constant, based off the success of this approach in simulating start-up experiments on JET [8]. This introduces an error in the generated current, but this error is expected to be comparable to experimental uncertainties.

The loop voltage induced by a change in the plasma current will cause electrons to be accelerated in a direction opposing the change in plasma current. In STs, the toroidal magnetic field is about two orders of magnitude greater than the poloidal field in the plasma core during start-up, such that the parallel velocity of electrons is essentially in the toroidal direction. The loop voltage induced by a change in the toroidal current will therefore affect the parallel motion of electrons,

$$\frac{\partial f}{\partial t} = -q_e \frac{V_L}{2\pi R_0} \frac{\partial f}{\partial p_\parallel} \tag{3.9}$$

where the value of V_L is obtained under the condition that (3.8) holds and R_0 is the major radius. Although an induced electric field will vary across the plasma, its value is taken at the centre of the plasma volume in order to account for the 0D nature of the model, in accordance with [8].

3.5 Orbital losses

The open magnetic field line configuration during start-up leads to losses of electrons, as electrons can freely stream along these field lines out of the plasma. For a constant, vertical magnetic field in an axisymmetric plasma, electrons will experience ∇B and curvature drifts, such that the guiding centre approximation (Appendix D) can be written as

$$V_Z = \frac{B_Z}{B} v_\parallel + \frac{m_e}{eBR}\left(\frac{v_\perp^2}{2} + v_\parallel^2\right)$$

for a toroidal field $B_\phi < 0$. In MAST, the vertical magnetic field $B_Z < 0$, and, as the second term on the right-hand-side, the drift term, is always positive, only electrons with $v_\parallel > 0$ can satisfy $V_Z = 0$. These electrons will be confined, while all other electrons with $V_Z \neq 0$ will be lost to either the top or bottom of the vessel. This effect leads to an asymmetric confinement of electrons, which can be used to generate a plasma current [21].

In a tokamak, however, the magnetic field is not constant, and its curvature leads to the additional confinement of electrons through the magnetic mirror effect. Further, as a current is generated, the magnetic field line configuration changes, and so will the confinement of electrons. This dependence of the electron confinement on the magnetic field structure is very important and must be studied in detail in order to quantify this loss mechanism.

In non-inductive start-up models [8], the electron losses are approximated through a loss time, and detail of the magnetic field structure and its influence on electron confinement is neglected. In order to fully describe the effect of electron losses, a combination of the loss time and electron confinement is considered, such that the loss term is approximated by

$$\left(\frac{\partial f}{\partial t}\right)_{\text{loss}} = -\frac{f}{\tau_{\text{loss}}} P_{\text{loss}}(p_\parallel, p_\perp) \tag{3.10}$$

where τ_{loss} is the characteristic loss time and $P_{\text{loss}}(p_\parallel, p_\perp)$ is the probability of an electron being lost or confined. This term and its dependence on the magnetic field will be discussed in detail in Chapter 4.

3.6 Collisions in a tokamak plasma

Collisions play an important role in plasmas through the ionisation of neutral atoms, the excitation and subsequent radiation of ions and atoms, and Coulomb collisions between

electrons and ions. As experiments concluded that the majority of the plasma current is carried by energetic electrons, which undergo very few collisions, ionisation effects are not expected to contribute to the current drive. The collision term therefore only describes the effect of Coulomb collisions between electrons and ions, resulting in pitch-angle scattering.

The Fokker-Planck collision operator describes the local collisional relaxation process of distribution functions in plasmas under the assumption of binary, small-angle collisions [48–50], and can be written as the divergence of a flux,

$$\frac{\partial f}{\partial t} = -\vec{\nabla} \cdot \vec{S}_c$$

where, in cylindrical coordinates,

$$\vec{\nabla} \cdot \vec{S}_c = \frac{1}{p_\perp} \frac{\partial}{\partial p_\perp} p_\perp S_\perp + \frac{\partial}{\partial p_\parallel} S_\parallel$$

with

$$S_\perp = -D_{\perp\perp} \frac{\partial f}{\partial p_\perp} - D_{\perp\parallel} \frac{\partial f}{\partial p_\parallel} + F_\perp f$$
$$S_\parallel = -D_{\parallel\perp} \frac{\partial f}{\partial p_\perp} - D_{\parallel\parallel} \frac{\partial f}{\partial p_\parallel} + F_\parallel f$$

and $p_\parallel$ is the momentum parallel and $p_\perp$ the momentum perpendicular to the background magnetic field. Collisions are best described in spherical coordinates, in which there are no mixed derivative terms, but due to RF power being best described in cylindrical coordinates, and expected to be the dominant term, the collision operator has to be written in cylindrical coordinates.

The cylindrical coordinate functions are related to spherical coordinates through

$$\begin{pmatrix} D_{\perp\perp} \\ D_{\perp\parallel} \\ D_{\parallel\perp} \\ D_{\parallel\parallel} \end{pmatrix} = \begin{pmatrix} \sin^2\theta & \sin\theta\cos\theta & \sin\theta\cos\theta & \cos^2\theta \\ \sin\theta\cos\theta & -\sin^2\theta & \cos^2\theta & -\sin\theta\cos\theta \\ \sin\theta\cos\theta & \cos^2\theta & -\sin^2\theta & -\sin\theta\cos\theta \\ \cos^2\theta & -\sin\theta\cos\theta & -\sin\theta\cos\theta & \sin^2\theta \end{pmatrix} \begin{pmatrix} D_{vv} \\ D_{v\theta} \\ D_{\theta v} \\ D_{\theta\theta} \end{pmatrix} \tag{3.11}$$

and

$$\begin{pmatrix} F_\perp \\ F_\parallel \end{pmatrix} = \begin{pmatrix} \sin\theta & \cos\theta \\ \cos\theta & -\sin\theta \end{pmatrix} \begin{pmatrix} F_v \\ F_\theta \end{pmatrix} \tag{3.12}$$

where θ is the angle between $p_\parallel$ and $p = \sqrt{p_\parallel^2 + p_\perp^2}$.

The collision operator can therefore be written as the sum of 6 terms,

$$\begin{aligned}\frac{\partial f}{\partial t} = &\frac{1}{p_\perp}\frac{\partial}{\partial p_\perp} p_\perp \left[D_{\perp\perp}\frac{\partial f}{\partial p_\perp} + D_{\perp\parallel}\frac{\partial f}{\partial p_\parallel} - F_\perp f \right] \\ &+ \frac{\partial}{\partial p_\parallel}\left[D_{\parallel\parallel}\frac{\partial f}{\partial p_\parallel} + D_{\parallel\perp}\frac{\partial f}{\partial p_\perp} - F_\parallel f \right]\end{aligned} \tag{3.13}$$

where the mixed derivative terms $D_{\parallel\perp}$ and $D_{\perp\parallel}$ complicate any numerical approximation, and an approximation must therefore be found which preserves positivity and conserves energy and particle number. The numerical approximation to the Fokker-Planck collision operator will be discussed in Chapter 5.

3.6.1 Approximations to the collision operator

The collision operators D and F could be obtained from the Rosenbluth potentials [48] or the Landau integrals [49], but, as this increases the complexity and the computational time required to solve the problem, and collisions are not expected to be dominant, approximations to the collision operator can be obtained.

3.6.1.1 Electron-electron collisions

The simplest approximation to make is that of an isotropic background Maxwellian. As the majority of the current is carried by energetic electrons which undergo very few collisions, the effect of self-collisions between electrons in the distribution is approximated with a background Maxwellian of the same temperature and density as the distribution itself. This leads to

$$D_{v\theta} = D_{\theta v} = F_\theta = 0$$

while

$$\frac{\partial f}{\partial \theta} = 0$$

and the only operators of interest are[1]

$$\begin{aligned} D_{vv} &= \frac{\Gamma}{2p}\left(\frac{\mathrm{erf}(u)}{u^2} - \frac{\mathrm{erf}'(u)}{u}\right) \\ D_{\theta\theta} &= \frac{\Gamma}{4p}\left(\left(2 - \frac{1}{u^2}\right)\mathrm{erf}(u) + \frac{\mathrm{erf}'(u)}{u}\right) \\ F_v &= -\frac{\Gamma}{p^2}\left(\mathrm{erf}(u) - u\,\mathrm{erf}'(u)\right) \end{aligned} \tag{3.14}$$

where $u = p\,/\,p_t$ and p_t is the thermal momentum of electrons in the background Maxwellian distribution.

As the distribution is not a Maxwellian, this approximation will lead to an error, while also not conserving energy. Appendix I studies the accuracy of this approximation and shows that it leads to an error of $\sim 10\%$ which is acceptable given the experimental uncertainties.

3.6.1.2 Electron-ion collisions

Relative to electrons, ions are considered to be massive, with $p_e \gg p_i$, such that the approximations $m_i \to \infty$ and $v_i \to 0$ can easily be made. This leads to a collision operator,

$$\begin{aligned} D_{vv} &= 0 \\ D_{\theta\theta} &= \Gamma\frac{Z_i}{2v} \\ F_v &= 0 \end{aligned} \tag{3.15}$$

where Z_i is the atomic number of the ions. This collision operator is a good approximation for describing the electron-ion collisions, especially as the injected RF beam heats only electrons. The population of ions will therefore remain cold, such that the approximation $p_e \gg p_i$ is always valid.

3.6.1.3 Collision Rate

The collision rate is given by

$$\Gamma = \frac{n_e\, q_e^4\, \ln\Lambda}{4\pi\,\varepsilon_0^2\, m_e^2} \tag{3.16}$$

where $\ln\Lambda$ is the Coulomb logarithm, taken to be a constant equal to 15 (see Appendix E).

[1]The error function is defined as

$$\mathrm{erf} = \frac{2}{\sqrt{\pi}}\int_0^u \exp(-x^2)dx$$

3.7 Radiofrequency heating

An important aspect of microwave plasma current start-up is the interaction between the injected microwave beam and electrons, which is important for both plasma heating and CD. This plasma-wave interaction is described by the dispersion relation, which describes the propagation and absorption of a RF beam through a plasma, and quasilinear theory, which describes the effect of an injected RF beam on the electron distribution function (see Appendix A).

The idea behind RF CD is that the injected RF power interacts with a selection of electrons in resonance with the beam. These electrons are accelerated by the electric field of the RF beam, and, by controlling which electrons are accelerated, an asymmetry in the distribution function is created which could lead to the generation of a current.

This plasma-wave interaction leads to the diffusion of electrons in momentum space. If the injected beam is perpendicular to the magnetic field, the wave vector perpendicular to the magnetic field, $k_\perp$, will typically be a few orders of magnitude greater than the wave vector parallel to the magnetic field, $k_\parallel$, and electrons will predominantly gain a kick in perpendicular momentum. The effect of the interaction on the electron distribution function can therefore be approximated by [23],

$$\left(\frac{\partial f}{\partial t}\right)_{\text{RF heating}} = \frac{1}{p_\perp}\frac{\partial}{\partial p_\perp}\left(p_\perp D \frac{\partial f}{\partial p_\perp}\right) \tag{3.17}$$

where the diffusion coefficient D represents the location in momentum space where diffusion takes place, or where the resonance condition,

$$\omega - k_\parallel v_\parallel - n\omega_c = 0 \tag{3.18}$$

is satisfied. The resonance condition is spatially dependent through the magnetic field in the cyclotron frequency,

$$\omega_c = \frac{q_e B}{m_e \gamma} \tag{3.19}$$

and relativistic through the Lorentz factor γ. The diffusion coefficient is therefore written

as a volume averaged quantity,

$$D(p_{\parallel}, p_{\perp}) = D_0 \left\langle \exp\left[-\left(\frac{\omega - k_{\parallel} v_{\parallel} - n\omega_c}{\Delta\omega} \right)^2 \right] \right\rangle_{\text{Volume}} \tag{3.20}$$

where D_0 is a constant and $\Delta\omega$ the resonance width.

During start-up, the toroidal magnetic field is about two orders of magnitude greater than the poloidal magnetic field, such that the magnetic field dependence in the cyclotron frequency can be approximated by the toroidal field only, and $B \approx B_0/R$. This implies that the diffusion coefficient only depends on the radial distance R, and the volume average is significantly simplified.

3.7.1 D_0 and the power absorbed

In the case of a constant magnetic field in the single particle model, D_0 is found by calculating the increment in perpendicular velocity as an electron passes through the beam [23]. However, due to the spatial dependence of the resonance condition, and the 0D nature of the distribution function, a different method of determining the value of D_0 is required.

Consider the power density absorbed per unit volume, which can be calculated from the distribution function with [23],

$$\frac{dP_d}{dV} = \frac{1}{2} m_e \int v^2 \left(\frac{\partial f}{\partial t} \right)_{\text{RF heating}} \mathrm{d}^3 p$$

such that the power density absorbed is given by,

$$P_d = \frac{1}{2} m_e \int_V \mathrm{d}V \int v^2 \left(\frac{\partial f}{\partial t} \right)_{\text{RF heating}} \mathrm{d}^3 p \tag{3.21}$$

where V is the plasma volume.

The amount of RF power absorbed by the plasma is related to the well-known formula [40],

$$A = 1 - e^{-\tau} \tag{3.22}$$

where τ is the optical depth and A is the power absorbed, such that the total power absorbed from the ray can be related to the power absorbed calculated from the distribution function,

$$P_d = A P_0 \tag{3.23}$$

and the value of D_0 can be calculated in order to ensure this equality holds. The total injected power is given by P_0.

For an injected RF beam, the dispersion relation (see Appendix A) can be solved to obtain the damping, from which the optical depth and power absorbed, equation (3.22), can be calculated. Equating this to the power absorbed calculated from the distribution function, equation (3.21), the value of the diffusion constant D_0 can be determined.

3.7.2 Absorption width $\Delta\omega$

Electrons in resonance with the injected RF beam can "see" the electric field and be accelerated by it to gain a kick in energy. Absorption is therefore localised in momentum to those electrons which satisfy the resonance condition. Due to the spatial dependence of the magnetic field contained in the cyclotron frequency, however, the resonance condition also depends on position, and a volume average is taken to account for this. Further, the RF beam is divergent in space, such that absorption does not occur along a single line, but rather across a region in space. These effects, along with the inhomogeneity of the magnetic field, introduces a resonance width $\Delta\omega$, as absorption is not localised to a single point in space. The resonance width is then created by the variance of the magnetic field across the distance over which absorption takes place, due to the (non-relativistic) cyclotron resonance,

$$\omega_c \sim B \sim 1/R$$

which produces a resonance width

$$\Delta\omega \approx \omega \frac{\Delta R_{\mathrm{ECR}}}{R_{\mathrm{ECR}}} \tag{3.24}$$

where R_{ECR} is the location of the ECR and ΔR_{ECR} is the spatial width of the resonance layer. The derivation for this form of the resonance width relies on the wave vector being well defined and approximately constant across the region of absorption, when, in reality, the wave vector can evolve continuously while absorption takes place. This introduces a width in the value of the wave vector parallel to the magnetic field, $\Delta k_{\|}$, which can be written, in terms of the parallel refractive index,

$$\Delta\omega = \omega \frac{p_{\|}}{m_e c} \Delta N_{\|} \tag{3.25}$$

where $\Delta N_{\parallel} = \Delta k_{\parallel} c/\omega$.

The choice of using (3.24) or (3.25) will depend on the wave vector during absorption. In the case of EBW absorption, the value of $N_{\parallel}$, the refractive index of the wave parallel to the magnetic field, can vary significantly across the region of absorption, and (3.25) would be better suited for calculating $\Delta\omega$. In some other cases, however, such as EC absorption, the value of $N_{\parallel}$ remains roughly constant across the region of absorption, and (3.24) is better suited for calculating $\Delta\omega$.

3.7.3 Determining the wave parameters

Implementing the RF heating term requires knowledge of the wave parameters resulting in the absorption of the injected RF wave. This includes the parallel refractive index $N_{\parallel}$ and how it varies across the region of absorption, to obtain the variance in the parallel refractive index $\Delta N_{\parallel}$ or the resonance layer width ΔR_{ECR}. Appendix A describes the solution to the hot plasma dispersion relation, which can be used to obtain the wave parameters and absorption.

In MAST, a 28 GHz beam, placing the ECR at $R = 0.4\,\mathrm{m}$, is injected from the low field side as O-mode. The O-mode beam propagates through the plasma and is reflected off a grooved mirror-polariser on the central rod as an X-mode beam. The X-mode then propagates back into the plasma, through the ECR, and is converted to an EBW at the UHR. Finally, the EBW propagates back into the plasma and is totally absorbed before it reaches the ECR. A schematic of the EBW start-up scheme is shown in figure 3.2(a).

Experiments concluded, along with ray-tracing, that $\sim 95\%$ of the injected power is absorbed from the EBW [6, 11], such that the absorption from the O- and X-mode can be neglected. EBWs are longitudinal, short-wavelength electrostatic waves which can have large values for the refractive index N. The relationship between the parallel and perpendicular refractive indices are related to the magnetic field [26],

$$\frac{N_{\parallel}}{N_{\perp}} \sim \frac{B_{\theta}}{B_{\phi}} \tag{3.26}$$

where B_{θ} is the poloidal and B_{ϕ} the toroidal components of the magnetic field. Typically $B_{\phi} \gg B_{\theta}$ during start-up, resulting in small values for $N_{\parallel}$, with $N_{\parallel}$ having different signs above and below the midplane [28].

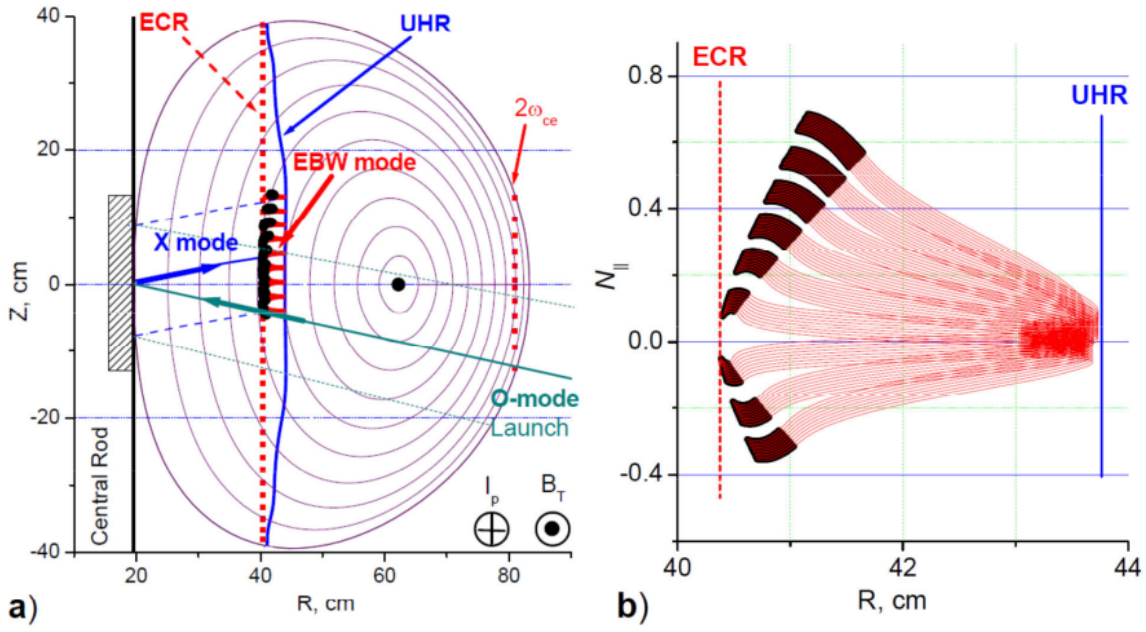

(a) (b)

Figure 3.2: (a) EBW start-up scheme shows the absorption region of EBW rays to be predominantly above the midplane. (b) EBWs develop $N_{||} > 0$ above the midplane and $N_{||} < 0$ below the midplane after the formation of CFS. Figures adopted from [6].

As the EBW propagates towards the ECR, the value of $N_{||}$ develops further due to the poloidal plasma inhomogeneity, while the beam diverges in space to allow for the excitation of EBWs with different values of $N_{||}$ at the UHR. EBWs can develop large values of $N_{||}$, as shown in figure 3.2(b), with typical values in the range $0.3 - 0.5$, while EBWs with $N_{||} = 1$ have also been detected [6, 11].

In MAST, the poloidal field is about two orders of magnitude greater than the toroidal field, such that

$$\tan\theta = \frac{N_\perp}{N_{||}} \sim \frac{B_\phi}{B_\theta} \approx 10^2$$

and $\theta \sim 89.4°$. In order to see how the refractive index varies across the region of absorption, the electrostatic approximation is solved for $\theta = 90°, 89°$ and $88°$, using an approximate relativistic dispersion relation, discussed in Appendix A [51].

The parallel and perpendicular refractive indices, as well as the imaginary component of N, is shown in figure 3.3 for a density $n_e = 5 \times 10^{18}\,\mathrm{m}^{-3}$ and temperature $T_e = 500\,\mathrm{eV}$ as a function of magnetic field.

The EBW will propagate from the low magnetic field side and be entirely absorbed before

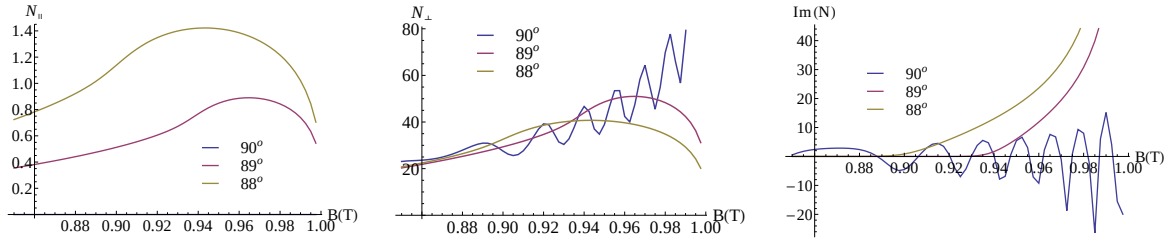

(a) (b) (c)

Figure 3.3: The (a) parallel and (b) perpendicular refractive indices, and (c) the imaginary part of the refractive index as a function of magnetic field strength for a density $n_e = 5 \times 10^{18}\,\mathrm{m}^{-3}$ and temperature $T_e = 500\,\mathrm{eV}$.

it reaches the ECR at $B = 1\,\mathrm{T}$, as the absorption coefficient is given by

$$\alpha = 2\frac{\omega}{c}N_i$$

where N_i is the imaginary component of the refractive index. The absorption coefficient is related to the optical depth τ through

$$\tau = \int \alpha \mathrm{d}s$$

where s is the path along the ray, and the total absorption is given by

$$A = 1 - e^{-\tau}$$

such that the absorption from the EBW is high. The oscillation of the refractive index for $\theta = 90°$ is due to the accuracy of the approximation, which is worse the smaller the value of $N_\parallel$. However, as the propagation is not exactly perpendicular, the value of $N_\parallel$ is generally large and varies significantly over the region of absorption.

Experiments suggested that electron densities are lower than the $n_e = 5 \times 10^{18}\,\mathrm{m}^{-3}$ used in figure 3.3. In order to see the effect of density on the refractive index of the EBW, consider figure 3.4, which shows the refractive index as a function of electron density, for different propagation angles, an electron temperature of $T_e = 500\,\mathrm{eV}$ and magnetic field strength $B = 0.99\,\mathrm{T}$. For lower densities, the UHR,

$$\omega^2 = \omega_p^2 + \omega_c^2$$

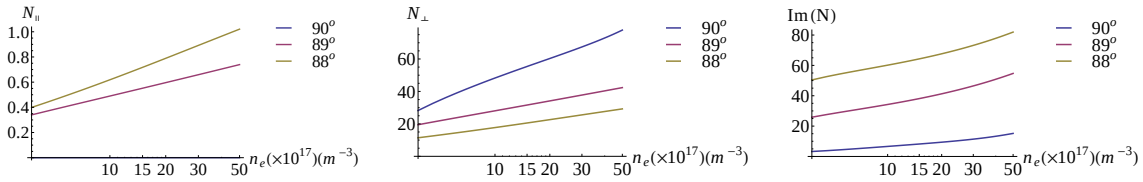

(a) (b) (c)

Figure 3.4: The (a) parallel and (b) perpendicular refractive indices, and (c) the imaginary part of the refractive index as a function of density for $B = 0.99\,\mathrm{T}$ and temperature $T_e = 500\,\mathrm{eV}$.

which depends on the electron density and determines the magnetic field strength where the EBW originates, is located very close to the ECR, and therefore the magnetic field chosen here is close to the ECR where $B = 1\,\mathrm{T}$.

It is important to note that absorption remains high for low densities, while the value of $N_{\parallel}$ reduces by about a factor 2 from $n_e = 5 \times 10^{18}\,\mathrm{m}^{-3}$ to $n_e = 3 \times 10^{17}\,\mathrm{m}^{-3}$. Although the range of magnetic field over which absorption occurs will be smaller for lower densities, as the UHR is located closer to the ECR, the RF beam diverges in space, and the beam is absorbed over a vertical range along the UHR, as shown in figure 3.2(b), and the value of $N_{\parallel}$ can still vary greatly.

The wave parameters could therefore be obtained from ray-tracing, but, as the value of $N_{\parallel}$ varies across the beam and across space, in order to obtain a global parameter describing the wave absorption an approximate value is more appropriate. The absorption width $\Delta\omega$ is important in describing the variance in the wave parameter, while the volume average contained in equation (3.20) is important to capture the spatial variance of the magnetic field across the region of absorption.

The EBW develops values of $N_{\parallel} = 0.3 - 0.5$ across the region of absorption, but as the wave diverts in space, an absorption width of $\Delta N_{\parallel} = 1$ is used along with equation (3.25). Alternatively, if it is assumed that the EBW has a well-defined wave vector along its absorption path, the absorption width can be calculated using equation (3.24) with $\Delta R = 0.05$.

3.7.4 Analytical Approximation to D_0

The diffusion constant D_0 is determined from the condition that the power absorbed calculated from the distribution function equals the total power absorbed,

$$P_d = AP_0$$

where A is the fraction of power absorbed and P_0 is the injected power. As an example, the value of D_0 can be calculated theoretically, in order to determine its dependence on the various plasma and wave parameters. In order to calculate a theoretical expression for D_0, a number of approximations, including taking the non-relativistic limit and assuming a Maxwellian distribution function, are made in order to simplify the integrals to forms which can be calculated analytically.

The absorbed power P_d is calculated using equation (3.21), which, when equating to the absorbed power AP_0 leads to

$$\begin{aligned} AP_0 &= \frac{1}{2} m_e \int_V \mathrm{d}V \int v^2 \left(\frac{\partial f}{\partial t}\right)_{\text{RF heating}} \mathrm{d}^3 p \\ &= \frac{1}{2} m_e \int_V \mathrm{d}V \int v^2 \frac{1}{p_\perp} \frac{\partial}{\partial p_\perp} p_\perp D_0 \left\langle \exp\left[-\left(\frac{\omega - k_\parallel v_\parallel - n\omega_c}{\Delta\omega} \right)^2 \right] \right\rangle_{\text{Volume}} \frac{\partial f}{\partial p_\perp} \mathrm{d}^3 p \\ &= \frac{1}{2} m_e \frac{1}{V} \int_V \mathrm{d}V \int_V \mathrm{d}V \int v^2 \frac{1}{p_\perp} \frac{\partial}{\partial p_\perp} p_\perp D_0 \exp\left[-\left(\frac{\omega - k_\parallel v_\parallel - n\omega_c}{\Delta\omega} \right)^2 \right] \frac{\partial f}{\partial p_\perp} \mathrm{d}^3 p \end{aligned} \tag{3.27}$$

when substituting equations (3.17) and (3.20) in. The volume average of the diffusion operator is written explicitly in the last line, which leads to the second volume integral. For simplicity, one of the volume integrals is discarded, using

$$\frac{1}{V} \int_V \mathrm{d}V = 1$$

Although this is not mathematically correct, due to the spatial dependence of the cyclotron resonance, the effect of the volume integral on the spatial dependence of the cyclotron resonance will be approximated later on, such that the second volume integral cancels with the $1/V$ term, and it is therefore performed here.

As D_0 is independent of momentum, define

$$I_W = \frac{1}{2} m_e \int_V \mathrm{d}V \int v^2 \frac{1}{p_\perp} \frac{\partial}{\partial p_\perp} p_\perp \exp\left[-\left(\frac{\omega - k_\parallel v_\parallel - n\omega_c}{\Delta\omega} \right)^2 \right] \frac{\partial f}{\partial p_\perp} \mathrm{d}^3 p \tag{3.28}$$

such that the diffusion constant D_0 can then be determined from,

$$D_0 = \frac{AP_0}{I_W} \tag{3.29}$$

and the integrals in I_W must be performed.

In order to find an analytical approximation to the value of D_0, first consider the volume integral in the expression for I_W (3.28). For simplicity, the plasma cross-section is considered to be circular in the poloidal plane, such that,

$$\int \mathrm{d}V = 2\pi R_0 \int r \, \mathrm{d}r \, \mathrm{d}\theta$$

where R_0 is the major radius, r is the radius of the plasma volume and θ is the angle around the poloidal plane, as shown in figure 3.5.

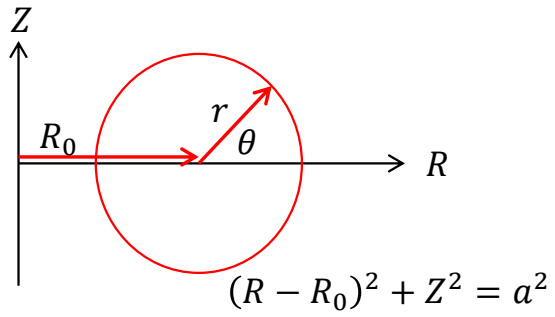

Figure 3.5: The coordinates for a circular plasma volume in the poloidal plane.

The plasma cross section is then described by the equation,

$$(R - R_0)^2 + Z^2 = a^2$$

where a is the minor radius, such that the volume integral can be written in terms of R and

Z,

$$\begin{aligned}\int \mathrm{d}V &= 2\pi R_0 \int \mathrm{d}R \int \mathrm{d}Z \\ &= 2\pi R_0 \int_{R_0-a}^{R_0+a} \mathrm{d}R \int_{-\sqrt{a^2-(R-R_0)^2}}^{\sqrt{a^2-(R-R_0)^2}} \mathrm{d}Z \\ &= 2\pi R_0 \int_{R_0-a}^{R_0+a} 2\sqrt{a^2-(R-R_0)^2}\,\mathrm{d}R\end{aligned}$$

where the integral over $\mathrm{d}Z$ can be performed under the assumption that the magnetic field (and therefore all terms) is independent of Z. As the toroidal field, which varies like $\sim 1/R$, is typically two orders of magnitude greater than the poloidal field, and it only depends on the radial distance R, this approximation is accurate.

This reduces the integral I_W to

$$\begin{aligned}I_W = \frac{2\pi R_0}{m_e} &\int_{R_0-a}^{R_0+a} \mathrm{d}R\sqrt{a^2-(R-R_0)^2} \\ &\int \frac{p^2}{\gamma^2}\frac{1}{p_\perp}\frac{\partial}{\partial p_\perp} p_\perp \exp\left[-\left(\frac{\omega - k_\parallel v_\parallel - n\omega_c}{\Delta\omega}\right)^2\right]\frac{\partial f}{\partial p_\perp}\mathrm{d}^3p\end{aligned}$$

Next, consider the momentum integral,

$$\int \mathrm{d}^3p = 2\pi \int p_\perp \mathrm{d}p_\perp \int \mathrm{d}p_\parallel$$

In the non-relativistic limit ($\gamma = 1$), the diffusion term does not depend on $p_\perp$, and the integral can be done analytically,

$$\begin{aligned}I_W &\sim \int \mathrm{d}p_\perp\, p^2 \frac{\partial}{\partial p_\perp} p_\perp \exp[\cdots]\frac{\partial f}{\partial p_\perp} \\ &= p^2 p_\perp \exp[\cdots]\frac{\partial f}{\partial p_\perp}\bigg|_0^\infty - \int \mathrm{d}p_\perp\, 2p_\perp^2 \exp[\cdots]\frac{\partial f}{\partial p_\perp}\end{aligned}$$

of which the first term must equal zero due to boundary conditions. The non-relativistic approximation is not trivial, as relativistic effects are known to be important for absorption (see Appendix A and figure A.3 for example), but such an approximation ensures the resonance condition within the exponential term depends on $p_\parallel$ only, and the $p_\perp$ integral can be done analytically.

The diffusion coefficient can be rewritten, for absorption around the fundamental reso-

nance ($n = 1$),

$$\exp\left[\cdots\right] = \exp\left[-\left(\frac{\omega - k_\parallel v_\parallel - n\omega_c}{\Delta\omega}\right)^2\right] = \exp\left[-\left(\frac{p_\parallel - p_{\parallel 0}}{\Delta p}\right)^2\right]$$

such that the $p_\parallel$ integral,

$$\int_{-\infty}^{\infty} \mathrm{d}p_\parallel \exp\left[-\left(\frac{p_\parallel - p_{\parallel 0}}{\Delta p}\right)^2\right]\frac{\partial f}{\partial p_\perp} = \Delta p\sqrt{\pi}\frac{\partial f}{\partial p_\perp}\bigg|_{p_\parallel = p_{\parallel 0}}$$

where $p_{\parallel 0} = p_{\parallel 0}(R)$ is the solution to the resonance condition.

Assuming a Maxwellian distribution,

$$f_M = \frac{n_e}{\pi^{3/2}p_t^3}\exp\left[-\frac{p_\parallel^2 + p_\perp^2}{p_t^2}\right]$$

where p_t is the thermal momentum, the $p_\perp$ integral can be performed,

$$\begin{aligned}
\int \mathrm{d}p_\perp\, p_\perp^2 \frac{\partial f}{\partial p_\perp}\bigg|_{p_\parallel = p_{\parallel 0}} &= \int \mathrm{d}p_\perp\, p_\perp^2 \frac{n_e}{\pi^{3/2}p_t^3}\left(-\frac{2p_\perp}{p_t^2}\right)\exp\left[-\frac{p_{\parallel 0}^2 + p_\perp^2}{p_t^2}\right] \\
&= -\frac{2n_e}{\pi^{3/2}p_t^2}\exp\left[-\frac{p_{\parallel 0}^2}{p_t^2}\right]\int \mathrm{d}p_\perp \left(\frac{p_\perp^3}{p_t^3}\right)\exp\left[-\frac{p_\perp^2}{p_t^2}\right] \\
&= -\frac{2n_e}{\pi^{3/2}p_t^2}\exp\left[-\frac{p_{\parallel 0}^2}{p_t^2}\right]\frac{p_t}{2}
\end{aligned}$$

to obtain for I_W,

$$I_W = \frac{8\pi n_e}{m_e}R_0\frac{\Delta p}{p_t}\int \mathrm{d}R \exp\left[-\frac{p_{\parallel 0}^2}{p_t^2}\right]\sqrt{a^2 - (R - R_0)^2} \tag{3.30}$$

where $p_{\parallel 0} = p_{\parallel 0}(R)$ and D_0 is given by (3.29).

Absorption in real space only occurs over a small region ΔR_{ECR} around R_{ECR}, such that the integral over R can be approximated,

$$\int \mathrm{d}R \exp\left[-\frac{p_{\parallel 0}^2}{p_t^2}\right]\sqrt{a^2 - (R - R_0)^2} \approx \exp\left[-\frac{p_{\parallel 0}^2}{p_t^2}\right]R_{\mathrm{ECR}}\Delta R_{\mathrm{ECR}}$$

with the absorption width, in the non-relativistic limit,

$$\Delta R_{\mathrm{ECR}} \approx 2|N_{\|}|\frac{p_t R_{\mathrm{ECR}}}{m_e c}$$

since $\omega - \omega_c = k_{\|} p_{\|}/m_e$ and $\omega - \omega_c \approx \omega\, \Delta R_{\mathrm{ECR}}/R_{\mathrm{ECR}}$. The additional volume integral, discarded earlier, would be performed here with no change in the result, as the spatial dependence is approximated with the location and width of the resonance R_{ECR}.

Combining all terms, the expression for D_0 becomes

$$D_0 = \frac{A P_0 m_e^2 c}{16\pi n_e \Delta p |N_{\|}| R_0 R_{\mathrm{ECR}}^2 \exp\left[-\frac{p_{\|0}^2}{p_t^2}\right]} \tag{3.31}$$

with Δp the absorption width in momentum space, and $p_{\|0}$ the solution to the resonance condition.

Absorption will be very weak ($A \to 0$) for a Maxwellian distribution if $p_{\|0} > p_t$. For significant absorption ($A \to 1$) to occur there must be a large number of electrons in resonance with the RF wave, which in the case of a Maxwellian distribution relates to $p_{\|0} \leq p_t$. This further reduces the expression for D_0 to

$$D_0 = \frac{A P_0 m_e^2\, c\, \exp(1)}{16\pi n_e \Delta p |N_{\|}| R_0 R_{\mathrm{ECR}}^2}$$

under the assumption $p_{\|0} = p_t$. The value of D_0 is therefore proportional to the amount of power absorbed AP_0, and inversely proportional to the electron density n_e, while the wave parameters determine the exact value of D_0.

Consider an example where a 50 kW, 28 GHz RF beam is fully absorbed ($A = 1$) by a plasma with density $n_e = 10^{18}\,\mathrm{m}^{-3}$ and temperature $T_e = 10\,\mathrm{eV}$. The wave parameters are taken to be $N_{\|} = 1$ and $\Delta p = 2\,\mathrm{eV}$, while $R_0 = 0.6\,\mathrm{m}$, $a = 0.4\,\mathrm{m}$ and the ECR is located at $R_{\mathrm{ECR}} = 0.4\,\mathrm{m}$. This gives an analytical value

$$D_0 = 6.4\,\mathrm{MeV}^2.c^{-2}.\mathrm{s}^{-1} \tag{3.32}$$

which compares well to the value obtained numerically,

$$D_0 = 7.2\,\mathrm{MeV}^2.c^{-2}.\mathrm{s}^{-1}$$

considering the number of approximations made. The numerical value is obtained by solving equation (3.27) numerically, including relativistic effects, and for a Maxwellian distribution of the same temperature, while all other parameters are the same as given above. The value of $N_{\parallel} = 1$ might not be in agreement with the approximation that $p_{\parallel 0} = p_t$, especially as the temperature $T_e = 10\,\mathrm{eV}$, but these values were only chosen as an example in order to show the dependences of D_0 in a simplified analytical example.

3.8 Summary

The development of models are useful and necessary in order to gain a better understanding of and make further predictions for experiments. Currently, no models capable of simulating non-inductive start-up exist, as existing start-up models neglect detailed contributions of RF power to the current drive (CD) [8, 9, 44, 45], while models capable of modelling RF CD do so under the assumption of CFS [23, 42, 43], and can therefore not be used to model non-inductive start-up. Studies into non-inductive start-up, on the other hand, have therefore mainly focused on using single particle orbits as a means of explaining the formation of CFS under RF power alone [12, 14, 15, 46]. These models, although useful, are unable to simulate the entire start-up process and study the various dependences and relationships between different start-up variables.

This chapter discusses the challenges faced with developing models for studying non-inductive start-up. Approximations and assumptions in developing a 0D model for studying the electron distribution function in two momentum dimensions, under the effect of several terms, is introduced, i.e.

$$\frac{\partial f}{\partial t} = \text{source} - \text{loss} + \text{RF heating} + \text{induction} + \text{collisions}$$

where $f = f(p_{\parallel}, p_{\perp}, t)$.

In order to ensure the model is tractable and computationally manageable, the assumption is made that the main physics can be captured within these terms, with appropriate volume averaging and approximations to account for the spatial dependences of some of these effects. The source term models cold electrons entering the system through ionisations; the loss term models electrons being lost by streaming out of the plasma along the open magnetic field lines; the RF heating term describes the plasma-wave interaction resulting in

electrons gaining a kick in momentum; the induction term describes the initiation of a loop voltage through plasma induction; and the collision term describes both electron-electron and electron-ion collisions.

The RF heating term results from the plasma-wave interaction, for which quasilinear theory describes the effect of an EM field on the distribution function. Electrons in resonance with the injected RF beam will gain a kick in energy, with the location of the interaction determined by the magnetic field and wave parameters, obtained from the dispersion relation. As the absorbed wave diverges in space, and due to the inhomogeneity of the magnetic field, an absorption width is introduced for describing the interaction. The value for the absorption width, as well as the parallel refractive index $N_{\|}$, can be obtained from an approximate solution to the electrostatic dispersion relation, but, as this solution describes the local absorption of a wave and the RF heating term describes the global effect, an approximate value is used.

The loss term, describing the loss of electrons streaming out of the plasma volume along the open magnetic field lines during start-up, is discussed in detail in Chapter 4, while the numerical approximation to the distribution function is discussed in Chapter 5. Results are discussed in Chapter 6, with comparisons made to experiments, as well as studies into the CD mechanism and experimentally observed effects, followed by conclusions and recommendations for future work in Chapter 7.

Chapter 4

Electron orbital losses

An important aspect of start-up is the change in the magnetic field line topology - from open field lines to closed flux surfaces (CFS) - driven by the generation of a plasma current. Creating CFS greatly improves confinement as if field lines are open, electrons can freely stream out of the plasma volume and into the vessel walls during the initial start-up phase.

In 0D models, the simplest representation of this loss mechanism uses the average time it takes for a thermal electron to be lost [8], but this is often inadequate as the momentum dependence of the electron losses can be important. In an axisymmetric plasma where the toroidal magnetic field is stronger than the poloidal magnetic field, the guiding centre approximation predicts that electrons are only subjected to ∇B and curvature drifts, which can be cancelled for a selection of electrons by adding a small vertical field. In this way, the confinement of electrons will be asymmetric in parallel momentum, and can contribute to the generated plasma current [21]. It is therefore important to understand how this asymmetric confinement evolves as the magnetic field line configuration evolves from open field lines to CFS.

The study of this preferential confinement of electrons has been used to explain the formation of CFS through the study of single particle orbits [12,14]. In order to do a quantitative study of non-inductive start-up, however, it is necessary to study the time evolution of the confinement of electrons as a function of changing magnetic field configuration, which is created by the sum of the vacuum magnetic field and the self-field generated by the plasma current.

Experiments suggested that the majority of the plasma current is carried by energetic electrons, which are created by an interaction with the injected RF beam [6, 11]. As these

electrons interact with the beam around the ECR layer, the assumption is made that all energetic electrons originate from this layer. By tracing out the orbits of these electrons using the guiding centre approximation (Appendix D), it can be determined which electrons are lost and confined, based on their initial velocities for a specific magnetic field line configuration.

The dependence of this electron confinement on the magnetic field line configuration is then studied in detail by varying the vacuum poloidal field strength, the current density profile and total plasma current. In addition, the effect of a vertical shift of the magnetic midplane and the spatial dependence of the origin of the electron orbits are studied in order to fully quantify the electron confinement. Experiments used a combination of a vertical shift and vacuum poloidal field ramp-up to generate large plasma currents, and, if the asymmetric confinement of electrons is responsible for the generation of plasma current, it is crucial to understand how these effects impact the confinement of electrons.

In this chapter, the particle loss time τ_{loss} is first introduced, followed by a detailed study of how the confinement of electrons depends on the vacuum poloidal field, current density profile and plasma current in order to formulate an algebraic expression for electron confinement that can be implemented in the mathematical representation of the kinetic model. Lastly, this expression is compared to numerically determined electron confinement for the conditions of experiments conducted on MAST.

4.1 Particle loss time

During start-up, electrons can freely stream along the open magnetic field lines out of the plasma volume. Modelling this loss mechanism is crucial for studying start-up, as it plays an important role in electron particle and energy balance [8], while it has been postulated that the asymmetric confinement of electrons could lead to the formation of a plasma current [21].

The first ingredient required to study the losses of electrons is an approximation for the time it takes for an electron to be lost out of the plasma volume to the vessel wall, τ_{loss}. An electron can be lost in two ways: electrons can freely stream along the open magnetic field lines out of the plasma during start-up; or electrons can drift across magnetic field lines, due to random collisions in the plasma. These loss mechanisms are termed parallel and perpendicular losses, respectively, with the parallel loss mechanism dominating electron losses until CFS have formed.

In parallel transport, the electrons stream along the magnetic field lines out of the plasma volume. This loss mechanism is particularly dominant for an open magnetic field line configuration, and can be represented by [8, 9],

$$\tau_{\parallel} = a_{\perp}(t)\frac{B_{\phi}}{B_Z}/v_{\parallel}$$

where $a_{\perp}(t)$ is the perpendicular distance out of the plasma volume, B_Z is the vertical magnetic field and B_{ϕ} the toroidal magnetic field. As this expression is only valid for open field lines, it has to be modified to allow for the formation of CFS as this significantly modifies the connection length and the time it takes for an electron to stream out of the plasma volume [8]. Assuming the first CFS forms at a plasma current I_{CFS}, then,

$$\tau_{\parallel} = a_{\perp}\ \exp\left[\frac{I_p}{I_{\mathrm{CFS}}}\right]\frac{B_{\phi}}{B_Z}/v_{\parallel} \tag{4.1}$$

where $a_{\perp}$ is the vertical distance out of the plasma volume, and the exponential term has been added to account for the formation of CFS [8]. The vertical distance is used as electrons are lost to the top or bottom of the vessel, as will be discussed later, but this is typically replaced with the minor radius, as this is a good approximation of the distance an electron has to travel out of the plasma volume.

Perpendicular loss becomes dominant after the formation of CFS. This loss mechanism is due to particle drifts across magnetic field lines, due to random collisions in the plasma. The Bohm diffusion model is typically used [2, 52], which provides a diffusion coefficient,

$$D_{\mathrm{Bohm}} = \frac{1}{16}\frac{T_e}{B} \tag{4.2}$$

where 1/16 is an empirical factor introduced by Bohm, T_e is measured in eV, and B is measured in T[1].

[1] If B is measured in T, then note that

$$\mathrm{T} = \frac{\mathrm{V\ s}}{\mathrm{m}^{-2}}$$

and

$$\mathrm{V} = \frac{\mathrm{eV}}{e}$$

where e is the charge of an electron in units of elementary charge, not Coulomb ($1\,\mathrm{V} = 1\,\mathrm{eV}/1e$), and the electron charge is neglected in calculations as the charge of an electron is equal to 1 unit of elementary charge.

The related diffusion velocity is then given by

$$v_{\text{Bohm}} = \frac{2D_{\text{Bohm}}}{a} \tag{4.3}$$

where a is the minor radius. Accordingly, the particle confinement time is[2]

$$\tau_{\perp} = \frac{a}{v_{\text{Bohm}}} = 8a^2 \frac{B}{T_e} \tag{4.4}$$

The total particle loss time τ_{loss} can then be calculated according to

$$\frac{1}{\tau_{\text{loss}}} = \frac{1}{\tau_{\parallel}} + \frac{1}{\tau_{\perp}} \tag{4.5}$$

and is shown in figure 4.1 for a typical thermal electron, with increasing temperature and plasma current. The parallel loss mechanism dominates at early times, as the magnetic field lines are open. The average time it takes for an electron to be lost initially decreases, as the generation of a plasma current increases the strength of the vertical magnetic field, such that electrons can stream out of the plasma faster. As the curvature of the magnetic field increases, due to the increasing plasma current, the perpendicular loss mechanism starts to dominate, as the parallel loss time tends to infinity once CFS are fully formed.

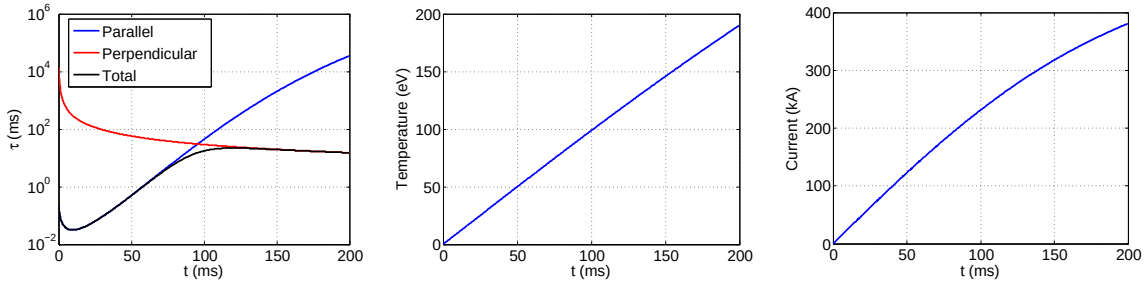

(a) (b) (c)

Figure 4.1: An example of (a) the typical loss time of a thermal electron in MAST as a function of time, with (b) the temperature and (c) the current increasing with time.

The parallel loss time depends on the magnetic field B_{ϕ}/B_Z, which depends both on position and the plasma current, as the self-field created by the plasma current changes the value of B_Z. Capturing these spatial effects in a 0D model is challenging, so the following assump-

[2] An example from [52] notes that for $B = 2.3\,\text{T}$, $T_e = 3\,\text{eV}$ and for TEXTOR vacuum vessel dimensions, $\tau_{\perp} = 0.5 - 1.5\text{s}$.

tions (based on MAST experiments) are made: firstly, energetic electrons are more likely to be lost than thermal electrons. These energetic electrons are created by an interaction with the injected RF beam, such that they all originate around the ECR layer where $B_\phi \approx 1\,\mathrm{T}$. Secondly, the value of B_Z depends on the vacuum poloidal field strength and the plasma current, and is therefore both time and position dependent. Consider the plasma current to be carried by an infinitely thin wire located on the midplane at the ECR layer. In MAST, the vertical vacuum poloidal field $B_V < 0$ and the toroidal magnetic field $B_\phi < 0$ typically, with $I_P > 0$. The magnetic field created by the plasma current will therefore increase B_Z on the outboard side and decrease B_Z on the inboard side. Further, $B_R < 0$ typically, such that electrons with $v_\parallel > 0$ will travel to the inboard side into regions of smaller B_Z, while electrons with $v_\parallel < 0$ will travel to the outboard side and regions of larger B_Z. This implies that electrons with $v_\parallel < 0$ will be lost faster than electrons with $v_\parallel > 0$.

The loss time for electrons can be determined by tracing out their orbits using the guiding centre approximation (Appendix D). An algebraic expression for the vertical field B_Z is then fitted to the numerical data to obtain

$$B_Z[\mathrm{mT}] = \begin{cases} 0.8B_V[\mathrm{mT}] & v_\parallel > 0 \\ 0.8B_V[\mathrm{mT}]\exp\left(\frac{|v_\parallel|}{c}\right) & v_\parallel < 0 \end{cases} \tag{4.6}$$

which leads to an asymmetry in the loss time, shown in figure 4.2 for a vertical vacuum poloidal field $B_V = 10$ mT for different values of I_P, for energetic electrons originating from the ECR layer on the midplane.

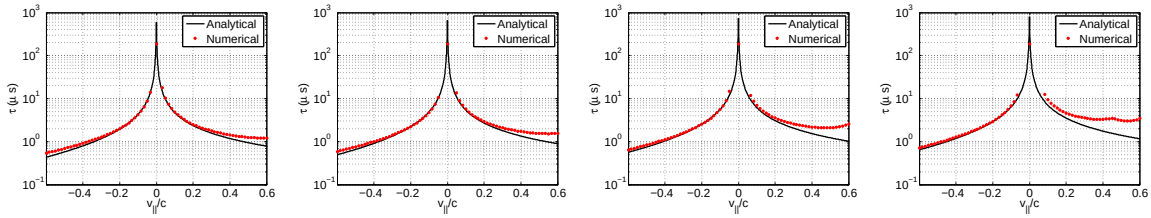

(a) (b) (c) (d)

Figure 4.2: The empirical loss time (black) compared to the numerical loss time (red) for $B_V = 10$ mT, with (a) $I_P = 2$ kA, (b) $I_P = 4$ kA, (c) $I_P = 6$ kA, and (d) $I_P = 8$ kA, where $v_\perp = 3 \times 10^7\,\mathrm{m.s^{-1}}$ and $a_\perp = 1$.

The analytical equation for the loss time, calculated using the empirical fit for B_Z, compares well to the numerical loss time for electrons with $v_\parallel < 0$, but large discrepancies are

found for electrons with $v_\parallel/c > 0.2$. This approximation is sufficient for two reasons: firstly, very few electrons will have large $v_\parallel$ as the RF heating mainly increases the perpendicular velocity of electrons and $v_\parallel$ will only increase through collisional pitch-angle scattering. Secondly, the loss time does not take into account the fact that certain electrons will be confined. Instead, it assumes that all electrons are lost, even though the curvature of the magnetic field allows electrons to complete confined (trapped or passing) orbits. It will be shown later that electrons with $v_\parallel > 0$ are more likely to be confined than electrons with $v_\parallel < 0$, with the likelihood of an electron being confined increasing with increasing $v_\parallel$. This explains the increase in the loss time for increasing $v_\parallel$, and the discrepancy will be corrected by weighting the loss time with a factor describing the likelihood of an electron being lost/confined.

As the loss time assumes that all electrons are lost, and gives the average time it takes for an electron to stream out of the plasma volume, the loss term has to contain an additional factor which ensures that confined electrons are not lost. The loss term is therefore given by

$$\left(\frac{\partial f}{\partial t}\right)_{\text{loss}} = -\frac{f}{\tau_{\text{loss}}(p_\parallel, p_\perp)} P_{\text{loss}}(p_\parallel, p_\perp) \tag{4.7}$$

where P_{loss} can be seen as the probability of an electron being lost or confined. Although not a true probability, it will equal 0 if an electron is confined and 1 if an electron is lost. As the confinement of an electron will depend on its origin, values in between 0 and 1 indicates the likelihood of an electron being lost/confined, and attempts to capture the spatial distribution of electron orbits.

Ideally, the loss time should be found by tracing out the orbit of every single electron in order to obtain the exact loss time, but this is computationally too expensive, and therefore approximations have to be made to ensure the 0D model is tractable. The next section describes the empirical derivation of P_{loss}, and studies the various effects influencing its shape.

4.2 Particle confinement

The open magnetic field line configuration plays an important role during start-up, as electrons can freely stream along these field lines out of the plasma. In order to improve the confinement of electrons, a plasma current has to be generated for CFS to form. A possible method of generating a plasma current is by preferentially confining electrons moving

along the magnetic field in one direction, while electrons moving in the opposite direction are lost [21]. This method of current generation by the preferential confinement of electrons has been used to explain the formation of CFS [12, 14], and will be used here to study the losses of electrons.

In an axisymmetric plasma, where the toroidal magnetic field is orders of magnitude stronger than the poloidal field, as is the case during start-up in STs, the guiding centre approximation can be used to study electron orbits (see Appendix D). Consider, for simplicity, a vacuum magnetic field with $B_Z < 0$ and $B_\phi < 0$, as is the case in MAST. The guiding centre approximation predicts curvature and ∇B drifts in the Z-direction, such that the guiding centre equation of motion in the Z-direction can be written as the sum of a parallel motion and drift terms,

$$V_Z = \frac{B_Z}{B} v_\parallel - \text{sign}(B_\phi) \frac{m_e}{eBR} \left(\frac{v_\perp^2}{2} + v_\parallel^2 \right) \tag{4.8}$$

which can only equal zero if $v_\parallel > 0$ as the drift term is always positive for $B_\phi < 0$ and $B_Z < 0$. Electrons that satisfy $V_Z = 0$ will complete passing orbits and be confined, while electrons with $v_\parallel < 0$ will be lost upwards and electrons with $v_\parallel > 0$ lost downwards. For a toroidal field $B_\phi[\text{T}] = -0.4/R$, the $V_Z = 0$ characteristics for $B_Z = -10\,\text{mT}$ is shown in figure 4.3. The confinement map forms a parabola, due to the $v_\parallel^2$ factor in the drift term.

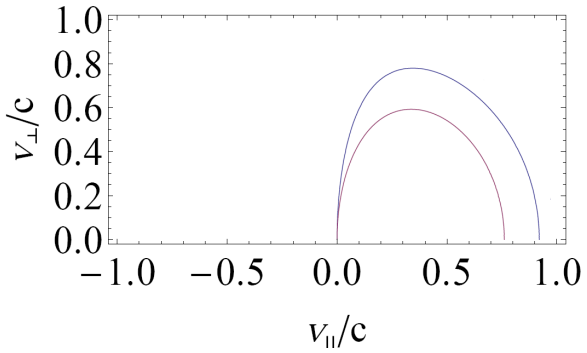

Figure 4.3: The solution to $V_Z = 0$ for electrons originating at $R = 0.4$ (blue) and $R = 0.2$ (red), for a constant vacuum poloidal field $B_Z = -10\,\text{mT}$ and a toroidal field $B_\phi[\text{T}] = -0.4/R$.

A plasma current will modify the magnetic field and change the confinement of electrons. Consider the vacuum poloidal field with constant $B_V = -10$ mT and a toroidal field $B_\phi[\text{T}] = -0.4/R$. A plasma current of $I_P = 2\,\text{kA}$ is added with a current density profile (see Appendix

B) with parameters,

$$R_0 = 0.6 \quad ; \quad R_p = 0.7 \quad ; \quad a = 0.4 \quad ; \quad b = 1 \quad ; \quad \delta = 0.7 \quad ; \quad \alpha = 1 \qquad (4.9)$$

which introduces a radial component of the magnetic field $B_R < 0$ below the midplane and $B_R > 0$ above the midplane, as shown in figure 4.4, leading to the creation of trapped orbits due to the magnetic mirror effect.

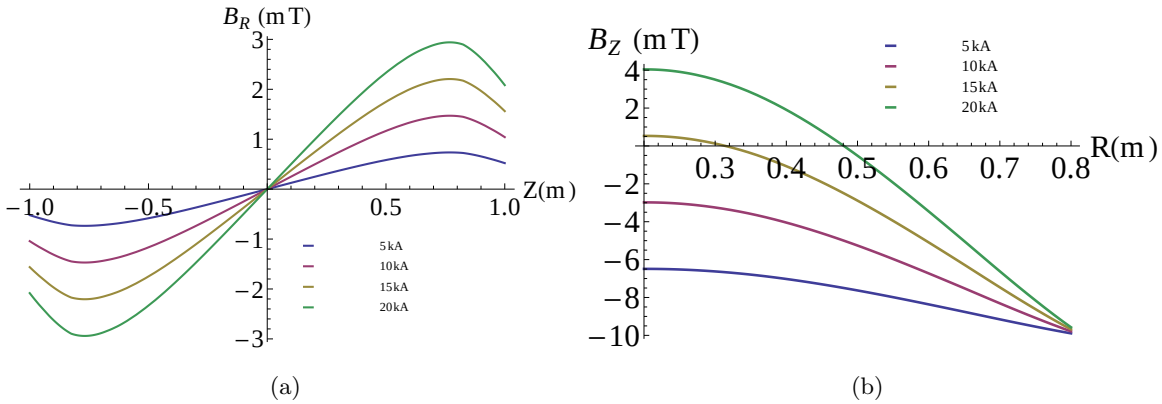

(a) (b)

Figure 4.4: The (a) radial magnetic field at the ECR, $R = 0.4\,\text{m}$, and (b) vertical magnetic field at the midplane, $Z = 0\,\text{m}$, generated by a constant vacuum poloidal field $B_V = -10$ mT and a plasma current profile (4.9) with different values of I_P.

There are three main regions of confinement initially, pictured in figure 4.5:

1. Trapped orbits with initial velocity $v_\parallel > 0$ have $V_Z < 0$ and drift downward into a region where $B_R < 0$. This allows the electron to drift to the inboard side, to a region of higher B, and its $v_\parallel$ decreases. The electron reaches a deflection point where $V_Z > 0$, and the electron starts drifting upward. Still drifting to the inboard side, $v_\parallel$ continues decreasing as B increases, until it equals zero at the mirror point and is reflected back towards the outboard side with $v_\parallel < 0$. The electron now drifts upwards across the midplane, where $B_R > 0$ and the electron again drifts to the inboard side towards a second mirror point, where it is again reflected towards the outboard side with $v_\parallel > 0$. Drifting upwards another deflection point is reached where $V_Z < 0$, and the electron drifts back downwards to its origin, completing a trapped orbit.

2. Passing orbits with initial velocity $v_\parallel > 0$ have $V_Z > 0$ and drift upwards into a region where $B_R > 0$. This allows the electron to drift to the outboard side, into a region

of lower B, such that $v_{\|}$ increases. Eventually the electron reaches a deflection point, where $V_Z < 0$, and the electron drifts downwards. The electron will drift across the midplane, and the change in sign in B_R will allow the electron to drift to the inboard side, to a region of higher B. As B increases, $v_{\|}$ decreases, and eventually $V_Z > 0$ at the deflection point, such that the electron drifts upwards back to its origin to complete a passing orbit.

3. Trapped electrons with initial velocity $v_{\|} < 0$ complete similar orbits to trapped orbits with $v_{\|} > 0$, with the origin on the inboard side of the orbit and $V_Z > 0$ initially.

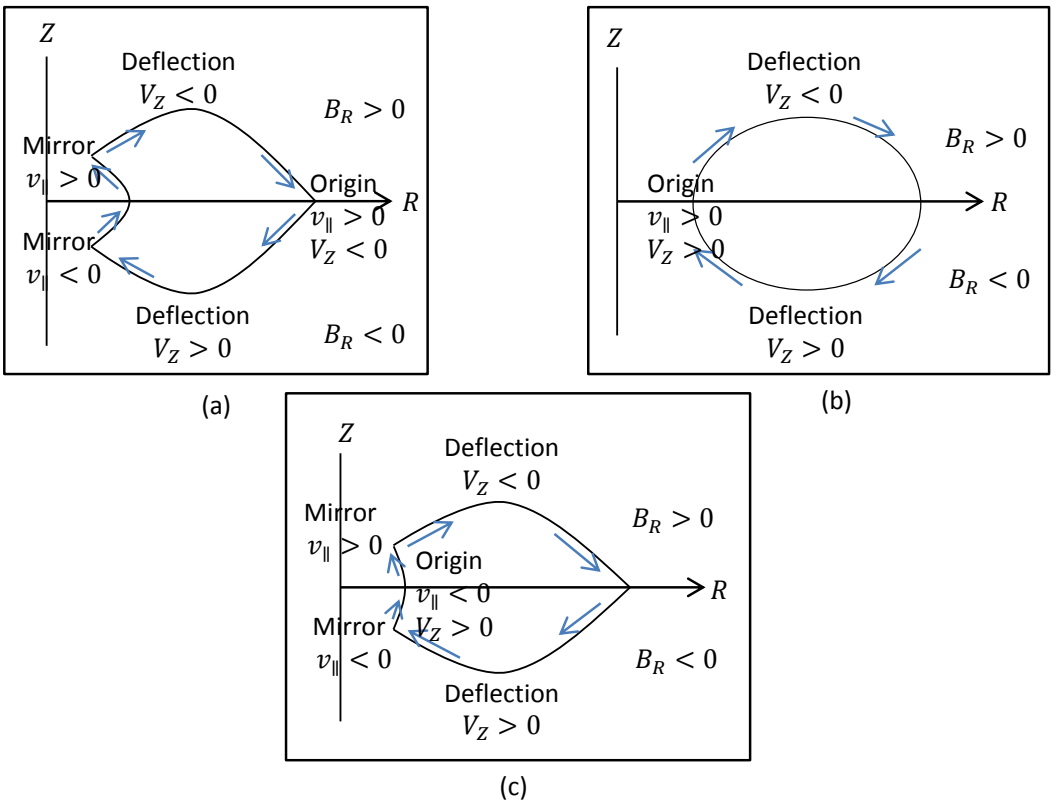

Figure 4.5: Schematic of the confined particle orbits found during start-up (open magnetic field lines): (a) trapped orbit with initial $v_{\|} > 0$, (b) passing orbit with initial $v_{\|} > 0$, and (c) trapped orbit with initial $v_{\|} < 0$. The origin of each orbit is on the midplane at the ECR.

A mirror point is reached where $v_{\|} \to 0$ and the electron is reflected, leading to trapped orbits. This happens typically when the electron drifts to the inboard side, as the toroidal field $B_\phi \sim 1/R$. In contrast, a deflection point is reached where $V_Z = 0$ and the vertical direction an electron moves in changes. In order for an electron to be confined, by completing

either a trapped or passing orbit, either a mirror or deflection point, or both, must be reached.

The drift term is always positive, so if $v_\parallel < 0$ the parallel term is always positive and a deflection point can never be reached. If $v_\parallel > 0$, however, the two terms can be comparable in size, such that the parallel term dominates for large $v_\parallel$, while the drift term dominates for small $v_\parallel$. This effect implies that electrons with $v_\parallel > 0$ will be better confined than electrons with $v_\parallel < 0$, as electrons with $v_\parallel < 0$ have to reach a mirror point in order to be confined, but won't reach it if $v_\parallel$ is too large, while electrons with $v_\parallel > 0$ have comparable parallel and drift terms, such that deflection points can be reached.

Electrons with large $v_\parallel < 0$ have $V_Z > 0$ and drift upwards into a region of $B_R > 0$. This allows the electron to travel to the inboard side and a region of larger B, decreasing $v_\parallel$. If the initial $v_\parallel$ is sufficiently large, however, a mirror point will never be reached, and the electron is lost.

Similarly, electrons with large $v_\parallel > 0$ have $V_Z < 0$ and drift downwards into a region of $B_R < 0$. This allows the electron to travel to the inboard side and a region of larger B, decreasing $v_\parallel$. If the initial $v_\parallel$ is large enough, deflection and mirror points are never reached, and the electron continues drifting downwards and is eventually lost.

These loss mechanisms rely on the fact that B_R is weak, and therefore the radial drift is small. As the plasma current increases, so does the magnitude of the poloidal field, as shown in figure 4.4. This allows electrons to drift further radially, accessing regions of higher B, and more electrons reach deflection and mirror points, such that confinement improves for increasing plasma currents.

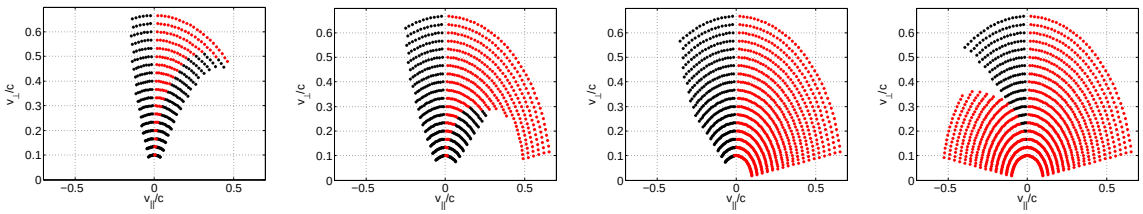

(a) (b) (c) (d)

Figure 4.6: The confinement map for electrons originating from the midplane on the ECR line for a constant vacuum poloidal field $B_V = -10$ mT, with a plasma current of (a) 5 kA, (b) 10 kA, (c) 15 kA, and (d) 20 kA. Confined electrons complete trapped (black) or passing (red) orbits, while the white space corresponds to lost electrons.

Figure 4.6 shows the confinement of electrons originating from the midplane for increasing plasma current, with the corresponding magnetic field and vector potential shown in figures

4.7 and 4.8, respectively. As experiments concluded that the majority of the plasma current is carried by energetic electrons, which are created by an interaction with the injected RF beam along the ECR layer, the confinement of these energetic electrons, originating from the ECR layer on the midplane, are studied. Their orbits are traced out using the guiding centre approximation (see Appendix D) for a particular magnetic field line configuration. If the electron completes a confined (trapped or passing) orbit, its initial velocity is plotted on a graph. The collection of these initial velocities, leading to confined orbits, are shown as confinement maps in figure 4.6 for a constant vertical vacuum poloidal field and increasing plasma current, and it is these plots that P_{loss} represents.

An important point is where CFS first start to form, or when all electrons with $v_{\parallel} > 0$ are confined, but not all electrons with $v_{\parallel} < 0$. This occurs around $I_P = 15\,\text{kA}$ for the example shown in figure 4.6. The importance of this point will become clear later on, but due to its importance, this point, the value of the plasma current where the first CFS start to form, or where all electrons with $v_{\parallel} > 0$ are confined, is labelled I_{CFS}.

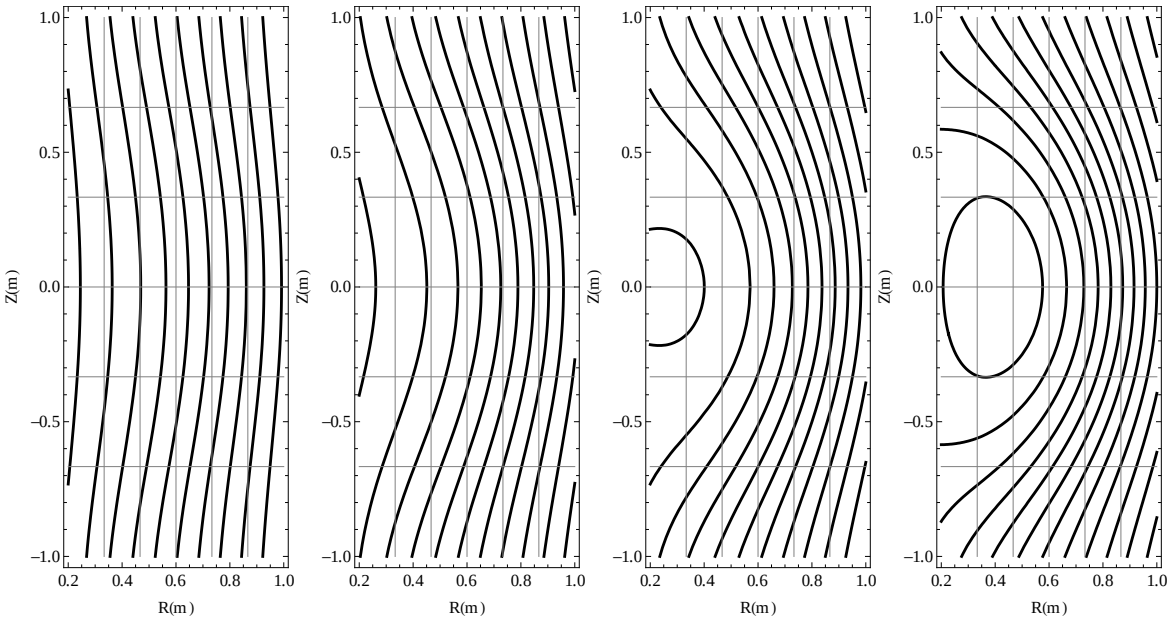

Figure 4.7: The magnetic field created by a constant vacuum poloidal field $B_V = -10$ mT and a plasma current of (a) 5 kA, (b) 10 kA, (c) 15 kA, and (d) 20 kA.

At this point, B_Z becomes positive on the inboard side, as shown in figure 4.4, such that electrons with $v_{\parallel} < 0$ can also complete passing orbits, similar to those described in figure 4.5(b).

A further region of confinement is present for electrons with large $v_{\parallel} > 0$ around $I_P = 10$kA, as shown in figure 4.6(b). This is simply a broadening of the initial parabolic solution of $V_Z = 0$ (fig. 4.3), and the passing orbits are similar to those described in figure 4.5(b).

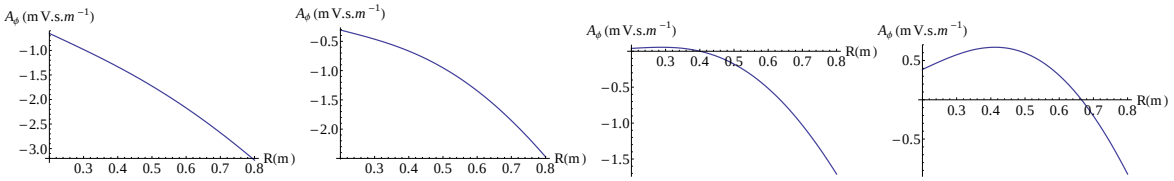

Figure 4.8: The vector potential along the midplane for a constant vacuum field $B_V = -10$ mT, with a plasma current of (a) 5 kA, (b) 10 kA, (c) 15 kA, and (d) 20 kA.

For the example considered here, the first CFS forms around $I_{\mathrm{CFS}} = 15\,\mathrm{kA}$, when all electrons with $v_{\parallel} > 0$ are confined. Confinement of all electrons with $v_{\parallel} < 0$ only occurs later, such that there exists an asymmetry in the confinement of electrons for the duration of plasma burn-through and current ramp-up, as shown in figure 4.6. It is this asymmetric confinement that can be used to generate a plasma current, and must therefore be modelled. The loss term is therefore described by equation (4.7),

$$\left(\frac{\partial f}{\partial t}\right)_{\mathrm{loss}} = -\frac{f}{\tau_{\mathrm{loss}}(p_{\parallel}, p_{\perp})} P_{\mathrm{loss}}(p_{\parallel}, p_{\perp})$$

where $\tau_{\mathrm{loss}}(p_{\parallel}, p_{\perp})$ is the average time it takes for an electron with momentum $(p_{\parallel}, p_{\perp})$ to be lost out of the plasma volume, given by equation (4.5), and P_{loss} is the probability of an electron being lost or confined.

As the probability of an electron being lost or confined has a big impact on the loss term, and possibly on the current drive mechanism, it is necessary to formulate an equation for describing this confinement of electrons.

The confinement of electrons, P_{loss}, depends on a number of factors, including the spatial dependence of the vacuum field, the origin of the electron orbit, the strength of the vacuum poloidal field, and the current density profile and total current. All these effects must be taken into account when formulating a mathematical expression describing the confinement of electrons, while still ensuring the model is tractable.

Before attempting to formulate an equation for describing the probability of an electron

being lost/confined, three factors and their effect on the confinement of electrons is first investigated. These are the dependence of the electron confinement on the (i) initial vertical position of an electron; (ii) on the vacuum poloidal field strength; and (iii) on the current density profile, which influences the shape of the magnetic field configuration.

4.2.1 Dependence of electron confinement on vertical position

Experiments concluded that the majority of the plasma current is carried by energetic electrons, which are created by an interaction with the injected RF beam [6, 11]. As such an interaction occurs at the ECR, the assumption is made that all energetic electrons originate from the ECR layer. However, this interaction could occur at any vertical position, while the plasma could also be shifted vertically such that the magnetic field is no longer symmetric around the machine midplane $Z = 0$.

In order to study the effect of a vertical shift of the magnetic field, consider a constant vertical vacuum poloidal field $B_V = -10\,\mathrm{mT}$ and a toroidal field $B_\phi[\mathrm{T}] = -0.4/R$. The current density profile (see Appendix B) is given by

$$R_0 = 0.6 \quad , \quad R_p = 0.7 \quad , \quad a = 0.4 \quad , \quad b = 1 \quad , \quad \delta = 0.7 \quad , \quad \alpha = 1$$

such that the magnetic field is symmetric around the machine midplane $Z = 0$, and $I_{\mathrm{CFS}} \approx 15\,\mathrm{kA}$ (the first CFS forms at a plasma current of $I_P = 15\,\mathrm{kA}$). As the field is symmetric around the midplane, electrons originating from $Z = \pm 10\,\mathrm{cm}$ will have the same confinement, and the confinement of electrons originating from the midplane upwards, in increments of 10 cm, is studied, with results for $I_P = 10\,\mathrm{kA}$ and $I_P = 20\,\mathrm{kA}$ shown in figures 4.9 and 4.10, respectively.

If the plasma were shifted up or down, the magnetic midplane is shifted, and the electron confinement would look the same as long as 0 cm is on the new magnetic midplane. For a magnetic field symmetric around a point Z_0, three conclusions to the effect an increase in Z_0 has on the confinement can be drawn:

1. Decreases the amount of electrons with large $v_\parallel > 0$ that are confined, as seen in figure 4.9, for a plasma current $I_P < I_{\mathrm{CFS}}$.

2. Decreases the amount of electrons with large $v_\parallel < 0$ that are confined, as seen in figure 4.10, for a plasma current $I_P > I_{\mathrm{CFS}}$.

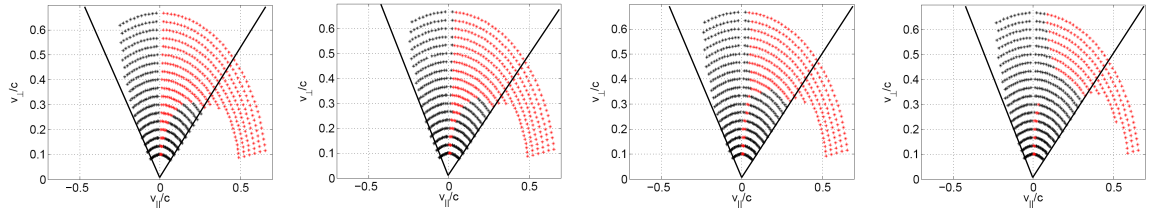

(a) (b) (c) (d)

Figure 4.9: The confinement map for electrons originating from the ECR line at (a) 0 cm, (b) ±10 cm, (c) ±20 cm, and (d) ±30 cm, for $I_P = 10$ kA. The black lines defines a loss cone, with electrons inside it being confined. This confinement area reduces slightly as electron orbits originate further from the midplane. Confined electrons complete trapped (black) or passing (red) orbits, while the white space corresponds to lost electrons.

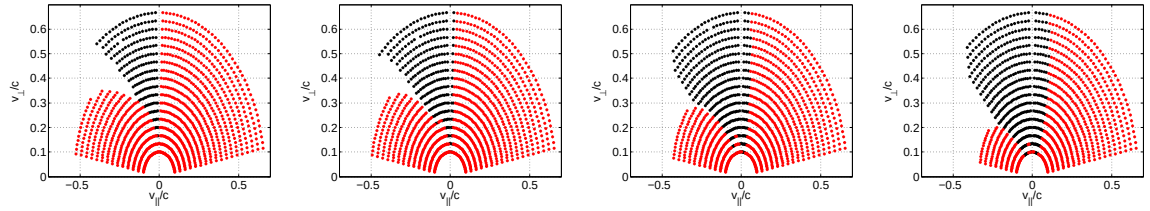

(a) (b) (c) (d)

Figure 4.10: The confinement map for electrons originating from the ECR line at (a) 0 cm, (b) ±10 cm, (c) ±20 cm, and (d) ±30 cm, for $I_P = 20$ kA, show that the confinement area slightly reduces as electron orbits originate further from the midplane. Confined electrons complete trapped (black) or passing (red) orbits, while the white space corresponds to lost electrons.

3. Figure 4.9 shows the existence of a loss cone, within which all electrons are confined. This area of confinement reduces slightly for increasing Z_0, for a plasma current $I_P < I_{\text{CFS}}$, as is also shown in Appendix G and figure G.3.

Experiments used a vertical shift of the magnetic midplane to help the formation of CFS [6,11], and, if the preferential confinement of electrons is responsible for the generation of plasma current, these three conclusions can explain why a vertical shift helps the formation of CFS. First, as there are very few electrons with large $v_{\|} > 0$, due to RF heating increasing the perpendicular velocity of electrons, the decrease in confinement of electrons with large $v_{\|} > 0$ is not a concern. Secondly, the narrowing of the confinement region will lead to an increase in the number of electrons lost, and as electrons with $v_{\|} < 0$ are lost faster than electrons with $v_{\|} > 0$, this will lead to an increase in the plasma current. Lastly, the decrease in confinement of electrons with large $v_{\|} < 0$, after the formation of the first CFS, will lead

to a further increase in the plasma current, as all electrons with $v_{\parallel} < 0$ are not confined, leading to further losses and a larger plasma current.

4.2.2 Dependence of electron confinement on vacuum magnetic field strength

The confinement of electrons depends on the magnetic field line configuration, which is influenced by a number of factors. Before attempting to formulate an equation for describing the probability of an electron being lost/confined, P_{loss}, a number of factors and their effect on the confinement of electrons are investigated. One of these factors is the strength of the vacuum poloidal field.

Increasing the strength of the vacuum poloidal field influences the confinement of electrons, as electrons can drift out of the plasma volume faster, while a larger plasma current will be needed for CFS to form, increasing the value of I_{CFS}. It is therefore important to study the relationship between the vacuum poloidal field strength and the confinement of electrons.

In order to do this, consider a current density profile (see Appendix B),

$$R_0 = 0.6 \quad , \quad R_p = 0.7 \quad , \quad a = 0.4 \quad , \quad b = 1 \quad , \quad \delta = 0.5 \quad , \quad \alpha = 1$$

and a toroidal magnetic field $B_\phi[\text{T}] = -0.4/R$. The confinement map of electrons originating on the ECR line $R = 0.4\,\text{m}$ and the midplane $Z = 0\,\text{m}$ is then compared for different values of the vertical vacuum poloidal field B_V.

First, the plasma current needed for CFS to form, I_{CFS}, must be determined in order to compare confinement maps where the ratio I_P/I_{CFS} is the same. For the given current density profile, and for a constant vacuum poloidal field, there exists a linear relationship between the value of B_V and I_{CFS}, given by

$$I_{\text{CFS}}[\text{kA}] = \frac{3}{2} B_V[\text{mT}] \tag{4.10}$$

For $B_V = -5$ mT, $I_{\text{CFS}} = 7.5$ kA, and the confinement for electrons originating from the ECR line on the midplane is shown in figure 4.11, for ratios $I_P/I_{\text{CFS}} = 1/3, 2/3, 1, 4/3$. The comparison for $B_V = -10$ mT, shown in figure 4.12, leads to three conclusions on the strength of the magnetic field:

1. The confinement of electrons within the loss cone only depends on the ratio I_P/I_{CFS}.

2. The confinement of electrons with large $v_{\parallel} > 0$, when $I_P < I_{\mathrm{CFS}}$, depends on the value of B_V, and therefore on the value of I_{CFS}.

3. The confinement of electrons with large $v_{\parallel} < 0$, when $I_P > I_{\mathrm{CFS}}$, depends on the value of B_V, and therefore on the value of I_{CFS}.

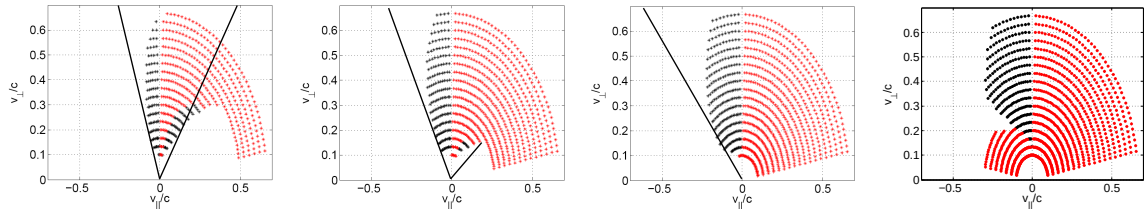

(a) (b) (c) (d)

Figure 4.11: The confinement map for electrons originating from the ECR line with a vacuum poloidal field of $B_V = -5$ mT, and a ratio of I_P/I_{CFS} of (a) 1/3, (b) 2/3, (c) 1, and (d) 4/3. For the chosen current density profile, $I_{\mathrm{CFS}} = 7.5$ kA. Confined electrons complete trapped (black) or passing (red) orbits, while the white space corresponds to lost electrons. The black lines defines a loss cone, with electrons inside it being confined.

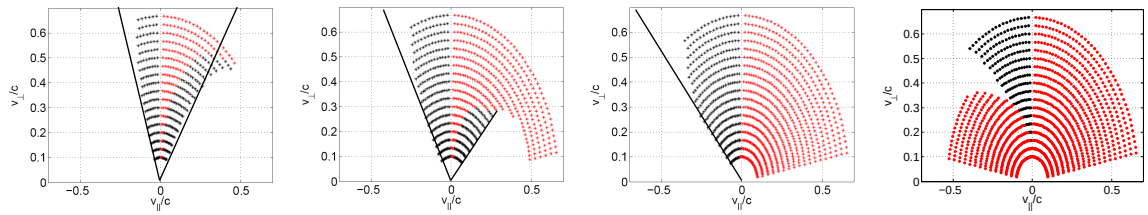

(a) (b) (c) (d)

Figure 4.12: The confinement map for electrons originating from the ECR line with a vacuum poloidal field of $B_V = -10$ mT, and a ratio of I_P/I_{CFS} of (a) 1/3, (b) 2/3, (c) 1, and (d) 4/3. For the chosen current density profile, $I_{\mathrm{CFS}} = 15$ kA. Confined electrons complete trapped (black) or passing (red) orbits, while the white space corresponds to lost electrons. The black lines defines a loss cone, with electrons inside it being confined.

Knowledge of the strength of the vacuum poloidal field is therefore contained in the value of I_{CFS}, while the electron confinement for different I_{CFS}, but the same ratio I_P/I_{CFS}, is similar, as long as the current density profile remains the same. Experiments showed that an increase in the vacuum poloidal field strength leads to a subsequent increase in the generated plasma current [6, 11]. If the asymmetric confinement of electrons is responsible

for the generation of a plasma current, an increase in the vacuum poloidal field strength, which leads to an increase in the value I_{CFS}, can lead to an increase in the plasma current I_P, as the asymmetry in the electron confinement is a function of the ratio I_P/I_{CFS}. Therefore, an increase in I_{CFS} leads to a subsequent increase in I_P, as the asymmetry of the electron confinement is sustained throughout.

4.2.3 Dependence of electron confinement on the current density profile

The confinement of electrons depends on the magnetic field line configuration, which is influenced by a number of factors. One of these factors is the current density profile, which influences the spatial structure of the magnetic field.

The previous section showed the importance of the value of I_{CFS}, the value of the plasma current where CFS first start to form and all electrons with $v_{\parallel} > 0$ are confined, as the strength of the vacuum poloidal field determines the value of I_{CFS}.

For a constant current density profile, the confinement of electrons largely depends only on the ratio I_P/I_{CFS}, as there exists a linear relationship between the vacuum poloidal field strength and the value of I_{CFS}. By changing the current density profile, however, the value of I_{CFS} would change, but, more importantly, such a change would also impact the confinement of electrons, as the spatial structure of the magnetic field is altered.

In order to investigate the effect of the current density profile on the confinement of electrons, consider four different current density profiles (see Appendix B),

Parameter	Profile 1	Profile 2	Profile 3	Profile 4
R_0	0.6	0.6	0.7	0.8
R_p	0.7	0.7	0.5	0.9
a	0.4	0.4	0.5	0.5
b	1	1.3	0.6	0.8
δ	0.5	0.1	0.2	0.8
α	1	2	1.5	1
I_{CFS}(kA)	15	11	15	15

shown in figures 4.13 and 4.14. The vacuum poloidal field is kept constant at $B_V = -10$ mT, while the toroidal magnetic field $B_\phi[\mathrm{T}] = -0.4/R$.

The values of I_{CFS} for the four different current density profiles differ, so in order to compare the electron confinement of each case, the ratio I_P/I_{CFS} is kept constant. The

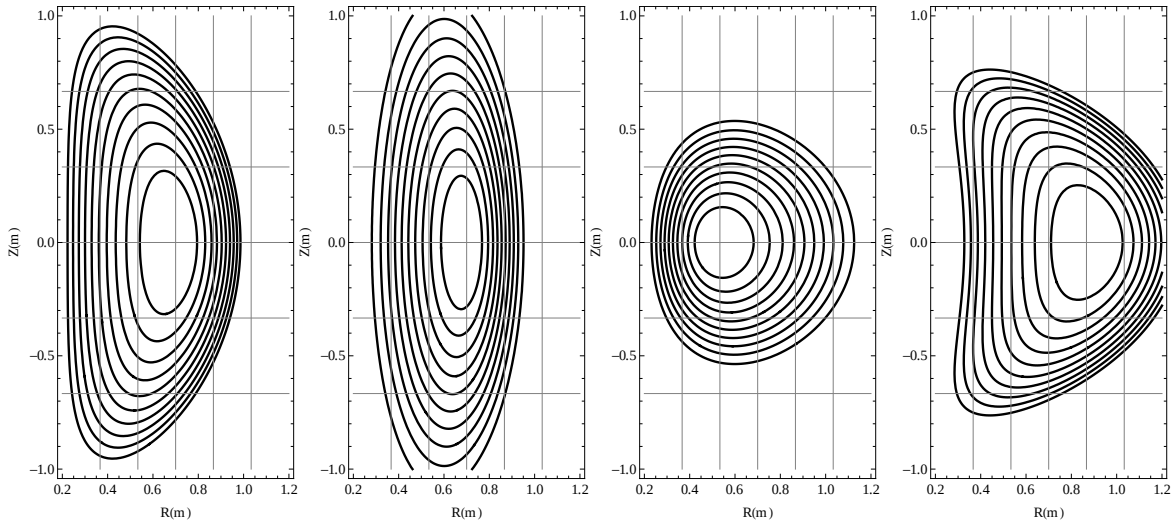

(a) (b) (c) (d)

Figure 4.13: Contours of constant j_ϕ for the four different current density profiles studied.

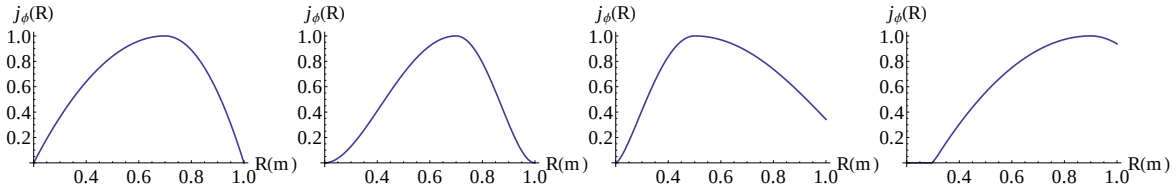

(a) (b) (c) (d)

Figure 4.14: The normalized $j_\phi(R)$ for the four different current density profiles studied as a function of R on the midplane $Z = 0$.

magnetic fields created by each current profile will be different, yet the confinement for electrons originating from the ECR line on the midplane is very similar, as can be seen for $I_P/I_{\mathrm{CFS}} = 1/2$ in figure 4.15 and $I_P/I_{\mathrm{CFS}} = 3/4$ in figure 4.16.

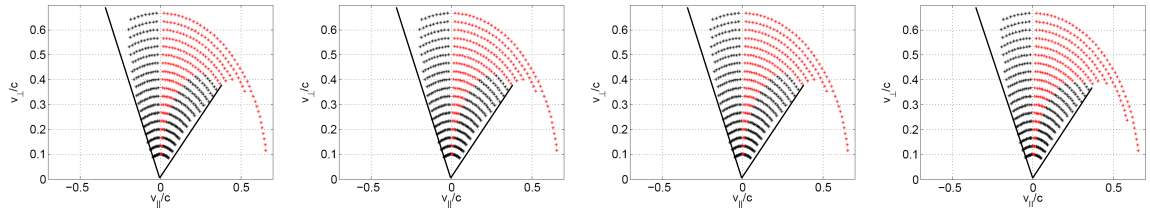

(a) (b) (c) (d)

Figure 4.15: The confinement map of electrons originating from the midplane with the magnetic field calculated using the four different current profiles and $I_P/I_{\mathrm{CFS}} = 1/2$. Confined electrons complete trapped (black) or passing (red) orbits, while the white space corresponds to lost electrons. The black lines defines a loss cone, with electrons inside it being confined.

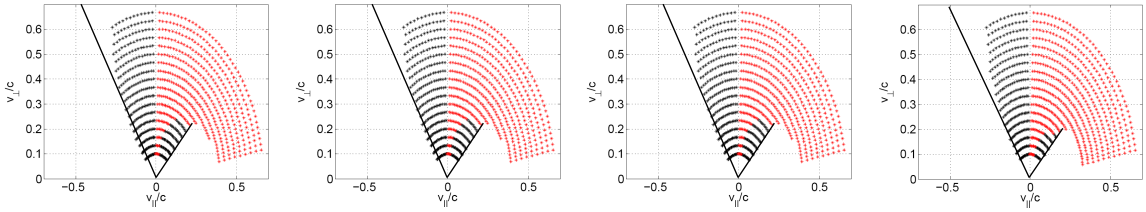

(a) (b) (c) (d)

Figure 4.16: The confinement map of electrons originating from the midplane with the magnetic field calculated using the four different current profiles and $I_P/I_{\mathrm{CFS}} = 3/4$. Confined electrons complete trapped (black) or passing (red) orbits, while the white space corresponds to lost electrons. The black lines defines a loss cone, with electrons inside it being confined.

The following conclusions can be drawn from this:

1. The confinement of electrons is insensitive to the particular shape of the magnetic field.

2. The ratio I_P/I_{CFS} is important to determine confinement.

3. The value of I_{CFS} takes into account not only the strength of the vacuum poloidal field, but also the shape of the current density profile, and is therefore all that is needed to define the electron confinement, along with the plasma current I_P and the vertical shift Z_0.

The value of I_{CFS} takes into account not just the strength of the vacuum poloidal field, but also the shape of the magnetic field. An important consequence of this is that the only parameter necessary for quantifying the confinement of electrons is I_{CFS}, as it takes into account all the knowledge of the spatial structure and strength of the magnetic field. Any uncertainty in the current density profile or vacuum poloidal field could therefore be reflected in an uncertainty in the value of I_{CFS}, as this single parameter contains knowledge of both.

4.2.4 Formulating an equation for $P_{\mathbf{loss}}(p_\parallel, p_\perp)$

The confinement of electrons depends on the magnetic field line configuration, which is influenced by a number of factors, including the vacuum poloidal field shape and strength, the current density profile, and total plasma current. The previous sections showed that the confinement of electrons largely depends on the ratio I_P/I_{CFS}, where I_{CFS} is the value of the plasma current where all electrons with $v_\parallel > 0$ are confined and the first CFS start to form.

The spatial structure of the magnetic field is determined by the vacuum poloidal field and the current density profile, but knowledge of this is contained in the parameter I_{CFS}. Any uncertainty in the spatial structure of the magnetic field could then be reflected in an uncertainty in the value of I_{CFS}. This ensures the 0D model remains tractable.

By studying the electron confinement under different conditions, an empirical fit for describing the probability of an electron being lost/confined is obtained,

$$P_{\mathrm{loss}}(p_{\parallel}, p_{\perp}) = 1 - \exp\left[-\ell \frac{p_{\parallel}^2}{p_{\perp}^2}\right] \tag{4.11}$$

where an expression for $\ell = \ell(p_{\parallel}, I_P, I_{\mathrm{CFS}}, Z_0)$ must be found. $P_{\mathrm{loss}}(p_{\parallel}, p_{\perp})$ is the probability for an electron to be lost or confined, such that it equals 0 (i.e. $\ell = 0$) if an electron is confined, and equals 1 (i.e. $\ell \to \infty$) if an electron is lost. The exponential term is used to account for the fact that the confinement region recedes for electron orbits originating further from the midplane, and therefore attempts to capture the spatial distribution of the origin of electron orbits. Further, the $p_{\perp}/p_{\parallel}$ factor in the exponential term is chosen as the confinement of electrons represents a loss cone, where electrons with a constant $p_{\perp}/p_{\parallel}$ have the same probability of being lost/confined.

In order to define $\ell = \ell(p_{\parallel}, I_P, I_{\mathrm{CFS}}, Z_0)$, the momentum plane is divided into five regions: firstly by differentiating between $p_{\parallel} > 0$ and $p_{\parallel} < 0$, and then dividing each region into cold, warm and hot by defining temperatures T_{cold} and T_W. A schematic is shown in figure 4.17, with there being no distinction between $v_{\parallel} > 0$ and $v_{\parallel} < 0$ in the cold region.

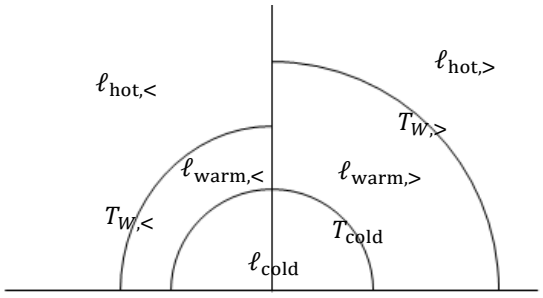

Figure 4.17: Schematic of the five areas into which the momentum plane is divided. A value for ℓ must be found in each area, in addition to the temperatures T_{cold} and T_W.

Electrons in the cold region, ℓ_{cold}, with $T_e < T_{\mathrm{cold}}$, are always confined. This is due to ions being lost at a much slower rate than electrons, such that an ambipolar electric field is created which electrostatically confines electrons with $T_e < T_{\mathrm{cold}}$ [53]. Electrons with

$T_e > T_{\text{cold}}$ have enough energy to overcome this electric field and be lost along the open magnetic field lines.

Equations for the different ℓ's is obtained by empirically fitting mathematical expressions to numerical data, and is discussed in Appendix G. There are two regions in which electrons are always confined,

$$\ell_{\text{hot},>} = 0 \tag{4.12}$$

and

$$\ell_{\text{warm},<} = 0 \tag{4.13}$$

while the confinement in the other two regions depends on I_{CFS}[kA], Z_0[m] and I_P[kA],

$$\ell_{\text{warm},>} = \max\left\{\frac{1}{2}\frac{I_{\text{CFS}}}{I_P}\exp\left[\frac{Z_0^2}{1}\frac{I_{\text{CFS}}}{I_P}\right]\tanh\left(0.01 I_{\text{CFS}}\right),\, 1\right\} \tag{4.14}$$

and

$$\ell_{\text{hot},<} = \max\left\{\left(2\frac{I_{\text{CFS}}}{I_P} - 1\right)\exp\left[\frac{Z_0}{0.6}\frac{I_{\text{CFS}}}{I_P}\right]\tanh\left(0.01 I_{\text{CFS}}\right),\, 1\right\} \tag{4.15}$$

such that $\ell_{\text{warm},>} \approx \ell_{\text{hot},<} \approx 1$ except when $I_P \ll I_{\text{CFS}}$.

Lastly, the temperatures differentiating between the hot and cold regions for $v_\parallel > 0$ and $v_\parallel < 0$ are given by

$$T_{W,>} = \frac{I_{\text{CFS}}}{15}\left(T_{\text{cold}} + 250(1 - T_{\text{cold}})\exp\left[-10\tanh\left(\frac{I_{\text{CFS}}}{20}\right)\left(\frac{I_P}{I_{\text{CFS}}}\right)^2\right] - a_{\text{loss}}\right)\exp\left[\frac{Z_0}{1}\right] \tag{4.16}$$

and

$$T_{W,<} = \frac{I_{\text{CFS}}}{15}\left(T_{\text{cold}} + (1 - T_{\text{cold}})\left(\frac{I_P}{I_{\text{CFS}}}\right)^{9.5} - b_{\text{loss}}\right) - \frac{Z_0}{0.8}\left(\frac{I_P}{I_{\text{CFS}}}\right)^{9.5} \tag{4.17}$$

respectively, where a_{loss} and b_{loss} is determined to ensure $T_{W,<} = T_{W,>} = T_{\text{cold}}$ when $I_P = I_{\text{CFS}}$ and $Z_0 = 0$, i.e.

$$\begin{aligned} a_{\text{loss}} &= T_{\text{cold}} + 250(1 - T_{\text{cold}})\exp\left[-10\tanh\left(\frac{I_{\text{CFS}}}{20}\right)\right] \\ b_{\text{loss}} &= T_{\text{cold}} + (1 - T_{\text{cold}}) \end{aligned} \tag{4.18}$$

4.3 Experimental effects

In this chapter, a mathematical expression for approximating the loss term was formulated. The loss term is given by (4.7)

$$\left(\frac{\partial f}{\partial t}\right)_{\text{loss}} = -\frac{f}{\tau_{\text{loss}}(p_\parallel, p_\perp)} P_{\text{loss}}(p_\parallel, p_\perp)$$

where $\tau_{\text{loss}}(p_\parallel, p_\perp)$ is the average time it takes for an electron with momentum $(p_\parallel, p_\perp)$ to be lost, and

$$P_{\text{loss}}(p_\parallel, p_\perp) = 1 - \exp\left[-\ell \frac{p_\parallel^2}{p_\perp^2}\right]$$

is the probability of an electron being lost or confined. The form of this equation is a heuristic choice, based on the loss cone form of the electron confinement, rather than a derivation or measurement. The function $\ell = \ell(p_\parallel, I_P, I_{\text{CFS}}, Z_0)$ determines the confinement of electrons, based on the vertical shift Z_0 and the value of I_{CFS}, the value of the plasma current where all electrons with $v_\parallel > 0$ are confined. The value of I_{CFS} contains information about the spatial structure and magnitude of the vacuum poloidal field as well as the current density profile.

In this section, the confinement of electrons determined numerically from experimentally obtained magnetic fields are compared to the mathematical predictions in order to explain two conclusions drawn by experiments with regards to the vacuum magnetic field [6, 11]:

1. Creating an up/down shift helps to create CFS

   From studying the loss term, creating an up/down shift enhances the asymmetry in the confinement of electrons. If this asymmetry is responsible for generating a current, then the greater the asymmetry, the greater the generated current, and therefore an up/down shift helps to form CFS. Of course, an up/down shift is more efficient before CFS forms, when electrons are only partially confined.

2. The most efficient way of achieving a higher plasma current is by increasing the strength of the vertical vacuum poloidal field B_V

   When the first CFS forms, all electrons with $v_\parallel > 0$ are confined, but not all electrons with $v_\parallel < 0$. If this asymmetry can be sustained, a larger current can be generated. It was shown that the asymmetry in the confinement of electrons depends largely only

on the ratio $I_P/I_{\rm CFS}$. Increasing the vacuum poloidal field strength B_V leads to an increase in $I_{\rm CFS}$, which leads to a subsequent increase in the plasma current I_P as the asymmetry in electron confinement is sustained.

Experiments use a combination of these two effects to generate a plasma current, by influencing the confinement of electrons. If the asymmetric confinement of electrons is responsible for the generated plasma current, then studying the confinement of electrons, and how manipulation of the magnetic field influences it, is crucial to understanding non-inductive start-up.

In this section, the confinement of electrons originating from the ECR layer on the machine midplane ($Z = 0$) are compared for numerical calculations, using the guiding centre orbit, and the mathematical expression, obtained from an empirical fit. The mathematical expression is plotted as an overlay on the numerical confinement of electrons with contours changing from $P_{\rm loss} = 1$ (red) to $P_{\rm loss} = 0$ (blue) in increments of 0.1. Electrons are lost for $P_{\rm loss} = 1$ and confined for $P_{\rm loss} = 0$.

4.3.1 MAST shot # 28941

Experiments combined the effects of a B_V ramp-up and an up/down shift to generate a large plasma current. Consider MAST shot #28941, for which the current carried in the poloidal field coils is shown in figure 4.18. The P6 coils carry current in opposite directions from 20 ms to about 100 ms, creating a radial magnetic field which results in an up/down shift of the magnetic midplane, the point about which B_Z is symmetric. Using the current in each poloidal field coil, the vacuum field can be reconstructed, and the vertical shift where B_Z is a maximum can be determined, as shown in figure 4.19(a). A current density profile (see Appendix B) with parameters,

$$R_0 = 0.6 \quad , \quad R_p = 0.7 \quad , \quad a = 0.4 \quad , \quad b = 1 \quad , \quad \delta = 0.7 \quad , \quad \alpha = 1 \tag{4.19}$$

and a shifted Z_0 is then imposed, and the total magnetic field is calculated. At each time step, the value of I_P necessary for the first CFS to form, $I_{\rm CFS}$, can be determined. These results are shown in figure 4.19(c) and compared to the actual (measured) plasma current.

The start-up shot is broken into three time periods:

1. $20 - 60$ ms

The vacuum field is approximately constant, with a vertical kick being created by the P6 coils to help the formation of CFS.

2. $60 - 120$ ms

   Ramp-up of the vacuum poloidal field B_V, which will lead to an increase in I_{CFS} such that the confinement of electrons remains asymmetric, leading to an increase in I_P.

3. $120 - 300$ ms

   The vacuum field remains approximately constant, such that an increase in I_P leads to the formation of CFS and the complete confinement of electrons.

For each time period, the magnetic field will be determined using the experimentally measured plasma current I_P, and the confinement of electrons calculated numerically and mathematically, using the empirical equation derived earlier, will be compared. The assumption is made that electrons will originate from the ECR line ($R = 0.4$ m) on the midplane ($Z = 0$ m).

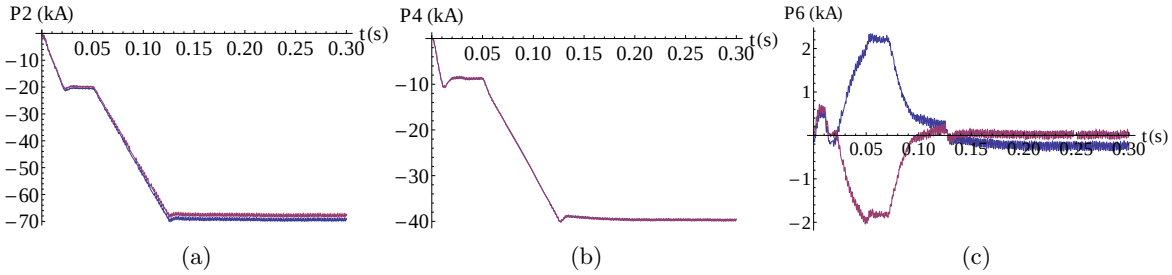

Figure 4.18: The current carried in the upper (blue) and lower (red) poloidal field coils (a) P2, (b) P4 and (c) P6.

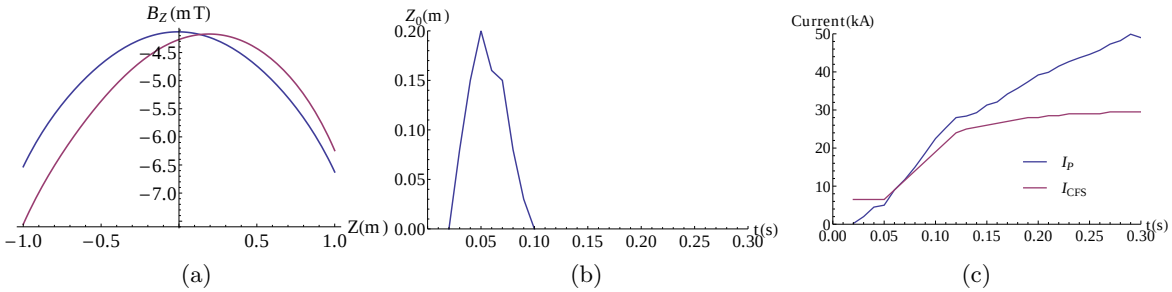

Figure 4.19: (a) The vacuum magnetic field B_Z along $R = 0.4$ m, after 20 ms (blue) and 50 ms (red), gives the vertical shift shown in (b). In (c) we compare I_{CFS} (blue) to the experimentally measured I_P (red).

4.3.1.1 Vertical shift: $20 - 60$ ms

During this initial period the vacuum poloidal field remains approximately constant, with a vertical kick initiated to help the formation of CFS. Introducing a vertical shift enhances the asymmetry in the confinement of electrons, such that a greater current can be generated in order to reach $I_P \approx I_{\text{CFS}}$. The ideal confinement is when all electrons with $v_{\parallel} > 0$ are confined, but not all electrons with $v_{\parallel} < 0$, which occurs when $I_P \approx I_{\text{CFS}}$.

The magnetic field is shown in figure 4.20, with the corresponding comparison of the confinement map between numerical and mathematical calculations shown in figure 4.21.

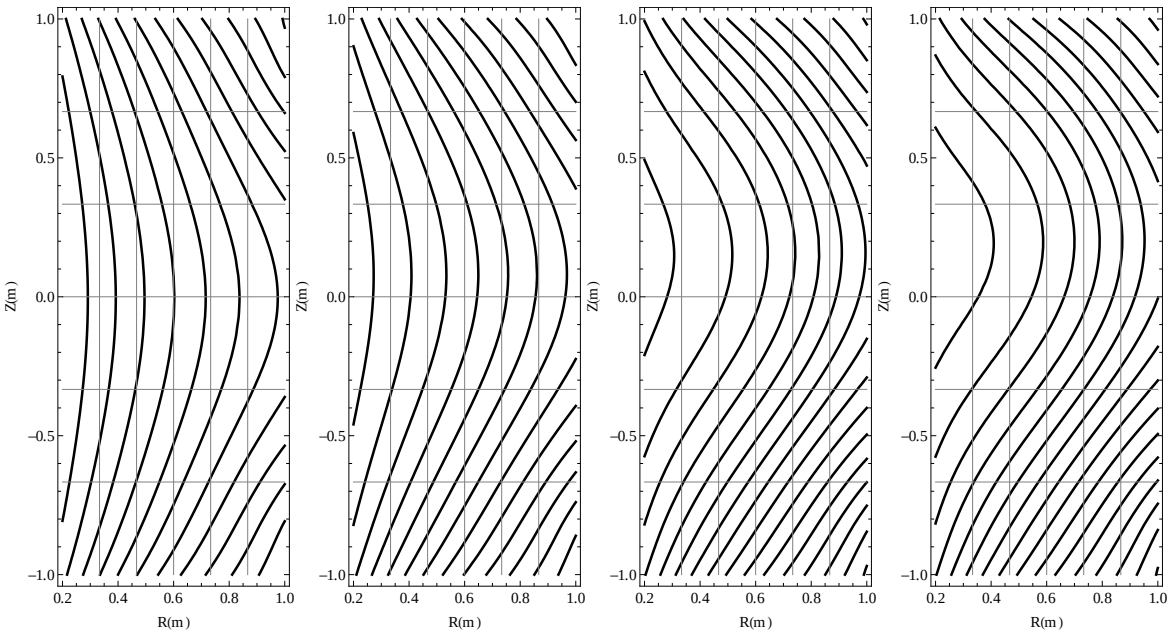

(a) (b) (c) (d)

Figure 4.20: Contour of constant magnetic field after (a) 20 ms, (b) 30 ms, (c) 40 ms, and (d) 50 ms for MAST shot #28941.

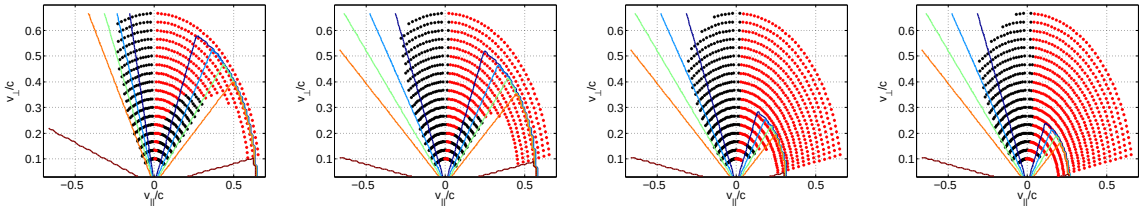

(a) (b) (c) (d)

Figure 4.21: Comparison of the confinement map shows a good agreement between the numerical, using the guiding centre orbit, and analytical, using the empirically derived equations, after (a) 20 ms, (b) 30 ms, (c) 40 ms, and (d) 50 ms. Electrons complete trapped (black) or passing (red) orbits, while the white space corresponds to electrons lost. The overlay plot is the analytical probability of an electron being lost/confined, with it changing from $P_{\text{loss}} = 1$ (red) to $P_{\text{loss}} = 0$ (blue) in increments of 0.2.

4.3.1.2 B_V ramp-up: $60 - 120$ ms

Once $I_P \approx I_{\text{CFS}}$, all electrons with $v_{\parallel} > 0$ are confined, but not all electrons with $v_{\parallel} < 0$. In order to maintain this asymmetry, while increasing the plasma current further, the vacuum poloidal field must be ramped-up. This leads to an increase in I_{CFS}, such that I_P can also increase while the asymmetry in the confinement of electrons is sustained.

The time evolution of the magnetic field is shown in figure 4.23. A small CFS is always present, but the depth of the magnetic well is shallow, as is seen from the magnetic vector potential in figure 4.22. The comparison of the confinement of electrons between numerical and mathematical calculations is shown in figure 4.24.

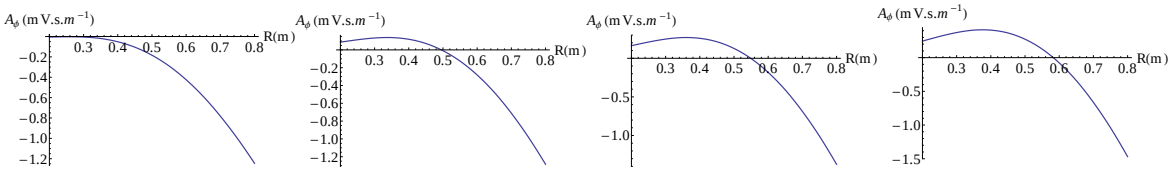

(a) (b) (c) (d)

Figure 4.22: The magnetic vector potential after (a) 70 ms, (b) 80 ms, (c) 90 ms, and (d) 100 ms for MAST shot #28941 shows the existence of a small CFS.

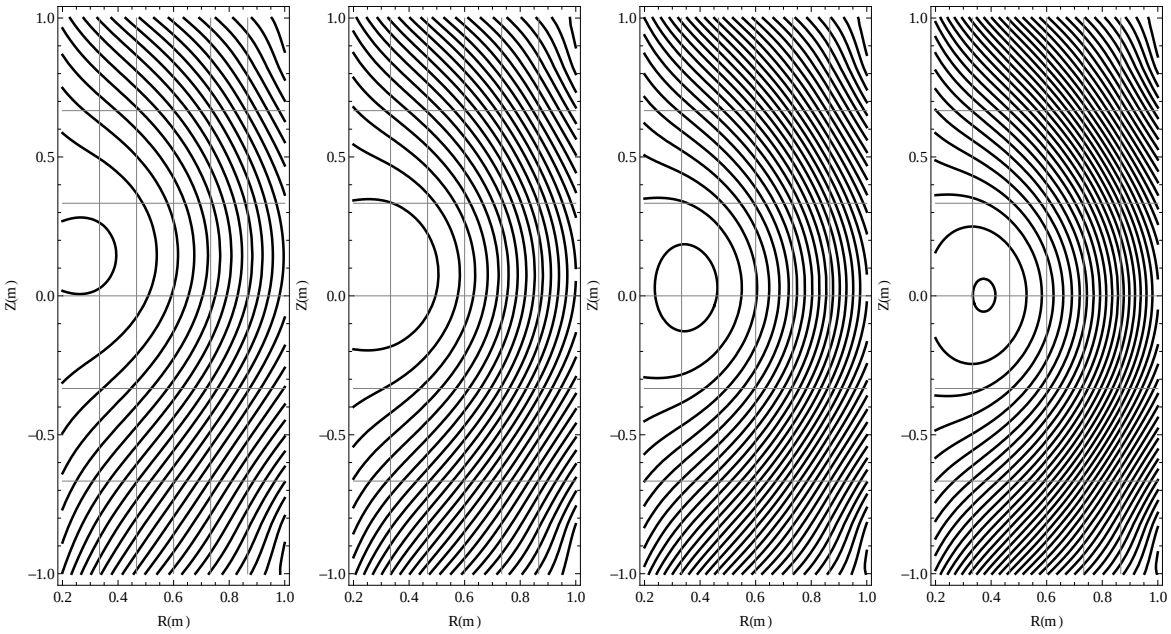

(a) (b) (c) (d)

Figure 4.23: Contours of constant magnetic field after (a) 70 ms, (b) 80 ms, (c) 90 ms, and (d) 100 ms for MAST shot #28941.

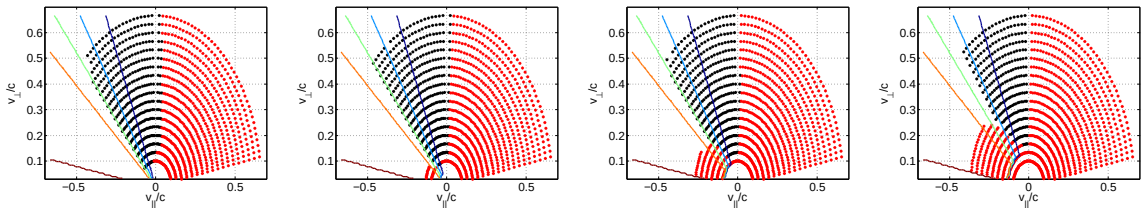

(a) (b) (c) (d)

Figure 4.24: Comparison of the confinement map shows a good agreement between the numerical, using the guiding centre orbit, and analytical, using the empirically derived equations, after (a) 70 ms, (b) 80 ms, (c) 90 ms, and (d) 100 ms. Electrons complete trapped (black) or passing (red) orbits, while the white space corresponds to electrons lost. The overlay plot is the analytical probability of an electron being lost/confined, with it changing from $P_{\text{loss}} = 1$ (red) to $P_{\text{loss}} = 0$ (blue) in increments of 0.2.

4.3.1.3 Constant B_V: $130 - 300$ ms

During this period the vacuum poloidal field is approximately constant, such that I_{CFS} remains constant, and an increase in I_P will eliminate any asymmetry in the confinement of electrons until all electrons are confined.

The time evolution of the magnetic field, shown in figure 4.25, shows that more CFS form, and the depth of these CFS also deepens, as can be seen from the vector potential in

figure 4.26. The comparison of the confinement map between numerical and mathematical calculations is shown in figure 4.27.

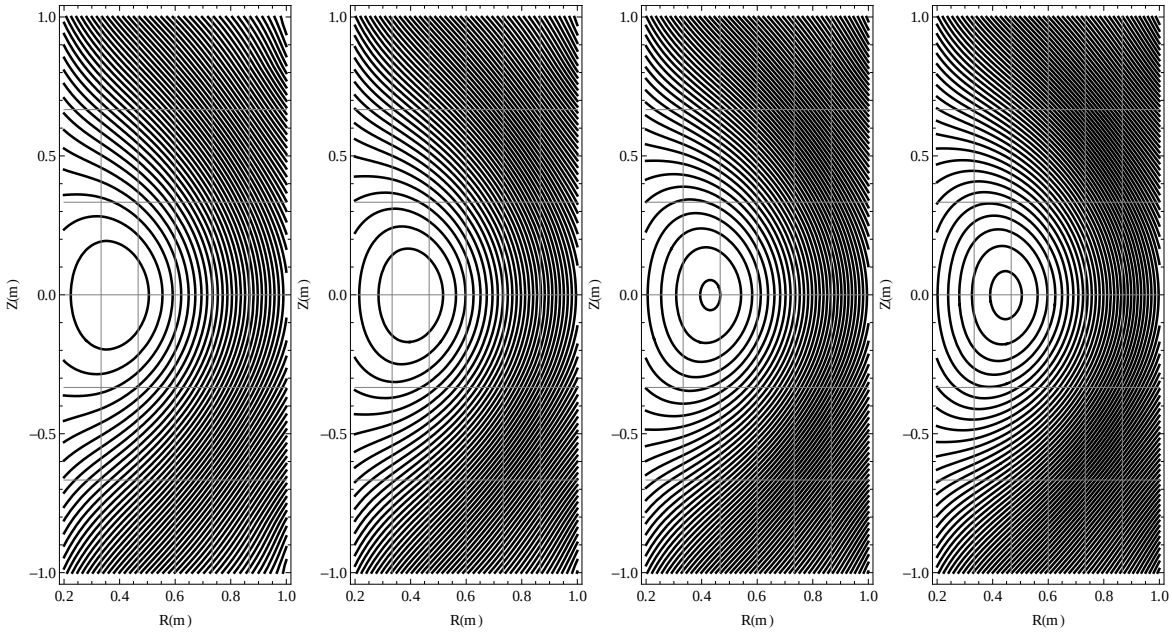

(a) (b) (c) (d)

Figure 4.25: Contours of constant magnetic field after (a) 150 ms, (b) 180 ms, (c) 210 ms, and (d) 240 ms for MAST shot #28941.

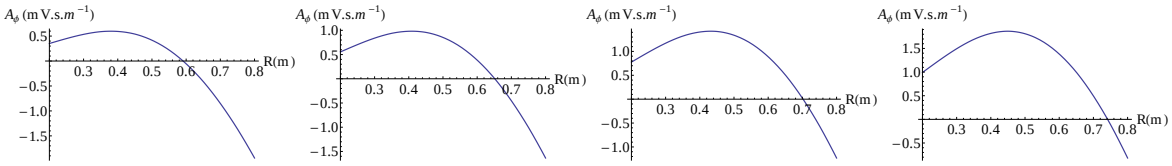

(a) (b) (c) (d)

Figure 4.26: The magnetic vector potential after (a) 150 ms, (b) 180 ms, (c) 210 ms, and (d) 240 ms for MAST shot #28941, shows the gradual deepening of the magnetic well and the formation of larger CFS.

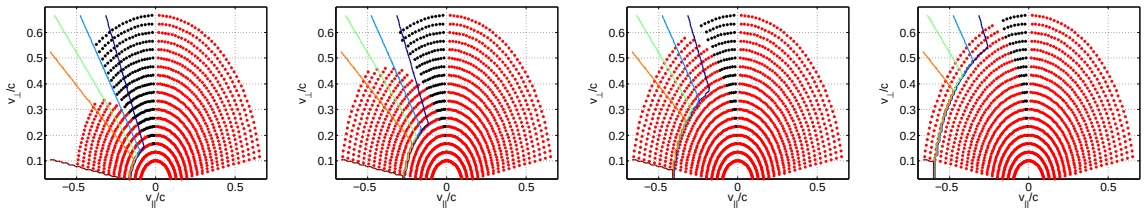

(a) (b) (c) (d)

Figure 4.27: Comparison of the confinement map shows a good agreement between the numerical, using the guiding centre orbit, and analytical, using the empirically derived equations, after (a) 150 ms, (b) 180 ms, (c) 210 ms, and (d) 240 ms. Electrons complete trapped (black) or passing (red) orbits, while the white space corresponds to electrons lost. The overlay plot is the analytical probability of an electron being lost/confined, with it changing from $P_{\text{loss}} = 1$ (red) to $P_{\text{loss}} = 0$ (blue) in increments of 0.2.

4.3.1.4 Confinement of cold electrons

The confinement of colder electrons during the initial start-up phase is shown in figure 4.28. After about 80 ms, all electrons with $T_e < 1$ keV are confined.

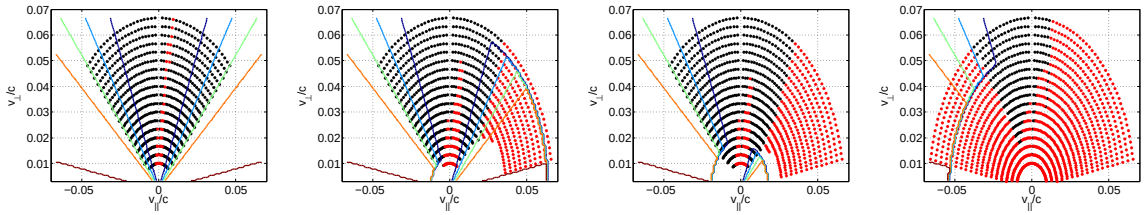

(a) (b) (c) (d)

Figure 4.28: Comparison of the confinement map determined numerically and theoretically after (a) 40 ms, (b) 60 ms, (c) 70 ms and (d) 80 ms. Electrons complete trapped (black) or passing (red) orbits, while the white space corresponds to electrons lost. The overlay plot is the analytical probability of an electron being lost/confined, with it changing from $P_{\text{loss}} = 1$ (red) to $P_{\text{loss}} = 0$ (blue) in increments of 0.2.

4.3.1.5 Comparison of loss time

The loss time is dominated by parallel losses of electrons streaming along the magnetic field lines out of the plasma during start-up while the magnetic field line configuration is open. The time it takes for an electron to be lost is determined by the vertical magnetic field B_Z, which changes as a current is generated. A comparison of the empirical and numerical loss times is shown in figure 4.29.

Electrons with $v_{\parallel} > 0$ are confined as I_P approaches I_{CFS}, which leads to a lack of data

on the loss times of these electrons. The value of B_Z is spatially dependent, to such an extent that the loss time can only be approximated. The value of B_Z is slightly modified from equation (4.6),

$$B_Z[\mathrm{mT}] = \begin{cases} 0.8|B_V[\mathrm{mT}] - \exp\left(I_P/I_{\mathrm{CFS}}\right)| & v_\parallel > 0 \\ B_V[\mathrm{mT}]\exp\left(\frac{|v_\parallel|}{c}\right) & v_\parallel < 0 \end{cases}$$

where the vacuum poloidal field B_V can be related to the value of I_{CFS},

$$B_V[\mathrm{mT}] \approx \left(\frac{2}{3} I_{\mathrm{CFS}}[\mathrm{kA}]\right) \tag{4.20}$$

in order to obtain the best fit of numerical and analytical loss times.

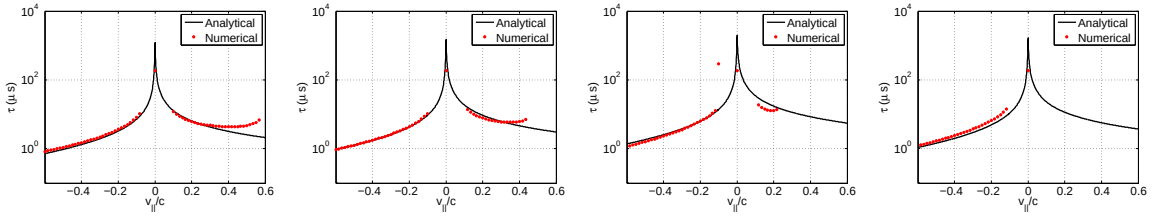

(a) (b) (c) (d)

Figure 4.29: Comparison of the loss time determined numerically (red) using the guiding centre approximation and empirically (black) using equation (4.6), after (a) 20 ms, (b) 30 ms, (c) 40 ms, and (d) 70 ms, for electrons with $v_\perp = 3 \times 10^7\,\mathrm{m.s}^{-1}$.

4.4 Summary

The change in magnetic field topology, from an initial open field line configuration to the formation of CFS, is a crucial part of start-up. During the initial open magnetic field line phase, electrons can freely stream out of the plasma volume along these field lines, and modelling this loss mechanism is important for particle and power balance [8], as well as its impact on current drive (CD).

In an axisymmetric system, where the toroidal field greatly exceeds the poloidal field, as is the case during start-up in MAST, the electron orbits can be approximated by the guiding centre approximation, which predicts ∇B and curvature drifts. The addition of a small vertical field will cancel the drift of a selection of electrons, such that certain electrons are confined while all others are lost. This preferential confinement of electrons creates an

asymmetry in the electron distribution function and ultimately generates a plasma current [21].

An analytical expression for the loss term is required in order to implement it in the mathematical description of the kinetic model. It is therefore approximated by

$$\left(\frac{\partial f}{\partial t}\right)_{\text{loss}} = -\frac{f}{\tau_{\text{loss}}(p_{\parallel}, p_{\perp})} P_{\text{loss}}(p_{\parallel}, p_{\perp})$$

where $\tau_{\text{loss}}(p_{\parallel}, p_{\perp})$ is the average time it takes for an electron of momentum $(p_{\parallel}, p_{\perp})$ to be lost, and

$$P_{\text{loss}}(p_{\parallel}, p_{\perp}) = 1 - \exp\left[-\ell \frac{p_{\parallel}^2}{p_{\perp}^2}\right]$$

is the probability of an electron being lost or confined. The function $\ell = \ell(p_{\parallel}, I_P, I_{\text{CFS}}, Z_0)$ describes the evolution of the electron confinement as a function of plasma current, I_{CFS}, the value of the plasma current where CFS first start to form and all electrons with $v_{\parallel} > 0$ are confined, and Z_0, the vertical shift of the plasma. The value of I_{CFS} is particularly important, as it contains knowledge of the vacuum poloidal field strength and shape, as well as the current density profile, such that any uncertainty in the vacuum poloidal field or current density profile can be represented by an uncertainty in the value of I_{CFS}.

The function $\ell = \ell(p_{\parallel}, I_P, I_{\text{CFS}}, Z_0)$ is parametrized in Appendix G, with its values given by equations (4.12 - 4.17). It is obtained by empirically fitting mathematical expressions to numerical data, obtained using the guiding centre approximation, in order to approximate the electron confinement. It is compared to the numerical data for experimental magnetic fields in order to illustrate two effects concerning the vacuum poloidal field that is believed to have an impact on the generated plasma current:

1. Creating an up/down shift helps to create CFS

   From studying the loss term, creating an up/down shift enhances the asymmetry in the confinement of electrons. If this asymmetry is responsible for generating a current, then the greater the asymmetry, the greater the generated current, and therefore an up/down shift helps to form CFS. Of course, an up/down shift is more efficient before CFS forms, when electrons are only partially confined.

2. The most efficient way of achieving a higher plasma current is by increasing the strength of the vacuum poloidal field B_V

When the first CFS forms, all electrons with $v_{\parallel} > 0$ are confined, but not all electrons with $v_{\parallel} < 0$. If this asymmetry can be sustained, a larger current can be generated. It was shown that the asymmetry in the confinement of electrons depends largely on the ratio I_P/I_{CFS}. Increasing the vacuum poloidal field strength B_V leads to an increase in I_{CFS}, which leads to a subsequent increase in the plasma current I_P as the asymmetry in electron confinement is sustained.

In conclusion, in this chapter a parametrized equation for studying the evolution of the electron loss term, as a function of the vacuum poloidal field and plasma current, has been derived empirically from numerical studies of the guiding centre orbits. Comparisons are made between the mathematical expression and numerical confinement maps for experimental magnetic fields, and agreement is found to be good.

Parametrizing the loss term is an important step in understanding the CD mechanism responsible for the generated current - especially as the asymmetric confinement of electrons could lead to the generation of a plasma current. What this chapter achieves is not just an understanding of how the confinement of electrons evolve as a function of plasma current, but also the ability to study its effect on the electron distribution function, for which the solution is considered in Chapter 5, and its contribution to the generated plasma current, discussed in Chapter 6.

Chapter 5

Numerical solution to the kinetic model

The start-up model developed in Chapter 3 considers the time evolution of the distribution function in the presence of a number of effects. These effects influence the shape of the distribution function by allowing electrons to gain or lose momentum, and by changing the number of electrons through the source and loss terms.

As an analytical solution for the distribution function does not typically exist, a numerical approximation for studying the time evolution of the distribution must be obtained. This involves obtaining numerical methods for approximating the advection and diffusion terms describing the various effects. Any numerical method used has to ensure the conservation of particle number (in the absence of source and loss terms) and the preservation of positivity. Although a number of numerical methods exist, the preservation of positivity, especially in two-dimensions, is a difficult condition to satisfy without the use of additional smoothing or averaging.

The collision operator in two-dimensional cylindrical coordinates poses a particular challenge as it contains mixed derivatives, and obtaining positivity preserving approximations has been studied for decades. Taitano *et al.* [54] devised a successful, albeit intensive, method for approximating the collision operator, while the method proposed by Yoon and Chang [55] does not guarantee the preservation of positivity if the distribution is far from equilibrium.

In addition to solving advection and diffusion type equations, the solution method for the distribution function also needs to be consistent with certain constraints, such as the

electron density and power absorbed, which can be obtained from experiment and/or other models. To ensure this consistency, a number of parameters have been included which can be fitted to ensure these conditions hold.

In this chapter, a positivity-preserving scheme for solving two-dimensional advection-diffusion equations, including mixed derivatives, is presented. The validity of the approximation is discussed through an example. The algorithm is applied to the collision term, which poses a particular challenge due to the presence of mixed derivatives. The assumption of local thermal equilibrium, based on the Chang-Cooper averaging scheme [56], ensures the equilibrium distribution under the effect of collisions is the Maxwellian distribution, as required. Lastly, an example is considered to illustrate how parameters are fitted to certain conditions which ensures that the distribution function has the correct density, that the correct amount of power is absorbed, and that Lenz's law is satisfied.

5.1 Positivity-preserving scheme for two-dimensional advection-diffusion equations

The start-up model proposed in Chapter 3 simulates the time evolution of the electron distribution function in two-dimensional cylindrical coordinates $(p_\parallel, p_\perp)$. The various effects impacting the distribution function are written as advection-diffusion terms in momentum space, while the source and loss terms are written as constants depending on momentum. Due to the complexity of these equations, numerical approximations must be found as analytical solutions do not exist.

In order to obtain a numerical approximation to the distribution function $f(p_\parallel, p_\perp)$, the solution domain is divided into $2N \times N$ equally spaced grid points, with

$$p_{\parallel,i} = \Delta p/2 - p_{\max} + (i-1)\Delta p$$
$$p_{\perp,j} = \Delta p/2 + (j-1)\Delta p$$

where $i \in (1, 2N)$ and $j \in (1, N)$, and $\Delta p = p_{\max}/N$. There are twice as many grid points in the parallel direction, as $p_\parallel \in (-p_{\max}, p_{\max})$, while $p_\perp \in (0, p_{\max})$, where $p_{\max}$ is defined as the maximum momentum on the grid in each direction. The assumption is made that $f \to 0$ as $p_\parallel \to \pm\infty$ and $p_\perp \to \infty$, and therefore $p_{\max}$ should be large enough to ensure this condition holds.

The terms under which the distribution function evolves include, amongst others, derivatives of f with respect to momentum. Neglecting the source and loss terms, there are two common types of derivatives: the linear advective equation,

$$\frac{\partial f}{\partial t} + a\frac{\partial f}{\partial x} = 0$$

and the diffusion equation,

$$\frac{\partial f}{\partial t} + \frac{\partial}{\partial x}D\frac{\partial f}{\partial x} = 0$$

as well as mixed derivative terms. A numerical approximation to equations of these form must be found which ensures the conservation of particle number (flux-conserving) and the preservation of positivity. Although these type of equations have received a lot of attention in the literature [57–61], lower-order methods for obtaining positivity-preserving solutions in two-dimensions in the presence of mixed derivatives have not, as these equations would typically be solved with higher-order flux limiting schemes or through the change of coordinate system. As higher-order schemes are less robust and more intensive than lower-order methods, and a change of coordinate system is not always possible, lower-order methods are preferred here.

In this section, a lower-order scheme for solving equations of this type is presented, and it is demonstrated that it preserves positivity, while producing the same order of accuracy as standard finite-difference methods. The following sections consider the numerical approximation to each equation: the linear advection, diffusion, and mixed derivative equations, separately, before an approximation for the time derivative and an example are considered to test the accuracy of the numerical approximations.

5.1.1 Linear advection equation

The first equation to consider is the one-dimensional linear advection equation,

$$\frac{\partial f}{\partial t} + \frac{\partial (af)}{\partial x} = 0 \tag{5.1}$$

where $a = a(x)$ and $f = f(x,t)$. For simplicity, assume $a > 0$, such that fluid flows from small x to larger values of x. For $a < 0$, the direction of flow is reversed, while stagnation points are created where a changes sign on the solution domain and special care must be taken

when obtaining a numerical approximation in order to ensure the conservation of particle number.

The approximation to $f(x)$ at the i^{th} node, where $x = x_i = i\Delta x$, is written as $f(x_i) = f_i$ and leads to the semi-discrete conservation form,

$$\frac{\partial f}{\partial t} = -\frac{1}{\Delta x}\left(F_{i+1/2} - F_{i-1/2}\right) \tag{5.2}$$

where $F_{i\pm1/2} = a_{i\pm1/2} f_{i\pm1/2}$. For $a > 0$, the first term on the right-hand-side describes the decrease in the amount of fluid at f_i through the boundary $i + 1/2$, while the second term describes the increase in the amount of fluid at f_i through the boundary $i - 1/2$. For $a < 0$, the direction of fluid flow is reversed.

The value of $a_{i\pm1/2}$ can simply be evaluated at the boundary

$$a_{i\pm1/2} = a(x \pm \Delta x/2)$$

but, as the values of f are not known at the boundaries $f_{i\pm1/2}$, obtaining an expression for $f_{i\pm1/2}$ that preserves the positivity of f is more complicated.

The idea is to find a scheme which ensures that, for any non-negative initial solution $f(x, t_0)$, the evolving solution $f(x, t)$ remains non-negative for all $t \geq t_0$. Standard finite-difference schemes, such as averaging

$$f_{i+1/2} = \frac{1}{2}(f_i + f_{i+1})$$

are not positivity-preserving and will introduce false extrema due to overshoot and undershoot [61].

In order to preserve positivity, a flux limiter is applied,

$$f_{i+1/2} = f_i + \frac{1}{2}\phi_{i+1/2}(f_i - f_{i-1}) \tag{5.3}$$

where the limiter ϕ is typically a nonlinear function of neighbouring fluxes that defines a higher-order accurate scheme in smooth monotone regions of the solution, where no oscillations will arise, while in regions of sharp gradients the limiter must prevent oscillations and enforce positivity [61].

In general, first-order methods have the advantage of keeping the solution monotonically

varying in regions where the solution should be monotone, even though the accuracy isn't very good, while second-order methods give much better accuracy on smooth solutions, but fail near discontinuities. The idea of the flux limiter is to then combine the best features of both methods [60].

For $\phi = 0$ the scheme is first-order accurate and commonly referred to as the donor-cell-upwind (DCU) method. There exist various schemes for calculating values for ϕ such that the scheme is higher-order accurate [60], but in this section the scheme proposed by Hundsdorfer [61] will be used. This scheme gives

$$\phi_{i+1/2} = \max(0, \min(2r, \min(2, K(r)))) \tag{5.4}$$

with

$$r_{i+1/2} = \frac{u_{i+1} - u_i}{u_i - u_{i-1}} \tag{5.5}$$

and

$$K(r) = \frac{1 + 2r}{3} \tag{5.6}$$

to provide a second-order accurate positivity-preserving solution to the linear advection equation (5.1) in both one and two dimensions.

In the mathematical description of the kinetic model, linear advective terms will be approximated using the first-order DCU scheme derived in this section. The second-order Hundsdorfer scheme will be used in an example, used to test the robustness and acuracy of the solution to the mixed derivatives, discussed later.

5.1.2 Diffusion equation

The second type of differential equation to consider is the one-dimensional diffusion equation,

$$\frac{\partial f}{\partial t} + \frac{\partial}{\partial x} D \frac{\partial f}{\partial x} = 0 \tag{5.7}$$

where the diffusion coefficient $D = D(x)$ and $f = f(x, t)$.

A second-order accurate numerical approximation is straightforward to achieve, by taking a second-order derivative to obtain

$$\frac{\partial}{\partial x} D \frac{\partial f}{\partial x} = \frac{1}{\Delta x} \frac{\partial}{\partial x} D \left[f\left(x + \frac{\Delta x}{2}\right) - f\left(x - \frac{\Delta x}{2}\right) \right] + \mathcal{O}(\Delta x^2)$$

and taking it again to obtain the approximation

$$\frac{\partial f}{\partial t} = \frac{1}{\Delta x^2}\left[D\left(x+\frac{\Delta x}{2}\right)\left(f_{i+1}-f_i\right) - D\left(x-\frac{\Delta x}{2}\right)\left(f_i - f_{i-1}\right)\right] + \mathcal{O}(\Delta x^2) \tag{5.8}$$

which satisfies all the criteria of a positivity-preserving numerical method for both $D(x) > 0$ and $D(x) < 0$, in one and two dimensions, and is second-order accurate. This approximation is used for all diffusion-type equations in the kinetic model.

5.1.3 Mixed derivatives

The last type of differential equation is the mixed derivative. These equations are encountered in the Fokker-Planck collision operator, when writing it in cylindrical coordinates. In spherical coordinates, the collision operator does not contain any mixed derivatives, but if the distribution function is solved in spherical coordinates, the RF heating term will contain mixed derivatives. As collisions are not expected to be dominant, and as cylindrical coordinates is the natural coordinate system for solving the RF heating, the distribution function is solved in cylindrical coordinates.

Mixed derivative equations can be written as

$$\frac{\partial f}{\partial t} + \frac{\partial}{\partial x} D \frac{\partial f}{\partial y} = 0 \tag{5.9}$$

where $D = D(x, y)$ and $f = f(x, y, t)$.

Positivity-preserving approximations to mixed derivative equations are challenging and are normally obtained through a change of coordinates in order to eliminate the mixed derivative. As this is not always possible, a positivity-preserving approximation must be found. By rewriting the mixed derivative as a linear advective equation, the positivity-preserving approximation of Section 5.1.1 can be applied. This can be achieved by defining the function

$$v = \frac{1}{f}\frac{\partial f}{\partial y} \tag{5.10}$$

such that the mixed derivative equation (5.9) can be rewritten as

$$\frac{\partial f}{\partial t} + \frac{\partial}{\partial x} D \cdot v \cdot f = 0 \tag{5.11}$$

where $v = v(x, y, f)$.

The result is a nonlinear advection equation, which can be approximated using second-order positivity-preserving schemes, such as the Hundsdorfer scheme discussed in Section 5.1.1, while the nonlinearity can be resolved through Picard iteration, discussed later. A more straightforward solution is through Picard linearizing, where the function v is determined from the known values of f^n in order to find the solution f^{n+1} at the next time step.

The function $v \to \infty$ as $f \to 0$, but in order to deal with such singularities, it is assumed that the grid is fine enough and the function smooth enough such that the difference between neighbouring nodes is small, such that $|f_{j+1} - f_{j-1}| \ll f_j$, and the function

$$v_j = \frac{1}{f_j}\frac{\partial f_j}{\partial y} = \frac{1}{2\Delta y}\frac{f_{j+1} - f_{j-1}}{f_j} \approx 0$$

if $f_j < \epsilon$, where $\epsilon \ll 1$. The value of ϵ will depend on the particular problem, as well as the relative values of f and coarseness of the grid, but in this work $\epsilon = 10^{-16}$ is more than sufficient. The value of $v_{j\pm1/2}$ is calculated by averaging, as shown by equation 5.26.

To my knowledge this approach has not been used before, as standard central finite-differencing methods or intensive flux-limiting methods are typically used for approximating mixed derivative equations. It will be shown later that this approach is advantageous to using a central finite-differencing method, as it guarantees the preservation of positivity, and is therefore used for approximating all mixed derivative-type equations in the kinetic model.

5.1.4 Explicit and implicit evolution in time

Apart from obtaining numerical approximations to the derivatives in momentum space, an approximation for the time derivative is needed as well. In order to determine a method for approximating the time derivative, consider the equation

$$\frac{\partial f}{\partial t} = F(f, t, x) \tag{5.12}$$

where the function $F(f, t, x)$ could depend on f, t, or x in any way.

The distribution function should be evolved in time, such that, after n steps, the distribution function at node i is given by the numerical approximation,

$$f(x = x_i, t = t_n) = f_i^n$$

To approximate the time derivative in (5.12), either the forward Euler method,

$$f^{n+1} = f^n + \Delta t\, F(f^n, t^n) + \mathcal{O}(\Delta t) \tag{5.13}$$

which solves f explicitly, or the backward Euler method,

$$f^{n+1} = f^n + \Delta t\, F(f^{n+1}, t^{n+1}) + \mathcal{O}(\Delta t) \tag{5.14}$$

which solves f implicitly, could be used. Both methods have their advantages, which can be illustrated with an example. Consider the first-order linear advection equation with a constant $a > 0$,

$$\frac{\partial f}{\partial t} = -\frac{a}{\Delta x}\Big(f_i - f_{i-1}\Big)$$

which can be solved explicitly, by using the forward Euler method (5.13),

$$f_i^{n+1} = f_i^n - \lambda\Big(f_i^n - f_{i-1}^n\Big) \tag{5.15}$$

or implicitly, using the backward Euler method (5.14),

$$f_i^{n+1} = f_i^n - \lambda\Big(f_i^{n+1} - f_{i-1}^{n+1}\Big) \tag{5.16}$$

where

$$\lambda = a\frac{\Delta t}{\Delta x}$$

is the Courant number [62]. For the explicit equation (5.15) $\lambda \leq 1$ to ensure a stable solution (i.e. flux-conserving and positivity-preserving). The implicit equation (5.16), on the other hand, is unconditionally stable, allowing arbitrarily large time steps Δt as the condition $\lambda \leq 1$ is no longer required. Solutions using the implicit method are obtained by setting up and solving a matrix equation, as discussed in Appendix H.

Both the explicit and implicit methods are first-order accurate in time. Higher-order methods exist, such as the θ-splitting scheme, which is a combination of the forward and backward Euler methods,

$$f^{n+1} = f^n + \Delta t\Big[\theta F(f^n, t^n) + (1-\theta)F(f^{n+1}, t^{n+1})\Big] \tag{5.17}$$

and is second-order accurate in time and known as the Crank-Nicolson scheme for $\theta = 1/2$ [63]. Unfortunately this method is not unconditionally stable as it contains an explicit part to the solution, even though it is more stable than the forward Euler method.

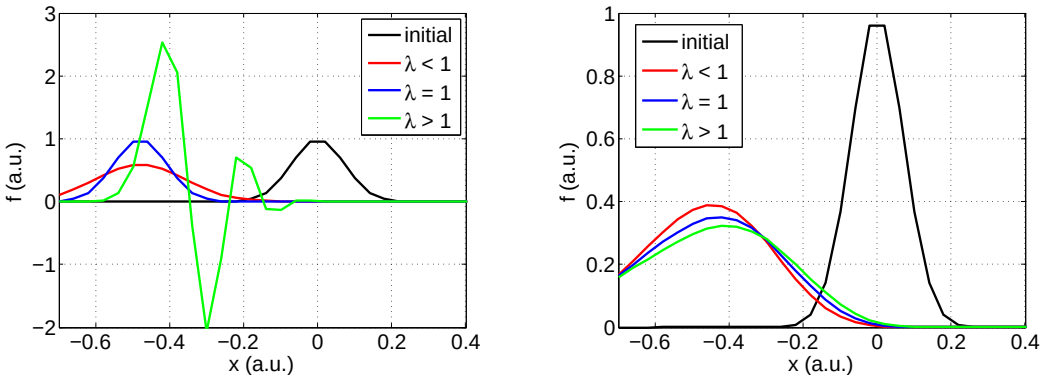

Figure 5.1: Comparison of the (a) explicit and (b) implicit solutions to the linear advection equation with a constant $a = 1$, for different choices of λ.

The comparison of the explicit and implicit solutions to the linear advection equation, for a constant $a = 1$, is shown in figure 5.1 for different values of λ. For the explicit method, the initial condition is exactly reproduced if $\lambda = 1$, while it becomes smeared out if $\lambda < 1$ and becomes unstable for $\lambda > 1$. In comparison, the implicit method is always stable, but smearing occurs irrespective of the value of λ.

The explicit method is perhaps the ideal method of evolving the distribution function in time, but when solving f under several effects, the condition $\lambda = 1$ cannot be satisfied for each term, and Δt will have to be chosen in such a way that $\lambda \leq 1$ for all terms, which can lead to very small values of Δt. In contrast, the implicit method, although it introduces smearing, remains unconditionally stable, regardless of the step size Δt, and is therefore the preferred method for evolving the distribution function in time.

5.1.5 Constant terms

The previous sections deal with the numerical approximations to differential equations, but the source and loss terms are represented by constant terms in the kinetic model. The loss term can be written as

$$\frac{\partial f}{\partial t} = c_{\text{loss}}\, f \tag{5.18}$$

where $c_{\text{loss}} < 0$ and $f = f(x,t)$, while the source term can be written as

$$\frac{\partial f}{\partial t} = c_{\text{source}} \tag{5.19}$$

where $c_{\text{source}} > 0$. Approximations to these terms are straightforward as, for the loss term, the change in the value of f at position x is only related to the value of the node itself and the value of c_{loss} at that point. Explicitly, the loss term can be approximated with

$$f_i^{n+1} = f_i^n \left(1 + c_{\text{loss}} \Delta t\right)$$

and it is clear that, if $|c_{\text{loss}}| > 1/\Delta t$ the value at f_i will become negative (assuming $f > 0$ for all x). As the distribution function f must remain non-negative at all positions x, in order to obtain an explicit approximation the time step Δt must be very small to ensure $f > 0$ always. As electron losses can be large, especially for large momenta, an explicit method for evolving the distribution function in time can not be considered.

The implicit method,

$$\left(1 - c_{\text{loss}} \Delta t\right) f_i^{n+1} = f_i^n$$

will ensure that $f > 0$ for all x and for any Δt, and is therefore used to approximate the loss term.

For the source term, the change in f at x is only related to the value of c_{source}, and the explicit method,

$$f_i^{n+1} = f_i^n + c_{\text{source}} \Delta t$$

can be used to obtain an approximation.

The source and loss terms are therefore approximated with a combination of the implicit and explicit methods to ensure $f > 0$ for all x. The loss term is approximated with the implicit method, while the source term is approximated with the explicit method. The time evolution of the distribution function can then be studied under both effects simultaneously,

$$\left(1 - c_{\text{loss}} \Delta t\right) f_i^{n+1} = f_i^n + c_{\text{source}} \Delta t$$

where $c_{\text{loss}} < 0$ represents the loss term and $c_{\text{source}} > 0$ represents the source term.

5.1.6 Two-dimensional diffusion including mixed derivatives

In order to test the proposed scheme for obtaining a numerical approximation to the mixed derivative terms of Section 5.1.3, consider the two-dimensional diffusion equation,

$$u_t = u_{xx} + u_{xy} + u_{yx} + u_{yy} \tag{5.20}$$

with initial condition

$$u(x, y, t = 0) = \exp\left[-x^2 - y^2\right]$$

and open boundary conditions, such that the grid on which $u(x, y, t)$ is solved must be large enough to ensure $u = 0$ to within numerical error at the boundaries always.

An analytical solution can be obtained by performing a change of coordinates to eliminate the mixed derivatives, to obtain

$$U(x, y, t) = \frac{1}{\sqrt{1 + 8t}} \exp\left[-\left(\frac{1}{2}x^2 + \frac{1}{2}y^2 - xy\right) - \frac{1}{1 + 8t}\left(\frac{1}{2}x^2 + \frac{1}{2}y^2 + xy\right)\right] \tag{5.21}$$

which can be compared to the numerical approximation through

$$E_{\text{rms}} = \sqrt{\frac{1}{N^2}\sum_{i,j}(u_{i,j} - U_{i,j})^2} \tag{5.22}$$

where N is the number of grid points in both the x- and y-directions.

The solution is obtained on a uniform grid size $x, y \in (-10, 10)$ with $\Delta x = \Delta y = 20/N$, and $\Delta t = 0.1$ for 20 timesteps. The initial and final functions, at $t = 0$ and at $t = 2$, are shown in figure 5.2.

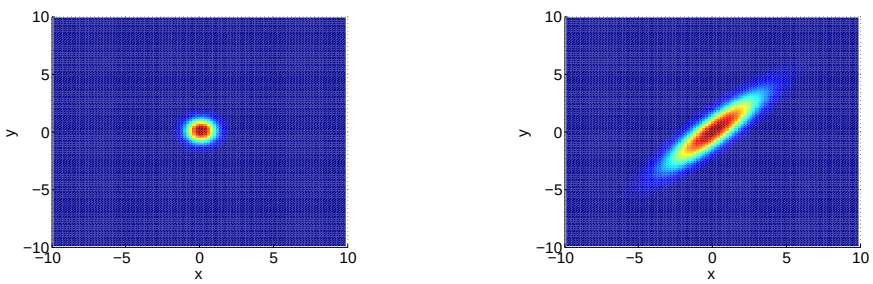

Figure 5.2: The (a) initial and (b) final solutions of the two-dimensional diffusion equation example considered in equation (5.20).

The numerical solution to the diffusion terms u_{xx} and u_{yy} are given in Section 5.1.2, while the mixed derivatives are solved in three ways:

1. The nonlinear scheme of Section 5.1.3 along with the second-order Hundsdorfer scheme as described in Section 5.1.1

2. The nonlinear scheme of Section 5.1.3 along with the first-order DCU scheme as described in Section 5.1.1

3. A second-order central finite-difference method where the boundary values are determined as an average, i.e. $u_{i+1/2} = \frac{1}{2}(u_i + u_{i+1})$

Comparisons of the analytical and numerical solutions are shown in figure 5.3 along with a comparison of the accuracy of the solution through the value of E_{rms}. As expected, the central finite-difference scheme does not preserve positivity, while both the first-order DCU and second-order Hundsdorfer schemes preserve positivity. The central finite-difference and Hundsdorfer schemes are both second-order accurate, while the DCU scheme is first-order accurate, as expected. For small N, the grid is very coarse, such that variations between neighbouring cells are great, and the Hundsdorfer scheme is effectively first-order as the flux-limiter $\phi \approx 0$ due to large variations between neighbouring nodes. When increasing N the Hundsdorfer scheme improves to become second-order accurate.

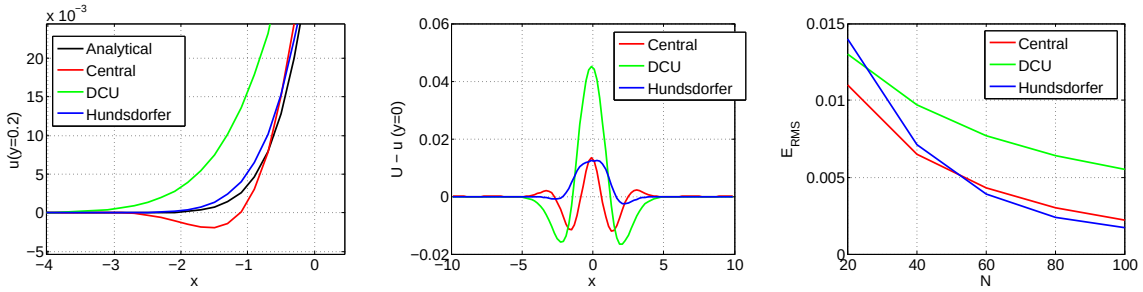

(a) (b) (c)

Figure 5.3: (a) The comparison of analytical to numerical solutions shows that the central finite-difference scheme does not preserve positivity. (b) The difference between analytical and numerical approximations for $y = 0$, with $N = 100$ grid points. (c) The comparison of E_{RMS} for different numerical methods, as a function of number of grid points N.

Although higher-order methods for solving two-dimensional advection-diffusion equations with mixed derivatives can be obtained with the use of flux limiters, these are often complicated and less robust than lower-order methods. Lower-order methods, on the other

hand, tend to be less accurate, and do not guarantee the preservation of positivity, as illustrated with the use of the central finite-difference scheme. The proposed positivity-preserving scheme therefore improves the accuracy of lower-order methods by ensuring the preservation of positivity while providing the same order of accuracy as other finite-difference methods.

5.2 Collisions in cylindrical coordinates

In this section the numerical approximation to the collision operator is discussed in the absence of all other terms. The collision operator describes the effect of electron-electron collisions, and, in the absence of other terms, the steady-state distribution will be a Maxwellian distribution.

The numerical approximation to this term requires special attention due to the presence of mixed derivatives, while the steady-state distribution is a strongly (exponentially) varying function of momentum, which inhibits the positivity-preserving nature of most numerical approximations. In this section, a positivity-preserving scheme, which produces the correct steady-state distribution, is derived using the numerical approximations discussed in the previous section.

5.2.1 The Fokker-Planck collision operator

The Fokker-Planck collision operator, along with the Vlasov and Maxwell's equations, forms the basis for weakly coupled plasmas in all collisionality regimes. It is mathematically very well defined, as it enforces conservation of density, momentum and energy, preserves positivity of the distribution function, and satisfies the Boltzmann H-theorem, such that the solution is given by the Maxwellian distribution function. Despite this, however, it is a stiff advection-diffusion operator in velocity space, and nonlinear when solving the collision operators from the Rosenbluth potentials [48] or Landau integrals [49], which leads to several difficulties in dealing with it numerically [54].

Further, the Fokker-Planck collision operator is best described in spherical coordinates (p, θ), but, in the framework of RF start-up, where RF power is best described in cylindrical coordinates $(p_\parallel, p_\perp)$, an approximation to the Fokker-Planck collision operator in cylindrical coordinates is required. This introduces a further complication, as the collision operator in

cylindrical coordinates,

$$\begin{aligned}\frac{\partial f}{\partial t} = \frac{1}{p_\perp}\frac{\partial}{\partial p_\perp} p_\perp \left[D_{\perp\perp}\frac{\partial f}{\partial p_\perp} + D_{\perp\parallel}\frac{\partial f}{\partial p_\parallel} - F_\perp f \right] \\ + \frac{\partial}{\partial p_\parallel}\left[D_{\parallel\parallel}\frac{\partial f}{\partial p_\parallel} + D_{\parallel\perp}\frac{\partial f}{\partial p_\perp} - F_\parallel f \right]\end{aligned} \tag{5.23}$$

contains mixed derivatives. Obtaining the values of the coefficients D and F was discussed in Section 3.6.

The approximation to the one-dimensional collision operator has been studied for decades, but the two-dimensional approximation has only recently been studied in detail. One of these studies was done by Yoon and Chang [55], who attempted an extension to the positivity-preserving scheme first introduced by Chang and Cooper [56], but their method does not guarantee positivity when the solution is far from equilibrium. A more successful approach was introduced by Taitano *et al.* [54], who proposed a fully implicit finite volume algorithm for solving the Rosenbluth-Fokker-Planck equation, conserving mass, momentum and energy, and preserving positivity, through the use of flux limiters. As this approach is intensive, the lower-order scheme proposed in the previous section for approximating two-dimensional advection-diffusion equations is used here for approximating the collision operator.

5.2.2 Numerical approximation to the collision operator

A numerical approximation to the Fokker-Planck collision operator (5.23) must be found, as analytical solutions are not available, apart from at equilibrium. A numerical approximation can be obtained by using the schemes discussed in Section 5.1.

The advective terms $F_\parallel$ and $F_\perp$ describe the slowing down of electrons due to electron-electron collisions, and are approximated, for simplicity, with the first-order DCU scheme, discussed in Section 5.1.1. The reason for using the first-order scheme will be illustrated in the next section.

The diffusion terms $D_{\perp\perp}$ and $D_{\parallel\parallel}$ describe pitch-angle scattering due to electron-electron and electron-ion collisions, and are approximated with the second-order scheme discussed in Section 5.1.2.

The mixed derivative terms, also describing pitch-angle scattering due to electron-electron and electron-ion collisions, are solved with the nonlinear scheme proposed in Section 5.1.3.

This is done by defining the function

$$g(p_\parallel, p_\perp) = \frac{1}{f}\frac{\partial f}{\partial p_\parallel} \tag{5.24}$$

such that the $D_{\perp\parallel}$-term can be written as,

$$\begin{aligned}\frac{\partial f}{\partial t} &= \frac{1}{p_\perp}\frac{\partial}{\partial p_\perp} p_\perp D_{\perp\parallel}(p_\parallel, p_\perp)\,\frac{\partial f}{\partial p_\parallel} \\ &= \frac{1}{p_\perp}\frac{\partial}{\partial p_\perp} p_\perp D_{\perp\parallel}(p_\parallel, p_\perp)\, g(p_\parallel, p_\perp)\, f\end{aligned}$$

which is similar to a linear advection equation. The first-order DCU scheme is then used to obtain a numerical approximation.

The values of g can easily be obtained numerically with

$$g(p_\parallel, p_\perp) = \frac{1}{f}\frac{\partial f}{\partial p_\parallel} = \frac{1}{2\Delta p}\frac{f_{i+1,j} - f_{i-1,j}}{f_{i,j}} + \mathcal{O}(\Delta p^2) \tag{5.25}$$

and

$$g_{i,j+1/2} = \frac{1}{2}\Big(g_{i,j+1} + g_{i,j}\Big) \tag{5.26}$$

The $D_{\parallel\perp}$-term is treated in a similar way by defining the function,

$$h(p_\parallel, p_\perp) = \frac{1}{f}\frac{\partial f}{\partial p_\perp} \tag{5.27}$$

such that,

$$\begin{aligned}\frac{\partial f}{\partial t} &= \frac{\partial}{\partial p_\parallel} D_{\parallel\perp}(p_\parallel, p_\perp)\frac{\partial f}{\partial p_\perp} \\ &= \frac{\partial}{\partial p_\parallel} D_{\parallel\perp}(p_\parallel, p_\perp)\, h(p_\parallel, p_\perp)\, f\end{aligned}$$

and again the first-order DCU scheme can be used to obtain a numerical approximation.

This numerical method allows a first-order solution to the Fokker-Planck collision operator in cylindrical coordinates that conserves density and preserves positivity. As this scheme is only first-order accurate, a large number of grid points are required to provide an accurate approximation, as will be shown later. In order to improve on this and ensure the steady-state approximation has the correct equilibrium distribution, Chang and Cooper devised a weighted average scheme [56], based on the assumption of local thermal equilibrium. This scheme was extended to a two-dimensional solution by Yoon and Chang [55],

but the preservation of positivity was not guaranteed in their solution. In the next section, this method will be applied to the two-dimensional collision operator, using the numerical method discussed here. It will be shown that the approximation guarantees the preservation of positivity, while producing the correct equilibrium distribution in the absence of all other terms.

5.2.3 δ-splitting

Under the effect of collisions only, the steady-state solution to the Fokker-Planck collision operator is a Maxwellian distribution function, which is a strongly (exponentially) varying function of momentum. In order to ensure the preservation of positivity and the correct equilibrium distribution, Chang and Cooper [56] introduced an average weighting scheme, as central finite-difference schemes will require a very fine grid to accurately resolve the strongly varying nature of the Maxwellian distribution. This scheme has been extended to two-dimensions, but the resulting approximation does not guarantee the preservation of positivity [55]. Using the numerical approximations discussed in the previous section, however, an approximation to the two-dimensional collision operator is found, using the averaging scheme introduced by Chang and Cooper, that guarantees the preservation of positivity and produces the correct equilibrium distribution in the absence of all other terms.

Consider the collision operator,

$$\frac{\partial f}{\partial t} + \nabla \cdot \vec{S}_c = 0$$

where the flux $\vec{S}_c$ will approach zero if the distribution is in steady-state. If the numerical scheme for solving the time evolution of f does not guarantee the conservation of particle number under the divergene of a flux, then the assumption $\vec{S}_c = 0$ will ensure the conservation of particle number. If the numerical scheme ensures the conservation of particle number by construction, however, as the flux-conserving scheme used in this work, then the assumption $\vec{S}_c = 0$ improves the accuracy of the approximation, as will be shown later.

The scheme introduced by Chang and Cooper therefore assumes local thermal equilibrium and $\vec{S}_c = 0$, in order to ensure the conservation of particle number and the preservation of positivity. This condition can be used to derive a weighting parameter for the advective terms of the two-dimensional collision operator in cylindrical coordinates, $F_{\|}$ and $F_{\perp}$.

First, consider the $p_\perp$ part of the collision operator,

$$\frac{\partial f}{\partial t} = \frac{1}{p_\perp}\frac{\partial}{\partial p_\perp} p_\perp \left[D_{\perp\perp}\frac{\partial f}{\partial p_\perp} + D_{\perp\parallel}\frac{\partial f}{\partial p_\parallel} - F_\perp f \right]$$

for which the flux,

$$D_{\perp\perp}\frac{\partial f}{\partial p_\perp} + D_{\perp\parallel}\, g\, f - F_\perp\, f$$

will equal zero if the distribution is in local thermal equilibrium. Under this assumption, the flux can be rewritten as

$$\frac{\partial f}{\partial p_\perp} = \frac{1}{D_{\perp\perp}}\Big(F_\perp - D_{\perp\parallel}\cdot g \Big) f$$

which leads to the solution

$$\begin{aligned} f_{i,j+1} &\sim f_{i,j}\exp\left[\frac{F_\perp - D_{\perp\parallel}\cdot g}{D_{\perp\perp}}\Delta p \right] \\ &= f_{i,j}\exp\Big[A_g - B_g \Big] \end{aligned}$$

where

$$A_g = \frac{F_\perp}{D_{\perp\perp}}\Delta p \qquad ; \qquad B_g = \frac{D_{\perp\parallel}\cdot g}{D_{\perp\perp}}\Delta p \tag{5.28}$$

The aim is to write the discretized form of the $F_\perp$-term in equation (5.23) as,

$$\frac{\partial f}{\partial t} = \frac{1}{\Delta p}\left[\left(\frac{p_\perp - \Delta p/2}{p_\perp} \right) F_\perp \left(p_\parallel, p_\perp - \frac{\Delta p}{2} \right) \delta_\perp f_{i,j} - \left(\frac{p_\perp + \Delta p/2}{p_\perp} \right) F_\perp \left(p_\parallel, p_\perp + \frac{\Delta p}{2} \right) \delta_\perp f_{i,j+1} \right]$$

by introducing, and solving, for $\delta_\perp$. The discretized form of the flux in the $p_\perp$-direction (see equation (5.23)), at the $(p_\perp + \Delta p/2)$-boundary and for $D_{\perp\parallel}\cdot g > 0$, gives

$$\begin{aligned} &\frac{1}{\Delta p} D_{\perp\perp,j+1/2}(f_{i,j+1} - f_{i,j}) + D_{\perp\parallel,j+1/2} g_{j+1/2} f_{i,j+1} - F_{\perp,j+1/2}\, f_{i,j+1}\, \delta_\perp = 0 \\ &\qquad \Rightarrow f_{ij} e^{A_g} e^{-B_g} - f_{ij} + B_g\, f_{ij} e^{A_g} e^{-B_g} - A_g e^{A_g} e^{-B_g} f_{ij}\, \delta_\perp = 0 \end{aligned}$$

and equals zero under the assumption of local thermal equilibrium. Therefore,

$$\delta_\perp = \frac{1}{A_g}\Big(1 + B_g - e^{B_g - A_g} \Big) \tag{5.29}$$

with the same result obtained at the $(p_\perp - \Delta p/2)$-boundary.

For $D_{\perp\|} \cdot g < 0$, $\delta_\perp$ is obtained as,

$$\delta_\perp = \frac{1}{A_g}\left(1 + (B_g - 1)e^{B_g - A_g}\right) \tag{5.30}$$

with A_g and B_g given by (5.28).

Next, consider the flux in the $p_\|$-direction,

$$D_{\|\|}\frac{\partial f}{\partial p_\|} + D_{\|\perp}\, h\, f - F_\| f$$

which equals zero under the assumption of local thermal equilibrium. The aim is to write the $F_\|$-term as, for $F_\| > 0$,

$$\frac{\partial f}{\partial t} = \frac{1}{\Delta p}\left[F_\|\left(p_\| - \frac{\Delta p}{2}, p_\perp\right)\delta_\| \, f_{i-1,j} - F_\|\left(p_\| + \frac{\Delta p}{2}, p_\perp\right)\delta_\| \, f_{i,j}\right]$$

and for $F_\| < 0$,

$$\frac{\partial f}{\partial t} = \frac{1}{\Delta p}\left[F_\|\left(p_\| - \frac{\Delta p}{2}, p_\perp\right)\delta_\| \, f_{i,j} - F_\|\left(p_\| + \frac{\Delta p}{2}, p_\perp\right)\delta_\| \, f_{i+1,j}\right]$$

and find a solution for $\delta_\|$.

In this case there are four possibilities,

$F_\|$	$D_{\|\perp} \cdot h$	$\delta_\|$
> 0	> 0	$\frac{1}{A_h}\left(e^{A_h - B_h} + B_h e^{A_h - B_h} - 1\right)$
< 0	> 0	$\frac{1}{A_h}\left(1 + B_h - e^{B_h - A_h}\right)$
> 0	< 0	$\frac{1}{A_h}\left(e^{A_h - B_h} - 1 + B_h\right)$
< 0	< 0	$\frac{1}{A_h}\left(1 - e^{B_h - A_h} + B_h e^{B_h - A_h}\right)$

where

$$A_h = \frac{F_\|}{D_{\|\|}}\Delta p \qquad ; \qquad B_h = \frac{D_{\|\perp} \cdot h}{D_{\|\|}}\Delta p$$

The assumption of local thermal equilibrium is necessary in order to ensure the equilibrium distribution is a Maxwellian in the absence of all other terms, as will be shown later. When including other terms, the inclusion of this scheme will only be important in regions where collisions are dominant, which will be in regions of momentum space where other

terms are negligibly small, typically at large p. At these momenta, the distribution will vary exponentially, and therefore δ-splitting is required to ensure stability.

In general, additional terms can be added when deriving the expressions of $\delta_{\parallel}$ and $\delta_{\perp}$. For example, the RF heating term, which is mathematically represented by a term similar to the $D_{\perp\perp}$ term in the collision operator, can be added to the flux in the $p_{\perp}$ direction. This will lead to an additional term in the expression for $\delta_{\perp}$, which accounts for the effect of RF heating.

The advantage of δ-splitting is that it greatly improves the accuracy of the solution for coarse grids. Note that, as $N \to \infty$, $\Delta p \to 0$ and $A \to 0$ as well as $B \to 0$. Therefore, $\delta \to 1$ and the impact of δ-splitting is negligible. Of course, as $N \to \infty$, the exponential difference of f between two neighbouring nodes becomes negligible, and therefore δ-splitting is no longer required. The effect of δ-splitting is therefore more pronounced for coarse grids, and, as will be shown later, it greatly improves the accuracy.

Unfortunately, there exists a competing effect with regards to the stability of δ-splitting. Consider a Maxwellian f,

$$f \sim \exp\left(-p^2\right)$$

and therefore

$$g \sim -p$$

In the limit $p \to \infty$, $A \to 0$ as required, but $B \to \infty$ due to the presence of the function g, which then leads to $\delta \to \infty$. Numerically, this introduces problems, as terms that are large lead to instabilities by creating ill-conditioned matrices when solvinf f implicitly. The value of δ must therefore be limited to some maximum $\delta_{\max}$. Fortunately there is the competing effect that $\delta \to 1$ for increasing N, such that, if N is large enough, the value of $\delta_{\max}$ is irrelevant as δ is always small enough for a stable solution, while the cut-off value $\delta_{\max}$ only comes into effect at large p where there are very few particles.

5.2.4 Collision tests

The previous sections discussed the numerical approximations to the two-dimensional collision operator in cylindrical coordinates. Although the kinetic model contains several terms, and the time evolution of the distribution function must be solved under the effect of all these terms, the numerical approximation to the collision operator is the most complicated

due to the presence of mixed derivatives. The accuracy of these approximations need to be thoroughly tested before using it to study the time evolution of the distribution function under all effects.

In particular, accurate approximations for the collision operator in two-dimensional cylindrical coordinates that preserves positivity and ensures the correct equilibrium distribution tend to be very intensive [54], while approximations based on the central finite-difference scheme does not guarantee the preservation of positivity [55]. The numerical approximation proposed in the previous sections would therefore be an improvement on current, lower-order finite-difference approximations, and its accuracy is therefore tested, while the dependence on grid size, the robustness of the method, and the validity of δ-splitting and the impact of the choice of $\delta_{\max}$ is also considered.

5.2.4.1 Grid size

In order to test the collision operator, consider an initial Maxwellian distribution with $T_e = 20\,\text{eV}$ colliding with a fixed background Maxwellian distribution at $T_b = 10\,\text{eV}$, such that the assumption made in deriving the collision operators is always true. The dependence on grid size can then be tested by keeping the grid size, $p_{\max}$, fixed while varying the number of grid points N.

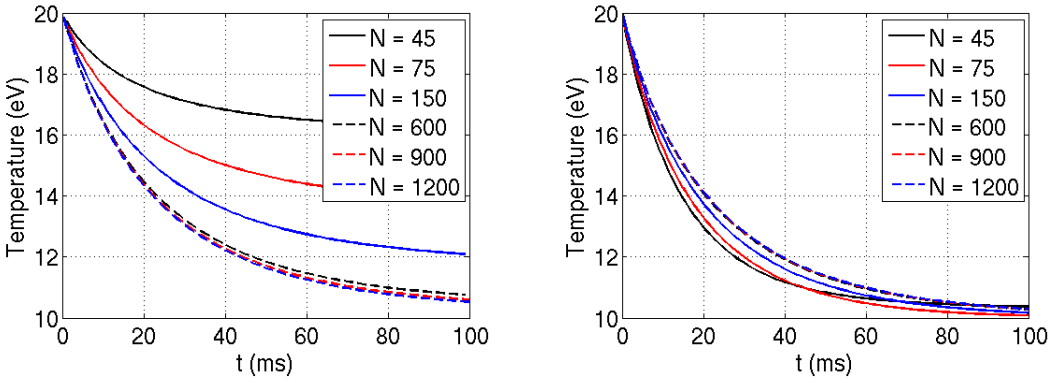

Figure 5.4: The time evolution of the temperature (a) without δ-splitting and (b) when including the δ-splitting method with $\delta_{\max} = 2$, for an initial Maxwellian distribution with $T_e = 20$ eV colliding with a fixed background distribution at $T_b = 10$ eV.

The grid size is set to $p_{\max} = 45 \times 10^{-3}\,\text{MeV}/c$, with the electron density kept constant at $n_e = 10^{14}\,\text{m}^{-3}$. The number of grid points are varied from $N = 45$ to $N = 1200$, which

corresponds to $p_t = 5\Delta p$ to $p_t = 80\Delta p$, respectively, where p_t is the thermal momentum of the distribution. Results, shown in figure 5.4, are compared for $\delta = 1$, which corresponds to the collision operator without the use of δ-splitting, to the case when using δ-splitting, with $\delta_{\max} = 2$.

The δ-splitting method greatly improves the accuracy of the numerical approximation to the collision operator, while a much larger number of grid points are necessary for convergence in the case without δ-splitting. For large grid sizes, the temperature evolution is similar for both cases, as expected, as $\delta \to 1$ as $N \to \infty$, and the effect of δ-splitting becomes negligible.

5.2.4.2 Effect of $\delta_{\max}$

It was noted before that $\delta \to \infty$ as $p \to \infty$, which leads to large terms which create ill-conditioned matrices and numerical instabilities. Fortunately, there is the competing effect that $\delta \to 1$ as $N \to \infty$, such that for sufficiently large matrices there won't be any numerical issues. In most cases, however, N will not be large enough to ensure that δ has a reasonable value everywhere on the grid, and some maximum value $\delta_{\max}$ is needed to ensure a stable solution.

As an example, consider an initial Maxwellian distribution with $T_e = 20$ eV colliding with a fixed background distribution at $T_b = 10$ eV. Let $p_{\max} = 45 \times 10^{-3}\,\mathrm{MeV}/c$ and $n_e = 10^{14}\,\mathrm{m}^{-3}$. In order to see the effect of $\delta_{\max}$, let $N = 150$, as the effect of $\delta_{\max}$ is less pronounced for larger values of N.

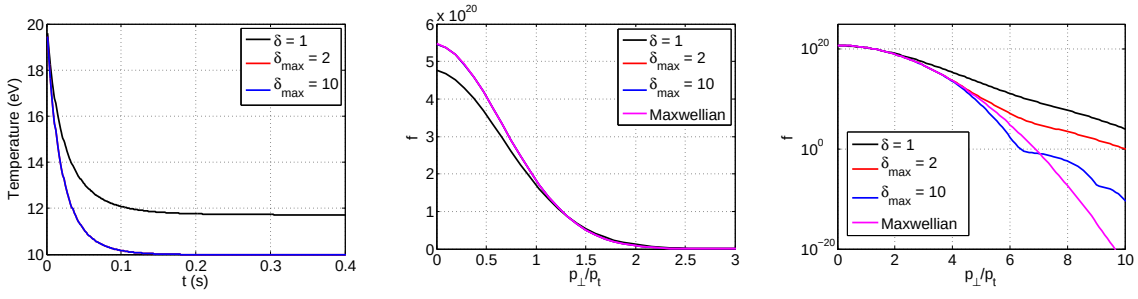

(a) (b) (c)

Figure 5.5: (a) The time evolution of the temperature for different choices of δ and $\delta_{\max}$, and the comparison of the distribution functions for these choices to the background Maxellian as (b) a function of $p_\perp$, and (c) on a log scale, plotted at $t = 1\,\mathrm{s}$.

Equilibrium is reached after 1 s, and the distribution functions at this time, as well as the temperature evolution, are compared in figure 5.5. Without δ-splitting ($\delta = 1$), the

wrong equilibrium temperature is reached, while for $\delta_{\max} = 2$ and for $\delta_{\max} = 10$ there are no differences in the temperature evolution.

Comparing the distribution functions to the background distribution shows the effect of $\delta_{\max}$. Firstly, for $\delta = 1$ the distribution is different to the background distribution, due to them having different temperatures. Comparing the $\delta_{\max} = 2$ and $\delta_{\max} = 10$ distributions to the background distribution, it is clear that there are no differences for $p_\perp < 4p_t$, where the majority of electrons are, and therefore the correct temperature is obtained. The differences are in the high p tail, with $\delta_{\max} = 2$ underestimating the relaxation, and $\delta_{\max} = 10$ overestimating the relaxation.

Larger values of $\delta_{\max}$ lead to ill-conditioned matrices as equilibrium is approached, so for numerical stability, the value of $\delta_{\max}$ must be small. Of course, as $N \to \infty$ the value of $\delta \to 1$, and there will be no need for $\delta_{\max}$. In practice, however, the matrix will hardly ever be large enough to allow this to happen, so it will be necessary to specify a value for $\delta_{\max}$. Fortunately, this value will only impact regions of large p, where there are very few electrons and the choice of $\delta_{\max}$ will not influence the macroscopic quantities. It is therefore sufficient to set $\delta_{\max} = 2$.

5.2.5 Temperature equilibration

A good test of the numerical approximations to collision operators is the relaxation rate of two distributions colliding with each other. In this case, the distributions will equilibrate according to,

$$\frac{dT_a}{dt} = \nu(T_b - T_a) \tag{5.31}$$

with ν the collision frequency, and

$$\frac{dT_a}{dt} = -\frac{dT_b}{dt}$$

and subscripts a and b indicating the temperatures of the two distributions.

The collision frequency for a Maxwellian distribution colliding with a background Maxwellian is given by [64],

$$\nu = \frac{8}{3\sqrt{\pi}} \left(\frac{e^2}{4\pi\varepsilon_0} \right)^2 \frac{4\pi n_e \lambda}{m_e^2 \sqrt{\left(v_{t,a}^2 + v_{t,b}^2 \right)}} \tag{5.32}$$

where $v_{t,a}^2 = 2T_a/m_e$ is the thermal velocity of distribution a.

5.2.5.1 Stability

The stability of the approximation to the collision operator can be tested by allowing two distributions in equilibrium to collide with each other. Of course, if both distributions are Maxwellian with the same temperature, the system is already at equilibrium and the temperature should remain fixed.

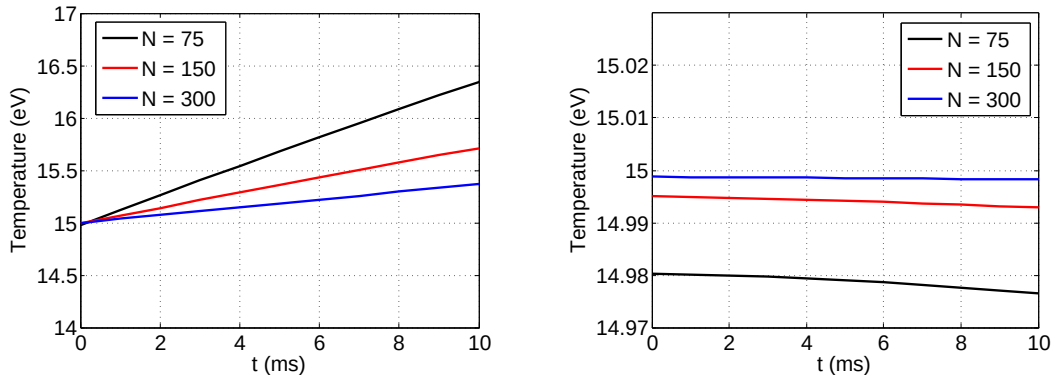

(a) (b)

Figure 5.6: The time evolution of the temperature (a) without δ-splitting and (b) when including the δ-splitting method with $\delta_{\max} = 2$, for two distributions of the same temperature $T_a = T_b = 15$ eV colliding with each other. The initial differences in temperature are due to the finite size of the grid.

Consider therefore two initial Maxwellian distributions with $T_a = T_b = 15\,\mathrm{eV}$. Let the grid size be $p_{\max} = 45 \times 10^{-3}, \mathrm{MeV}/c$, and the density $n_e = 10^{14}\,\mathrm{m}^{-3}$. Results, shown in figure 5.6 for different values of grid points N, show that, by using δ-splitting, the system remains more stable than without it.

5.2.5.2 Equilibration

The relaxation of two distributions colliding with each other is a good test of the numerical approximation to the collision operator, especially as it can be compared to an analytical solution. Consider therefore two initial Maxwellian distributions colliding with each other. Let $T_a = 20\,\mathrm{eV}$ and $T_b = 10\,\mathrm{eV}$, with $p_{\max} = 45 \times 10^{-3}\,\mathrm{MeV}/c$, $n_e = 10^{14}\,\mathrm{m}^{-3}$ and $N = 600$. The resultant temperature evolution, when using δ-splitting with $\delta_{\max} = 2$, is shown in figure 5.7.

The collision operator assumes that the distributions are Maxwellian, which is of course not always true. The numerical approximation reaches the wrong equilibrium temperature

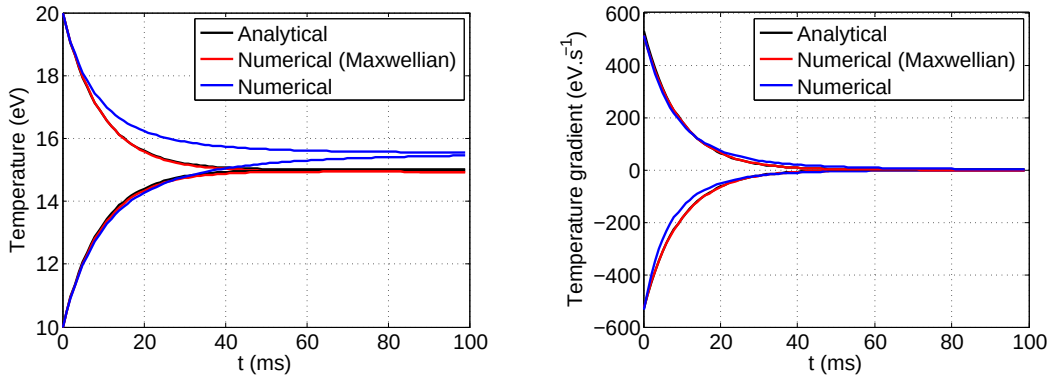

(a) (b)

Figure 5.7: The time evolution of the temperature (a) and the temperature gradient (b) for two distributions colliding with each other, compared to the analytical formula. For the Numerical (Maxwellian) curve, the distributions have been constrained to be Maxwellian at each time step.

due to the assumption of collisions with a background Maxwellian breaking down. The colder part of the distribution collides more frequently compared to the warmer part of the distribution, allowing it to react faster. This leads to the colder part of the distribution heating up faster than the warmer part of the distribution cools down, and the equilibrium temperature is higher than the total energy in the system.

By constraining the distributions to always be Maxwellian (by replacing it with a Maxwellian of the same temperature after each time step), the correct behaviour is obtained. In this case, the assumption of collisions with a background distribution is always true, and relaxation occurs at the theoretically predicted rate. This procedure is not followed when studying the time evolution of the distribution function under all effects, as the distribution is expected to be very different from a Maxwellian distribution. It was only done here as a test.

5.2.5.3 Time test

The treatment of the mixed derivatives introduces a non-linearity which can be solved through a Picard iteration. A Picard iteration is necessary if the approximation to the distribution function is obtained from an implicit equation,

$$\hat{D} f^{n+1} = f^n$$

where the matrix $\hat{D}$, containing the differential operators on f, is dependent on f^{n+1}. The treatment of the mixed derivatives in the Fokker-Planck collision operator introduces a non-linearity in the matrix equation, as the matrix $\hat{D}$ depends on the distribution f^{n+1} through the functions g and h. These non-linearities can be solved through Picard iteration,

$$\hat{D}(f^k)f^{k+1} = f^n$$

where the known distribution f^k is used to determine the functions g and h, in order to solve f^{k+1}. This iteration will continue until two consecutive solutions are sufficiently similar, i.e.

$$\frac{||f^{k+1} - f^k||}{||f^k||} < \epsilon$$

where ϵ is some small number.

Alternatively, the non-linearities can be solved through Picard linearisation, where only a single iteration is performed. Picard linearising requires a smaller time step in order to obtain an accurate approximation, but is computationally less expensive.

To illustrate this, consider two initial Maxwellian distributions with $T_a = 20\,\text{eV}$ and $T_b = 10\,\text{eV}$ colliding with each other. Let $N = 150$ and $p_{\text{max}} = 45 \times 10^{-3}\,\text{MeV}/c$ such that $p_t = 10\Delta p$. The density is $n_e = 10^{14}\,\text{m}^{-3}$ such that the collision time $\tau \approx 20\,\text{ms}$.

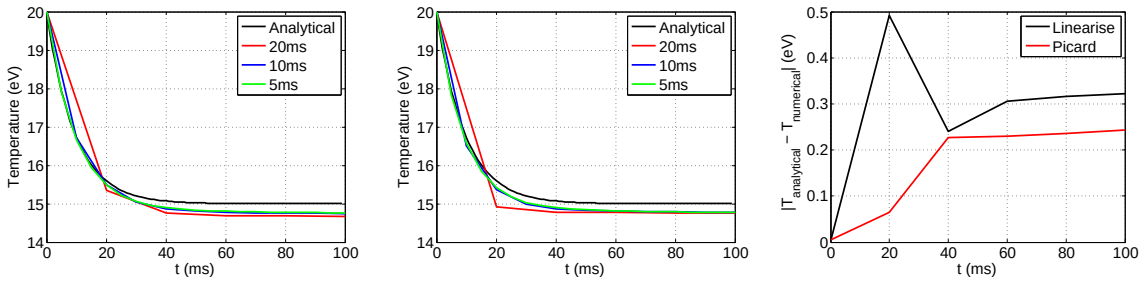

Figure 5.8: The time evolution of the temperature of a distribution function at $T_a = 20\,\text{eV}$ colliding with a distribution at $T_e = 10\,\text{eV}$, for different choices of Δt for (a) Picard linearizing, (b) Picard iterating, (c) and the comparison of the two methods for $\Delta t = 20\,\text{ms}$ to the analytical temperature.

The time evolution of the temperature for different values of Δt is shown in figure 5.8. As expected, convergence is achieved for larger time steps when solving the distribution through Picard iteration as compared to Picard linearising. However, obtaining an approximation

through Picard iteration is computationally more expensive as it is necessary to iterate over the solution f^{n+1}.

Yoon and Chang [55] noticed the same result, that by calculating the collision operators explicitly from the known values f^n in order to evolve implicitly to f^{n+1}, a small error is created through Picard linearization, compared to Picard iteration, but with the reduction in computational time, this error can be reduced by decreasing the time step.

5.3 Obtaining a consistent solution

The previous sections in this chapter have dealt with obtaining numerical approximations to the differential operators representing the various effects under which the time evolution of the distribution function is studied, as an analytical solution is not available. Apart from solving the differential equations, the solution to the distribution function also needs to be consistent with some pre-determined conditions. The density and power absorbed, for example, can be obtained from experiment and/or other models, and the solution to the distribution function has to be consistent with these observables.

For this reason, there are a number of parameters which have to be fitted to ensure these conditions hold. The source term ensures the distribution function has the correct density, by fitting the value of S_0; the RF heating term has a constant, D_0, which is determined under the condition that the correct power is absorbed; and the loop voltage, V_L, is fitted under the condition that Lenz's law holds.

As an example, consider the start-up simulation

$$\frac{\partial f}{\partial t} = \text{source} + \text{EBW heating} + \text{collisions} + \text{loop voltage}$$

where all power is absorbed as EBW and the density evolution is known. The value of each parameter is then fitted to ensure the distribution function remains consistent with these conditions.

5.3.1 Electron density

The electron density is assumed to evolve according to

$$n_e(t) = n_{e0}\left(0.1 + 0.9\tanh\left(\frac{t}{t_0}\right)\right) \tag{5.33}$$

where $t_0 = 0.05\,\mathrm{s}$ and $n_{e0} = 1 \times 10^{18}\,\mathrm{m}^{-3}$. The value of S_0 must evolve as a function of time to ensure the density calculated from the distribution function,

$$n_e(t) = 2\pi \int \mathrm{d}p_\parallel \int p_\perp \,\mathrm{d}p_\perp \, f(p_\parallel, p_\perp, t)$$

equals the known density (5.33) to within some predetermined accuracy.

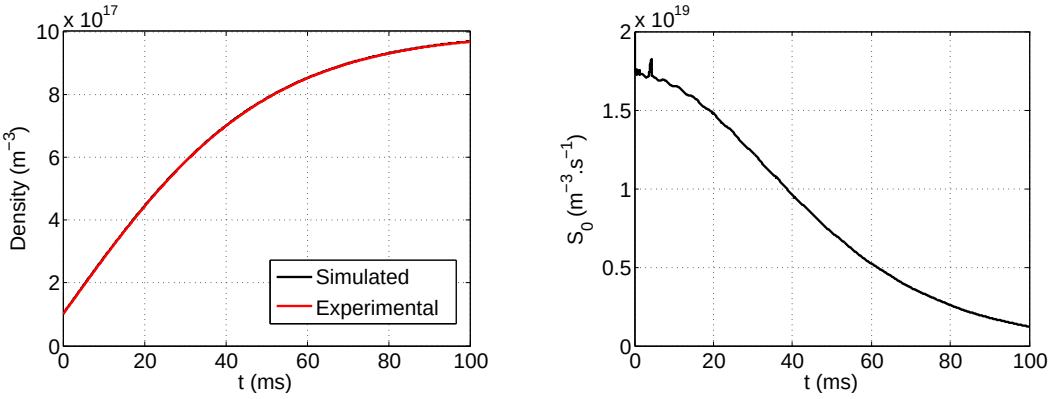

(a) (b)

Figure 5.9: The time evolution of (a) the electron density, and (b) the value of S_0, the rate at which cold electrons are added to the system.

Figure 5.9 shows the time evolution of the density and the value of S_0. It shows no difference between the simulated density obtained from the distribution function and the known density, while the value of S_0 gradually decreases. In this example, in the absence of electron losses, and with the increase in electron density slowing with time, the rate at which electrons are added to the system will always decrease, as the rate of increase in electron density decreases, and this is reflected in the value of S_0.

5.3.2 Power absorbed

The constant D_0 is fitted to ensure that the power absorbed calculated from the distribution function,

$$P_d = \frac{1}{2} m_e 2\pi \int \mathrm{d}p_\parallel \int p_\perp \,\mathrm{d}p_\perp \, v^2 \left(\frac{\partial f}{\partial t}\right)_{\text{RF heating}}$$

equals the total power absorbed

$$P_d = AP_0$$

where A is the absorption coefficient and P_0 is the total input power. Figure 5.10 shows the time evolution of the power absorbed, as well as the value of D_0. The maximum difference between the simulated and experimental power absorbed is 1%, which is controlled by iterating over the value of D_0 until such accuracy is obtained.

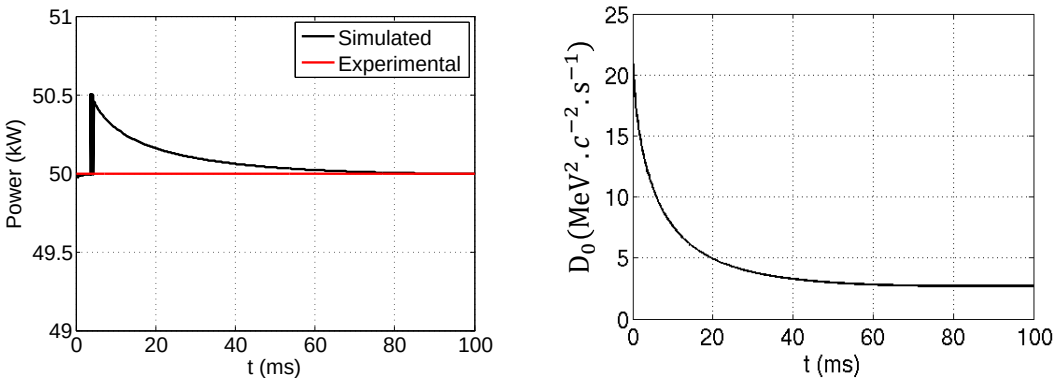

(a) (b)

Figure 5.10: The time evolution of (a) the power absorbed, and (b) the diffusion constant D_0.

The value of D_0 depends on a number of factors, including the electron density and temperature, the wave parameters, and the shape of the distribution function. In Chapter 3, a simplified expression for the value of D_0 was derived, given by equation (3.31), which gives the relationship of D_0 to the electron density, power absorbed, and temperature as

$$D_0 \sim \frac{AP_0 \exp\left[1/p_t^2\right]}{n_e} \tag{5.34}$$

such that, as the density and temperature increases, the value for the diffusion constant D_0 decreases, as is shown.

5.3.3 Loop voltage

The loop voltage is induced by a changing magnetic field, which results from a change in the plasma current, according to Lenz's law,

$$V_L = -L_P \frac{dI_P}{dt}$$

where the self-inductance $L_P = 6.5 \times 10^{-7}$ H, as discussed in Section 3.4. The value of V_L is calculated so that Lenz's law holds. The resultant value for V_L, and the plasma current, is shown in figure 5.11.

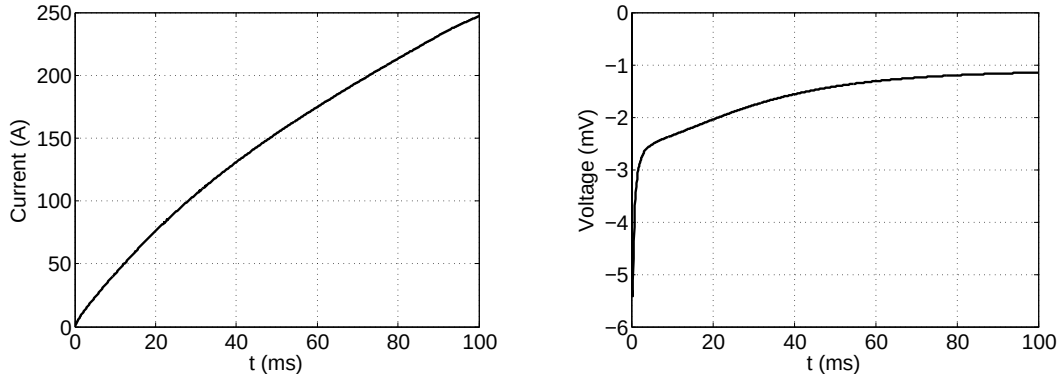

(a) (b)

Figure 5.11: The time evolution of (a) the simulated plasma current, and (b) the loop voltage calculated according to Lenz's law.

The loop voltage is obtained through an implicit iteration,

$$V_L = -L_P \frac{I_P^{n+1} - I_P^n}{\Delta t} \tag{5.35}$$

where the plasma current I_P^n is known, and the plasma current at the next time step, I_P^{n+1}, is calculated under the effect of a loop voltage V_L, which is iterated over until equation (5.35) is satisfied. The loop voltage is implemented according to

$$\frac{\partial f}{\partial t} = -q_e \frac{V_L}{2\pi R_0} \frac{\partial f}{\partial p_{\|}}$$

where R_0 is the major radius. The value of the loop voltage, V_L, remains roughly constant for the constant increase in plasma current, as shown in figure 5.11.

5.4 Summary

The electron distribution function is studied in the presence of a number of effects, some of which allow electrons to gain or lose momentum. These effects can be represented with advection-diffusion type differential equations, to which a numerical approximation is required, as it is not possible to solve them analytically. Any numerical method used must

conserve density (in the absence of source and loss terms) and preserve positivity of the solution.

In this chapter, a positivity-preserving scheme for solving two-dimensional advection-diffusion equations, including mixed derivatives, has been discussed. The treatment of the mixed derivatives introduces a non-linearity, which can be treated through a Picard linearisation.

The scheme is applied to the Fokker-Planck collision operator, which contains mixed derivatives in cylindrical coordinates. Under the assumption of local thermal equilibrium, based on the Chang-Cooper average scheme [56], the correct equilibrium distribution function is ensured, which is important in regions where collisions are dominant.

Examples show that thermal equilibration occurs at the predicted, theoretical rate as long as the assumption made in calculating the collision operators are satisfied. In general, the Rosenbluth potentials [48] or the Landau integrals [49] can be used to calculate the collision operators, but in this work the assumption is made that the distribution collides with a background Maxwellian distribution.

A comparison of Picard iteration and linearisation, due to the non-linearity introduced in the treatment of the mixed derivatives, is made to show that Picard iteration converges for larger time steps than Picard linearisation, but it is computationally more expensive. In the framework of RF start-up, where collisions are not expected to be dominant, the time step will be determined by the plasma-wave interaction, which will typically be much shorter than typical collision times, and Picard linearisation is sufficient for solving the mixed derivative terms.

Lastly, in order to ensure the solution to the distribution function is consistent with some pre-determined conditions, it is shown how a number of parameters are fitted to ensure these conditions hold. In this way, the distribution function has the correct density, the correct amount of power is absorbed, and Lenz's law is always satisfied.

Using these methods for obtaining a solution to the kinetic model, the time evolution of the electron distribution function can be studied to investigate the current drive mechanism, the role of the vacuum magnetic field, and make comparisons to experiments.

Chapter 6

Numerical simulation of EBW plasma current start-up in MAST

Non-inductive plasma current start-up was successfully demonstrated on MAST with the use of RF beams [6, 11]. Along with simulations, it was confirmed that the power is absorbed from EBWs, but how this absorption leads to the generation of a plasma current is less well understood.

In particular, the presence of energetic electrons, which undergo few collisions, questions the validity of a current drive (CD) mechanism relying on collisions, such as the Fisch-Boozer mechanism. Other prominent theories include the current generated by the preferential confinement of electrons, but studies into this have only been qualitative in nature, relying on the study of single particle orbits [12, 14, 15].

In this chapter, the time evolution of the electron distribution function, introduced in Chapter 3, is studied under several effects in order to determine the CD mechanism responsible for the generated current observed in RF experiments. In particular, the CD mechanism responsible for the initiation of a plasma current during start-up, when the magnetic field line configuration is open, and the formation of closed flux surfaces (CFS), are studied, as well as the effect of the vacuum poloidal field on the generated current, in accordance with experimental observations.

Chapter 4 studied the dependence of the orbital loss term as a function of plasma current, and how it depends on the magnetic field. It was shown that the open magnetic field line configuration leads to a preferential confinement of electrons, which could lead to the generation

of a plasma current. This effect, along with the Fisch-Boozer mechanism, the preferential heating of electrons moving in one direction to create an anisotropic plasma resistivity to generate a current, is studied in detail under experimental conditions to determine the CD mechanism responsible for the initiation of a plasma current and the formation of CFS.

Further experimentally observed effects, such as the effect of a vertical shift and vacuum poloidal field ramp-up, are considered in order to obtain explanations for their observed effect on the generated plasma current. A comparison to experiment is made to show the validity of the model and support the CD mechanism responsible for the generated plasma current.

This chapter is laid out as follow: first, the Fisch-Boozer mechanism and the generation of current by the preferential confinement of electrons are considered and discussed as potential CD mechanisms. Second, the effect of the vacuum magnetic field during start-up is discussed, before comparisons to experiment are made, including a study of the dependence of the generated current on power and density. Finally, the direct EBW current drive due to a non-zero parallel refractive index is considered.

6.1 Collisional current drive

The Fisch-Boozer mechanism [19], based on the preferential heating of electrons moving in one direction to produce an anisotropic plasma resistivity, is an attractive concept for CD using EC waves. This CD mechanism is driven by collisions, and has been all but excluded as the CD mechanism responsible for the observed current generation during EBW start-up due to the current being carried by energetic electrons which undergo very few collisions [11, 16], but its effect on the generated current is studied here for completeness.

In order to study the effect of the Fisch-Boozer mechanism, consider a start-up simulation

$$\frac{\partial f}{\partial t} = \text{source} + \text{RF heating} + \text{collisions} + \text{loop voltage}$$

where all electron losses are excluded, such that the effect of EBW heating and collisions on the generation of a plasma current can be studied. This scenario is similar to that encountered after the formation of CFS, as all electrons are considered confined and orbital losses are neglected. For illustration purposes, the assumption is made that the EBW has a well-defined wave vector, such that the value of $N_{\|}$ is fixed across the region of absorption,

which has a width $\Delta R = 0.05\,\mathrm{m}$, as obtained from ray-tracing [6, 29]

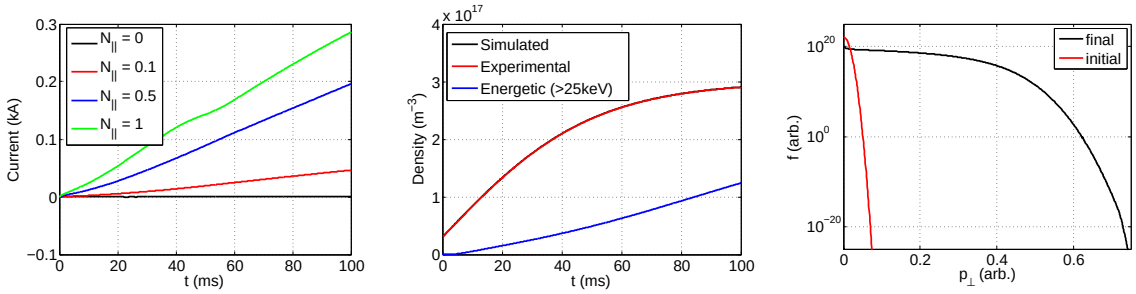

(a) (b) (c)

Figure 6.1: The time evolution of (a) the plasma current and (b) the electron density, and (c) a comparison of the distribution functions for the Fisch-Boozer mechanism.

The Fisch-Boozer mechanism is illustrated in figure 6.1(a): the preferential heating of electrons with $p_\parallel > 0$ through an EBW with $N_\parallel > 0$, generates a positive current, while EBWs with $N_\parallel = 0$ fails to gain a directionality with respect to the magnetic field, and therefore does not generate a plasma current [13, 65]. The resonance condition,

$$\omega - k_\parallel v_\parallel - n\omega_c = 0$$

is satisfied for electrons with $v_\parallel > 0$, as $\omega - n\omega_c > 0$ for EBW absorption and $k_\parallel > 0$. This provides a directionality with respect to the magnetic field, and the greater the value of $k_\parallel$, the greater the plasma current. A schematic of the Fisch-Boozer CD mechanism is shown in figure 6.2.

Figure 6.1(b) shows the electron density, and the population of energetic electrons. The time evolution of the electron density is assumed known, with the simulated density fitted to this known density,

$$n_e = n_{e0}\left(0.1 + 0.9\tanh\left[\frac{t}{t_0}\right]\right)$$

where $n_{e0} = 3\times10^{17}\,\mathrm{m}^{-3}$ and $t_0 = 0.05\,\mathrm{s}$. The flattening of the distribution function, shown in figure 6.1(c), establishes a population of energetic electrons. In order for all the power to be absorbed, electrons are accelerated to increasingly higher energies as there are no loss terms, and, due to the large value of $N_\parallel$, even fast electrons can still interact with the EBW.

The schematic (figure 6.2) shows an exaggerated scenario, as there won't be a definite population of energetic electrons, but rather a smooth extension of the distribution to higher energies, as shown in figure 6.1(c). The non-zero value of $N_\parallel$ allows for an asymme-

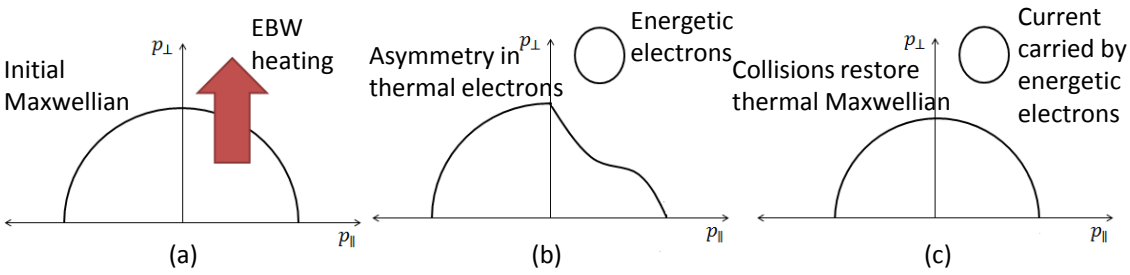

Figure 6.2: Schematic of the collisional current-drive: (a) The preferential heating of electrons through EBWs generates (collisionless) energetic electrons (b) which creates an asymmetry amongst the collisional thermal electrons. Collisions lead to the restoration of a Maxwellian amongst the thermal electrons (c) such that the thermal electrons carry no current, and the current is carried by the energetic electrons. In reality, collisions are not sufficiently strong to fully restore the Maxwellian, and the EBW heating will flatten the distribution in $p_\perp$, as shown in figure 6.1(c), rather than create a well-defined group of energetic electrons.

try amongst the thermal (collisional) electrons to form, and as collisions restore a thermal Maxwellian, an asymmetry amongst the energetic electrons forms and a current is generated. In this way, an EBW with optimal $N_\parallel$, gaining a directionality with respect to the magnetic field, can generate a current [28], but due to the formation of energetic electrons, the current is small, excluding the Fisch-Boozer mechanism as a major contributor to the CD [11, 16].

6.2 Current generation by the preferential confinement of electrons

The open magnetic field line configuration during start-up allows electrons to freely stream out of the plasma volume. The addition of a small vertical magnetic field, however, leads to the preferential confinement of a selection of electrons for which the parallel motion along the magnetic field line cancels with the orbital drift term [21]. This preferential confinement has been used to describe the initiation of CFS, using single particle orbits [12, 14, 15], and it was shown in Chapter 4 that, until CFS form, the confinement of electrons moving along the magnetic field is much better than electrons moving counter to the magnetic field.

In order to study the preferential confinement of electrons as a possible CD mechanism, consider a start-up simulation,

$$\frac{\partial f}{\partial t} = \text{source} + \text{RF heating} + \text{loss} + \text{loop voltage} + \text{collisions}$$

where the vertical component of the vacuum poloidal field $B_V = 6\,\mathrm{mT}$ is fixed. In order to see the effect of the loss term on the generated current, simulations with and without collisions are performed, and compared to the case with no loss term. The previous section showed that the preferential heating of electrons moving in one direction is necessary to generate a current. The assumption is therefore made that the EBW has a value of $N_{\|} = 0.5$ across the region of absorption with a width $\Delta R = 0.05\,\mathrm{m}$.

The comparison of the simulated plasma current in three different scenarios is shown in figure 6.3(a). The current generated by collisions, in the absence of electron losses, is small due to the formation of energetic electrons and the low collisionality, as discussed in the previous section. However, in the absence of collisions, the current generated by the preferential confinement of electrons is even smaller. The EBW heating increases the perpendicular momentum of electrons, which improves their confinement (in general electrons with $p_{\perp}/p_{\|}$ greater than some number is confined, such that increasing $p_{\perp}$ improves the probability that an electron will be confined), while the parallel momentum of electrons remains fixed. The loss rate of electrons increases with increasing $v_{\|}$ through the parallel loss time, i.e.

$$\tau_{\|} = a \exp\left[\frac{I_P}{I_{\mathrm{CFS}}}\right] \frac{B_\phi}{B_Z} \Big/ v_{\|}$$

where B_ϕ and B_Z is the toroidal and vertical magnetic fields, respectively, a is the minor radius, and I_{CFS} is the value of the plasma current where CFS first start to form. As the parallel velocities of electrons remain unchanged under EBW heating, the electron loss rate remains small, electron losses are minimal and a small current is generated.

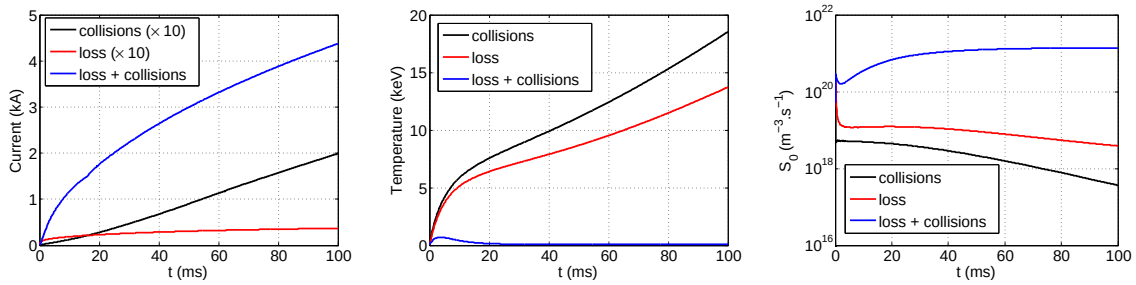

Figure 6.3: The time evolution of (a) the plasma current, (b) the electron temperature, and (c) the value of S_0 for three different CD scenarios.

The generated current when including both collisions and losses are of the order of a few

kA - in agreement with experimental measurements. In this case collisions allow the parallel momentum of electrons to be increased through pitch-angle scattering, leading to greater losses and a generated current more than 10 times greater than before. The preferential confinement of electrons is therefore responsible for the greater part of the generated current, with collisions only "feeding" the loss term by increasing the parallel momentum of electrons through pitch-angle scattering. A schematic of the mechanism is shown in figure 6.4.

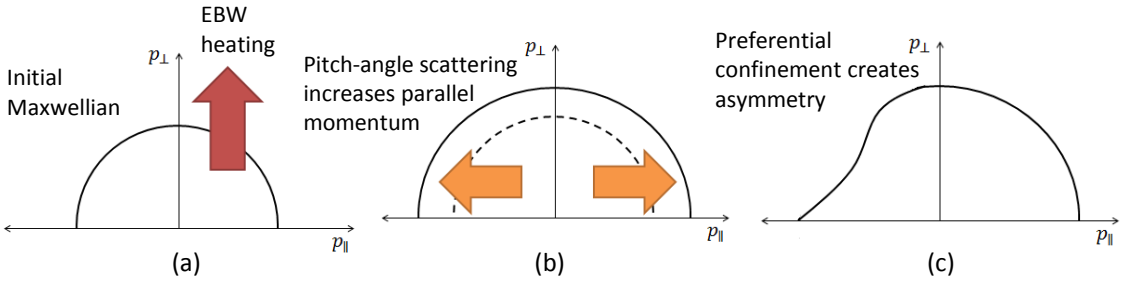

Figure 6.4: Schematic of the current drive mechanism through the preferential confinement of electrons. (a) EBW heating increases the temperature of the distribution and (b) the parallel momentum of electrons through pitch-angle scattering. (c) The preferential confinement of electrons with $p_\parallel > 0$, coupled with the greater loss of electrons with $p_\parallel < 0$, leads to an increase in the generated current.

By relating the average energy in each distribution to a pseudo-temperature, the "temperatures" of the three cases are compared in figure 6.3(b). As all three simulations have the same density evolution and EBW power absorbed, electron energy balance can be used to describe the differences in observed temperature, i.e.

$$\frac{3}{2}\frac{d}{dt}\left(n_e T_e\right) = P_{\mathrm{EBW}} - P_{\mathrm{loss}}$$

First, in the absence of electron losses, a very high temperature is reached. In this case, all the absorbed power leads to an increase in the temperature, as there are no losses. Secondly, in the presence of electron losses, but excluding collisions, the temperature is slightly lower, as very few electrons are lost and P_{loss} is small. The EBW heating increases the perpendicular momentum of electrons, such that the electron loss rate, which increases for increasing parallel momentum, remains small. Including the effects of both collisions and orbital losses, however, greatly reduces the temperature, to the order of hundreds of eV, which is comparable to temperatures inferred from experiments. In this case, collisions increase the parallel momentum of electrons through pitch-angle scattering, "feeding" the

loss term and increasing P_{loss}. This leads to the loss of fast, warm electrons, while cold electrons remain in the system, leading to a reduction in the electron temperature.

Figure 6.3(c) shows the electron injection rate for the three different cases considered. As all three cases have the same time evolution of density, the value of S_0 needs to be adjusted depending on the number of electrons lost. Adding the loss term leads to an increase in the value of S_0, while having both collisions and orbital losses lead to an even greater increase, as more electrons are lost.

The CD mechanism is therefore based on the preferential confinement of electrons, created by the open magnetic field line configuration, while collisions act to increase the rate of electron losses by increasing the parallel momentum of electrons through pitch-angle scattering.

The value of $N_{\parallel}$ plays a different role for the current generated by the preferential confinement of electrons compared to the Fisch-Boozer mechanism. In this case, as electrons with $p_{\parallel} > 0$ are confined better than electrons with $p_{\parallel} < 0$, an optimal current will be driven by heating electrons with $p_{\parallel} > 0$. As electrons with a large ratio $p_{\perp}/p_{\parallel}$ tend to be confined, and EBW heating increases $p_{\perp}$, heating electrons with $p_{\parallel} > 0$ will improve their confinement, while electrons with $p_{\parallel} < 0$ are lost, resulting in an optimal current. In contrast, heating electrons with $p_{\parallel} < 0$ will improve the confinement of electrons that are lost at the faster rate, resulting in smaller losses and a smaller current. In order to heat electrons with $p_{\parallel} > 0$ requires $N_{\parallel} > 0$, which is similar to that required for the Fisch-Boozer mechanism to generate a positive current. Having $N_{\parallel} > 0$ will therefore generate an optimal current with regards to the preferential confinement of electrons, while enhancing that current through the Fisch-Boozer mechanism.

6.3 Vacuum field effects

The previous sections studied the CD mechanism responsible for generating a plasma current under EBW power during start-up, when the magnetic field line configuration is open. Experiments conducted on MAST further showed that the vacuum poloidal field plays an important role in EBW start-up for two reasons. First, while the toroidal magnetic field sets the radial location of the ECR and absorption, the vacuum poloidal field, along with the self-field generated by the plasma current, determines the local magnetic field in the region

of absorption, which determines the parallel refractive index $N_{\|}$ and therefore the selection of electrons, in momentum space, which are accelerated. As was shown in the previous sections, the value of $N_{\|}$ is important to generate an optimal current, with the value of $N_{\|}$ in the region of absorption being determined by the vacuum poloidal field, as will be shown in this section.

Secondly, the strength and spatial distribution of the vacuum poloidal field determines the value of I_{CFS}, the value of the plasma current where all forward electrons are confined and the first CFS start to form. As was shown in Chapter 4, an increase in the value of the vertical strength of the vacuum poloidal field B_V leads to an increase in the value of I_{CFS}. This can then lead to an increase in the value of the plasma current I_P, as the asymmetric confinement of electrons remains roughly constant for a constant ratio I_P/I_{CFS}, such that an increase in I_{CFS} can lead to a subsequent increase in I_P.

The previous sections studied the two prominent CD mechanisms and concluded that the preferential confinement of electrons, created by the open magnetic field line configuration, is responsible for the generated current during start-up. In order to further validate this CD mechanism, it needs to be consistent with experimental observations regarding the vacuum poloidal magnetic field: the vertical kick and B_V ramp-up.

6.3.1 Vertical kick

The Fisch-Boozer mechanism relies on the preferential heating of electrons moving in one direction to generate a plasma current. Similarly, the preferential confinement of electrons, created by the open magnetic field line configuration, preferentially confines electrons moving in one direction, leading to the generation of a plasma current. In order to heat the preferentially confined electrons, to generate an optimal current, a favourable value for $N_{\|}$ is required. For experiments conducted on MAST, this requires $N_{\|} > 0$.

In experiments conducted on MAST the vertical vacuum poloidal field $B_V < 0$, leading to $N_{\|} < 0$ above the midplane and $N_{\|} > 0$ below the midplane. As absorption occurs predominantly above the midplane, the plasma has to be shifted upwards to ensure $N_{\|} > 0$ in the region of absorption [6, 11].

A vertical shift of the plasma can be achieved by generating a radial field, through the P6 coils on MAST. Experiments testing this effect were conducted on MAST, and shot #17299 observed the formation of CFS by providing a vertical shift of about 20 cm throughout the

plasma, creating $N_{\|} > 0$ in the region of absorption [11].

After the formation of CFS, the vertical field changes sign in the mode conversion (MC) zone, and the plasma must be shifted back downwards to ensure $N_{\|} > 0$. This downshift was implemented in shot #18158, and showed a sustainment of the plasma current, while the current decayed in previous experiments where this downshift was not implemented [11].

Apart from generating a favourable $N_{\|}$ in the MC zone, a vertical shift also influences the electron confinement, as was shown in Chapter 4. It acts to enhance the asymmetry of the confinement, in such a way that larger plasma currents can be generated.

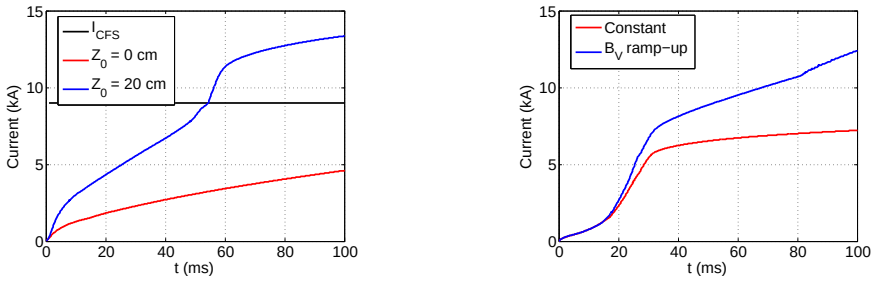

(a) (b)

Figure 6.5: (a) The time evolution of the plasma current when shifting the plasma upwards ($Z_0 = 20\,\text{cm}$) to create a favourable value for $N_{\|}$, compared to not shifting the plasma. (b) The time evolution of the plasma current for a constant B_V and a ramped-up B_V.

Experiments and ray-tracing have shown that the value of $N_{\|}$ changes as the EBW propagates towards the ECR layer [6, 11]. In order to account for a change in the value of $N_{\|}$, let $\Delta N_{\|} = 1$. Two cases are compared: $Z_0 = 20\,\text{cm}$ with $N_{\|} = 0.5$, and $Z_0 = 0\,\text{cm}$ with $N_{\|} = 0$. The vacuum poloidal field is constant, leading to a constant value of I_{CFS}. The comparison of the generated plasma current, for an input power $P_0 = 50\,\text{kW}$, is shown in figure 6.5(a), showing a large increase in current, and the formation of CFS, when shifting the plasma upwards, as observed experimentally.

Notice that a plasma current is generated for $N_{\|} = 0$, in contrast to the generated current through the Fisch-Boozer mechanism, where a non-zero value for $N_{\|}$ is required to ensure the EBW gains a directionality with respect to the background magnetic field. This is further evidence that the preferential confinement of electrons, created by the open magnetic field line configuration, is responsible for the generated plasma current. As electrons with $p_{\|} < 0$ are lost at a faster rate than electrons with $p_{\|} > 0$, a current will be generated irrespective of which electrons are heated. In order to generate an optimal current, electrons with $p_{\|} > 0$,

corresponding to $N_{\|} > 0$, should be heated. In this way, the confinement of these electrons are further improved, while electrons with $p_{\|} < 0$ are lost. In contrast, heating electrons with $p_{\|} < 0$ will improve the confinement of these electrons, leading to smaller losses and a smaller current, as observed in figure 6.5(a) for $N_{\|} = 0$.

6.3.2 B_V ramp-up

Experiments showed that the most efficient method of generating large plasma currents and keeping the plasma in equilibrium is to apply a vacuum poloidal field ramp-up [6, 11]. This was demonstrated in shot #28941 where a vertical shift of the plasma, created by generating a radial field B_R, helped to create CFS, before an increase in the plasma current was observed by increasing the vertical strength of the vacuum poloidal field B_V, as was discussed in Chapter 2.

It was shown in Chapter 4 that increasing the vacuum poloidal field strength leads to an increase in the value of I_{CFS}, the value of the plasma current where the first CFS start to form. An increase in I_{CFS} can lead to a subsequent increase in I_P while keeping the asymmetry of the loss term intact, as this asymmetry depends on the ratio I_P/I_{CFS}, generating larger plasma currents.

In order to test this, consider two cases based on the vacuum poloidal fields in MAST: one where the vertical component of the vacuum poloidal field $B_V = 3\,\mathrm{mT}$ is constant, and one with a linearly increasing vacuum poloidal field from $B_V = 3\,\mathrm{mT}$ to $B_V = 6\,\mathrm{mT}$ after 100 ms. No vertical shift is applied ($B_R = 0$), but the assumption is made that $N_{\|} = 0.5$ and $\Delta N_{\|} = 1$. Results for a 50 kW input is shown in figure 6.5(b).

Increasing the strength of the vertical vacuum poloidal field B_V leads to the generation of larger plasma currents, as the asymmetry of the loss term can be sustained for longer. In the case of a constant B_V, CFS form after $\sim$ 40ms, and a collisional current drive is responsible for further increase in the plasma current. As was discussed in Section 6.1, this current is small, leading to a small increase in current after CFS is formed.

By ramping-up the vacuum poloidal field B_V, the plasma current can increase along with an increase in I_{CFS}, as CFS never completely form and the preferential confinement of electrons remains the responsible CD mechanism. As was shown in Section 6.2, this CD mechanism is more efficient at generating a plasma current compared to the Fisch-Boozer mechanism, and by ramping-up the vacuum poloidal field, CFS never fully form and the

preferential confinement of electrons remains the responsible CD mechanism.

6.4 Comparison to experiment

The previous sections showed that the preferential confinement of electrons, created by the open magnetic field line configuration, is responsible for the generation of a plasma current under EBW power, and also how the vacuum poloidal field can be used to generate larger plasma currents. Experiments used a combination of these effects, a vertical shift and vacuum field ramp-up, to achieve large plasma currents. In order to compare the plasma current to experiment, the time evolution of the vacuum magnetic field and vertical shift of MAST shot #28941 is replicated in the simulations.

As the value of the parallel refractive index $N_{\|}$ of the absorbed EBW can vary greatly across the region of absorption, from negative to positive values up to $N_{\|} = 1$, and the solution to the hot plasma dispersion relation (see Appendix A) describes local absorption, while the required values for $N_{\|}$ and $\Delta N_{\|}$ should describe the effect of global absorption from the EBW, the values of $N_{\|}$ and $\Delta N_{\|}$ can only be approximated. From ray-tracing [6,11] and from obtaining solutions to $N_{\|}$ for typical MAST plasma parameters (see Section 3.7.3), it is assumed that $N_{\|} = 0.5$ with $\Delta N_{\|} = 1$, with these values remaining unchanged throughout the start-up simulation, while all power is assumed to be absorbed from the EBW, with $P_0 = 50\,\mathrm{kW}$.

The density evolution is modelled by,

$$n_e = n_{e0}\left(0.1 + 0.9\tanh\left[\frac{t}{t_0}\right]\right)$$

where $n_{e0} = 3 \times 10^{17}\,\mathrm{m}^{-3}$ and $t_0 = 0.05\,\mathrm{s}$.

The simulated plasma current compares very well to the experimentally measured current, as shown in figure 6.6. The vertical shift helps the formation of CFS around 50 ms when $I_P \approx I_{\mathrm{CFS}}$, after which a B_V ramp-up leads to an increase in the value of I_{CFS}. The plasma current I_P increases along with I_{CFS} as the asymmetry of the loss term is sustained and the preferential confinement of electrons leads to an increase in the generated plasma current. After the B_V ramp-up, around 150 ms, the increase in plasma current slows down as CFS form, electron confinement improves, and the Fisch-Boozer mechanism becomes the dominant form of current generation.

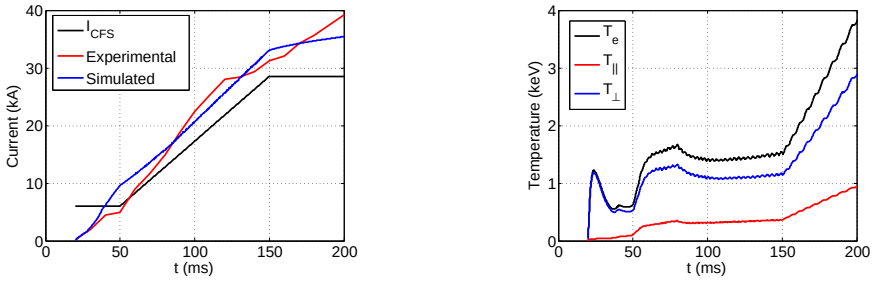

(a) (b)

Figure 6.6: The time evolution of (a) the plasma current, comparing simulation and experiment, and (b) the electron temperature.

The simulated temperature remains below 2 keV during the ramp-up phase, after which it greatly increases once CFS forms around 150 ms. At this point, electrons are completely confined and there are no losses, such that all the absorbed power acts to increase the electron temperature. This is not realistic, but as there are no loss terms for the power to be dissipated, this increase in temperature is seen.

After the formation of CFS, additional terms, such as radiation losses and ionisation effects, direct EBW CD, bootstrap current and electric fields, should be included to accurately model the distribution function. The artificial increase in temperature and the difference between the simulated and experimental current is an indication that the current model is insufficient for modelling the plasma after the formation of CFS, and the inclusion of additional terms is necessary to accurately model the plasma in this regime.

The mathematical formulation of the kinetic model was done under several assumptions and approximations, which leads to uncertainties in the measured current, while the numerical approximation itself has an error associated with it. Appendix I studies the accuracy of all assumptions and approximations, and show that the largest uncertainties are due to the uncertainty in the values of the self-inductance L_P, the value of the plasma current where CFS first start to form I_{CFS}, and due to approximating the electron-electron collision operator with a background Maxwellian. An uncertainty of about $10-20\%$ should therefore be attached to the simulated values, due to the uncertainties attached with the various assumptions and approximations made in formulating a mathematical expression for the kinetic model, but this acceptable compared to experimental uncertainties.

6.4.1 Energy of current-carrying electrons

The presence of energetic electrons during start-up questioned the validity of a collisionally driven CD mechanism [6, 11, 14, 16]. It was shown in Section 6.1 that the Fisch-Boozer mechanism, where the preferential heating of electrons moving in one direction around the torus creates an anisotropic plasma resistivity to generate a current, only generates small plasma currents. This is due to the EBW heating generating large populations of energetic electrons, which undergo very few collisions, and, as the Fisch-Boozer mechanism relies on collisions in order to generate a plasma current, the generated current is small.

The preferential confinement of electrons, on the other hand, can generate significant current, and supports all experimental observations investigated thus far. A further test for the validity of the CD mechanism can be performed by calculating the energies of the electrons carrying the majority of the current, in support of experimental observations. Figure 6.7 shows that the majority of the plasma current is carried by electrons with energies $10 - 25\,\mathrm{keV}$ during the vacuum field ramp-up phase, while the majority of electrons have energies less than $10\,\mathrm{keV}$. This compares well to experimental conclusions, which suggests that electrons with energies $\sim 25\,\mathrm{keV}$ are responsible for the majority of the current, even though the large majority of electrons have energies much lower.

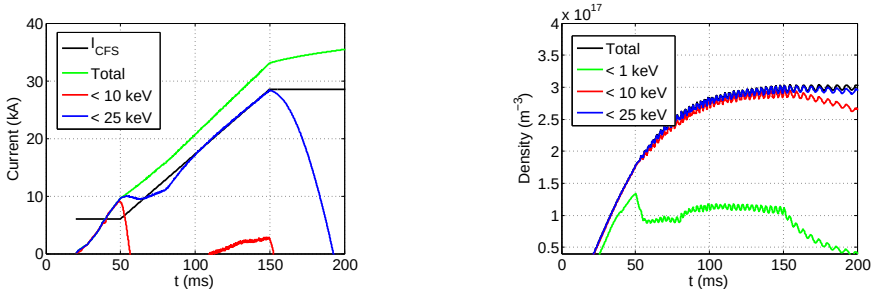

(a) (b)

Figure 6.7: The time evolution of (a) the plasma current, shows that the majority of current is carried by electrons between $10 - 25\,\mathrm{keV}$ during the vacuum field ramp-up, with this energy increasing after CFS start to form. Although the current is carried by these energetic electrons, the majority of electrons have energies less than $10\,\mathrm{keV}$, as is shown in (b) the time evolution of the electron density.

Figure 6.7 shows that the thermal electrons carries a negative current. As the EBW predominantly accelerates electrons with $p_{\parallel} > 0$ to larger $p_{\perp}$, while injecting negligible momentum in the parallel direction (see Section 6.6), an asymmetry is created amongst the

colder, thermal electrons. As there are more thermal electrons with $p_{\|} < 0$, the thermal electrons carry a negative current. The energetic electrons with energies $10 - 25\,\text{keV}$ compensate for this negative current with a larger positive current.

After the vacuum field ramp-up phase, the energies of the electrons responsible for carrying the majority of the plasma current increases, as the confinement of electrons improves and collisions become responsible for the current drive, as described in Section 6.1.

6.4.2 Effect of $N_{\|}$ on start-up

The value of the parallel refractive index, $N_{\|}$, plays an important role during start-up, as it determines which electrons in momentum space are accelerated. The Fisch-Boozer mechanism requires a non-zero value for $N_{\|}$ in order to gain a directionality with regards to the background magnetic field, while the preferential confinement of electrons generates an optimal current when $N_{\|} > 0$ and electrons with $p_{\|} > 0$, which are confined better than electrons with $p_{\|} < 0$, are accelerated by the EBW.

In order to see the effect of the value of $N_{\|}$ on the start-up simulation, the value of $N_{\|}$ is varied from $N_{\|} = 0.5$ to $N_{\|} = -0.5$, with results shown in figure 6.8 for a $50\,\text{kW}$ input. The simulated plasma current for $N_{\|} = 0.5$ and $N_{\|} = 0.05$ shows almost no difference, while CFS never forms for $N_{\|} = -0.5$. The absorbed power is equal, to within error, for all three cases, with the values of D_0 adjusted in order to ensure this.

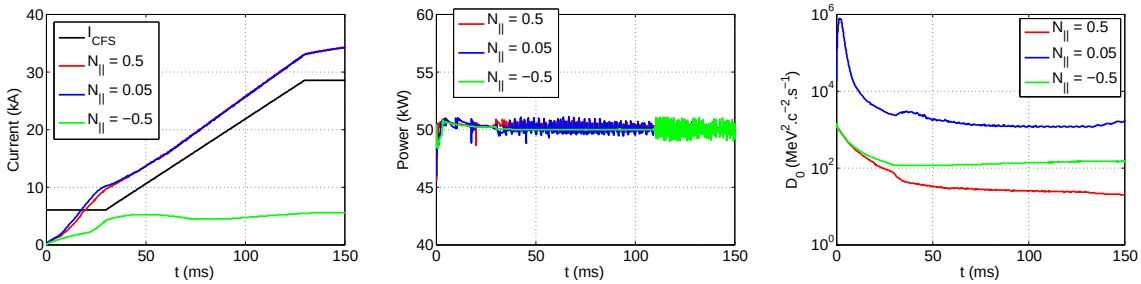

(a) (b) (c)

Figure 6.8: The time evolution of (a) the plasma current, (b) the absorbed RF power and (c) the value of D_0 for different values of $N_{\|}$.

For $N_{\|} = -0.5$, the generated current, in the absence of electron losses, will be negative, as electrons with $p_{\|} < 0$ are heated. However, during start-up, electrons with $p_{\|} > 0$ are confined much better than electrons with $p_{\|} < 0$, and, even though electrons with $p_{\|} < 0$ are heated, the majority of these electrons will still be lost and the confined electrons with

$p_\parallel > 0$ will be responsible for generating a current.

In order to generate a negative current, the direction of the vacuum poloidal field must be reversed. As electrons experience ∇B and curvature drifts, the guiding centre approximation gives

$$V_Z = \frac{B_Z}{B} v_\parallel + \frac{m_e}{eBR}\left(\frac{v_\perp^2}{2} + v_\parallel^2\right)$$

for $B_\phi < 0$. In MAST, the vertical component of the vacuum poloidal field $B_V < 0$, such that $B_Z < 0$ initially, and, as the drift term is always positive, only electrons with $v_\parallel > 0$ can satisfy $V_Z = 0$ for a constant B_Z and be confined, leading to a positive current. If $B_Z > 0$, only electrons with $v_\parallel < 0$ will satisfy $V_Z = 0$ resulting in a negative current.

This serves as further evidence that the preferential confinement of electrons is responsible for the generation of a plasma current. Of course, the value of $N_\parallel$ should be such that it enhances the current, rather than decreasing it. If electrons with $p_\parallel > 0$ are preferentially confined, then $N_\parallel > 0$ would ensure an optimal current.

6.5 Effect of power and density on current drive efficiency

The previous sections showed that the preferential confinement of electrons, created by the open magnetic field line configuration, is responsible for generating a current under EBW power during start-up. This CD mechanism is consistent with experimental observations that the majority of the plasma current is carried by energetic electrons, while explanations for the influence of the vacuum poloidal field on the generated plasma current have also been obtained.

The final experimental observation that requires an explanation is the observation that there exists a linear relationship between the injected power and generated current, with an efficiency of about 1 A/W. In order to see if such a relationship exists, it is necessary to first understand the influence of power and density on the generated current, as the injected power will also affect the electron density.

Consider three shots at different input powers, but similar vacuum magnetic fields, shown in figure 6.9. Detailed measurements of electron density for these experiments are not available, as the plasma density was below the Thomson scattering sensitivity limit [29]. Estimates made from interferometric measurements and the change in line integrated density (figure 6.9(c)) indicate that the electron density decreases for increasing power, while the

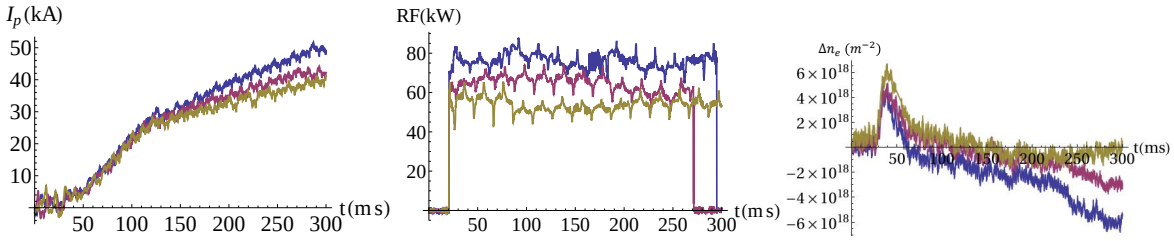

(a) (b) (c)

Figure 6.9: The time evolution of (a) the plasma current, (b) the injected RF power and (c) the change in line integrated density for three shots on MAST, #28941 (blue), #28949 (red) and #28950 (yellow).

generated plasma current is similar until about 150 ms, after which it increases for increasing power, creating the linear relationship between generated current and injected power. In order to understand this, the effect of density and power is first investigated on the separate CD mechanisms, before the effect of the vacuum field, power and density on the entire start-up simulation is considered.

6.5.1 Effect of density

In order to gain an understanding of the relationship between the generated current and injected power, the dependence of the generated current on density and power is studied separately, as the injected power will have an effect on the electron density, which will then impact the plasma current.

In order to see the effect of density on the generated current, the generated current is studied under constant power $P_0 = 50\,\mathrm{kW}$ in the absence of electron losses, in the absence of collisions, and in the presence of both electron losses and collisions. Results are shown in figure 6.10 for different electron densities.

The current generated by the Fisch-Boozer mechanism decreases for increasing electron density, as shown in figure 6.10(a). For the same power absorbed, higher density distributions will have lower temperatures and increased collisionality. This will force the distribution to be closer to Maxwellian, thereby reducing the anisotropy in the plasma resistivity.

The current generated by the preferential confinement of electrons, however, increases as the density is increased, as shown in figure 6.10(b). As electrons with $p_\parallel < 0$ are lost faster than electrons with $p_\parallel > 0$, increasing the density will result in greater losses, and therefore a greater plasma current.

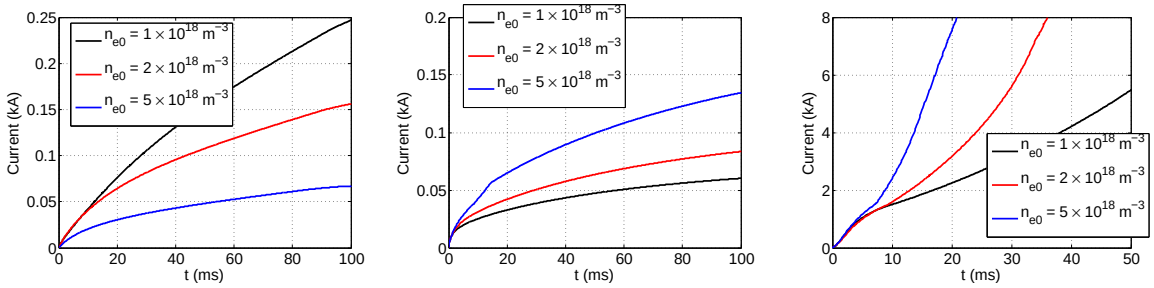

(a) (b) (c)

Figure 6.10: The time evolution of the plasma current for (a) collisional current drive, (b) current drive by the preferential confinement of electrons, and (c) for the combination of the two, for different electron densities.

Figure 6.10(c) shows the evolution of plasma current when including both collisions and orbital losses for different electron densities. The increase in density results in greater losses, which leads to a greater plasma current, similarly to the case without collisions, and the generated current is proportional to the electron density.

6.5.2 Effect of power

The dependence of plasma current on injected power is shown in figure 6.11. In this case, the electron density is kept constant, and the power absorbed is varied. The current generated by the Fisch-Boozer mechanism is shown to increase when increasing the absorbed power, as higher power will lead to higher temperatures and decreased collisionality, leading to a greater anisotropy in the plasma resistivity.

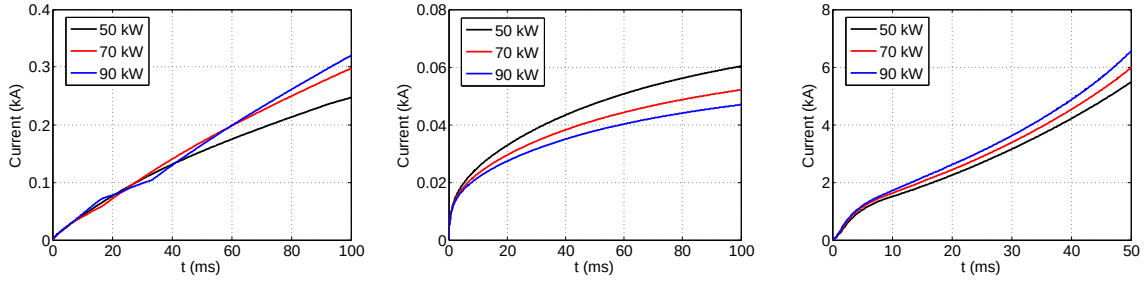

(a) (b) (c)

Figure 6.11: The time evolution of the plasma current for (a) collisional current drive, (b) current drive by the preferential confinement of electrons, and (c) for the combination of the two, for different input power.

In the absence of collisions, the current generated by the preferential confinement of

electrons decreases for increasing power, but increases when collisions are included. As EBW power mainly increases the perpendicular momentum of electrons, increasing the power will create more electrons with large $p_\perp$, which reduces the probability of an electron being lost. In the absence of collisions, electrons can not be pitch-angle scattered into regions of larger $p_\parallel$ and greater losses, such that the overall losses decrease, and the generated plasma current is smaller.

When including both losses and collisions, increasing the power leads to an increase in the temperature, including the parallel temperature. Therefore, electrons have, on average, larger values of $p_\parallel$, and, as the electron loss rate increases for increasing $p_\parallel$, increasing the power leads to greater losses and larger plasma currents.

6.5.3 Influence of power and density on start-up

The previous sections showed that, in the presence of both collisions and electron losses, the generated plasma current increases for both increasing density and increasing power. In order to gain an understanding of the linear relationship between injected power and generated current, as observed by experiments [6], both the power and density should be varied, but, as the time evolution of the electron density is not known nor modelled, such a study canot be done. Experimental measurements suggested that the electron density decreases for increasing power, but in order to investigate the linear relationship between the injected power and generated plasma current, the effect of power and density is studied separately.

Consider therefore a start-up simulation where the time evolution of the vacuum magnetic field is based on shot #28941. The wave parameters $N_\parallel = 0.5$ and $\Delta N_\parallel = 1$, and the density evolution is modelled by

$$n_e = n_{e0}\left(0.1 + 0.9\tanh\left[\frac{t}{t_0}\right]\right)$$

where $t_0 = 0.05\,\mathrm{s}$. The simulated plasma current, for varying electron densities n_{e0} and injected power P_0 is shown in figure 6.12.

Results show that the generated plasma current is the same for the duration of the B_V ramp-up, provided that the density and injected power is high enough, with differences only occurring after CFS form around 150 ms.

During the B_V ramp-up, the preferential confinement of electrons are responsible for the

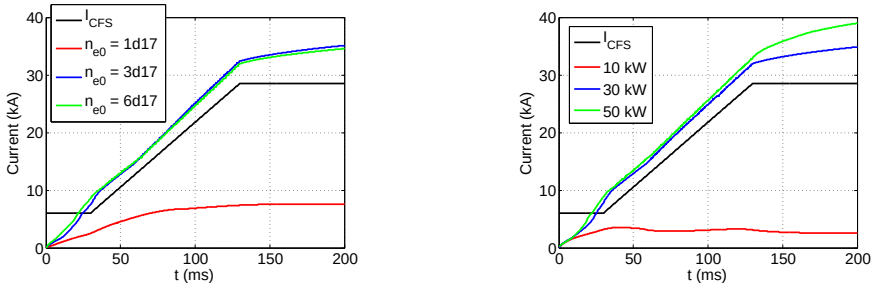

Figure 6.12: The time evolution of the plasma current for (a) different electron densities with $P_0 = 50\,\mathrm{kW}$, and (b) different input power with $n_{e0} = 3 \times 10^{17}\mathrm{m}^{-3}$.

increase in current, and the rate of increase is determined by the time evolution of I_{CFS}. After CFS forms, however, the Fisch-Boozer mechanism becomes the dominant mechanism for current generation. Figure 6.12(a) shows the current decreasing for increasing density, as would be expected for the Fisch-Boozer mechanism, and similarly figure 6.12(b) shows the current increasing for increasing power, as expected for the Fisch-Boozer mechanism.

It has also been observed in experiments that, for a fixed vacuum poloidal field strength, increasing the injected power does not increase the total generated current, but only decreases the amount of time it takes for CFS to form [14]. This can be observed in the first $\sim 30\,\mathrm{ms}$ when I_{CFS} is constant. Increasing the power, or density, decreases the amount of time it takes for $I_P > I_{\mathrm{CFS}}$ and CFS to start forming. As the preferential confinement of electrons is the mechanism responsible for generating the current, and the current generated by this mechanism increases for increasing density and power, such a result is not surprising.

The experimental conclusion that there exists a linear relationship between injected power and generated current is therefore only true for the Fisch-Boozer mechanism, as the comparison is made after CFS have formed, and not for the current generated by the preferential confinement of electrons, which is the dominant mechanism during start-up. As the current generated by the Fisch-Boozer mechanism increases for increasing power and decreases for increasing density, and the density decreases for increasing power, it is expected that there would be some proportionality between the generated plasma current and injected power, but only for the Fisch-Boozer mechanism, and not for the current generated by the preferential confinement of electrons. Instead, the generated current up to the point where CFS forms depends on the time evolution of I_{CFS} and is independent of the density and power, as long as the density and power are large enough for the current to keep up with the time

evolution of I_{CFS}.

It is possible that the increase in I_{CFS} can be faster for higher power, however, as experiments suggests that the density decreases for increasing power and the generated current decreases for decreasing density, increasing the power may not lead to a faster increase in current, as the density will decrease. In order to study these competing effects the time evolution of the density must be studied and modelled, but this is beyond the scope of this work.

6.5.4 Time evolution of the electron density

The previous section showed that the generated current is determined by the time evolution of the vacuum poloidal field, or the value of I_{CFS}, while the linear relationship between injected power and generated current, as measured by experiments, is only true for the Fisch-Boozer mechanism after the formation of CFS.

Electron density measurements for experiments conducted on MAST are not readily available as the electron density was below the Thomson scattering sensitivity limit. Interferometric measurements was used to get an approximate value for the electron density, but the time evolution of this density is not known exactly [29]. In other experiments similar to the EBW start-up, conducted on the LATE and TST-2 device, measurements indicate that the electron density remains approximately constant, with a slight decrease in density before the formation of CFS [14, 16–18, 66, 67].

In all the simulations performed up to this point, the electron density was assumed to increase, but, as electrons are lost during start-up, the electron density could decrease. This loss mechanism is balanced with an ionisation rate, which depends on the electron density and temperature, as well as the exact form of the electron distribution function, and studying the time evolution of the electron density is therefore a complicated function and beyond the scope of this work.

An increasing electron density was used for simplicity, as it is easier to fit the value of S_0 if the density obtained from the distribution function increases as a function of time in accordance with the known density. If the electron density is decreasing, then, unless the loss term is large enough to ensure that $S_0 > 0$, S_0 will have to be negative for the distribution function to give the correct density, which is not physical, and an increasing density evolution is therefore easier to model.

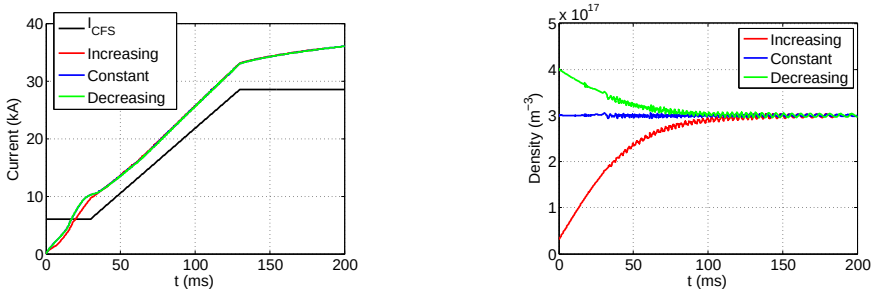

(a) (b)

Figure 6.13: The time evolution of (a) the plasma current and (b) the electron density for different forms of the time evolution of the electron density, with $P_0 = 50\,\text{kW}$, shows that the generated plasma current is independent of the shape of the density evolution.

For completeness, figure 6.13 shows the generated plasma current for an increasing, decreasing, and constant electron density. It shows that the generated current is independent of the form of the time evolution of the electron density. This implies that the choice of an increasing density evolution has no impact on the results discussed in previous sections, and the same results would have been obtained had the electron density been decreasing with time. In order to make a complete study of the generated plasma current during start-up, the electron density should also be modelled, but this is beyond the scope of this work.

6.6 Direct EBW current drive

This chapter investigates the CD mechanism responsible for the generation of a plasma current under EBW power during start-up. Due to the open magnetic field line configuration encountered during start-up, the preferential confinement of electrons leads to the generation of a plasma current. It was shown how the value of the parallel refractive index of the EBW, $N_{\|}$, influences the generated current, and how this value is influenced by the vacuum poloidal field. It was further shown how the vacuum poloidal field strength influences the generated current, and that the majority of the generated current is carried by energetic electrons, as deduced from experiments. Lastly, the effect of density and absorbed power on the generated current was studied, and it was shown that the linear relationship between the injected and generated current, as observed by experiments, is only true for the Fisch-Boozer mechanism, after the formation of CFS, while an increase of the vacuum poloidal field determines the increase in the generated plasma current before the formation of CFS.

The preferential confinement of electrons can be used to describe all the experimental conclusions, but additional CD mechanisms, such as a direct EBW current drive, due to a non-zero value of $N_\parallel$, have been neglected thus far. In this section, the impact of the direct EBW CD will therefore be studied.

The plasma-wave interaction is modelled as a diffusion of electrons in perpendicular momentum, due to the perpendicular refractive index of the absorbed wave being orders of magnitude greater than the parallel refractive index. The ratio of the parallel to perpendicular refractive indices are related to the magnetic field components [26],

$$\frac{N_\parallel}{N_\perp} \approx \frac{B_\theta}{B_\phi}$$

where B_θ is the poloidal field and B_ϕ the toroidal field. Typically, in the region of absorption during start-up, the toroidal field is about two orders of magnitude greater than the poloidal field, and therefore the parallel refractive index is small, such that the direct current drive of EBW, due to a non-zero $N_\parallel$, can be neglected.

As the value of $N_\parallel$ is non-zero, however, the EBW does contribute directly to the generated current. In order to show its effect, the EBW heating term is approximated by the diffusion term,

$$\frac{\partial f}{\partial t} = D_0 \left(D_\perp \frac{1}{p_\perp} \frac{\partial}{\partial p_\perp} p_\perp D \frac{\partial f}{\partial p_\perp} + D_\parallel \frac{\partial}{\partial p_\parallel} D \frac{\partial f}{\partial p_\parallel} \right) \tag{6.1}$$

where D_0 is calculated in the usual way and

$$D = \left\langle \exp\left[-\left(\frac{\omega - k_\parallel v_\parallel - n\omega_c}{\Delta\omega} \right)^2 \right] \right\rangle_{\text{volume}}$$

while expressions for $D_\perp$ and $D_\parallel$ must be found.

From quasilinear theory (Appendix A), the diffusion operator can be written as [30, 68],

$$\frac{\partial f}{\partial t} = \lim_{V\to\infty} \pi q^2 \sum_n \int \frac{d^3k}{V} \hat{L} p_\perp \delta(\omega - k_\parallel v_\parallel - n\omega_c) |\psi|^2 p_\perp \hat{L} f$$

where

$$\hat{L} = \left(1 - N_\parallel \frac{v_\parallel}{c}\right) \frac{1}{p_\perp} \frac{\partial}{\partial p_\perp} + N_\parallel \frac{v_\perp}{c} \frac{1}{p_\perp} \frac{\partial}{\partial p_\parallel}$$

and the polarization

$$\psi = E^+ J_{n-1} + E_- J_{n+1} + \frac{p_\parallel}{p_\perp} E_z J_n$$

with

$$E^{\pm} = \frac{1}{2}(E_x \pm iE_y)e^{\mp i\theta}$$

Here, the diffusion operator is written in the resonant limit, as only electrons in resonance with the RF wave will participate in diffusion, as given by the resonance condition in the delta function. Further, the direction of diffusion is restricted, as given by the operator $\hat{L}$,

$$v_\perp^2 + \left(v_\parallel - \frac{\omega}{k_\parallel}\right)^2 = \text{constant} \tag{6.2}$$

such that diffusion is directed along circles centred at $v_\parallel = \omega/k_\parallel$. This then provides two conditions for diffusion: that only electrons in resonance will take part, and that diffusion occurs along the circles defined by equation (6.2).

Using this, the diffusion operators are approximated by

$$\begin{aligned} D_\perp &= \left(1 - N_\parallel \frac{v_\parallel}{c}\right) \\ D_\parallel &= N_\parallel \frac{v_\perp}{c} \end{aligned} \tag{6.3}$$

and it is clear that, even for $N_\parallel \approx 1$, the diffusion in parallel momentum will be small compared to perpendicular diffusion as $D_\parallel \ll D_\perp$ unless $v \approx c$.

A simple explanation follows from relativistic mechanics [68], where $E^2 = p^2c^2 + m_e^2c^4$ and $\Delta E = v\Delta p$. From quantum mechanics, it is known that if a particle gains energy $\Delta E = \hbar\omega$, the wave will lose the same amount of energy. Further, a particle can gain parallel momentum $\Delta p_\parallel = \hbar k_\parallel$ such that the "parallel energy" is written as $\Delta E_\parallel = v_\parallel \Delta p_\parallel = \hbar k_\parallel v_\parallel$.

By taking the ratio of total energy to parallel energy, the total energy can be written as $\Delta E = v_\perp \Delta p_\perp + v_\parallel \Delta p_\parallel$, which gives

$$0 = v_\perp \Delta p_\perp + \left(1 - \frac{\omega}{k_\parallel v_\parallel}\right) v_\parallel \Delta p_\parallel$$

In the non-relativistic case, this integrates to

$$v_\perp^2 + \left(v_\parallel^2 - \frac{\omega}{k_\parallel}\right)^2 = \text{constant}$$

which is the same result as (6.2).

The effect of the direct EBW current drive, where the diffusion operator is given by

equations (6.1) and (6.3), is shown in figure 6.14 for $N_{\|} = 0.5$.

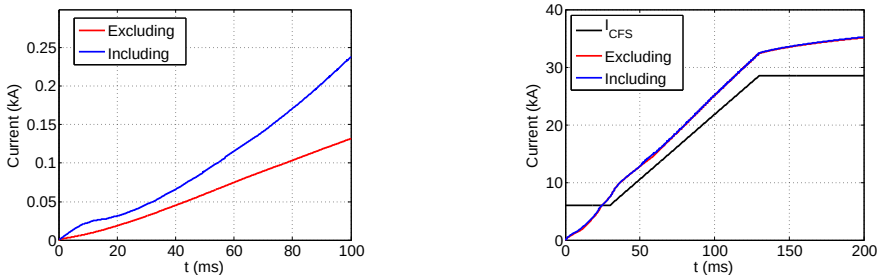

(a) (b)

Figure 6.14: The time evolution of the plasma current (a) in the absence of electron losses and (b) for a full start-up based on the experimental vacuum field evolution.

In the absence of electron losses the direct EBW current drive increases the current by almost a factor 2. This is a significant effect, but, as the current generated by the Fisch-Boozer mechanism is small, the resultant current, after adding the effect of a direct EBW current drive, is still small, even though it is double the current when excluding this effect. More importantly, when adding electron losses the difference in the generated current, when excluding and including the effect of a direct EBW current drive, is negligible, as the current generated by the preferential confinement of electrons is much greater than the direct EBW current drive.

6.7 Summary

EBW-assisted plasma current start-up has been demonstrated successfully in a number of experiments. An important aspect of start-up is the change in the magnetic field topology, from an open field line configuration to the formation of CFS, which is governed by the initiation of a plasma current. The generated current is mainly driven by the absorption of EBW power, and carried by energetic electrons, while larger currents are generated through an increase of the vacuum poloidal field strength [6, 11].

Previous studies into the CD mechanism have focused mainly on pressure-driven currents and the study of single particle orbits for the initiation of CFS through a preferential confinement of electrons based on the open magnetic field line structure [12, 14, 15]. In this chapter, it was shown that collisions are responsible for only a small part of the CD, while the preferential confinement of electrons, created by the open magnetic field line configuration

and controlled by the vacuum magnetic field, is responsible for the majority of the generated current.

The Fisch-Boozer mechanism, based on the preferential heating of electrons moving in one direction to create an anisotropic plasma resistivity, generates plasma currents much smaller than those observed in experiments. The current generated by the preferential confinement of electrons, however, can generate currents similar to those observed in experiments.

The open magnetic field line configuration leads to the preferential confinement of electrons, due to the vertical magnetic field cancelling out the perpendicular ∇B and curvature drifts for a selection of electrons. Collisions then act to "feed" the loss region by increasing the parallel momentum of electrons through pitch-angle scattering, increasing the rate at which electrons are lost, which leads to larger plasma currents being generated.

The location of RF heating, in this case through EBWs, depends on the local magnetic field in the mode conversion (MC) zone. In MAST, the MC zone is located just above the midplane, and, to ensure $N_{\|} > 0$, the magnetic field midplane must be shifted upwards. Once CFS start to form, however, the poloidal magnetic field reverses direction in the MC zone, and the magnetic field midplane must be shifted back downwards to ensure $N_{\|} > 0$ remains. This vertical shift also influences the confinement of electrons, and helps the formation of CFS.

The preferential confinement of electrons is an effect that disappears once CFS are completely formed and all electrons are confined. It can, however, be controlled through the use of the vacuum poloidal magnetic field in order to generate larger plasma currents. If the plasma current $I_P = I_{\mathrm{CFS}}$ is the value where all forward electrons, moving along the magnetic field, are confined and the first CFS start to form, then by increasing the value of I_{CFS}, larger values of I_P can be achieved while keeping the asymmetry of the loss term intact. The value of I_{CFS} is related to the vertical strength of the vacuum poloidal field B_V, such that an increase in B_V can be used to achieve greater plasma currents.

Experiments used a combination of a vertical shift and B_V ramp-up to achieve large plasma currents, and it is shown that simulations agree well with experiment. Simulations also show that the majority of the plasma current is carried by electrons with energies $10 - 25\,\mathrm{keV}$, which compares well to experimental conclusions.

The dependence of the generated current on the electron density and injected power has been studied as experiments concluded that there exists a linear relationship between the

generated current and injected power. It is shown that the current increases for increasing power and density, but, for a similar evolution of the vacuum magnetic field, the generated current is the same until CFS form. After the formation of CFS, the Fisch-Boozer mechanism becomes the dominant CD mechanism, and it is shown that the current generated by collisions increases for increasing power, but decreases for increasing density.

This is supported by experiments, which suggest that the electron density decreases for increasing power. During the B_V ramp-up phase, the generated current is independent of the injected power, and determined by the time evolution of I_{CFS}. Once CFS form, the current increases with increasing power, as is the case for the Fisch-Boozer mechanism. Further, as in the experiments the density decreases with increasing power, this will also lead to an increase in the generated current, as is the case for the Fisch-Boozer mechanism.

The conclusion that the generated current is linearly dependent on the injected RF power is therefore only true for the current after CFS forms and the Fisch-Boozer mechanism, and not for the current generated by the preferential confinement of electrons, which is the dominant mechanism during start-up. In order to fully study the effect of injected power on the generated current, the time evolution of the electron density must be studied, but this is beyond the scope of this work.

Chapter 7

Summary and recommendations for future work

This thesis reports on the development of a kinetic model for studying non-inductive start-up of tokamak plasmas. Electron Bernstein wave (EBW)-assisted plasma current start-up has previously been demonstrated successfully in a number of experiments, but investigations into the current drive (CD) mechanism responsible have been qualitative at best and theoretical explanations for several experimentally observed effects are still lacking [6, 11, 12, 14, 15].

An important part of start-up is the transition from the initial open magnetic field line configuration to the formation of closed flux surfaces (CFS). The change in magnetic field topology brings about a change in dynamics and is driven by the initiation of a plasma current. A particular question to answer is the CD mechanism responsible for the current generation, and it is this fundamental question that this thesis aims to answer.

In order to gain an understanding of the CD mechanism repsonsible for the observed current generation, a kinetic model has been developed to study the time evolution of the electron distribution function. The distribution function is studied under several effects, including an electron source, orbital losses, collisions, plasma induction, and EBW heating.

The electron distribution function can be used to calculate several observables, including the plasma current, electron density and temperature, and power absorbed, from which conclusions regarding the CD mechanism can be drawn. In addition, experiments drew several conclusions, regarding the effect of the vacuum magnetic field, the role of energetic electrons and the dependence of the generated plasma current on the injected power, for

which no explanations have previously been given, but which can now be explained with the help of the developed kinetic model.

In this chapter, the findings are summarised, and suggestions for future work are made.

7.1 Kinetic model for studying EBW start-up

There are two main methods for studying non-inductive start-up. The first method is the particle approach, where the motion and interactions of millions of representative particles is simulated using Monte Carlo methods. However, as there are $10^{18} - 10^{20}$ electrons in a typical tokamak plasma, this approach is computationally too expensive to quantitatively study various effects thought to be important during start-up.

The second method is a kinetic approach, where the time evolution of the electron distribution function is studied. This approach allows the study of the motion and interactions of electrons, while avoiding the need to simulate all electrons. In order to capture all effects thought to be important during start-up, the distribution function is ideally studied in three spatial and three momentum dimensions, but in practice major simplifications can be made to ensure the model is tractable and computationally manageable, while still containing sufficient physics.

In this thesis, the electron distribution function is studied under several effects thought to be important during start-up,

$$\frac{\partial f}{\partial t} = \text{source} + \text{losses} + \text{EBW heating} + \text{collisions} + \text{loop voltage}$$

where $f = f(p_\parallel, p_\perp, t)$. In order to ensure the model is tractable and computationally manageable, the distribution function is studied in two momentum and zero spatial dimensions. As a number of terms are spatially dependent, appropriate volume averages and approximations are taken to account for this.

The source term describes electrons entering the system through ionisation effects, and is modelled by

$$\frac{\partial f}{\partial t} = \frac{S_0}{\pi^{3/2} p_0^3} \exp\left[-\frac{p_\parallel^2 + p_\perp^2}{p_0^2}\right]$$

where p_0 is the momentum corresponding to the thermal velocity of a 2 eV Maxwellian distribution and S_0 is the rate at which electrons are added to the system, determined in

such a way that the density calculated from the distribution function is consistent with some pre-determined time dependent electron density, which could be obtained from experiment or from particle and energy balance.

The collision term describes electron-electron and electron-ion collisions. Electron-electron collisions are approximated by assuming that the distribution collides with a background Maxwellian distribution of the same representative temperature as the distribution itself, while electron-ion collisions are approximated using the high-velocity limit [43]. These approximations allow analytical formulations of the collision operator, which accelerates computation time. Of course, the distribution function is not a Maxwellian, and so these approximations introduce an error into the calculation, but, as the current is predominantly carried by energetic electrons [6, 11] which undergo very few collisions, this approximation can be made.

The loop voltage term describes the effect of plasma induction. As a plasma current is initiated, the self-induction of the plasma will generate a loop voltage V_L to oppose the increase in plasma current, according to Lenz's law

$$V_L = -L_P \frac{dI_P}{dt}$$

where L_P is the self-inductance and I_P is the plasma current. The loop voltage is determined in such a way that Lenz's law is always satisfied.

7.1.1 Electron losses

During start-up, the magnetic field line configuration is open, such that electrons can freely stream out of the plasma volume. In an axisymmetric plasma in the start-up phase, the toroidal field B_ϕ is much greater than the poloidal field, such that the guiding centre approximation (see Appendix D) can be used to calculate ∇B and curvature drifts. In the presence of a constant, vertical magnetic field B_Z, the guiding centre equation can be written as

$$V_Z = \frac{B_Z}{B} v_\parallel + \frac{m_e}{eBR}\left(\frac{v_\perp^2}{2} + v_\parallel^2\right)$$

for $B_\phi < 0$. In MAST, $B_Z < 0$, and, as the drift term is always positive, only electrons with $v_\parallel > 0$ can satisfy $V_Z = 0$ and be confined. As the vertical magnetic field B_Z is not constant and the radial field B_R is non-zero, more electrons around the $V_Z = 0$ characteristic are

confined due to mirror effects. This leads to a preferential confinement of electrons, which can lead to the generation of a plasma current. The electron confinement is dependent on the spatial structure of the magnetic field, with the magnetic field line configuration, and therefore also the confinement of electrons, changing with the generation of a plasma current. The loss term is therefore described by

$$\frac{\partial f}{\partial t} = -\frac{f}{\tau_{\text{loss}}} P_{\text{loss}}(p_{\parallel}, p_{\perp})$$

where τ_{loss} is the typical time it takes for an electron to be lost out of the plasma volume, while P_{loss} describes the probability of an electron being lost/confined.

The probability of an electron being lost/confined depends on the magnetic field line structure, and has been studied in detail. Chapter 4 describes the formulation of an empirical equation for describing its evolution as a function of the vertical shift of the plasma Z_0, the value of the plasma current where CFS first start to form I_{CFS}, and the plasma current I_P. The parameter I_{CFS} is particularly important, as it contains knowledge of the spatial dependence and strength of the vacuum poloidal field as well as the current density profile. Any change in either of those will result in a change in the value of I_{CFS}. It is convenient to have all these dependences contained in a single parameter, as any uncertainty can easily be captured by varying the value of I_{CFS}.

7.1.2 Plasma-wave interaction

For experiments conducted on MAST, the injected RF beam underwent a double mode conversion (MC), from the externally launched O-mode to X-mode via a grooved mirror-polariser on the central rod, and from X-mode to the EBW at the upper hybrid resonance (UHR). The EBW is subsequently absorbed, accelerating electrons along its electric field. This interaction is modelled by the EBW heating term as a diffusion of electrons in perpendicular momentum,

$$\left(\frac{\partial f}{\partial t}\right)_{\text{EBW heating}} = \frac{1}{p_{\perp}} \frac{\partial}{\partial p_{\perp}} p_{\perp} D \frac{\partial f}{\partial p_{\perp}}$$

where

$$D(p_{\parallel}, p_{\perp}) = D_0 \left\langle \exp\left[-\left(\frac{\omega - k_{\parallel} v_{\parallel} - \omega_c}{\Delta\omega} \right)^2 \right] \right\rangle_{\text{volume}}$$

and D_0 is determined in such a way as to ensure the power absorbed by the distribution function equals the total power absorbed. For absorption around the fundamental electron cyclotron resonance (ECR), only electrons satisfying the resonance condition,

$$\omega - k_{\|} v_{\|} - \omega_c = 0$$

where $k_{\|}$ is the parallel component of the wave number and $\omega_c = \omega_{c0}/\gamma$ is the relativistic cyclotron frequency, can absorb energy from the beam, while the volume average ensures that contributions from all parts in space are taken into account due to the spatial dependence of the magnetic field contained in the cyclotron resonance.

The plasma-wave interaction is determined by the absorption of RF power under specific wave parameters. These parameters can be obtained by solving the dispersion relation (Appendix A) to obtain the wave vector parallel to the magnetic field $k_{\|}$ as well as the total power absorbed. As the dispersion relation describes the local propagation and absorption of the wave, and the wave diverges in space, the resonance width $\Delta\omega$ is introduced to account for the fact that the refractive index is not constant across the region of absorption.

7.1.3 Numerical solution

The various terms influencing the electron distribution function can either change the momentum or the number of electrons in the system. The time evolution of the electron distribution function is therefore written as a time dependent two-dimensional advection-diffusion equation with source and loss terms, for which a numerical approximation must be found to study the time evolution of the electron distribution function.

The distribution function must always be non-negative everywhere, which poses problems for solving, in particular, the mixed derivative terms contained in the collision operator. Chapter 5 describes a numerical scheme for solving the advection-diffusion type equations, and, in particular, an approximation to the mixed derivative terms, in which they are written as linear advection equations. The numerical scheme evolves the distribution function under the preservation of positivity and the conservation of particle number in the absence of source and loss terms.

7.2 Current drive mechanism

EBW-assisted plasma current start-up has previously been demonstrated successfully in a number of experiments. An important aspect of start-up is the change in the magnetic field topology, from an open field line configuration to the formation of CFS, which is governed by the initiation of a plasma current. The generated current is mainly driven by the absorption of EBW power, and carried by energetic electrons, which undergo very few collisions and so questions the validity of a collisionally dominated CD mechanism [6, 11].

Previous studies into the CD mechanism have focused mainly on pressure-driven currents and the study of single particle orbits for the initiation of CFS through a preferential confinement of electrons based on the open magnetic field line structure. These studies provided some qualitative support for the CD mechanism [12, 14, 15], but more detailed, quantitative studies are necessary to determine the dominant CD mechanism responsible for the observed current, while also providing insight into further experimentally observed effects which are not understood.

There are two main CD mechanisms. Firstly, the Fisch-Boozer mechanism [19], based on the preferential heating of electrons moving in one direction to create an anisotropic plasma resistivity, generates plasma currents much smaller than those observed in experiments. In this work it was shown that the second mechanism, the preferential confinement of electrons, is responsible for the majority of the plasma current during start-up before CFS forms, and can generate currents similar to those observed in experiments.

The open magnetic field line configuration leads to the preferential confinement of electrons, due to the parallel motion of electrons along the vertical magnetic field cancelling out the perpendicular ∇B and curvature drifts for a selection of electrons. Collisions then act to "feed" the loss term by increasing the parallel momentum of electrons through pitch-angle scattering, increasing the rate at which electrons are lost, which leads to larger plasma currents being generated.

Collisions are therefore only responsible for a small part of the current, while the preferential confinement of electrons are responsible for the majority of the generated current and the formation of CFS. After the formation of CFS, the collisional mechanism, in addition to a direct EBW current drive, will be responsible for a further rise in the plasma current.

7.3 Comparison to experiment

As discussed in the previous section, the open magnetic field line configuration establishes an asymmetric confinement of electrons, which leads to the generation of a plasma current. In order to further test the validity of such a current drive mechanism, comparisons are made to experiment.

Experiments conducted on MAST generated currents up to 73 kA with up to 100 kW of input power, using a combination of vacuum field effects, the vertical kick and B_V ramp-up. Further, experiments concluded that the majority of the plasma current is carried by energetic electrons with energies ~ 25 keV, while a linear relationship between the generated plasma current and injected RF power was also observed [6, 11]. These experimental observations are discussed in the following sections.

7.3.1 Vertical kick

The location of RF heating is determined by the toroidal magnetic field B_ϕ. The parallel refractive index $N_\parallel$, however, is determined by the local poloidal magnetic field. For experiments conducted on MAST, in which the injected power is absorbed from the excited EBW, absorption occurs primarily just above the midplane. In order to ensure an optimal current is generated, $N_\parallel > 0$ is required, but, as the vertical magnetic field $B_Z < 0$ during start-up, $N_\parallel < 0$ above and $N_\parallel > 0$ below the midplane. In order to ensure $N_\parallel > 0$ in the region of absorption, the midplane is shifted upwards by creating a radial magnetic field B_R through the P6 coils on MAST. After the formation of CFS, the vertical magnetic field B_Z changes sign and the midplane must be shifted back downwards to ensure $N_\parallel > 0$.

Apart from ensuring an optimal $N_\parallel$, the vertical kick also influences the confinement of electrons. It was shown in Section 4.2.1 that a vertical shift enhances the asymmetry in the confinement of electrons in such a way that a larger current can be generated, as was confirmed in Section 6.3.1. The vertical kick therefore helps to form CFS, and is an important part of the start-up procedure.

7.3.2 B_V ramp-up

The preferential confinement of electrons, created by the open magnetic field line configuration, asymmetrically confines electrons. This asymmetry is mainly dependent on the ratio

I_P/I_{CFS}, where I_{CFS} is the value of the plasma current where the first CFS start to form. The value of I_{CFS} is related to the vertical strength of the vacuum poloidal field B_V, such that an increase in the value of B_V will lead to an increase in the value of I_{CFS}. This can then lead to an increase in the plasma current I_P, as the asymmetry in the electron confinement can be sustained throughout.

Experiments conducted on MAST used this B_V ramp-up to generate large plasma currents, as was shown in Section 6.3.2. This observation supports the preferential confinement of electrons as the current drive mechanism responsible for the generation of a plasma current during start-up, before the formation of CFS.

7.3.3 Energy of current-carrying electrons

Experiments use a combination of a vertical shift and B_V ramp-up to achieve large plasma currents, and it is shown that simulations agree well with experiment. Simulations also show that the majority of the plasma current is carried by electrons with energies $10 - 25\,\mathrm{keV}$, which compares well to experimental conclusions, as was shown in Section 6.4.1.

7.3.4 Dependence on electron density and power absorbed

Finally, experiments conducted on MAST concluded that there exists a linear relationship between the generated plasma current and injected power, with an efficiency of about $1\,\mathrm{A/W}$ [6]. In order to study this dependence, the relationship between the generated plasma current, the electron density and injected power is studied. It is shown that the current increases for increasing power and density, but, for a similar evolution of the vacuum poloidal field, the generated current is the same until CFS form, provided the injected power and density is high enough. After the formation of CFS, the Fisch-Boozer mechanism becomes the dominant CD mechanism, and it is shown that the current generated by collisions increases for increasing power, but decreases for increasing density.

This is supported by experiments, which suggests that the electron density decreases for increasing power. During the B_V ramp-up phase, the generated current is independent of the injected power, and determined by the time evolution of I_{CFS}, provided the injected injected power and density is high enough. Once CFS form, the current increases for increasing power, as is the case for the Fisch-Boozer mechanism. Further, as the density decreases for increasing power, this will also lead to an increase in the generated current, as is the case

for the Fisch-Boozer mechanism.

The conclusion that the generated current is linearly dependent on the injected RF power is therefore only true for the current after CFS forms and the Fisch-Boozer mechanism, and not for the current generated by the preferential confinement of electrons, which is the dominant mechanism during start-up until CFS forms. In order to fully study the effect of injected power on the generated current, the time evolution of the electron density must be studied, but this is beyond the scope of this work.

7.4 Future development

In order to ensure the developed model is tractable and computationally manageable, the electron distribution function was studied in zero spatial and two momentum dimensions (0D2V). Only the terms thought to be important during start-up was included, while volume averages and approximations were taken to account for the 0D nature. Naturally, this led to several approximations and assumptions, such that several extensions and improvements could be applied to the model.

7.4.1 Collision operator

The collision operator describes the effect of self-collisions, as electrons collide with other electrons in the distribution. For simplicity, this collision operator was approximated with a background Maxwellian, such that an analytical expression can be used, reducing computation time. This assumption is based on the fact that the majority of the plasma current is carried by energetic electrons which undergo very few collisions, so the exact form of the collision operator should not be that important, even though it introduces an uncertainty of about 10% (see Appendix I).

In order to improve on the approximation, the collision operators can be determined from the known distribution, by solving either the Landau integrals [49] or the Rosunbluth potentials [48]. Including this additional step will increase the complexity and computational time, but will increase the accuracy of the solution.

7.4.2 Density evolution

Throughout this thesis, the time evolution of the electron density is assumed known, and the density of the distribution function is fitted to this density. As the majority of the plasma current is carried by energetic electrons which undergo very few collisions, ionisation effects were neglected, as the energetic electrons are not expected to contribute to it. In order to study the dependence of the plasma current on the injected power and make predictions for future STs, the time evolution of the electron density must be studied.

A good starting point will be start-up models for modelling inductive start-up, which have successfully modelled the density evolution [8]. The evolution of the electron density can be studied through particle balance [9],

$$\frac{dn_e}{dt} = n_e(\tau_{\text{ionisation}}^{-1} - \tau_{\text{loss}}^{-1})$$

where $\tau_{\text{ionisation}}$ is the ionisation rate and τ_{loss} is the loss rate, while more complicated models involve the electron power balance [8, 44].

The ionisation rate depends on a number of factors, including the electron density and temperature, as well as the exact shape of the distribution function. In order to accurately model the ionisation rate, these effects, including effects such as recombination and collisional excitation and radiation, must be included in modelling the time evolution of the electron distribution function.

7.4.3 Theoretical derivation of loss term

The open magnetic field line configuration allows electrons to freely stream out of the plasma volume. This loss mechanism was modelled by numerically studying the confinement of electrons and its dependence on the vacuum poloidal field strength, as well as its spatial dependence, and the current density profile, including its strength. A mathematical expression is then empirically fitted to these numerical plots in order to describe the evolution of the orbital loss term.

A more robust method in obtaining the loss term will be to obtain it theoretically, but any such derivation will be complicated due to the spatial dependence of the magnetic field.

7.4.4 Additional current drive mechanisms

According to Faraday's law, any change in magnetic field topology can generate an electric field. The vacuum poloidal field ramp-up phase, for example, generates an electric field E_ϕ,

$$-\frac{\partial B_Z}{\partial t} = \frac{E_\phi}{R}$$

due to the increase in the vertical poloidal field strength, and will lead to an increase in the plasma current.

Further electric fields are created due to the initiation of eddy-currents in the vessel wall. For an applied voltage V_ϕ, the plasma current can be solved using a two-ring model [8],

$$V_\phi = I_P R_P + L_P \frac{\mathrm{d}I_P}{\mathrm{d}t} + M\frac{\mathrm{d}I_V}{\mathrm{d}t}$$
$$V_\phi = I_V R_V + L_V \frac{\mathrm{d}I_V}{\mathrm{d}t} + M\frac{\mathrm{d}I_P}{\mathrm{d}t}$$

where I_V is the eddy-current in the vessel walls, R_V and L_V is the resistance and self-inductance of the vessel, respectively, M is the mutual inductance between the plasma and the vessel wall, and R_P and L_P is the plasma resistivity and self-inductance, respectively.

These eddy-currents can be significant until the plasma resistivity becomes much smaller than the vessel's electric resistance, and leads to a reduction in the plasma current [8].

The additional electric fields influence the current, but its implementation is complicated by the long time scales of the resistive diffusion time. Combining Ohm's and Faraday's laws lead to the well-known induction equation,

$$\frac{\partial \vec{B}}{\partial t} = \nabla \times (\vec{u} \times \vec{B}) + \frac{\eta}{\mu_0}\nabla^2 \vec{B}$$

where η is the plasma resistivity and $\vec{u}$ the plasma flow velocity. The first term on the right-hand-side is the advection term (magnetic field pulling plasma along with it) and the second term is the diffusion term (magnetic field lines propagating across and out of the plasma). The diffusion term has a characteristic time scale, called the resistive diffusion time scale, of

$$\tau_d = a^2 \mu_0 / \eta \tag{7.1}$$

with the plasma resistivity given by [2]

$$\eta \approx 2.5 \times 10^{-8} / T_e^{3/2}$$

where T_e is measured in keV. For MAST parameters, this results in a diffusion time scale of about $\tau_d \sim 0.5\text{s} - 200\text{s}$ for temperatures of $100\text{eV} - 5\text{keV}$. This implies that any induced electric field take a long time to diffuse through the plasma, such that spatial effects are important. It also implies that a "frozen-in" condition could exist, where externally created electric fields cannot propagate into the plasma, and including these electric fields are therefore complicated.

There exists a further CD mechanism, due to the pressure-ballooning force. In a fluid description, the outward pressure-ballooning force created by pressure gradients should be balanced by a $\vec{J} \times \vec{B}$ force, i.e.

$$\vec{J} \times \vec{B} = \nabla p$$

which could lead to the initiation of a plasma current. This current is associated with the pressure of the bulk electrons, and requires knowledge of the spatial distribution of electrons, but, as experiments concluded that the majority of the plasma current was carried by energetic electrons, it was neglected in this work.

7.4.5 Spatial dependence

Lastly, and perhaps the most difficult extension, is to include a spatial dependence.

The main difficulty associated with such an extension is due to the spatial motion of electrons. As electron orbits not only depends on their starting point but also their initial momenta, it is not possible to average over orbits, and some mapping of how electrons move in space is required. However, as confined electrons typically complete their orbits in $\sim \mu$s, which is a much shorter time scale than that of interest, mapping the movement of electrons in space might not be necessary.

Including a spatial dependence will make the EBW heating, the loop voltage, and the loss terms more accurate, as volume averages or approximations are no longer necessary to describe these. Unfortunately, including spatial dependences will complicate the solution to the distribution function, as it now becomes 3D or even 4D, dramatically increasing computational time.

Appendix A

Waves in a hot plasma

The electrical conductivity of a plasma allows it to couple to electric and magnetic fields, with the complex nature of particles and fields supporting a wide variety of wave phenomena. In the presence of an electric and magnetic field, this complex nature results in a solution to the motion of particles and propagation and absorption of waves, by coupling Maxwell's equations and the collisionless Boltzmann (or Vlasov) equation.

The derivation of the hot plasma dispersion relation, which describes the motion of waves in a plasma, was first introduced by Landau [31] for EM waves in the absence of a background magnetic field. The theory for waves in a plasma in the presence of a background magnetic field is well-known [30], and briefly discussed here.

The Vlasov equation in real space $(\vec{r}, \vec{p}, t)$, is given by

$$\frac{\partial f}{\partial t} + \vec{v} \cdot \vec{\nabla} f - e(\vec{E} + \vec{v} \times \vec{B}) \cdot \frac{\partial f}{\partial \vec{p}} = 0 \tag{A.1}$$

and can be separated into first- and second-order equations by introducing equilibrium and perturbation quantities,

$$\begin{aligned} f(\vec{r}, \vec{p}, t) &= f_0(\vec{p}, \epsilon^2 t) + \epsilon \tilde{f}_1(\vec{r}, \vec{p}, t) \\ \vec{B}(\vec{r}, t) &= \vec{B}_0(\vec{r}, t) + \epsilon \vec{\tilde{B}}_1(\vec{r}, t) \\ \vec{E}(\vec{r}, t) &= \epsilon \vec{\tilde{E}}_1(\vec{r}, t) \end{aligned}$$

where the perturbation quantities $\vec{\tilde{E}}_1$ and $\vec{\tilde{B}}_1$ are properties of the EM wave and marked with subscript 1, while the only equilibrium quantities are the magnetic field $\vec{B} = B_0 \hat{z}$ and the distribution function f_0. The assumption is made that the perturbation quantities are

small compared to equilibrium quantities, marked with subscript 0, as indicated by ϵ.

The Vlasov equation (A.1) can then be written as a first-order equation,

$$\left(\frac{\partial}{\partial t} + \vec{v}\cdot\vec{\nabla} - e(\vec{v}\times\vec{B}_0)\cdot\frac{\partial}{\partial\vec{p}}\right)\tilde{f}_1 = e(\vec{\tilde{E}}_1 + \vec{v}\times\vec{\tilde{B}}_1)\cdot\frac{\partial f_0}{\partial\vec{p}} \tag{A.2}$$

which describes the response of the distribution function to a known EM field, and a second-order equation,

$$\frac{\partial f_0}{\partial t} = e(\vec{\tilde{E}}_1 + \vec{v}\times\vec{\tilde{B}}_1)^*\cdot\frac{\partial\tilde{f}_1}{\partial\vec{p}} + \text{c.c} \tag{A.3}$$

which describes the slow variation due to the reaction of the wave distribution back on the distribution function.

The first-order equation (A.2) is used to obtain a solution to the plasma dispersion relation, while the second-order equation (A.3) is used to describe the effect of the plasma-wave interaction on the equilibrium distribution function.

A.1 Hot plasma dispersion relation

The dispersion relation describes the interaction between an EM wave and a plasma, by combining Maxwell's equations and the Vlasov equation in a self-consistent way. The first-order Vlasov equation (A.2), describing the effect of a known EM field on a distribution function, can be used to obtain the plasma current,

$$\vec{j} = -\frac{i\omega}{4\pi}\hat{\chi}\cdot\vec{E}$$

where $\hat{\chi}$ is the magnetic susceptibility. This, together with Maxwell's equations,

$$\nabla\times\vec{B} = \mu_0\vec{j} + \frac{1}{c^2}\frac{\partial\vec{E}}{\partial t}$$
$$\nabla\times\vec{E} = -\frac{\partial\vec{B}}{\partial t}$$

can be used to obtain the wave equation,

$$\vec{N}\times(\vec{N}\times\vec{E}) + \hat{\epsilon}\cdot\vec{E} = 0 \tag{A.4}$$

where the dielectric tensor is given by,

$$\hat{\epsilon}(\omega, \vec{k}) = \hat{1} + \hat{\chi}(\omega, \vec{k})$$

and the dimensionless vector $\vec{N}$

$$\vec{N} = \frac{\vec{k}c}{\omega} \tag{A.5}$$

has the direction of the wave vector $\vec{k}$ and the magnitude of the refractive index. The solution to the wave equation (A.4) is known as the dispersion relation.

A.1.1 Solution to the Vlasov equation

In order to solve the dispersion relation, a solution to the first-order Vlasov equation (A.2) is obtained by integrating along the zero-order trajectory,

$$f_1(\vec{r}, \vec{p}, t) = -q \int_{-\infty}^{t} dt^{'} (\vec{E}_1(\vec{r}^{'}, t^{'}) + \vec{v}^{'} \times \vec{B}_1(\vec{r}^{'}, t^{'})) \cdot \nabla_{p^{'}} f_0(\vec{p}^{'}) \tag{A.6}$$

from time $t^{'} = -\infty$ to $t^{'} = t$.

Maxwell's induction equation,

$$\nabla \times \vec{E} = -\frac{\partial \vec{B}}{\partial t}$$

along with the perturbative quantities $\vec{E}_1(\vec{r}^{'}, t^{'}) = \vec{E} \exp{(i\vec{k} \cdot \vec{r}^{'} - i\omega t^{'})}$, can be used to replace

$$\vec{B}_1 = \frac{\vec{k}}{\omega} \times \vec{E}_1$$

and, by making use of the vector identity,

$$\vec{a} \times (\vec{b} \times \vec{c}) = \vec{b}(\vec{a} \cdot \vec{c}) - \vec{c}(\vec{a} \cdot \vec{b})$$

the perturbation to the distribution function f_1 can be written as,

$$f_1(\vec{r}, \vec{p}, t) = -q \int_{-\infty}^{t} dt^{'} e^{(i\vec{k} \cdot \vec{r}^{'} - i\omega t^{'})} \vec{E} \cdot \left[\hat{1} \left(1 - \frac{\vec{v}^{'} \cdot \vec{k}}{\omega} \right) + \frac{\vec{v}^{'} \vec{k}}{\omega} \right] \cdot \nabla_{p^{'}} f_0(\vec{p}^{'}) \tag{A.7}$$

where $\hat{1}$ is the unit dyadic.

This is to be evaluated in the Lagrangian system of coordinates, along the zero order trajectory, $\vec{r}^{'}(t^{'})$, such that the end point of the trajectory is $\vec{r}^{'} = \vec{r}$ at $t^{'} = t$. For earlier

times the trajectory obeys the zero-order equation of motion,

$$\frac{d\vec{p}^{'}}{dt^{'}} = qB_0\vec{v}^{'} \times \hat{z} = \Omega\vec{p}^{'} \times \hat{z}$$

where $\vec{B_0} = B_0\hat{z}$ and

$$\vec{p} = \gamma m_0 \vec{v}$$
$$\gamma^2 = \left(1 - \frac{v^2}{c^2}\right)^{-1} = \frac{p^2}{m_0^2 c^2} + 1$$
$$\Omega = \frac{qB_0}{m} = \frac{\Omega_0}{\gamma}$$

In terms of Eulerian coordinates,

$$\tau = t - t^{'}$$
$$v_x = v_\perp \cos\phi \quad , \quad v_y = v_\perp \sin\phi$$
$$v_x^{'} = v_\perp \cos(\phi + \Omega\tau) \quad , \quad v_y^{'} = v_\perp \sin(\phi + \Omega\tau)$$
$$v_z^{'} = v_\parallel$$
$$x^{'} = x - \frac{v_\perp}{\Omega}(\sin(\phi + \Omega\tau) - \sin\phi)$$
$$y^{'} = y - \frac{v_\perp}{\Omega}(\cos(\phi + \Omega\tau) - \cos\phi)$$
$$z^{'} = z - v_\parallel\tau$$

where ϕ is the gyroangle. For the wave vector,

$$k_x = k_\perp \cos\theta \quad , \quad k_y = k_\perp \sin\theta$$
$$\vec{k}\cdot\vec{r}^{'} - \omega t^{'} = \vec{k}\cdot\vec{r} - \omega t + \beta$$
$$\beta = -\frac{k_\perp v_\perp}{\Omega}[\sin(\phi - \theta + \Omega\tau) - \sin(\phi - \theta)] + (\omega - k_\parallel v_\parallel)\tau$$

and the functions,

$$U = \frac{\partial f_0}{\partial p_\perp} + \frac{k_\parallel}{\omega}\left(v_\perp\frac{\partial f_0}{\partial p_\parallel} - v_\parallel\frac{\partial f_0}{\partial p_\perp}\right)$$
$$V = \frac{k_\perp}{\omega}\left(v_\perp\frac{\partial f_0}{\partial p_\parallel} - v_\parallel\frac{\partial f_0}{\partial p_\perp}\right)$$

is also introduced.

Substituting these equations into (A.7), the response of the distribution function to a

known EM field is written as

$$f_1(\vec{r},\vec{p},t) = -qe^{(i\vec{k}\cdot\vec{r}-i\omega t)}\int_0^\infty d\tau e^{i\beta}\Big[E_x U\cos(\phi+\Omega\tau)+E_y U\sin(\phi+\Omega\tau) \\ +E_z\Big(\frac{\partial f_0}{\partial p_\parallel}-V\cos(\phi-\theta+\Omega\tau)\Big)\Big] \tag{A.8}$$

A.1.2 Susceptibilities for arbitrary f_0

The integral (A.8) can be evaluated in order to obtain the plasma current,

$$\vec{j} = q\int d^3p\,\vec{v}f_1(\vec{r},\vec{p},t) = -\frac{i\omega}{4\pi}\hat{\chi}\cdot\vec{E}$$

which is related to the magnetic susceptibility. In order to evaluate the integral, the identities,

$$e^{iz\sin\phi} = \sum_{n=-\infty}^{\infty} e^{in\phi}J_n(z)$$
$$e^{-iz\sin(\phi+\Omega\tau)} = \sum_{n=-\infty}^{\infty} e^{-in(\phi+\Omega\tau)}J_n(z)$$

which lead to,

$$\int_0^{2\pi} d\phi e^{-iz[\sin(\phi+\Omega\tau)-\sin\phi]}\begin{pmatrix}\sin\phi\sin(\phi+\Omega\tau)\\ \sin\phi\cos(\phi+\Omega\tau)\\ \cos\phi\sin(\phi+\Omega\tau)\\ \cos\phi\cos(\phi+\Omega\tau)\\ 1\\ \sin\phi\\ \cos\phi\\ \sin(\phi+\Omega\tau)\\ \cos(\phi+\Omega\tau)\end{pmatrix} = 2\pi\sum_{n=-\infty}^{\infty} e^{-in\Omega\tau}\begin{pmatrix}(J_n')^2\\ -\frac{in}{z}J_nJ_n'\\ \frac{in}{z}J_nJ_n'\\ \frac{n^2}{z^2}J_n^2\\ J_n^2\\ -iJ_nJ_n'\\ \frac{n}{z}J_n^2\\ iJ_nJ_n'\\ \frac{n}{z}J_n^2\end{pmatrix} \tag{A.9}$$

are particularly helpful, where the argument of the Bessel functions is given by,

$$z = \frac{k_\perp v_\perp}{\omega_c} \tag{A.10}$$

Two integrals, d^3p and $d\tau$, need to be performed in order to find the susceptibility. If the EM field is weak, such that deviations on the order of a gyro-orbit does not occur, the

assumption can be made that the distribution function is constant over the gyrophase ϕ, and this integral can be performed first, as $d^3p = p_\perp dp_\perp dp_\parallel d\phi$. The dependence of τ, after making use of the identities, results in a simple integral,

$$-q\int_0^\infty d\tau \exp\left[i(\omega - k_\parallel v_\parallel - n\Omega)\tau\right] = \frac{-iq}{\omega - k_\parallel v_\parallel - n\Omega} \tag{A.11}$$

provided $\mathrm{Im}(\omega) > 0$.

Under the normalization $\int d^3p f_0(\vec{p}) = 1$, the susceptibility becomes

$$\hat{\chi} = \frac{\omega_p^2}{\omega\Omega_0}\int_0^\infty 2\pi p_\perp dp_\perp \int_{-\infty}^\infty dp_\parallel \left[\hat{e}_\parallel\hat{e}_\parallel\frac{\Omega}{\omega}\left(\frac{1}{p_\parallel}\frac{\partial f_0}{\partial p_\parallel} - \frac{1}{p_\perp}\frac{\partial f_0}{\partial p_\perp}\right)p_\parallel^2 + \sum_{n=-\infty}^{\infty}\frac{\Omega p_\perp U}{\omega - k_\parallel v_\parallel - n\Omega}\hat{T}_n\right] \tag{A.12}$$

where

$$\hat{T}_n = \begin{pmatrix} \frac{n^2J_n^2}{z^2} & \frac{inJ_nJ_n'}{z} & \frac{nJ_n^2p_\parallel}{zp_\perp} \\ -\frac{inJ_nJ_n'}{z} & (J_n')^2 & -\frac{iJ_nJ_n'p_\parallel}{p_\perp} \\ \frac{nJ_n^2p_\parallel}{zp_\perp} & \frac{iJ_nJ_n'p_\parallel}{p_\perp} & \frac{J_n^2}{p_\parallel^2}p_\perp^2 \end{pmatrix} \tag{A.13}$$

and the dielectric tensor is given by,

$$\hat{\epsilon} = \hat{1} + \hat{\chi}$$

The dispersion relation is then solved from the wave equation,

$$\hat{\varepsilon}\cdot\vec{E} + \vec{N}\times(\vec{N}\times\vec{E}) = 0 \tag{A.14}$$

or, in matrix form,

$$\begin{pmatrix} \varepsilon_{xx} - N^2\cos^2\theta & \varepsilon_{yx}^* & \varepsilon_{zx} + N^2\sin\theta\cos\theta \\ \varepsilon_{yx} & \varepsilon_{yy} - N^2 & \varepsilon_{yz}^* \\ \varepsilon_{zx} + N^2\sin\theta\cos\theta & \varepsilon_{yz} & \varepsilon_{zz} - N^2\sin^2\theta^2 \end{pmatrix}\begin{pmatrix} E_x \\ E_y \\ E_z \end{pmatrix} = 0 \tag{A.15}$$

where θ is the angle between the wave and the background magnetic field, and all ε's are functions of the refractive index $\vec{N} = \frac{\vec{k}c}{\omega}$.

A.2 Quasilinear theory

The solution to the second-order Vlasov equation (A.3) describes the slow time evolution of the equilibrium distribution function f_0. The solution to this equation describes the effect of the perturbation on the equilibrium distribution function, and is discussed in literature in detail [30, 68].

The equation can be written in vector notation as [68]

$$\frac{\partial f_0}{\partial t} = \frac{\partial}{\partial \vec{v}} \cdot \left(\hat{D} \cdot \frac{\partial f_0}{\partial \vec{v}} \right) \tag{A.16}$$

with the diffusion tensor defined by

$$\hat{D} = \lim_{V \to \infty} \sum_n \frac{q_e^2}{m_e^2} \int \frac{d^3k}{(2\pi)^3 V} \frac{i}{\omega - k_\parallel v_\parallel - n\omega_c} (\vec{a}_{n,k})^* (\vec{a}_{n,k}) \tag{A.17}$$

where

$$\begin{aligned} \vec{a}_{n,k} = \varepsilon_{n,k} & \left[\left(1 - \frac{k_\parallel}{\omega} v_\parallel \right) \hat{e}_\perp + \frac{k_\parallel}{\omega} v_\perp \hat{e}_z \right] \\ & + \epsilon_\parallel J_n \left[\hat{e}_z + \frac{n\omega_c}{\omega v_\perp} (v_\parallel \hat{e}_\perp - v_\perp \hat{e}_z) \right] \end{aligned} \tag{A.18}$$

The Bessel functions J_n have argument $z = k_\perp v_\perp / \omega_c$, and the unit vectors $\hat{e}_\perp$ and $\hat{e}_z$ have directions perpendicular and parallel to the background magnetic field, respectively. The polarization is given by

$$\varepsilon_n = \frac{1}{\sqrt{2}} \left(\epsilon_r e^{i\theta} J_{n+1} + \epsilon_\ell e^{-i\theta} J_{n-1} \right) \tag{A.19}$$

with

$$\begin{aligned} \epsilon_\ell &= \frac{E_x + iE_y}{\sqrt{2}} \\ \epsilon_r &= \frac{E_x - iE_y}{\sqrt{2}} \\ \epsilon_\parallel &= E_z \end{aligned} \tag{A.20}$$

where θ is the angle between perturbative and equilibrium fields, and E_x, E_y and E_z is the electric fields in the x, y and z directions, respectively.

The result is that the distribution function f_0 is diffused in velocity space where the resonance condition

$$\omega - k_\parallel v_\parallel - n\omega_c = 0$$

is satisfied, with the direction of diffusion determined by the polarization of the EM field and the value of the parallel refractive index $N_\parallel$ through the wavenumber $k_\parallel$.

A.3 Numerical solution to the dispersion relation

The dispersion relation is derived under the assumption that the EM fields can be separated into equilibrium and perturbative parts, and assuming that damping is weak. Under these assumptions, the dielectric tensor can be separated into hermitian and anti-hermitian parts, such that the wave equation (A.14) can be written as,

$$(\hat{\varepsilon}_h + i\hat{\varepsilon}_a - \hat{N}) \cdot \vec{E} = 0 \tag{A.21}$$

where $\hat{\varepsilon}_h$ is the hermitian and $\hat{\varepsilon}_a$ the anti-hermitian parts of the dielectric tensor.

A non-trivial solution only exists if the determinant of the matrix is zero, such that a solution is obtained by defining,

$$h(N) = |\hat{\varepsilon}_h(n) - \hat{N}| = 0 \tag{A.22}$$

and solving for N. The polarization vector can then be obtained from

$$(\hat{\varepsilon}_h(N) - \hat{N}) \cdot \vec{E} = 0 \tag{A.23}$$

and finally the absorption coefficient from

$$\alpha = \frac{\omega}{c}\vec{E}^* \cdot \hat{\varepsilon}_a \cdot \vec{E} \tag{A.24}$$

where the absorption coefficient $\alpha = 2k_i = 2\frac{\omega}{c}N_i$.

Obtaining a solution to the wave equation is not trivial, as the dielectric tensor is a function of the refractive index N, and therefore N must be determined by iterating over the solution in equation (A.22). Further, the susceptibility contains integrals of the form,

$$\int_0^\infty 2\pi p_\perp \, \mathrm{d}p_\perp \int_{-\infty}^\infty \mathrm{d}p_\parallel \frac{\Omega p_\perp U}{\omega - k_\parallel v_\parallel - n\Omega} \hat{T}_n$$

which is singular everywhere the resonance condition

$$\omega - k_{\parallel} v_{\parallel} - n\omega_c = 0 \tag{A.25}$$

is satisfied. These integrals can be solved by considering the $p_{\parallel}$ integral for a fixed value of $p_{\perp}$, and using the solution to a simple pole on a real axis [69],

$$\begin{aligned}\int_0^{\infty} f(x)dx &= \mathcal{P}\int_0^{\infty} f(x)dx + \pi i \mathrm{Res}(f(x=a)) \\ &= \lim_{r\to 0}\int_0^{a-r} f(x)dx + \pi i \mathrm{Res}(f(x=a)) + \lim_{r\to 0}\int_{a+r}^{\infty} f(x)dx\end{aligned}$$

where the pole is located at $x = a$ and $\mathcal{P}$ indicates the Cauchy Principal value.

The real part of the refractive index is then found by solving the two dimensional integral, using adaptive quadrature techniques (Appendix F), without evaluating the singularity. The singularities contribute to the imaginary part, which makes up the anti-hermitian part of the dielectric tensor, from which the damping is obtained.

A.3.1 Comparison to cold plasma dispersion relation

The solution to the hot plasma dispersion relation can be compared to the well-known cold plasma dispersion relation for perpendicular propagation in the EC range of frequencies,

$$\begin{aligned}N_X^2 &= 1 - \frac{\omega_p^2}{\omega^2}\frac{\omega^2 - \omega_p^2}{\omega^2 - \omega_p^2 - \omega_c^2} \\ N_O^2 &= 1 - \frac{\omega_p^2}{\omega^2}\end{aligned} \tag{A.26}$$

where ω_p and ω_c are the plasma and cyclotron frequencies, respectively. Two consequences are immediately evident from the cold plasma dispersion relation. Firstly, the O-mode has a density cut-off where $\omega^2 = \omega_p^2$. This is known as the high density cut-off for O-mode, beyond which the O-mode cannot propagate.

The second consequence is the existence of the upper hybrid resonance,

$$\omega^2 = \omega_p^2 + \omega_c^2 \tag{A.27}$$

where $N_X \to \infty$. It is at this point where the X-mode wave can couple to the electron Bernstein wave [37].

The refractive indices of O- and X-mode as a function of magnetic field strength are shown in figure A.1 for a 28 GHz wave, as was used on MAST. For a 28 GHz beam, the high density cut-off is $\sim 1 \times 10^{19}\,\mathrm{m}^{-3}$, so the considered density of $n_e = 5 \times 10^{18}\,\mathrm{m}^{-3}$ is below that.

The location of the UHR is evident for the X-mode around $B \approx 0.6\,\mathrm{T}$. For larger magnetic field values, the wave is known as slow X-mode, which couples to the EBW, while it is known as the fast X-mode for smaller magnetic field strengths.

The location of the ECR at $B = 1\,\mathrm{T}$ can be seen from the O-mode, where the value of the refractive index is scattered around the cold plasma dispersion value. Around the ECR, the wavelength reaches the size of the electron gyro- (Larmor) radius, and finite Larmor radius effects have to be taken into account. These effects lead to damping, and is neglected in the cold plasma dispersion relation, and the hot plasma dispersion relation must therefore be solved around the ECR [37].

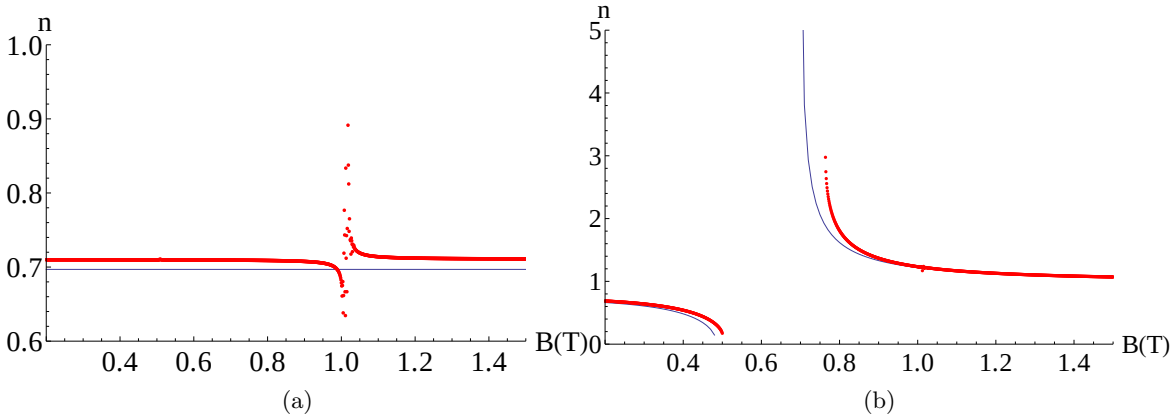

Figure A.1: Comparison of the analytical and numerically obtained refractive indices for perpendicular propagation for (a) O-mode and (b) X-mode. $n_e = 5 \times 10^{18}\,\mathrm{m}^{-3}$ and $f = 28\,\mathrm{GHz}$.

The O- and X-modes are distinguished by their polarisations. For perpendicular propagation, the O-mode is polarised along the magnetic field, $E_z = 1$, while the X-mode is a longitudinal wave, with $E_y = 1$.

For a wave propagating parallel to the magnetic field, the two solutions to the dispersion relation are known as R- and L-waves, from the direction of their circular polarisations. The direction of their polarisation is defined by $\mathrm{Im}(E_y/E_x)$, and equals 1 for the R-wave (right circular polarised) and -1 for the L-wave (left circular polarised).

Figure A.2 shows the polarisation obtained from solving the hot plasma dispersion relation for a magnetic field $B = 0.2\,\mathrm{T}$ and a 28 GHz wave. The R-mode turns into the O-mode, and L-mode turns into the X-mode as the angle changes from parallel (0°) to perpendicular (90°).

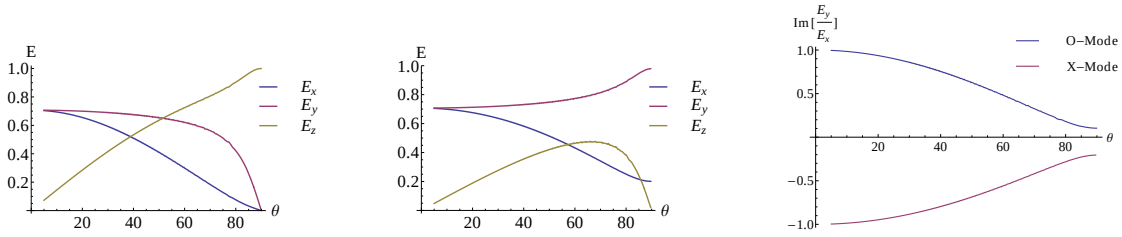

(a) (b) (c)

Figure A.2: The electric field components as a function of propagation angle for (a) O-mode, (b) X-mode, and (c) the circular polarization. $n_e = 5 \times 10^{18}\,\mathrm{m}^{-3}$, $f = 28\,\mathrm{GHz}$ and $B = 0.2\,\mathrm{T}$.

A.3.2 Absorption of electromagnetic waves

Around the ECR, damping can occur as electrons are in resonance with the wave, but this effect is not taken into account by the cold plasma dispersion relation. At this point, the wavelength reaches the size of the electron gyro- (Larmor) radius, and finite Larmor radius effects have to be taken into account. The hot plasma dispersion relation must then be solved to obtain both the refractive index and the absorption coefficient. The absorption of plasma waves has been intensively studied, and several analytical approximations exist which can be used to calculate both the refractive index and absorption coefficients [70].

A comparison of the absorption coefficient, for solving the hot plasma dispersion relation numerically and analytically, is shown in figure A.3 for a density $n_e = 10^{15}\,\mathrm{m}^{-3}$ and a 28 GHz wave around the fundamental ECR ($n = 1$). An electron must satisfy the relativistic resonance condition (A.25),

$$\frac{v^2}{c^2} = 1 - \left(\frac{\omega - k_\parallel v_\parallel}{\omega_c}\right)^2$$

in order to interact with the wave. For $k_\parallel = 0$, $\omega_c > \omega$ for real solutions to exist. This implies that, due to the relativistic mass shift, absorption can only occur at magnetic field strengths greater than 1 T for a 28 GHz wave, rather than just at $B = 1\,\mathrm{T}$, where the ECR is located. For $k_\parallel \neq 0$, the ECR is effectively shifted to $\omega - k_\parallel v_\parallel$ and absorption can occur at smaller magnetic field strengths due to the Doppler shift. The absorption for $\theta = 80°$ is shown in

figure A.3(b) to show the effect of the Doppler shift. Note that, for oblique propagation ($\theta = 80°$), the analytical damping does not take into account relativistic effects which leads to differences in the analytical and numerical damping.

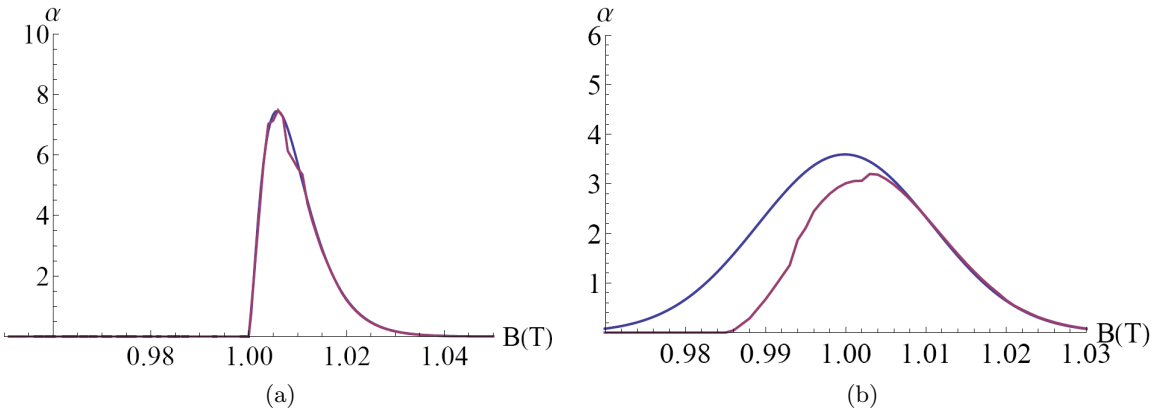

Figure A.3: Comparison of the analytical (blue) and numerical (red) absorption coefficient for the X-mode for (a) perpendicular and (b) quasi-perpendicular ($\theta = 80°$) propagation. The density $n_e = 10^{15}\,\mathrm{m}^{-3}$ and RF wave frequency $f = 28\,\mathrm{GHz}$.

A.4 Electron Bernstein waves

The solution to the refractive index of the X-mode tends to infinity at the UHR, where the cold wave couples to the electron Bernstein wave. EBWs are electrostatic short-wavelength modes, first discovered by Ira B Bernstein [34], who noticed that, for perpendicular propagation, the dispersion relation has multiple solutions, corresponding to the sum over Bessel functions, which produces the harmonics of the EBW [37].

EBWs arise from warm or hot terms in the dispersion relation, and can therefore not be described by the cold plasma dispersion relation. The electrostatic approximation is quite accurate for EBWs [35], and can be found by replacing the electric field vector $\vec{E}$ by a potential gradient $-\nabla\phi$ during the derivation of the hot plasma dispersion relation, such that the solution to the refractive index is obtained from

$$\vec{k} \cdot \hat{\epsilon} \cdot \vec{k} = 0 \tag{A.28}$$

which is known as the electrostatic approximation [30]. The electrostatic approximation is

applicable when

$$N^2 \gg |\epsilon_{ij}| \tag{A.29}$$

for all i and j. It is not valid at the UHR, where the X-wave also adopts an electrostatic character and its refractive index becomes large and the longitudinal electric field dominates. At this point, the refractive indices of the X- and EBW-modes coincide and they are coupled.

Approximate solutions to the electrostatic approximation have been studied for years [36, 38, 51], and are typically used in ray-tracing codes [37]. These approximations are calculated under certain approximations, but they lead to rather simple approximate dispersion relations for EBWs with reasonable accuracy within a wide range of plasma parameters.

A.4.1 Approximate dispersion relation for EBWs

The electrostatic approximation (A.28) leads to the general dispersion relation,

$$D = (\epsilon_{xx} N_\parallel^2 + 2\epsilon_{zx} N_\perp N_\parallel + \epsilon_{zz} N_\parallel^2)/N^2 = 0 \tag{A.30}$$

where $N_\parallel$ is the parallel component of the index of refraction along the magnetic field $\vec{B} = B_0 \hat{z}$, and $N_\perp$ is the perpendicular component of the refractive index. The assumption is made that the $\hat{x}$-direction is directed along the perpendicular wave direction, such that $k_y = 0$. This assumption can be made without any loss of generality, and implies that $k_\parallel = k_z$ and $k_\perp = k_x$.

EBWs typically experience strong damping $\mathrm{Im}(k_\perp) \sim \mathrm{Re}(k_\perp)$ which results in abrupt termination of the waves. As the anti-hermitian part of the dielectric tensor ϵ_a is distributed smoothly over the resonance region, the wave will be absorbed in a region where $\epsilon_a \ll \epsilon_h$, such that the imaginary part of the dispersion relation can be treated as a perturbation [38]. This allows

$$D = D_\mathrm{h} + iD_\mathrm{a}$$

where D_h is the real part of (A.30) and D_a is the imaginary part. The real part of the refractive index is then obtained from

$$\vec{N} \cdot \hat{\epsilon}_\mathrm{h} \cdot \vec{N} = 0$$

which can be written in the same form as equation (A.30), while the imaginary part can be

found as a perturbation to the roots of $\mathrm{Re}(N_\perp)$,

$$\mathrm{Im}N_\perp = -D_\mathrm{a} \Big/ \frac{\partial D_\mathrm{h}}{\partial N_\perp} \tag{A.31}$$

which provides good solutions to $\mathrm{Im}N_\perp$ for a wide range of plasma parameters [36].

In order to obtain solutions to the EBW, an approximate relativistic dispersion relation is solved [51]. The case of weak relativistic effects and small parallel refractive index was derived in [38], and generalized for a fully relativistic case and arbitrary value for the parallel refractive index [36]. These approximations are based on asymptotic formulae for Bessel functions with large order and argument, and, although they are rather useful, they contain a weak logarithmic singularity near the ECR. The approximate dispersion relation derived in [51] are singularity-free and much more accurate than that of [36, 38].

A.4.2 Numerical results for EBW

The dispersion for EBWs is solved using the approximate relativistic solution given in [51]. The refractive index depends on the electron density, magnetic field strength, propagation angle, and electron temperature. For MAST, $f = 28\,\mathrm{GHz}$, such that the ECR is located at $B = 1\,\mathrm{T}$. The UHR is located just below the ECR, depending on the electron density.

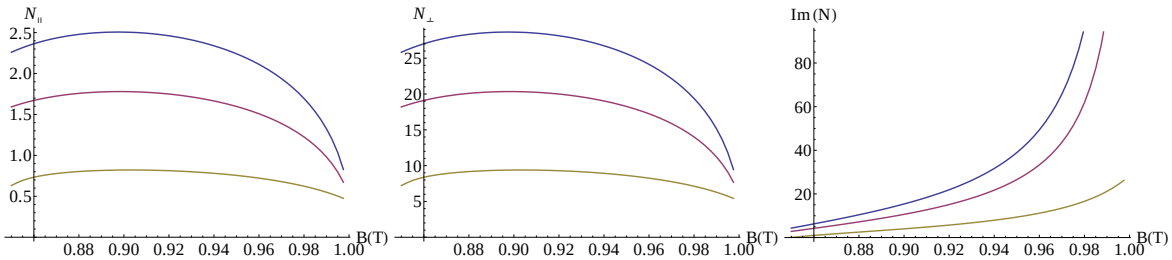

(a) (b) (c)

Figure A.4: The (a) parallel and (b) perpendicular refractive indices, and (c) the imaginary part of the refractive index as a function of magnetic field strength for $n_e = 3 \times 10^{18}\,\mathrm{m}^{-3}$ and propagation angle $\theta = 85°$, for electron temperatures $T_e = 500\,\mathrm{eV}$ (blue), $T_e = 1\,\mathrm{keV}$ (red), and $T_e = 5\,\mathrm{keV}$ (yellow).

The refractive indices, as well as the imaginary part, are shown in figure A.4 as a function of magnetic field strength for an electron density $n_e = 3 \times 10^{18}\,\mathrm{m}^{-3}$ and propagation angle

$\theta = 85°$. The damping of the EBW is strong, as

$$\alpha = 2\frac{\omega}{c}N_i$$

where N_i is the imaginary component of the refractive index. As the EBW is excited at the UHR and propagates towards the ECR from the low-field side, all the power will be absorbed before it reaches the ECR.

The applicability condition of the approximate relativistic dispersion relation for EBWs used is

$$\mu \gg \max(1, 2q), \qquad \sqrt{\mu} \gg 2q|N_\parallel|, \qquad N_\perp \gg \max(1, |N_\parallel|) \tag{A.32}$$

where $\mu = m_e c^2/T_e \sim 500/T_e(\text{keV})$ and $q = \omega/\omega_c \sim 1$. For the quasi-perpendicular case considered in figure A.4 all these conditions are satisfied. The method for calculating the imaginary part of the refractive index, by using equation (A.31), is not valid for strong damping, where $N_i > N_r$, as is the case close to the ECR. In a plasma, however, as the EBW propagates towards the ECR from the low-field side, it will be completely absorbed before $N_i > N_r$, and the method for calculating the imaginary part of the refractive index can be used.

The parallel refractive index is about one order of magnitude smaller than the perpendicular refractive index, as the angle $\theta = 85°$. The relationship between the parallel and perpendicular refractive indices are related to the magnetic field [26],

$$\tan\theta = \frac{N_\perp}{N_\parallel} \sim \frac{B_\phi}{B_\theta}$$

where B_ϕ is the toroidal magnetic field and B_θ the poloidal magnetic field. In typical start-up plasmas, the toroidal magnetic field is about two orders of magnitude greater than the poloidal field, which will lead to propagation angles very close to perpendicular.

The refractive indices, as well as the imaginary part, are shown in figure A.5 as a function of propagation angle for an electron density $n_e = 3 \times 10^{18}\,\text{m}^{-3}$ and $B = 0.95\,\text{T}$. The parallel refractive index decreases as the propagation angle tends to perpendicular, with the damping decreasing as well. Due to the large values of the parallel refractive index, EBWs are absorbed due to the Doppler shift, and as $\theta \to 90°$, the absorption due to the Doppler shift decreases, and absorption will only occur in the vicinity of the ECR, with the relativistic mass shift

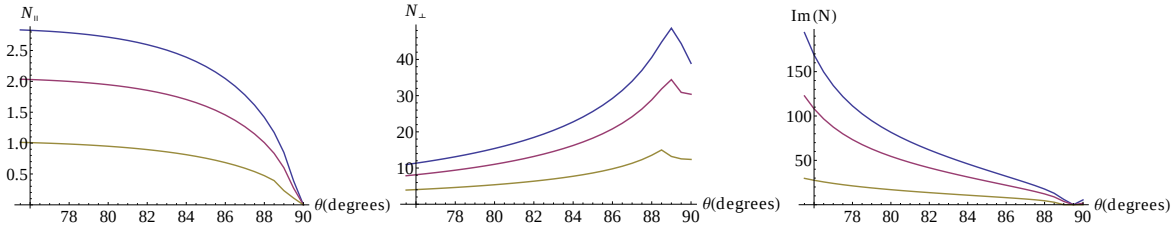

(a) (b) (c)

Figure A.5: The (a) parallel and (b) perpendicular refractive indices, and (c) the imaginary part of the refractive index as a function of propagation angle for $n_e = 3 \times 10^{18}\,\mathrm{m}^{-3}$ and $B = 0.95\,\mathrm{T}$, for electron temperatures $T_e = 500\,\mathrm{eV}$ (blue), $T_e = 1\,\mathrm{keV}$ (red), and $T_e = 5\,\mathrm{keV}$ (yellow).

exceeding the Doppler shift.

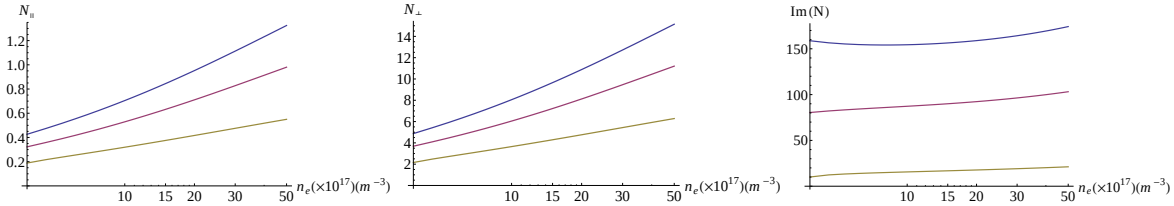

(a) (b) (c)

Figure A.6: The (a) parallel and (b) perpendicular refractive indices, and (c) the imaginary part of the refractive index as a function of electron density for $B = 0.99\,\mathrm{T}$ and propagation angle $\theta = 85°$, for electron temperatures $T_e = 500\,\mathrm{eV}$ (blue), $T_e = 1\,\mathrm{keV}$ (red), and $T_e = 5\,\mathrm{keV}$ (yellow).

The refractive indices, as well as the imaginary part, are shown in figure A.6 as a function of electron density for $B = 0.99\,\mathrm{T}$ and propagation angle $\theta = 85°$. As the electron density decreases, the UHR moves closer to the ECR, and a magnetic field $B = 0.99\,\mathrm{T}$ is chosen as the UHR can be very close to the ECR for lower densities.

The refractive indices increases for increasing density, with the ratio of perpendicular to parallel refractive indices remaining constant, as determined by the propagation angle $\theta = 85°$. The damping is very strong, but, as was discussed earlier, the EBW will be completely absorbed before $N_i > N_r$, and the method used for calculating the damping can be used.

In all cases considered here, the value of the refractive index decreases for increasing temperature, which is in agreement with other studies [37], where the absorption of the EBW for the first harmonic is proportional to $1/v_{th}^3$.

A.5 Kinetic simulations of O-X-B mode conversion

The previous sections considered plasma waves in the linear regime, where the electric and magnetic fields of the EM wave could be considered as perturbations to the equilibrium quantities. This implied that deviations of the electron orbit on the order of a gyro-orbit did not occur, and that the wave did not affect the thermal motion of electrons, or that the distribution function remained constant over a gyrophase.

This section considers kinetic simulations, where the motion of electrons can influence the particle-wave interactions. It is the result of a collaboration amongst colleagues from the University of Texas at Austin, IPP Garching and the University of York. This section outlines my contribution to the collaboration.

Electron kinetics can play a role in the excitation and propagation of EBWs, and while the linear regime has been studied extensively, the nonlinear regime, which is of interest in the context of heating and current drive, still presents a challenge [33, 37, 71, 72].

A self-consistent description of electron kinetics and wave propagation must resolve spatial and temporal scales associated with electron gyro-motion in order to correctly recover the physics relevant to EBWs. One suitable approach is the particle-in-cell (PIC) framework that uses macro-particles to simulate electrons and ions kinetically.

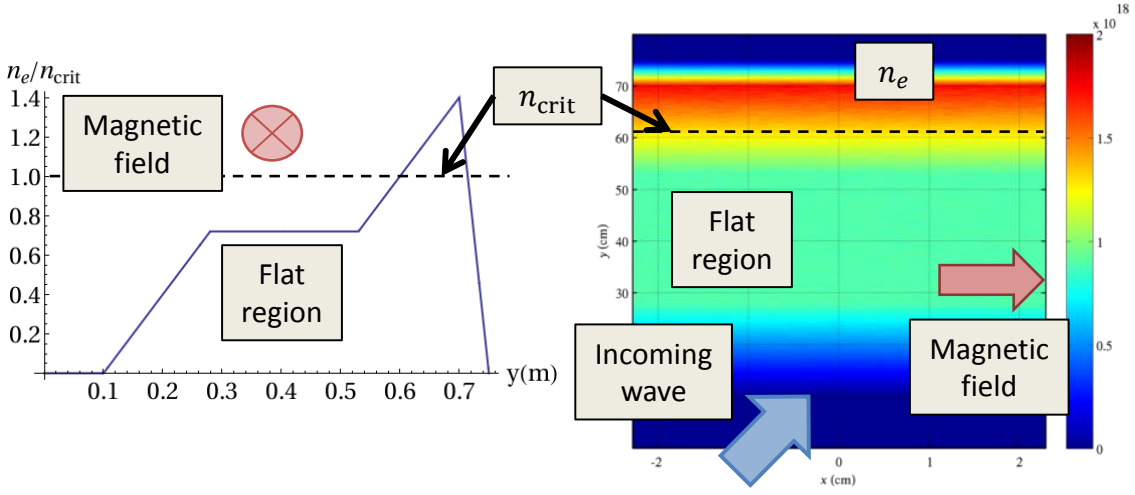

(a)

Figure A.7: Two-dimensional setup for PIC simulations of the O-X-B mode conversion.

A two-dimensional setup suitable for simulating EBW excitation is shown in figure A.7. The 2D setup allows for the wave to be launched at an angle to the magnetic field. The

magnetic field is directed in the x-direction, with the wave propagating in the $x-y$-plane at an angle of 40° to a magnetic field of 0.25 GHz.

The plasma density profile has a sharp density gradient followed by an extended flat region, and a high density region at the end. The first region contains the UHR, while the density gradient at the end goes above the cut-off density for O-mode. The density in the flat region is set at $n_e = 0.72 n_{\mathrm{crit}}$, where n_{crit} is the critical density.

The setup uses periodic boundary conditions, with the transverse size of the domain (along the x axis) set to $2\pi/k_{\parallel}$ to account for the wave periodicity.

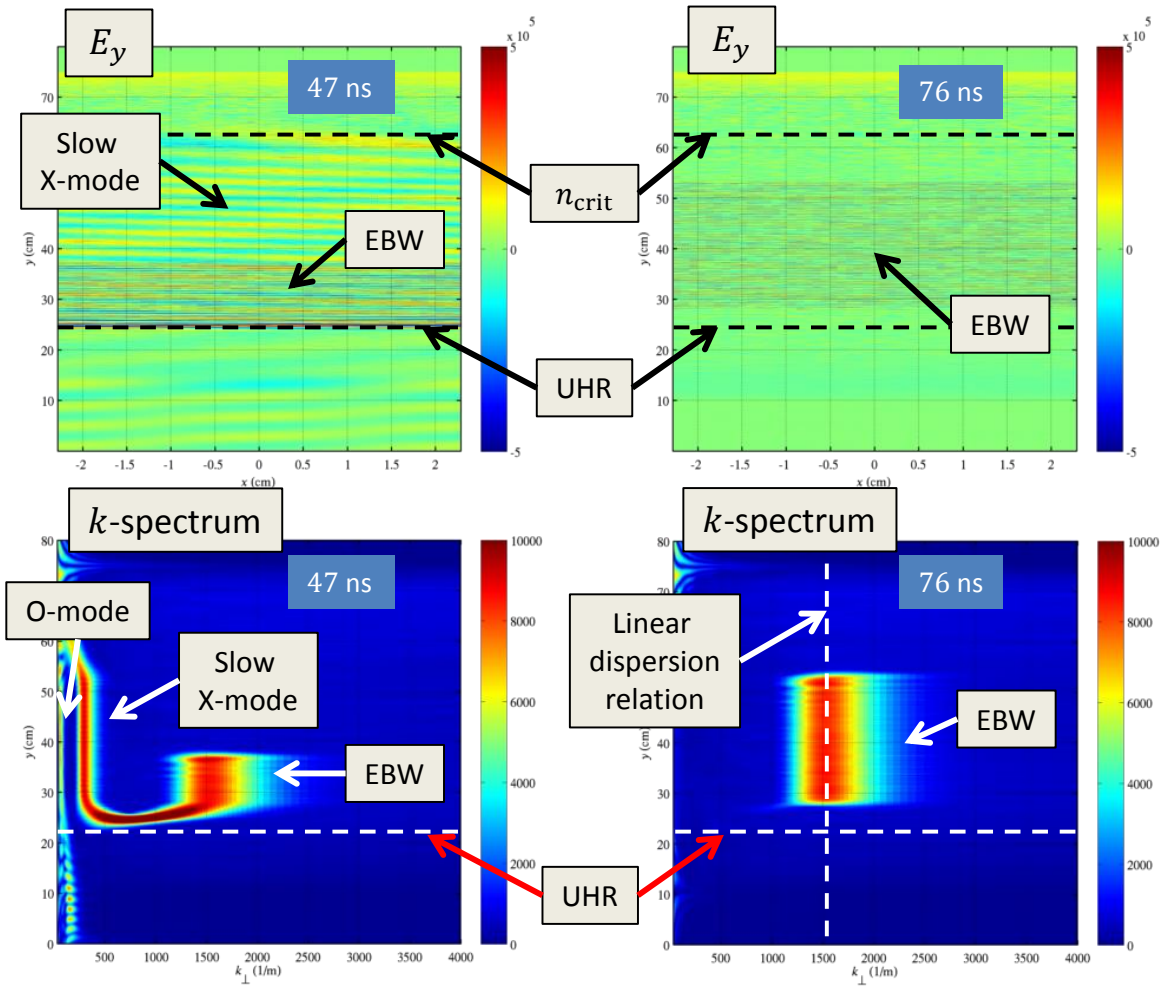

(a)

Figure A.8: Two-dimensional PIC simulation of the O-X-B mode conversion in a linear regime.

A plane wave with a maximum amplitude of 5×10^4 V/m is launched from the lower boundary at 40°. Its frequency is 10 GHz and its electric field is polarised in the plane of

the simulation (O-mode). The electron temperature is 1 keV, while the ions are treated as immobile.

The electric field E_y and corresponding k_y-spectra are shown as functions of y in figure A.8 at two different times. The left panels clearly illustrate the O-X-B conversion, with all three modes (O-mode, slow X-mode, and EBW) being clearly visible in the k-spectrum of the flat density region. The right panel demonstrates that the EBW propagates towards the high density region without appreciable energy loss. The vertical dashed line in the lower-right panel is k_y for EBW in the flat density region according to the linear dispersion relation. The simulated k_y for the EBW agrees well with the linear dispersion relation.

Further studies were conducted in the nonlinear regime where the wave amplitude is sufficiently high to appreciably affect the thermal electron motion. It was found that the ion mobility has a profound effect on the wave electric field structure in the nonlinear regime. Simulations show that high-amplitude short-scale oscillations of the longitudinal electric field are excited in the region below the high-density cut-off prior to the arrival of the EBW. These oscillations are not observed with immobile ions, and have been identified as lower-hybrid (LH) oscillations [72].

The study of mode conversion is an important aspect for non-inductive start-up as plasmas are typically over-dense and inaccessible to electromagnetic modes. The use of electrostatic waves, such as EBWs, are therefore important for heating and current drive. The mode conversion process in the linear regime has been studied in detail [33, 37], but still remains a challenge in the nonlinear regime. Simulations of the O-X-B mode conversion has been performed using a PIC code, to illustrate that the linear dispersion relation is recovered in the linear regime, while the importance of the ion mobility has been discussed in the nonlinear regime [71, 72].

For experiments conducted on MAST, nonlinear effects are not thought to be important, as the injected power remained low, while the ions remained cold. The hot plasma dispersion relation, calculated in the linear regime, is therefore sufficient for the study done in this thesis.

Appendix B

Toroidal Current Profile

The magnetic field consists of two parts: the vacuum magnetic field created by the poloidal field coils, and a magnetic field created by the plasma current. In order to find the magnetic field created by the plasma current, a mathematical expression for the current density profile is needed.

The simplest approach is to assume a parabolic profile for the current density j_ϕ,

$$j_\phi(R,Z) = j_0\left[1-\rho(R,Z)^2\right]^\alpha \tag{B.1}$$

for $\rho(R,Z) \leq 1$, where the peak current j_0 is calculated through the integral,

$$I_P = \int j_\phi \mathrm{d}R\,\mathrm{d}Z \tag{B.2}$$

to ensure the total current obtained from the density profile is consistent with the total current I_P.

The function $\rho(R,Z)$ is given by [12],

$$\rho(R,Z) = \frac{\sqrt{\left(\frac{R-R_p}{a}+\frac{\delta}{b^2}(Z-Z_p)^2\right)^2+\frac{1-\sigma^2}{b^2}(Z-Z_p)^2}+\sigma\left(\frac{R-R_p}{a}+\frac{\delta}{b^2}(Z-Z_p)^2\right)}{1-\sigma^2} \tag{B.3}$$

where

$$\sigma = \frac{R_p - R_0}{a}$$

is the radial shift of the current peak, a is the radial width, b is the vertical height, and δ is the triangularity. The current peak is located at (R_p, Z_p), with the centre of the profile at

(R_0, Z_0). A schematic of the profile is shown in figure B.1.

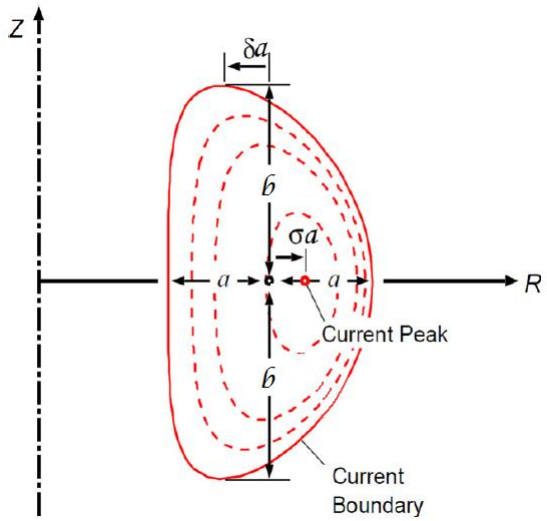

Figure B.1: Schematic of the current density profile.

In order to calculate the magnetic field produced by the current profile, a mesh grid of $N_R \times N_Z$ infinitely thin wires are created in the poloidal plane. The magnetic field created by a infinitely thin wire wrapped around a torus is known (see Appendix C), such that the magnetic field generated by each wire can be calculated at any point on the poloidal plane. The current in each wire is distributed according to j_ϕ.

A second mesh grid, shifted half a square up and to the left, is then created, with the magnetic field calculated at each of these points. An interpolation of these points gives the final magnetic field[1].

Consider, for example, the current density profile with parameters,

$$R_0 = 0.6 \quad , \quad Z_0 = 0 \quad , \quad R_p = 0.7 \quad , \quad a = 0.4 \quad , \quad b = 1 \quad , \quad \delta = 0.7 \quad , \quad \alpha = 1 \quad \text{(B.4)}$$

shown in figure B.2.

Consider a constant vacuum poloidal field with $B_Z = -10$ mT and no radial component, and a current density profile (B.4) with a plasma current $I_P = 20$ kA. The magnetic field created by the vacuum poloidal field, the current density profile, and the combined magnetic field is shown in figure B.2.

The magnetic field created by the current alone is centred at (R_0, Z_0), just like the current density profile, but adding the vacuum poloidal field to this shifts the centre of the magnetic

[1]The interpolation scheme is based on bilinear interpolation [73]

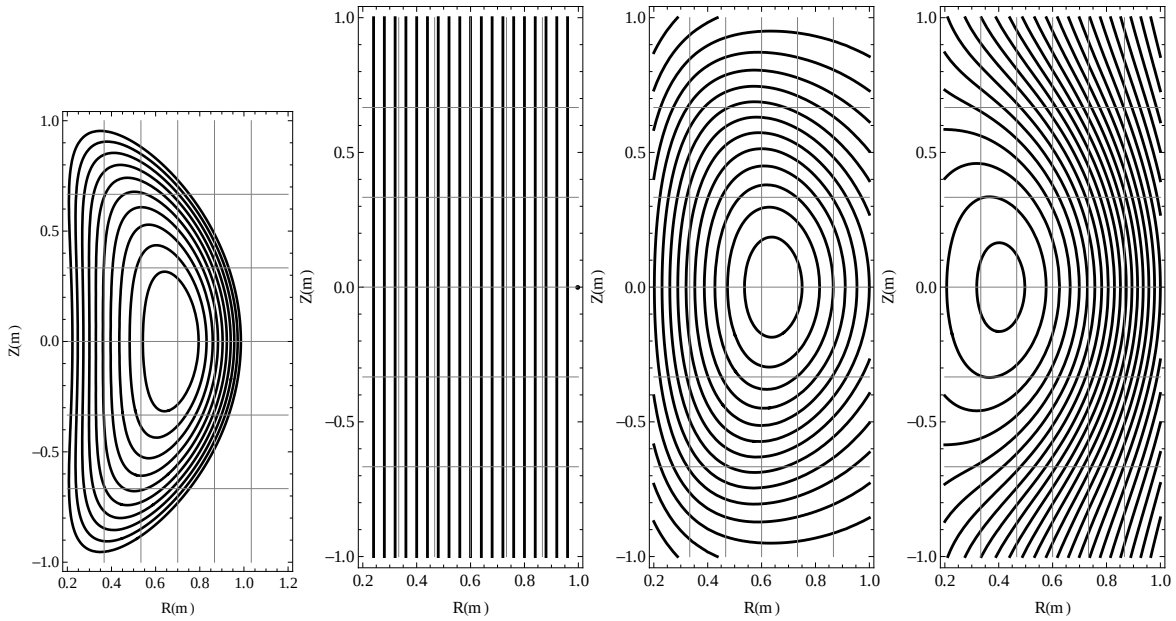

Figure B.2: (a) The current density profile (B.4), (b) the vacuum magnetic field, (c) the magnetic field created by the current density profile, and (d) the combined magnetic field.

field to the inboard side. This is due to the fact that, in this example, the vertical field created by the plasma current is positive on the inboard side, while the vacuum poloidal field is negative, which leads to a shift of the centre towards the inboard side.

Appendix C

Off-Axis Magnetic Field of a Current Loop

In the geometry of a tokamak, it is often necessary to calculate the off-axis magnetic field of a current loop. Since the plasma current and poloidal field coils form current loops, the magnetic field generated by these current loops must be calculated at any point in space. The solution for these magnetic fields on the axis of the current loop is easy to derive, but determining the off-axis magnetic field is a bit more difficult [74].

Consider a current loop of radius a in the $r-\phi$ plane (figure C.1). The vector potential for such a loop is given by

$$\vec{A}(r,z) = \frac{\mu_0 I}{4\pi} \int \frac{d\vec{\ell}}{x} \tag{C.1}$$

where x is the distance from an infinitesimally small current element to the point (r,z). Due to cylindrical symmetry, the angle ϕ will have no impact on the vector potential, and will only be a coordinate eventually integrated over. After determining the vector potential, the magnetic field can be calculated according to

$$\vec{B} = \vec{\nabla} \times \vec{A} \tag{C.2}$$

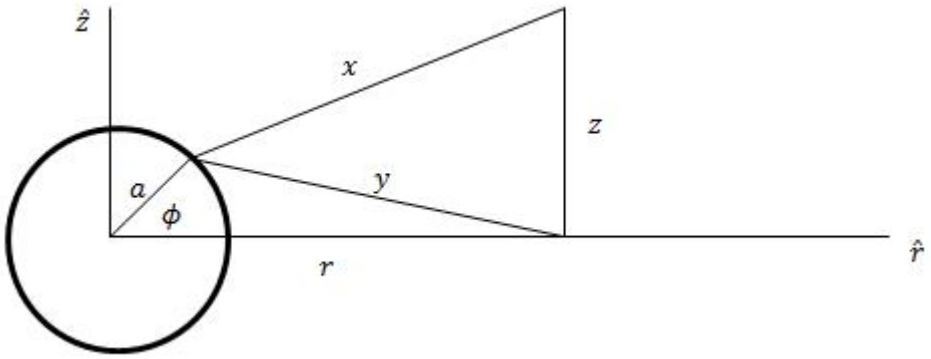

Figure C.1: The geometry employed to calculate the magnetic field generated by a current loop.

First consider the vector potential at an angle $\phi = 0$.

$$\begin{aligned}\vec{A}(\phi=0) &= \frac{\mu_0 I}{4\pi}\int_0^{2\pi}\frac{a\,d\phi\,\hat{\phi}}{(r^2+a^2-2ar\cos\phi+z^2)^{1/2}} \\ &= \frac{\mu_0 I}{4\pi}\int_0^{2\pi}\frac{a(-\hat{i}\sin\phi+\hat{j}\cos\phi)d\phi}{(r^2+a^2-2ar\cos\phi+z^2)^{1/2}} \\ &= A_i(\phi=0)\hat{i}+A_j(\phi=0)\hat{j}\end{aligned}$$

where $\hat{i}$ and $\hat{j}$ are the normal unit vectors in the Cartesian x and y directions. The vector potential along these directions are evaluated to give

$$A_i(\phi=0)=0$$

and

$$\begin{aligned}A_j(\phi=0) &= \frac{\mu_0 I}{4\pi}\int_0^{2\pi}\frac{a\,\cos\phi\,d\phi}{(r^2+a^2-2ar\cos\phi+z^2)^{1/2}} \\ &= \left(\frac{\mu_0 I}{k\pi}\sqrt{\frac{a}{r}}E_1(k)-\frac{\mu_0 I}{k\pi}\sqrt{\frac{a}{r}}E_2(k)-\frac{\mu_0 Ik}{2\pi}\sqrt{\frac{a}{r}}E_1(k)\right)\end{aligned}$$

where $E_1(k)$ and $E_2(k)$ are the complete elliptic integrals of the first and second kind, respectively, given by

$$\begin{aligned}E_1(k) &= \int_0^{\pi/2}\frac{d\theta}{\sqrt{1-k^2\sin^2\theta}} \\ E_2(k) &= \int_0^{\pi/2}\sqrt{1-k^2\sin^2\theta}\,d\theta\end{aligned}$$

and

$$k^2 = \frac{4ra}{z^2 + (a+r)^2} \tag{C.3}$$

If $\phi = 0$, $\hat{j} = \hat{\phi}$, but due to toroidal symmetry, this solution is valid for all values of ϕ, so

$$\vec{A} = \frac{\mu_0 I\sqrt{a}}{2\pi}\left(\frac{2}{k\sqrt{r}}E_1(k) - \frac{2}{k\sqrt{r}}E_2(k) - \frac{k}{\sqrt{r}}E_1(k)\right)\hat{\phi} \tag{C.4}$$

The magnetic field is calculated from equation (C.2) to obtain

$$\vec{B} = \frac{1}{r}\frac{\partial(rA_\phi)}{\partial r}\hat{z} - \frac{1}{r}\frac{\partial(rA_\phi)}{\partial z}\hat{r}$$

and therefore the magnetic field at position (r, z) of a current loop of radius a located at $z = 0$ is given by

$$\begin{aligned} B_z &= \frac{\mu_0 I}{2\pi\sqrt{z^2 + (a+r)^2}}\left(\frac{a^2 - z^2 - r^2}{z^2 + (r-a)^2}E_2(k) + E_1(k)\right) \\ B_r &= \frac{\mu_0 z I}{2\pi r\sqrt{z^2 + (a+r)^2}}\left(\frac{a^2 + z^2 + r^2}{z^2 + (r-a)^2}E_2(k) - E_1(k)\right) \end{aligned} \tag{C.5}$$

For a current loop placed at a vertical position z_i, the value of z is replaced by $z - z_i$.

Appendix D

Particle motion

Charged particles in a tokamak experiences a force due to the electric and magnetic fields present. In non-inductive start-up there is no external electric field, as the central solenoid is not used, and any electric field present, apart from the EM field of the injected RF beam, is created by charge separation. Assuming quasi-neutrality, only an external magnetic field will be present, such that charged particles experience the Lorentz force,

$$m\frac{\mathrm{d}^2\vec{r}}{\mathrm{d}t^2} = q\left(\frac{\mathrm{d}\vec{r}}{\mathrm{d}t} \times \vec{B}\right) \tag{D.1}$$

where m is the mass, q the charge, $\vec{B}$ the magnetic field and $\vec{r}$ the position vector with $\vec{v} = \frac{\mathrm{d}\vec{r}}{\mathrm{d}t}$ and $\vec{a} = \frac{\mathrm{d}^2\vec{r}}{\mathrm{d}t^2}$ the velocity and acceleration, respectively.

The particle will gyrate around the magnetic field lines due to its velocity perpendicular to the magnetic field $v_\perp$, while streaming along the magnetic field line due to its velocity parallel to the magnetic field $v_\parallel$.

If the gyration around the magnetic field is shorter than any other time scale involved, it can be neglected, and only the motion parallel and perpendicular to the magnetic field lines remains. This leads to the guiding centre approximation [2].

D.1 Guiding Centre Approximation

Consider the simple case where a homogeneous magnetic field lies along the $\hat{z}$-axis,

$$\vec{B} = B_0\hat{z} \tag{D.2}$$

such that the velocity is given by

$$\vec{v} = v_{\perp,x}\hat{x} + v_{\perp,y}\hat{y} + v_{\parallel}\hat{z} \tag{D.3}$$

where $v_{\parallel}$ is always in the same direction as $\vec{B}$.

In the cases of interest, the toroidal field B_ϕ is typically around two orders of magnitude greater than the poloidal field, such that $v_{\parallel}$ will always be in the direction of B_ϕ.

The perpendicular velocity describes the gyration around the magnetic field, while the parallel component describes the free streaming along the magnetic field line. The guiding centre equation of motion can then be written as,

$$\frac{\mathrm{d}\vec{r}_{gc}}{\mathrm{d}t} = \frac{\vec{B}}{B_0} v_{\parallel} \tag{D.4}$$

In reality, the magnetic field is not homogeneous nor along a straight line. This introduces two types of orbital drifts [47]:

∇B **Drift:** In a magnetic field with a transverse gradient the particle has a smaller Larmor radius on the part of its orbit with a stronger magnetic field, which leads to a drift perpendicular to both the magnetic field and its gradient,

$$\vec{v}_{\nabla B} = \frac{1}{2} r_L \frac{\vec{B} \times \nabla \vec{B}}{B^2} v_{\perp} \tag{D.5}$$

where the Larmor radius $r_L = \frac{m v_{\perp}}{qB}$. The gradient ($\nabla \vec{B}$) points in the direction of greatest increase ($\hat{R}$). The drift is in opposite directions for ions and electrons due to its dependence on particle charge.

Curvature Drift: If the magnetic field line is curved, the particle will experience a drift perpendicular to the plane in which the curvature lies,

$$\vec{v}_{\mathrm{curv}} = \frac{m}{q} \frac{v_{\parallel}^2}{B^2} \frac{\vec{R}_c \times \vec{B}}{R_c^2} \tag{D.6}$$

where $\vec{R}_c$ is the radius of curvature, directed towards the centre of the circle.

In a steady-state fusion plasma with $\vec{E} = 0$, an inhomogeneous, curved magnetic field produces these two guiding centre drifts. By assuming steady-state, the magnetic field

becomes effectively a vacuum magnetic field and a simplifying relationship exists between $\vec{v}_{\nabla B}$ and $\vec{v}_{\text{curv}}$ [47].

Using the identity,

$$\nabla(\vec{B}\cdot\vec{B}) = 2\vec{B}\times(\nabla\times\vec{B}) + 2\vec{B}\cdot\nabla\vec{B}$$

and the fact that $\nabla\times\vec{B}=0$ for a vacuum magnetic field, one can obtain,

$$\vec{B}\times\nabla B = -B\frac{\vec{B}\times\vec{R}_c}{R_c^2}$$

and the combined drift becomes, for electrons ($q_e=-e$),

$$\vec{v}_{\nabla B}+\vec{v}_{\text{curv}} = -\frac{m_e}{e}\left(\frac{v_\perp^2}{2}+v_\parallel^2\right)\frac{\vec{R}_c\times\vec{B}}{B^2R_c^2} \tag{D.7}$$

and each drift is in the same direction.

In a tokamak it is assumed that the toroidal magnetic field is much greater than the poloidal field. This leads to the assumption that the drift due to the poloidal field gradient and curvature can be neglected, even though the poloidal field tilts the vertical drift [15].

Assuming axisymmetry, the complete guiding centre equations are then given by,

$$\begin{aligned}
\frac{\mathrm{d}Z}{\mathrm{d}t} &= \frac{B_Z}{B}v_\parallel - \frac{m_e}{eBR}\left(\frac{v_\perp^2}{2}+v_\parallel^2\right)\\
\frac{\mathrm{d}R}{\mathrm{d}t} &= \frac{B_R}{B}v_\parallel\\
\frac{\mathrm{d}\phi}{\mathrm{d}t} &= \frac{B_\phi}{B}\frac{v_\parallel}{R}
\end{aligned} \tag{D.8}$$

where $q_e=-e$.

Note that $v_\parallel$ should always be in the same direction as $+\hat{\phi}$, and therefore $v_\parallel \parallel B_\phi$. If the direction of B_ϕ changes, then, in order to still have a right-handed coordinate system[1], the direction of both $+\hat{\phi}$ and $+\hat{z}$ changes. The guiding centre equation is therefore modified,

$$\frac{\mathrm{d}Z}{\mathrm{d}t} = \frac{B_Z}{B}v_\parallel - \text{sign}(B_\phi)\frac{m_e}{eBR}\left(\frac{v_\perp^2}{2}+v_\parallel^2\right) \tag{D.9}$$

such that $v_\parallel \parallel B_\phi$ always.

[1] A right-handed cylindrical coordinate system (R,ϕ,Z) corresponds to using the (index,middle,thumb) fingers. If the direction of $+\phi$ reverses, then so does the direction of $+Z$.

D.2 Conserved Quantities

There are three conserved quantities, the magnetic moment [2],

$$\mu = \frac{m v_\perp^2}{2B} \tag{D.10}$$

the angular momentum [75],

$$p_\phi = m\, r\, v_\parallel + q\, r\, A_\phi \tag{D.11}$$

and the magnitude of the velocity,

$$W = v_\parallel^2 + v_\perp^2 \tag{D.12}$$

D.3 Magnetic Mirror

The conservation of magnetic moment leads to a very important consequence: the confinement of particles in an effect known as the magnetic mirror. As a particle moves from a weak field region to a strong field region, and B increases, there must be an increase in $v_\perp$ in order for μ to remain constant. Since the total kinetic energy must also be conserved, the parallel velocity $v_\parallel$ must decrease [32].

If a particle can move to a region of sufficiently high B, its parallel velocity will tend to zero, and the particle will eventually be reflected back to a region of weak B, essentially trapping the particle between regions of high magnetic field.

Unfortunately this trap is not perfect, as particles with sufficiently large $v_\parallel$ may never reach a region of strong enough B to be reflected.

Appendix E

Coulomb collisions

The aim of this section is to derive the collision frequency ν, the number of collisions taking place per second. The derivation of collision frequency is done in many standard plasma physics textbooks [2, 47, 76], and only the main points are repeated here.

E.1 Binary Collisions between Charged Particles

Consider two particles interacting with each other with some force $\vec{F}$. Their equations of motion can be written as

$$m_1 \frac{d^2\vec{r}_1}{dt^2} = \vec{F}_{12} \quad ; \quad m_2 \frac{d^2\vec{r}_2}{dt^2} = \vec{F}_{21}$$

where $\vec{F}_{12}$ is the force on particle 1 due to particle 2, and $\vec{F}_{21}$ is the force on particle 2 due to particle 1. From Newton's 3rd law, $\vec{F}_{12} = -\vec{F}_{21}$, and combining gives,

$$m_r \frac{d^2\vec{r}}{dt^2} = \vec{F}_{12}(\vec{r})$$

where

$$m_r = \frac{m_1 m_2}{m_1 + m_2} \tag{E.1}$$

is the reduced mass, and $\vec{r} = \vec{r}_1 - \vec{r}_2$. This equation describes the centre-of-mass motion of the two particle system, and needs to be solved for the Coulomb force,

$$\vec{F}_{12} = \frac{q_1 q_2}{4\pi\epsilon_0} \frac{\vec{r}}{r^3} \tag{E.2}$$

where q_i is the charge of particle i.

The scenario for such a binary collision is illustrated in figure E.1. The goal is to calculate the scattering angle χ of a particle's trajectory resulting from a Coulomb collision as a function of its velocity $\vec{v}_1$ and impact parameter b.

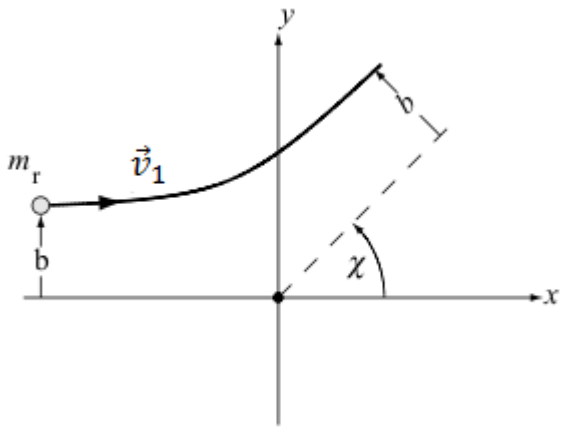

Figure E.1: Geometry of the collision orbit, with impact parameter b and scattering angle χ. Image adapted from [47].

The scattering angle $\chi = \chi(v_1, b)$ is given by

$$\cot\frac{\chi}{2} = \frac{b}{b_{90}} = \frac{4\pi\epsilon_0}{q_1 q_2} m_r\, v_1^2\, b \tag{E.3}$$

where the '90° impact parameter', which is obtained if a particle emerges at 90° to its initial direction, when $b = b_{90}$, is given by

$$b_{90} = \frac{q_1 q_2}{4\pi\epsilon_0}\frac{1}{m_r v_1^2} \tag{E.4}$$

A small impact parameter, which corresponds to a very close encounter, leads to a very large scattering angle, whereas a large impact parameter, corresponding to a distant collision, leads to small angle scattering. Of course, when $b = b_{90}$, the deflection angle is 90°. Also note that, as the particle velocity increases, the scattering angle decreases, as the particle spends less time in the vicinity of the centre of mass, corresponding to a weaker collision.

E.2 Collision Frequencies

The relaxation time τ, or collision frequency $\nu = 1/\tau$, characterizes the relaxation process of an electron with momentum $\vec{p}$ interacting with a stationary plasma of electrons or ions. Naturally, the electron will collide with the plasma, until it loses its directed momentum by colliding with the ions, or its energy by colliding with the electrons, and becomes part of the background plasma.

The collision frequency provides a good estimate of how long it takes for an initial distribution to relax to a Maxwellian, and is therefore of particular interest.

E.2.1 Test Particle Colliding with Stationary Targets

For a particle moving through a background of scatterers with density n_2, there are two types of collisions that can take place, resulting in either the loss of energy or a loss in momentum through a scattering in angle.

The total energy lost is found by summing the loss per collision over all collisions, which involves integrals over the impact parameter,

$$\int_0^\infty \left(\frac{b_{90}}{b}\right)^2 b \, \mathrm{d}b$$

which diverges logarithmically as $b \to \infty$.

The weak $1/r$ dependence of the Coulomb potential implies that its effect extends over a long range, however, the test particle will feel a much smaller potential from any target particle further than some critical distance away. This is because, in a plasma, the test particle is shielded from the electric field of all target particles further away than a Debye length λ_D. The consequence is that the integral can be performed with limits (b_{90}, λ_D), which leads to the introduction of the Coulomb logarithm,

$$\ln\Lambda = \ln\left(\frac{\lambda_D}{b_{90}}\right) = \ln\left[\left(\frac{\epsilon_0 T_e}{n_2 e^2}\right)^{1/2} \Big/ \left(\frac{q_1 q_2}{4\pi\epsilon_0 m_r v_1^2}\right)\right] \tag{E.5}$$

which has typical values $\ln\Lambda = 15 - 25$, as shown in figure E.2.

The resultant collision frequencies are obtained, for electron-electron collisions,

$$\nu_{Kee} = n_e \frac{e^4}{(4\pi\epsilon_0)^2} \frac{8\pi}{m_e^2 v_e^3} \ln\Lambda = \nu_{pee} \tag{E.6}$$

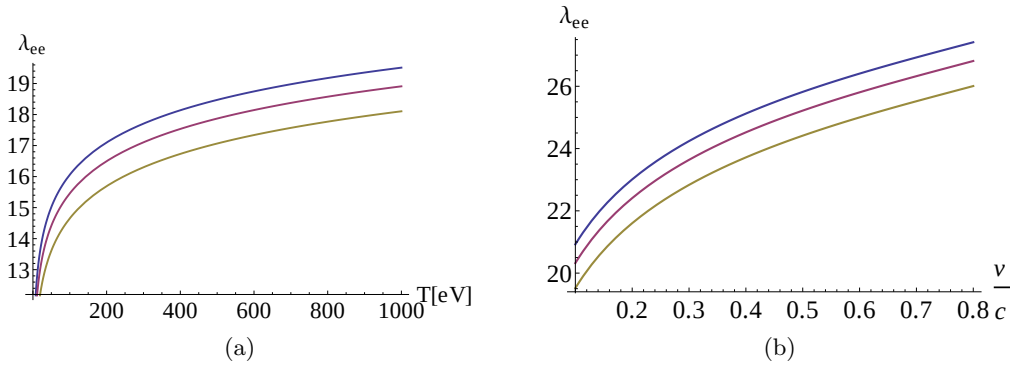

(a) (b)

Figure E.2: The value of the Coulomb logarithm $\ln\Lambda$ as a function of (a) temperature and (b) projectile velocity for electron densities $n_e = 3\times10^{17}\,\mathrm{m}^{-3}$ (blue), $n_e = 1\times10^{18}\,\mathrm{m}^{-3}$ (red) and $n_e = 5\times10^{18}\,\mathrm{m}^{-3}$ (yellow).

and for electron-ion collisions,

$$\nu_{Kei} = n_i \frac{Z^2 e^4}{(4\pi\epsilon_0)^2}\frac{8\pi}{m_e m_i v_e^3}\ln\Lambda \simeq \frac{Z^2 m_e}{m_i}\nu_{pee} \tag{E.7}$$

where Z is the ion charge number. Note that the electron-ion collision frequency is a factor m_e/m_i larger than the electron-electron collision frequency, such that electron-ion collisions occur on a shorter time scale than electron-electron collisions.

E.2.2 Thermal Distribution Collisions

The collision frequencies of equations (E.6, E.7) are calculated for stationary targets and single velocity projectiles, but in general both the targets and projectiles have some velocity distribution.

In order to calculate the collision frequency for electron-electron collisions, it is necessary to account for both moving targets and projectiles. This is done by using the average rate of momentum transfer per unit volume,

$$-\frac{d\vec{p}}{dt} = \int\int \vec{v}_r \frac{m_1 m_2}{m_1+m_2} v_r\, 4\pi b_{90}^2\, \ln\Lambda\, f_1 f_2\, \mathrm{d}^3v_1 \mathrm{d}^3v_2$$

where the projectile distribution f_1 collides with a target distribution f_2.

Assuming two Maxwellian distributions at different temperatures, the solution is given by [64],

$$\nu_{ee} = \frac{8}{3\pi^{1/2}} n_e \left(\frac{e^2}{4\pi\epsilon_0}\right)^2 \frac{4\pi}{m_e^{1/2}(2T_1+2T_2)^{3/2}}\ln\Lambda_e \tag{E.8}$$

with the collision time shown in figure E.3(a). Collision times for electron-electron collisions are of the order of ms for typical MAST parameters - short enough to be of importance for thermal electrons.

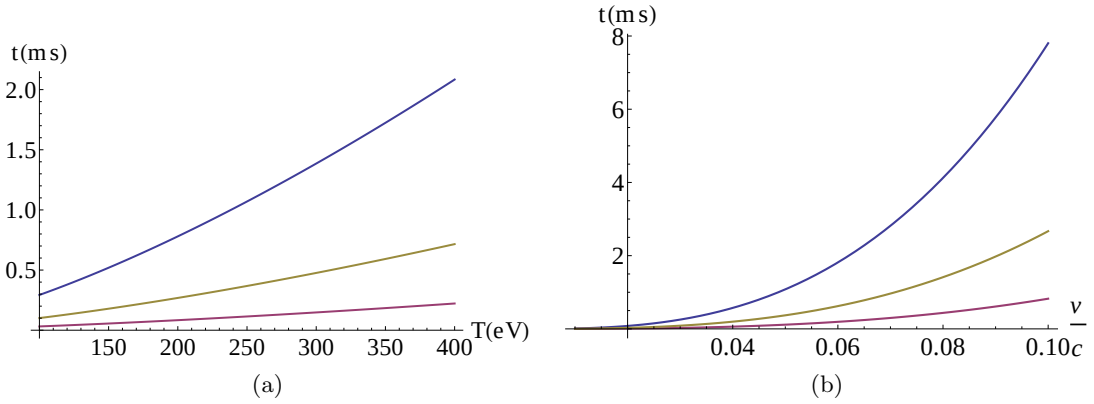

Figure E.3: (a) The collision time for electron-electron collisions of two Maxwellian distributions of the same temperature, and (b) for an energetic electron colliding with a much colder distribution, as a function of projectile velocity. In both plots, the collision time is shown for electron densities $n_e = 3\times10^{17}\,\mathrm{m}^{-3}$ (blue), $n_e = 1\times10^{18}\,\mathrm{m}^{-3}$ (yellow) and $n_e = 5\times10^{18}\,\mathrm{m}^{-3}$ (red).

The collision frequency of an energetic electron colliding with a background Maxwellian distribution of thermal velocity $\vec{v}_2$ is calculated by assuming

$$f_1 = n_1\delta(\vec{v} - \vec{v}_1)$$

for the energetic electron distribution, to obtain [77],

$$\nu_{ee} = 2n_e\left(\frac{e^2}{4\pi\epsilon_0}\right)^2\frac{4\pi}{m_e^2v^3}\ln\Lambda_e \tag{E.9}$$

where v is the velocity of the projectile. This expression is the same as an electron colliding with a stationary background (E.6), because the assumption is made that $v_1 \gg v_2$. The collision time for an energetic electron is plotted in figure E.3(b), and shows that, even for relatively small velocities, the collision time becomes very long. Collisions are therefore not expected to be that important during start-up, as the majority of the plasma current is carried by energetic electrons which undergo very few collisions.

Appendix F

Multidimensional adaptive quadrature strategies

The dispersion relation (Appendix A) contains two dimensional integrals with singularities that can only be solved numerically. In order to do this, adaptive quadrature strategies are used.

F.1 Adaptive quadrature in one dimension

Consider the integral,

$$I = \int_a^b f(x)\,\mathrm{d}x \tag{F.1}$$

for which I is the exact solution. The idea behind adaptive quadrature is to obtain a numerical estimate to the integral,

$$Q \approx \int_a^b f(x)\,\mathrm{d}x$$

and compare this to the exact solution,

$$\varepsilon \approx |Q - I|$$

where ε is the error of the numerical estimate. If the error $\varepsilon > \tau$, where τ is some predetermined accuracy, the interval is split into two. The numerical approximation to the integral on each interval is then calculated, and compared to the exact solution on that interval; if

the error is greater than $\tau/2$, the interval is divided again, and this process is repeated until the numerical approximation to the integral is within error of the exact solution. The approximations on each interval is then simply added up to obtain the estimate to the integral on the whole interval, and, as the approximate answer is within error on each subregion, the total estimate will be within error.

This method is ideal for integrals that contain singularities, as the value of $f(x)$ can fluctuate around the singularity, and a lot of subdivisions will be necessary in order to accurately resolve the singularity. In practice, however, the exact solution to the integral is not known, and other methods of determining the accuracy of the numerical approximation are necessary.

One such method is by using the Composite Simpson's Rule to determine the integral. On a given interval $[a, b]$, the numerical estimates can be calculated,

$$S_4 = \frac{h}{3}\Big[f(x_1) + 4f(x_2) + 2f(x_3) + 4f(x_4) + f(x_5)\Big]$$
$$S_2 = \frac{2h}{3}\Big[f(x_1) + 4f(x_3) + f(x_5)\Big]$$

with the error estimate given by,

$$\varepsilon > \frac{1}{15}|S_4 - S_2|$$

and the exact solution of the integral is not needed.

F.2 Adaptive quadrature in two dimensions

Consider the integral,

$$I = \int_{C_2} f(x, y)\,\mathrm{d}x\,\mathrm{d}y$$

where I is the exact solution of the integral, and C_2 is the integration domain.

Stroud [78] produced well-known formulas for solving integrals approximately in multiple dimensions. In two dimensions, the integral is approximated as,

$$Q[f] = \int_\Omega f(x, y)dx\,dy = \sum_{i=1}^{4} w_i\, f(x_i, y_i)$$

where the weights w_i and knots (x_i, y_i) are given for order 4 (for a square integration domain centred at $(0, 0)$ with size 1),

i	x_i	y_i	w_i
1	$-1/\sqrt{3}$	$-1/\sqrt{3}$	1
2	$1/\sqrt{3}$	$-1/\sqrt{3}$	1
3	$-1/\sqrt{3}$	$1/\sqrt{3}$	1
4	$1/\sqrt{3}$	$1/\sqrt{3}$	1

and for order 9,

i	x_i	y_i	w_i
1	0	0	64/81
2	$-\sqrt{0.6}$	$-\sqrt{0.6}$	25/81
3	$\sqrt{0.6}$	$1-\sqrt{0.6}$	25/81
4	$-\sqrt{0.6}$	$\sqrt{0.6}$	25/81
5	$\sqrt{0.6}$	$\sqrt{0.6}$	25/81
6	0	$-\sqrt{0.6}$	40/81
7	$-\sqrt{0.6}$	0	40/81
8	$\sqrt{0.6}$	0	40/81
9	0	$\sqrt{0.6}$	40/81

Similar to 1D adaptive quadrature, the two approximations, Q_4 and Q_9 on the integration domain Ω, is calculated. If the error,

$$|Q_9 - Q_4| < \tau \tag{F.2}$$

integration is stopped, otherwise the integration domain is divided into four regions and solved on each subregion with an error $\tau/4$.

In order to prevent an infinite amount of subdivisions, it is good practise to restrict the number of subdivisions to some maximum, and also start with some large number of initial subdivisions.

Appendix G

Empirical equation for $P_{\mathbf{loss}}(p_{\|}, p_{\perp})$

From studying particle orbits under different conditions, including changing the origin of the orbits, the vacuum poloidal field strength and shape, and the current density profile, including the plasma current, the probability of an electron being confined or lost is approximated by the function

$$P_{\text{loss}}(p_{\|}, p_{\perp}) = 1 - \exp\left[-\ell \frac{p_{\|}^2}{p_{\perp}^2}\right] \tag{G.1}$$

where an expression for $\ell = \ell(p_{\|}, I_P, I_{\text{CFS}}, Z_0)$ must be found. $P_{\text{loss}}(p_{\|}, p_{\perp})$ is the probability for an electron to be lost or confined, such that it equals 0 (i.e. $\ell = 0$) if an electron is confined, and equals 1 (i.e. $\ell \to \infty$) if an electron is lost.

In order to define $\ell = \ell(p_{\|}, I_P, I_{\text{CFS}}, Z_0)$, the momentum plane is divided into five regions: firstly by differentiating between $p_{\|} > 0$ and $p_{\|} < 0$, and then dividing each region into cold, warm and hot by defining temperatures T_{cold} and T_W. A schematic is shown in figure G.1.

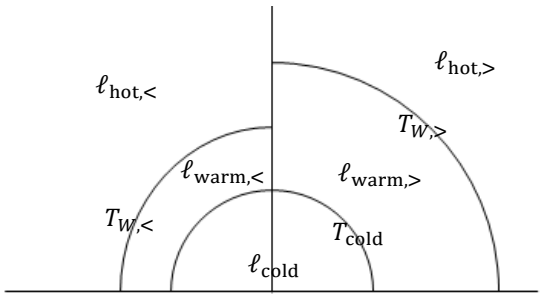

Figure G.1: Schematic of the five areas the momentum plane is divided into. A value for ℓ must be found in each area, in addition to the temperatures T_{cold} and T_W.

As the ion temperature is much lower than the electron temperature, and the mass of

ions is much greater than the mass of electrons, ions are lost at a much slower rate along the field lines. This leads to the creation of an ambipolar electric field, which electrostatically confines the thermal bulk of the electrons [53]. The temperature T_{cold} is therefore included to allow for the confinement of all electrons below this temperature.

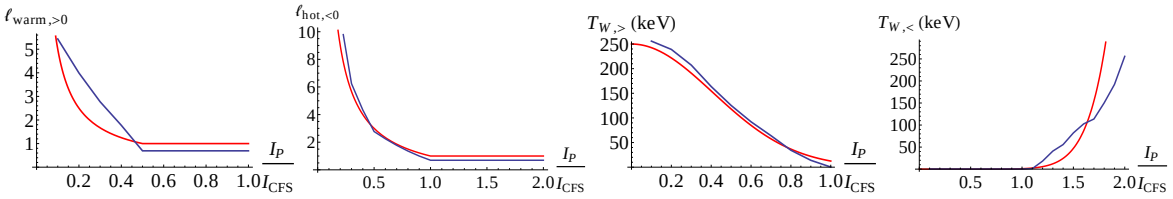

(a) (b) (c) (d)

Figure G.2: The values of (a) $a_{\text{warm},>}$, (b) $a_{\text{hot},<}$, (c) $T_{W,>}$ and (d) $T_{W,<}$ as a function of I_P/I_{CFS} for $B_Z = -10$ mT calculated numerically (blue) and theoretically (red).

Studying the confinement of electrons for $I_P/I_{\text{CFS}} = 0.1, 0.2, \cdots, 1.9, 2$, and ranging the vacuum poloidal field strength from $B_Z = -2, -4, \cdots, -18, -20$ mT, the mathematical expressions for ℓ are fitted to the numerically obtained values, as shown in figure G.2 for $B_Z = -10\,\text{mT}$. Firstly,

$$\ell_{\text{hot},>} = 0 \tag{G.2}$$

and

$$\ell_{\text{warm},<} = 0 \tag{G.3}$$

such that these electrons are always confined. Then,

$$\ell_{\text{warm},>} = \max\left\{\frac{1}{2}\frac{I_{\text{CFS}}}{I_P}\,,\,1\right\} \tag{G.4}$$

$$\ell_{\text{hot},<} = \max\left\{\left(2\frac{I_{\text{CFS}}}{I_P} - 1\right)\,,\,1\right\} \tag{G.5}$$

$$T_{W,>} = \frac{I_{\text{CFS}}}{15}\left(T_{\text{cold}} + 250(1 - T_{\text{cold}})\exp\left[-3\left(\frac{I_P}{I_{\text{CFS}}}\right)^2\right]\right) \tag{G.6}$$

and

$$T_{W,<} = \frac{I_{\text{CFS}}}{15}\left(T_{\text{cold}} + (1 - T_{\text{cold}})\left(\frac{I_P}{I_{\text{CFS}}}\right)^{9.5}\right) \tag{G.7}$$

where the factors $I_{\text{CFS}}/15$ are there to correct for the fact that the temperatures T_W evolve

differently for different magnitudes of the vacuum poloidal field. Of course, the magnitude of the vertical vacuum poloidal field B_V is simply taken into account in the value of I_{CFS} - the larger B_V the larger I_{CFS}.

The values of ℓ and T_W can also be influenced by a vertical shift of the plasma and a spatially varying vacuum poloidal field, while particular care has to be taken to their values around I_{CFS}.

G.1 Vertical shift Z_0

A vertical shift of the plasma is created by introducing a radial component to the vacuum poloidal field. This has the effect of shifting the magnetic midplane, where $B_R = 0$ and around which B_Z is symmetric, up or down. Such a shift influences the confinement of electrons, as shown in figure G.3 for the values of $\ell_{\mathrm{warm},>}$ and $\ell_{\mathrm{hot},<}$. The mathematical expressions for ℓ and T_W are then modified to

$$\ell_{\mathrm{warm},>} = \max\left\{\frac{1}{2}\frac{I_{\mathrm{CFS}}}{I_P}\exp\left[\frac{Z_0^2}{1}\frac{I_{\mathrm{CFS}}}{I_P}\right], 1\right\}$$

$$\ell_{\mathrm{hot},<} = \max\left\{\left(2\frac{I_{\mathrm{CFS}}}{I_P} - 1\right)\exp\left[\frac{Z_0}{0.6}\frac{I_{\mathrm{CFS}}}{I_P}\right], 1\right\}$$

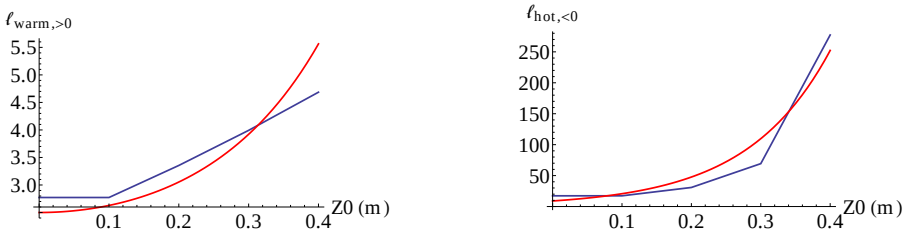

(a) (b)

Figure G.3: The values of (a) $a_{\mathrm{warm},>}$, and (b) $a_{\mathrm{hot},<}$ as a function of Z_0 for $B_Z = -8$ mT and $I_P/I_{\mathrm{CFS}} = 0.2$ calculated numerically (blue) and theoretically (red).

$$T_{W,>} = \frac{I_{\mathrm{CFS}}}{15}\left(T_{\mathrm{cold}} + 250(1 - T_{\mathrm{cold}})\exp\left[-3\left(\frac{I_P}{I_{\mathrm{CFS}}}\right)^2\right]\right)\exp\left[\frac{Z_0}{1}\right]$$

and

$$T_{W,<} = \frac{I_{\mathrm{CFS}}}{15}\left(T_{\mathrm{cold}} + (1 - T_{\mathrm{cold}})\left(\frac{I_P}{I_{\mathrm{CFS}}}\right)^{9.5}\right) - \frac{Z_0}{0.8}\left(\frac{I_P}{I_{\mathrm{CFS}}}\right)^{9.5}$$

where Z_0 is measured in metres.

G.2 Experimental vacuum fields

In the previous sections, the vacuum poloidal fields have been considered to be constant, vertical fields in space for determining the equations for ℓ and T_W. Experimental magnetic fields, however, are not constant, and this leads to further modification of the mathematical expressions for ℓ,

$$\ell_{\text{warm},>} = \max\left\{\frac{1}{2}\frac{I_{\text{CFS}}}{I_P}\exp\left[\frac{Z_0^2}{1}\frac{I_{\text{CFS}}}{I_P}\right]\tanh\left(0.01 I_{\text{CFS}}\right),\, 1\right\} \tag{G.8}$$

and

$$\ell_{\text{hot},<} = \max\left\{\left(2\frac{I_{\text{CFS}}}{I_P} - 1\right)\exp\left[\frac{Z_0}{0.6}\frac{I_{\text{CFS}}}{I_P}\right]\tanh\left(0.01 I_{\text{CFS}}\right),\, 1\right\} \tag{G.9}$$

In particular, this modification is due to the fact that the vacuum field has a radial component itself, which improves confinement when I_P/I_{CFS} is small. As I_P and I_{CFS} increases, the radial component of the vacuum poloidal field becomes negligible, as the overall radial field B_R is created by the plasma current. At small values of I_P and I_{CFS}, however, the radial field is created largely by the vacuum poloidal field, and as a radial field improves confinement, the confinement will always be better than predicted by the empirical equations, leading to the adjustments of equations (G.8, G.9).

G.3 Confinement at lower energy

The mathematical expressions describing the confinement of electrons have thus far been fitted to confinement mappings of energetic electrons only. As the plasma current approaches I_{CFS}, however, the confinement of lower energy electrons becomes important, as all electrons with $v_\parallel > 0$ are confined once $I_P = I_{\text{CFS}}$.

In order to study the confinement of lower energy electrons, let the vertical vacuum poloidal field $B_V = -10$ mT, and impose a current density profile (Appendix B)

$$R_0 = 0.6 \quad , \quad R_p = 0.7 \quad , \quad a = 0.4 \quad , \quad b = 1 \quad , \quad \delta = 0.7 \quad , \quad \alpha = 1$$

that gives $I_{\text{CFS}} \approx 14.5$ kA.

In this case, the vacuum poloidal field has no radial component, and the equations for $\ell_{\text{warm},>}$ and $\ell_{\text{hot},<}$ are given by (G.4) and (G.5), respectively. In order to accurately describe the evolution of the confinement of electrons, the temperatures T_W have to be updated to

$$T_{W,>} = \frac{I_{\text{CFS}}}{15}\left(T_{\text{cold}} + 250(1-T_{\text{cold}})\exp\left[-10\tanh\left(\frac{I_{\text{CFS}}}{20}\right)\left(\frac{I_P}{I_{\text{CFS}}}\right)^2\right] - a_{\text{loss}}\right)\exp\left[\frac{Z_0}{1}\right] \tag{G.10}$$

and

$$T_{W,<} = \frac{I_{\text{CFS}}}{15}\left(T_{\text{cold}} + (1-T_{\text{cold}})\left(\frac{I_P}{I_{\text{CFS}}}\right)^{9.5} - b_{\text{loss}}\right) - \frac{Z_0}{0.8}\left(\frac{I_P}{I_{\text{CFS}}}\right)^{9.5} \tag{G.11}$$

where a_{loss} and b_{loss} is determined in such a way as to ensure $T_{W,<} = T_{W,>} = 0$ when $I_P = I_{\text{CFS}}$ and $Z_0 = 0$, i.e.

$$\begin{aligned} a_{\text{loss}} &= T_{\text{cold}} + 250(1-T_{\text{cold}})\exp\left[-10\tanh\left(\frac{I_{\text{CFS}}}{20}\right)\right] \\ b_{\text{loss}} &= T_{\text{cold}} + (1-T_{\text{cold}}) \end{aligned} \tag{G.12}$$

with the results shown in figure G.4.

Around I_{CFS}, confinement changes very quickly. Up until the first CFS forms, $T_{W,<} = 0$, but rapidly increases thereafter, while $T_{W,>} \to 0$ as $I_P \to I_{\text{CFS}}$. Failure to accurately capture the change in T_W is due to the rapid change in confinement around the formation of CFS, but overall a good approximation is found.

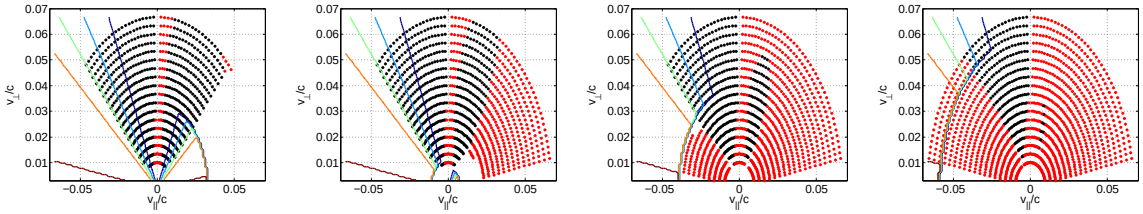

(a) (b) (c) (d)

Figure G.4: The confinement map of electrons originating from the midplane with $B_V = -10$ mT with (a) $I_P = 14$ kA, (b) $I_P = 14.5$ kA, (c) $I_P = 15$ kA and (d) $I_P = 15.5$ kA. Electrons complete trapped (black) or passing (red) orbits, while the white space corresponds to electrons lost. The overlay plot is the analytical probability of an electron being lost/confined, with it changing from $P_{\text{loss}} = 1$ (red) to $P_{\text{loss}} = 0$ (blue) in increments of 0.2.

Appendix H

Direct and iterative solutions to the matrix equations

The numerical approximation to the time evolution of the distribution function can be solved using an implicit method, which is unconditionally stable. The implicit method leads to the creation of a matrix equation,

$$\left(\hat{I} + \hat{D}\right) \vec{f}^{n+1} = \hat{I}\vec{f}^{n} \tag{H.1}$$

where the operator $\hat{D}$ refers to all derivatives to be taken on f, and $\hat{I}$ is the identity matrix.

If there are $2N \times N$ grid points, the matrix will be of size $(2N^2 \times 2N^2)$, so solving it with direct methods are computationally very expensive. Iterative methods, however, can provide accurate solutions to large matrix systems very quickly, and can also be parallelised for improved performance [79, 80].

There exist a few different iterative methods, but as the matrix is not symmetric, most methods do not guarantee convergence. The Jacobi method is best suited for this problem, as it guarantees convergence, works on non-symmetric matrices, and although convergence might be slow, can be effectively parallelised.

The idea behind an iterative method is to start from some initial guess $\vec{x}_0$, and implement some formula to obtain $\vec{x}_{k+1}$ from $\vec{x}_k$ until convergence is achieved. If the matrix equation is

$$\hat{A}\vec{x} = \vec{b}$$

then the residual of the solution $\vec{x}_k$ is defined as,

$$\vec{r}_k = \vec{b} - \hat{A}\vec{x}_k$$

and the goal is to minimize the error,

$$\frac{\|\vec{r}_k\|}{\|\vec{b}\|} < \epsilon$$

where ϵ is the desired accuracy of the solution.

The advantage is that, if the initial guess is close to the solution $\vec{x}_k$, only a few iterations are needed to ensure a small error. For sparse matrices only a mapping of multiplying the matrix with a vector is needed, and the matrix never changes during the iteration. Therefore, if the matrix-vector multiplication is fast and easy to do, iterating can be fast.

In the Jacobi method, the matrix is written as $\hat{A} = \hat{M} - \hat{N}$, where $\hat{M}$ is easily invertible, with the iteration given by [81],

$$\hat{M}\vec{x}_{k+1} = \hat{N}\vec{x}_k + \vec{b}.$$

The simplest choice is for $\hat{M}$ to be the diagonal of $\hat{A}$, such that

$$x_q^{k+1} = \frac{1}{a_{qq}}\left(b_q - \sum_{w=1, w\neq q} a_{qw}x_w^k\right) \tag{H.2}$$

where q and k are indices of the vectors $\vec{x}$ and $\vec{b}$, and a_{qq} refers to the qq^{th} entry of the matrix $\hat{A}$.

Appendix I

Quantifying the approximations and uncertainties in the kinetic model

In developing the 0D kinetic model for studying the time evolution of the electron distribution function, a number of approximations and assumptions were made. It is important to quantify the accuracy of these assumptions and approximations, in order to understand the uncertainty on any results obtained. In this Appendix, a number of simulations are done in order to quantify the accuracy or uncertainty involved with some of the assumptions and approximations made in developing the 0D kinetic model.

I.1 Numerical accuracy through electron energy balance

In obtaining a numerical approximation to the distribution function, a numerical error will be made due to the finite and discrete nature of the grid on which it is approximated. A useful measure in understanding the accuracy of each term is the absorbed power,

$$P_{\text{term}} = \frac{1}{2} m_e \int \mathrm{d}V \int \mathrm{d}^3 p \, v^2 \left(\frac{\partial f}{\partial t} \right)_{\text{term}} \tag{I.1}$$

which can be used in determining the electron energy balance,

$$\frac{3}{2} \frac{d}{dt} \left(n_e T_e \right) = \sum P_{\text{term}} \tag{I.2}$$

such that the temperature can be compared to the pseudo-temperature calculated from the average energy of the distribution function,

$$T_e = \frac{1}{2} m_e v_t^2$$

where

$$\frac{3}{2}\left(m_e v_t(\vec{r},t)\right)^2 = \frac{1}{n_e}\int p^2 f(\vec{r},\vec{p},t)\,\mathrm{d}^3 p$$

and v_t is the thermal velocity.

The idea is to perform a start-up simulation, calculating the power absorbed due to each term as well as the temperature and density from the distribution function and compare to see if energy balance, equation (I.2), holds.

In each case, the parameters used will be typical of the early phase for MAST start-up; the initial temperature $T_{e0} = 50\,\mathrm{eV}$, and the density $n_e = 5 \times 10^{17}\,\mathrm{m}^{-3}$, with all RF power absorbed. For the EBW heating, $P_0 = 50\,\mathrm{kW}$ and $N_\parallel = 0.5$ with $\Delta N_\parallel = 1$. The grid size is set to $p_{\max} = 0.4\,\mathrm{MeV}/c$ with the number of grid points $N = 400$. The distribution function is evolved in time for 10 ms, with $\Delta t = 10^{-4}\,\mathrm{s}$.

I.1.1 EBW heating

First consider the effect of EBW heating alone, such that the time evolution of the distribution function is studied under its effect, i.e.

$$\frac{\partial f}{\partial t} = \text{EBW heating}$$

which, by construction, conserves density.

For a plasma volume $V \approx 4.7\,\mathrm{m}^3$, the final temperature is $T_e = 985\,\mathrm{eV}$, which gives[1]

$$\begin{aligned} \frac{3}{2} V\left(n_e T_e - n_{e0} T_{e0}\right) &\approx 530\,\mathrm{J} \\ \int \mathrm{d}t\, P_{\mathrm{EBW}} &= 500\,\mathrm{J} \end{aligned} \tag{I.3}$$

such that energy is conserved to within about 6%.

[1] To get the correct units from (I.2), $\frac{3}{2} n_e T_e q_e V$, where T_e is measured in eV and $q_e = 1.602 \times 10^{19}\,\mathrm{C}$, and the right-hand side is calculated as $P\,\Delta t$

I.1.2 Loop voltage

Next, consider the effect of a loop voltage. Consider therefore the start-up simulation,

$$\frac{\partial f}{\partial t} = \text{EBW heating} + \text{Loop voltage}$$

which, by construction, conserves density.

A constant loop voltage of $V_L = -20\,\text{mV}$ is added, such that the final temperature is $T_e = 1200\,\text{eV}$. Electron energy balance gives,

$$\begin{aligned} \frac{3}{2}V\left(n_e T_e - n_{e0}T_{e0}\right) &\approx 630\,\text{J} \\ \int \text{d}t\, P_{\text{EBW}} &= 500\,\text{J} \\ \int \text{d}t\, P_{\text{voltage}} &= 100\,\text{J} \end{aligned} \tag{I.4}$$

which gives a difference of about 5%.

I.1.3 Orbital losses

Consider a start-up simulation,

$$\frac{\partial f}{\partial t} = \text{EBW heating} - \text{Loss} + \text{Source}$$

where the source term must be added to ensure the density remains constant.

For simplicity, a constant loss time is used, with $\tau = 10^{-4}$, and

$$\ell = \begin{cases} 1 & , \quad p_\parallel > 0 \\ 2 & , \quad p_\parallel < 0 \end{cases}$$

for the loss term (see Chapter 4). The final temperature obtained is $T_e = 780\,\text{eV}$, which

gives for the energy balance,

$$\begin{aligned} \frac{3}{2}V\left(n_e T_e - n_{e0}T_{e0}\right) &\approx 410\,\mathrm{J} \\ \int \mathrm{d}t\, P_{\mathrm{EBW}} &= 500\,\mathrm{J} \\ \int \mathrm{d}t\, P_{\mathrm{loss}} &= -100\,\mathrm{J} \\ \int \mathrm{d}t\, P_{\mathrm{source}} &= 5\,\mathrm{J} \end{aligned} \tag{I.5}$$

and a difference of about 2%.

I.1.4 Accuracy of heating, loop voltage, source and loss terms

The power of each term can be calculated, and, together with the temperature and density, electron energy balance can be used to determine the accuracy of each term. In this study, collisions have been neglected, and it was shown that all terms have a numerical accuracy of about 5%.

This accuracy can be improved by increasing the number of grid points, but this leads to an increase in the computational time. Given the experimental uncertainties, a numerical error of 5% is acceptable.

I.2 Electron-electron collisions

Electron-electron collisions are implemented under the assumption that the distribution collides with a background, Maxwellian distribution function. Of course, this is not always true, so, in order to test the validity of this assumption, define

$$\begin{aligned} \langle p_\parallel \rangle &= \frac{1}{n_e}\int |p_\parallel|\, f\, \mathrm{d}^3 p \\ \langle p_\perp \rangle &= \frac{1}{n_e}\int p_\perp\, f\, \mathrm{d}^3 p \\ \langle p_\parallel^2 \rangle &= \frac{1}{n_e}\int p_\parallel^2\, f\, \mathrm{d}^3 p \\ \langle p_\perp^2 \rangle &= \frac{1}{n_e}\int p_\perp^2\, f\, \mathrm{d}^3 p \end{aligned} \tag{I.6}$$

in order to be able to calculate how close the distribution f is to a Maxwellian. This is a useful comparison, as the collision operator relies on the approximation that the distribution

collides with a background Maxwellian distribution of the same temperature and density.

Consider the simulation,

$$\frac{\partial f}{\partial t} = \text{EBW heating} + \text{e-e collisions}$$

which conserves density by construction.

The initial temperature $T_{e0} = 50\,\text{eV}$, and the density $n_e = 5 \times 10^{17}\,\text{m}^{-3}$, with all power absorbed. For the EBW heating, $P_0 = 50\,\text{kW}$ and $N_\parallel = 0.5$ with $\Delta N_\parallel = 1$. The grid size is set to $p_{\max} = 0.4\,\text{MeV}/c$ and $N = 400$. The distribution function is evolved in time for 10 ms, with $\Delta t = 10^{-4}\,\text{s}$.

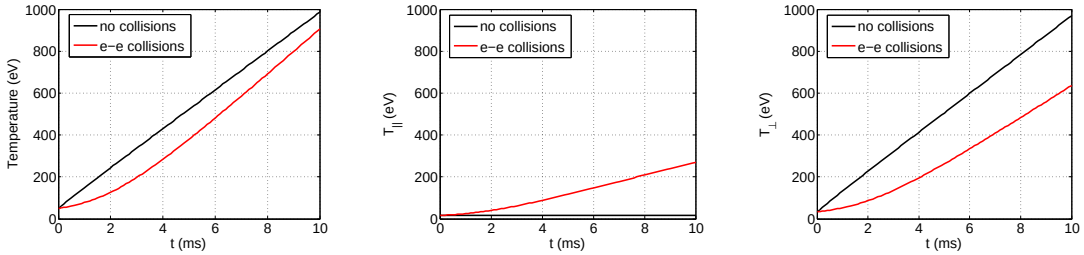

Figure I.1: A comparison of the time evolution of (a) the temperature, (b) $T_\parallel$ and (c) $T_\perp$, for simulations with and without electron-electron collisions.

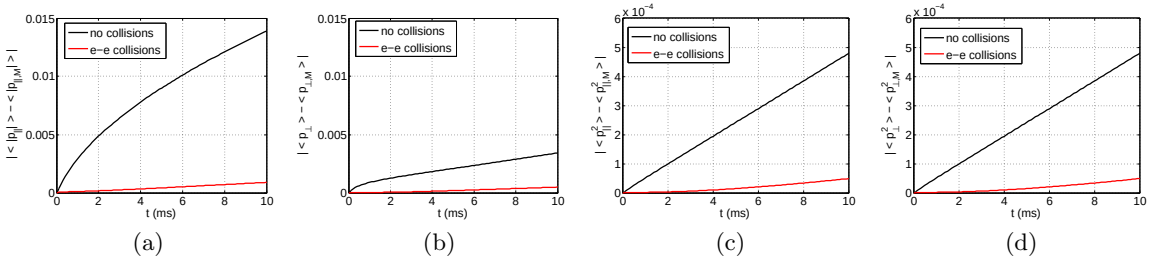

Figure I.2: The difference in moments calculated from the distribution itself and a Maxwellian of the same temperature and density, compared for simulations with and without electron-electron collisions.

Figure I.1 shows the temperature evolution with and without electron-electron collisions. The inclusion of electron-electron collisions leads to a reduction in the temperature of about 10%. This difference is due to the approximation of collisions with a background Maxwellian, as the distribution is subjected to self-collisions, but, as the distribution is not a Maxwellian distribution, the assumption made in approximating the collision operator is not true and

energy is not conserved.

Figure I.2 shows that including electron-electron collisions forces the distribution to be close to a Maxwellian, but as the RF heating term is dominant, the distribution deviates significantly from Maxwellian.

I.2.1 Effect of density

Increasing the density of the electron distribution will increase the collisionality, and therefore the effect of electron-electron collisions. Figure I.3 shows the difference in temperatures between including and excluding electron-electron collisions, for two different electron densities. Increasing the density leads to greater differences in the temperature, as collisions become more dominant, leading to greater losses in the energy.

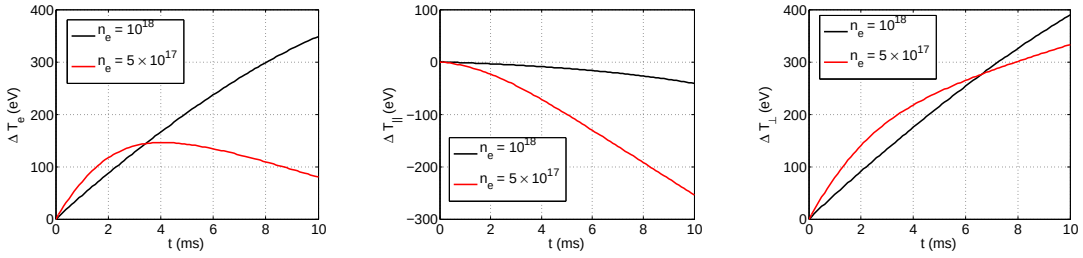

(a) (b) (c)

Figure I.3: A comparison of the time evolution of the differences between simulations with and without electron-electron collisions for (a) T_e, (b) $T_\parallel$, and (c) $T_\perp$, for $n_e = 5 \times 10^{17}\,\mathrm{m}^{-3}$ and $n_e = 10^{18}\,\mathrm{m}^{-3}$.

I.2.2 Effect of grid size

The assumption in determining the electron-electron collision operator is made that the distribution is a Maxwellian. As this assumption is not true, the collision operator leads to energy losses. In order to see the numerical accuracy of the electron-electron collision operator, consider the same simulation as before, but with an increase in the number of grid points. The resultant temperature, shown in figure I.4 shows very little difference between the two cases, indicating that the error in the electron-electron collision operator is due to the assumption of a background Maxwellian, and not due to the discrete nature of the numerical grid.

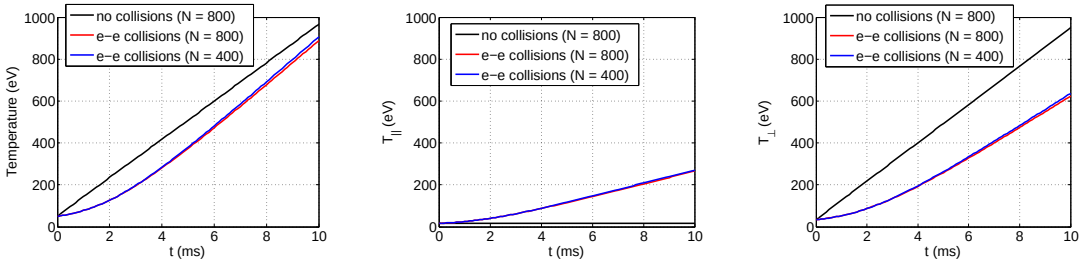

Figure I.4: A comparison of the time evolution of (a) the temperature T_e, (b) $T_\parallel$, and (c) $T_\perp$, for electron-electron collisions with $N = 400$ and $N = 800$.

I.2.3 Uncertainty in the electron-electron collision operator

The electron-electron collision operator describes self-collisions between electrons in the plasma. It should therefore conserve energy, but, as the collision operator is approximated by a Maxwellian and the distribution will hardly ever be Maxwellian, this assumption leads to energy losses. This is supported by the fact that grid size have a very small effect on energy balance, while increasing the density leads to an increase in the amount of energy lost, as collision become more dominant, leading to greater energy losses.

The electron-electron collision operator can be calculated with the Landau integrals [49] or Rosenbluth potentials [48], but this greatly increases both the complexity of the problem and the required computational power. As the expectation is that the current is carried by energetic electrons, which undergo very few collisions, and collisions are therefore not expected to be dominant, electron-electron collisions are approximated by a background Maxwellian collision operator.

The conclusion was made that, during the initial open magnetic field line configuration, the preferential confinement of electrons is responsible for the majority of the observed current, with collisions only "feeding" the loss term by increasing the parallel momentum of electrons through pitch-angle scattering. Including an approximate collision operator would therefore be sufficient, as the collisions are not responsible for the observed current, but rather the asymmetric confinement of electrons which leads to losses of particular electrons.

I.3 Electron-ion collisions

Electron-ion collisions are approximated by the high-velocity limit, which approximates ions as being heavy, stationary objects. Such a collision operator should conserve energy, and should therefore not influence the temperature of the distribution.

Consider the simulation,

$$\frac{\partial f}{\partial t} = \text{EBW heating} + \text{e-i collisions}$$

which conserves density by construction.

The initial temperature $T_{e0} = 50\,\text{eV}$, and the density $n_e = 5 \times 10^{17}\,\text{m}^{-3}$, with all power absorbed. For the EBW heating, $P_0 = 50\,\text{kW}$ and $N_\parallel = 0.5$ with $\Delta N_\parallel = 1$. The grid size is set to $p_{\max} = 0.4\,\text{MeV}/c$ and $N = 400$. The distribution function is evolved in time for 10 ms, with $\Delta t = 10^{-4}\,\text{s}$.

Figure I.5 shows the temperature evolution when including and excluding electron-ion collisions. The addition of electron-ion collisions have a very small effect on the overall temperature, as expected, while increasing $T_\parallel$, due to pitch-angle scattering, and decreasing $T_\perp$.

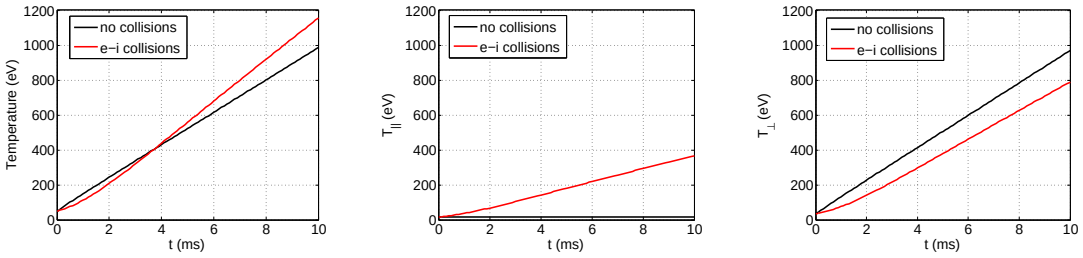

(a) (b) (c)

Figure I.5: A comparison of the time evolution of (a) T_e, (b) $T_\parallel$, and (v) $T_\perp$, for simulations with and without electron-ion collisions.

I.3.1 Effect of density

Increasing the electron density will increase the rate of collisions. Figure I.6 shows the difference in the temperature for simulations with and without electron-ion collisions for different electron densities. As was the case with electron-electron collisions, the increase in density leads to an increase in collisionality, which leads to greater differences in the electron

temperature.

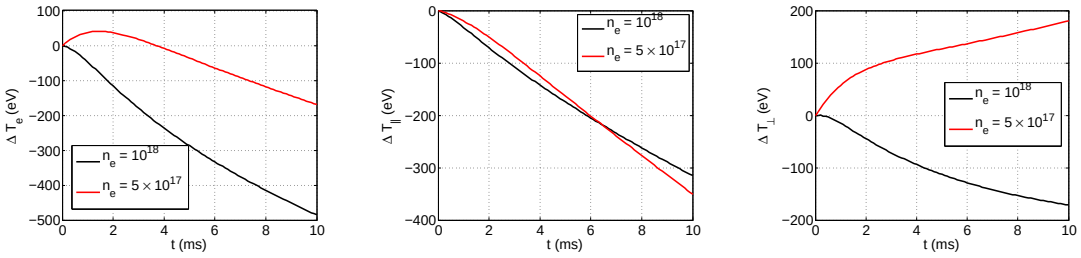

(a) (b) (c)

Figure I.6: A comparison of the time evolution of the differences between simulations with and without electron-ion collisions for (a) T_e, (b) $T_\parallel$, and (c) $T_\perp$, for $n_e = 5 \times 10^{17}\,\mathrm{m}^{-3}$ and $n_e = 10^{18}\,\mathrm{m}^{-3}$.

I.3.2 Effect of grid size

Figure I.7 shows the electron temperature for increasing number of grid points N, when including electron-ion collisions. The increase in temperature with the addition of electron-ion collisions, as observed before, becomes smaller when increasing the number of grid points, implying that the electron-ion collision operator conserves energy, with the finite grid size leading to a numerical uncertainty.

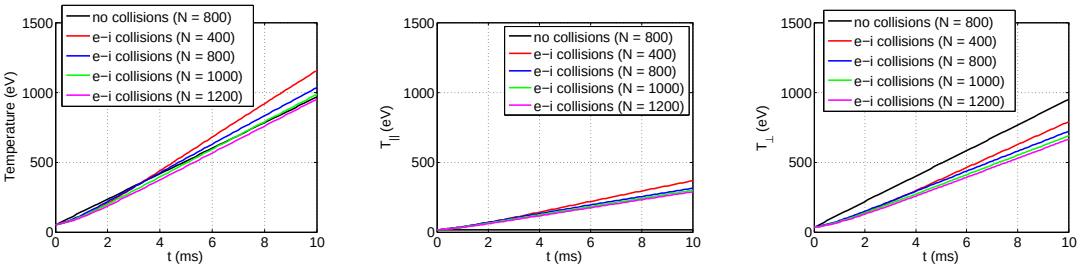

(a) (b) (c)

Figure I.7: A comparison of the time evolution of (a) the temperature T_e, (b) $T_\parallel$, and (c) $T_\perp$, for electron-ion collisions with different grid sizes.

I.3.3 Accuracy of the electron-ion collision operator

The error in the electron-ion collision term is numerical, as this collision operator should conserve energy regardless of the shape of the distribution function. The error is proportional to n_e^2 through the collision rate Γ, equation (3.16), and decreases for increasing grid size. The

grid size can be increased by either increasing the number of grid points N, or by increasing the temperature, through the thermal momentum p_t.

I.4 Uncertainty in the self-inductance

The generation of a plasma current leads to a time-varying current, which induces an electric field. According to Lenz's law, this electric field will oppose the increase in plasma current,

$$V_L = -L_P \frac{\mathrm{d}I_P}{\mathrm{d}t}$$

where L_P is the self-inductance of the plasma.

The self-inductance is a function of the plasma volume and magnetic field strength, such that it is not constant during start-up. The assumption is made, however, that $L_P = 6.5 \times 10^{-7}\,\mathrm{H}$ and constant, even though its value can change by $\pm 10\%$ during start-up. A constant value was used in previous 0D start-up models to great effect [8], and a similar approach has therefore been used in this work.

In order to see the effect of L_P on the generated plasma current, consider a start-up simulation where all electrons are confined. The density evolution is given by

$$n_e = n_{e0}\left(0.1 + 0.9\tanh\left[\frac{t}{t_0}\right]\right)$$

where $n_{e0} = 3 \times 10^{17}\,\mathrm{m}^{-3}$ and $t_0 = 0.05\,\mathrm{s}$. 50 kW of injected power is absorbed as EBW with $N_\parallel = 0.5$. Figure I.8 shows the generated current by changing the value of L_P by $\pm 10\%$, in the absence of electron losses.

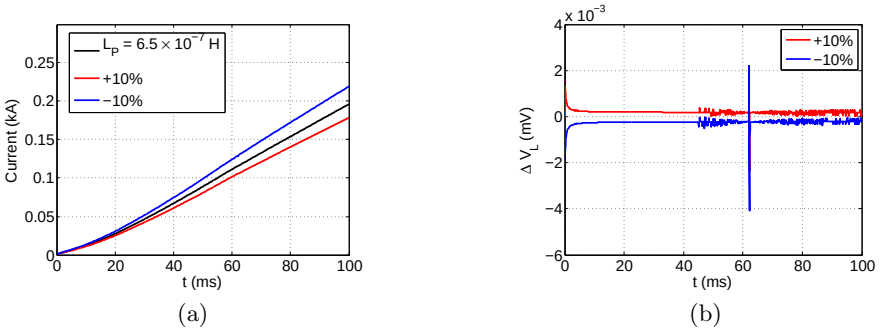

(a) (b)

Figure I.8: The time evolution of (a) the plasma current for different values of the self-inductance V_L and (b) the difference between the generated loop voltages between $L_P = 6.5 \times 10^{-7}\,\mathrm{H}$ and an increase and decrease of 10%.

As expected, increasing the value of L_P leads to a decrease in the overall current, as the generated loop voltage increases. An increase in the self-inductance implies that the plasma is working harder to prevent an increase in the plasma current, leading to a larger loop voltage which deccelerates electrons, and the resultant plasma current is smaller. As the loop voltage is negative, an increase in L_P will lead to a larger negative V_L, and the difference ΔV_L, plotted in figure I.8(b) is positive. For a decrease in L_P, the loop voltage V_L is a smaller negative value, and the difference ΔV_L is negative.

A $\sim 10\%$ uncertainty in the value of L_P will lead to a $\sim 10\%$ uncertainty in the generated plasma current. The value of L_P remains approximately constant during start-up, and therefore a $\sim 10\%$ uncertainty in its value, leading to a $\sim 10\%$ uncertainty in the plasma current, could be expected.

I.5 Uncertainty in I_{CFS}

The value of I_{CFS} contains knowledge of the spatial dependence and strength of the vacuum poloidal field and plasma current density, such that a change in any of these will lead to a change in the value of I_{CFS}. The uncertainty in how these spatially dependent factors affect the loss term is therefore contained in a single variable, I_{CFS}, and any uncertainty in its value will lead to an uncertainty in the simulated plasma current.

The value of I_{CFS} largely depends on the vacuum poloidal field strength, but, as was shown in Chapter 4, a change in the current density profile will change the value of I_{CFS}. It is therefore necessary to investigate the effect of a change in the value of I_{CFS} on the generated current. In order to do this, consider a constant vertical vacuum poloidal field $B_V = 3\,\mathrm{mT}$. The value of $I_{\mathrm{CFS}}[\mathrm{kA}] = 1.5 B_V[\mathrm{mT}]$ and is varied by $\pm 10\%$. The generated plasma current in each case is shown in figure I.9.

In each case, a 10% difference in the value of I_{CFS} leads to a $\sim 8\%$ difference in the generated current. As the exact current density profile is not known, the exact value of I_{CFS} is not known, and an uncertainty of $\sim 10\%$ could be expected, but this is acceptable compared to experimental uncertainties.

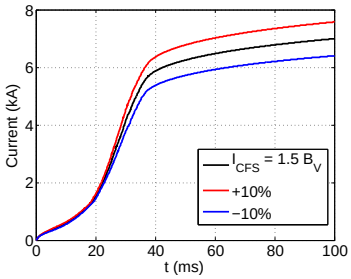

(a)

Figure I.9: The time evolution of the plasma current for different values of I_{CFS}.

Glossary

Commonly used abbreviations:

B_V	vertical vacuum poloidal field
CD	current drive
CFS	closed flux surfaces
EBW	electron Bernstein wave
EC	electron cyclotron
ECCD	electron cyclotron current drive
ECR	electron cyclotron resonance
ECRH	electron cyclotron resonance heating
EM	electromagnetic
HFS	high field side
I_{CFS}	the value of the plasma current where CFS first start to form
LFS	low field side
MAST	Mega Amp Spherical Tokamak
MCF	Magnetic confinement fusion
NBI	Neutral beam injection
RF	Radiofrequency
ST	Spherical tokamak
UHR	upper hybrid resonance

References

[1] ITER Organization, *Science*, viewed 9 August 2017, https://www.iter.org/sci/whatisfusion

[2] J. Wesson, *Tokamaks* (Clarendon Press, 2004).

[3] J.D. Lawson, *Proc. Phys. Soc.* **B70**, 6 (1957).

[4] EURO*fusion*, *Tokamak Principle*. [ONLINE] Available at: https://www.euro-fusion.org/2011/09/tokamak-principle-2/?view=gallery-11. [Accessed 21 September 2017].

[5] Y-K.M. Peng and D.J. Strickler, *Nucl. Fusion* **26**, 769 (1986).

[6] V.F. Shevchenko *et al.*, *EPJ Web of Conf.* **87**, 02007 (2015).

[7] B. Lloyd *et al.*, *Plasma Phys. Control. Fusion* **46**, B477 (2004).

[8] H.T. Kim *et al.*, *Nucl. Fusion* **52**, 103016 (2012).

[9] B. Lloyd *et al.*, *Nucl Fusion* **31**, 2031 (1991).

[10] C.B. Forest, Y.S. Hwang, M. Ono and D.S. Darrow, *Phys. Rev. Lett.* **68**, 3559 (1992).

[11] V.F. Shevchenko *et al.*, *Nucl. Fusion* **50**, 022004 (2010).

[12] T. Maekawa, T. Yoshinaga, M. Uchida, F. Watanabe and H. Tanaka, *Nucl. Fusion* **52**, 083008 (2012).

[13] C.B. Forest, P.K. Chattopadhyay, R.W. Harvey and A.P. Smirnov, *Phys. Plasmas* **7**, 1352 (2000).

[14] T. Yoshinaga, M. Uchida, H. Tanaka and T. Maekawa, *Phys. Rev. Lett.* **96**, 125005 (2006).

[15] A. Ejiri and Y. Takase, *Nucl. Fusion* **47**, 403 (2007).

[16] T. Maekawa *et al.*, *Nucl. Fusion* **45**, 1439 (2005).

[17] A. Ejiri *et al.*, *Nucl. Fusion* **46**, 709 (2006).

[18] T. Yoshinaga, M. Uchida, H. Tanaka and T. Maekawa, *Nucl. Fusion* **47**, 210 (2007).

[19] N.J. Fisch and A.H. Boozer, *Phys. Rev. Lett.* **45**, 720 (1980).

[20] J.G. Cordey, T. Edlington and D.F.H. Start, *Plasma Phys.* **24**, 73 (1982).

[21] K.L. Wong, R. Horton and M. Ono, *Phys. Rev. Lett.* **45**, 117 (1980).

[22] C.B. Forest *et al.*, *Phys. Plasmas* **1**, 1568 (1994).

[23] M.R. O'Brien, M. Cox and D.F.H. Start, *Nucl. Fusion* **26**, 1625 (1986).

[24] V.F. Shevchenko *et al.*, *Proc. 13th Joint Workshop on ECE and ECRH*, 255 (2004).

[25] V.F. Shevchenko *et al.*, *Fusion Sci. Technol.* **52**, 202 (2007).

[26] A.G. Litvak, E.V. Suvorov and M.D. Tokman, *Phys. Lett. A* **188**, 64 (1994).

[27] H.P. Laqua *et al.*, *Phys. Rev. Lett.* **90**, 075003 (2003).

[28] V.F. Shevchenko, Y. Baranov, M. O'Brien and A. Saveliev, *Phys. Rev. Lett.* **89**, 265005 (2002).

[29] V.F. Shevchenko *et al.*, arXiv:1501.01798 [physics.plasm-ph] (2015).

[30] T.H. Stix, *Waves in Plasmas* (New York, 1992).

[31] L.D. Landau, *J. Phys. U.S.S.R.* **10**, 25 (1946).

[32] F.F. Chen, *Introduction to plasma physics and controlled fusion* (New York, 1984).

[33] A.D. Piliya and E.N. Tregubova, *Plasma Phys. Control. Fusion* **47**, 143 (2005).

[34] I.B. Bernstein, *Phys. Rev.* **109**, 10 (1958).

[35] S. Puri, F. Leuterer and M. Tutter, *J. Plasma Phys.* **9**, 89 (1973).

[36] A.N. Saveliev, *Plasma Phys. Control. Fusion* **47**, 2003 (2005).

[37] H.P. Laqua, *Plasma Phys. Control. Fusion* **49**, R1 (2007).

[38] A.D. Piliya, A.Yu Popov and E.N. Tregubova, *Plasm Phys. Control. Fusion* **45**, 1309 (2003).

[39] A.D. Piliya, A. Yu Popov and E.N. Tregubova, *Plasma Phys. Control. Fusion* **47**, 379 (2005).

[40] V. Petrillo, G. Lampis and C. Maroli, *Plasma Phys. Control. Fusion* **29**, 877 (1987).

[41] M. Gryaznevich, V. Shevchenko and A. Sykes, *Nucl. Fusion* **46**, S573 (2006).

[42] R. Prater *et al.*, *Nucl. Fusion* **48**, 035006 (2008).

[43] C.F.F. Karney, *Comput. Phys. Rep.* **4**, 183 (1986).

[44] B. Lloyd, P.G. Carolan and C.D. Warrick, *Plasma Phys. Control. Fusion* **38**, 1627 (1996).

[45] H.T. Kim *et al.*, *Plasma Phys. Control. Fusion* **55**, 124032 (2013).

[46] T. Maekawa *et al.*, *Plasma Sci. Tech.* **13**, 342 (2011).

[47] J. Freidberg, *Plasma Physics and Fusion Energy* (Cambridge University Press, 2007).

[48] M.N. Rosenbluth, W.M. MacDonald and D.L. Judd, *Phys. Rev.* **107**, 1 (1957).

[49] L.D. Landau, *Zh. Eksper. i Theoret. Fiz.* **7**, 19 (1937).

[50] S. Chandrasekhar, *Rev. Modern Phys.* **15**, 1 (1943).

[51] A.N. Saveliev, *Plasma Phys. Control. Fusion* **49**, 1061 (2007).

[52] T. Wauters *et al.*, *Plasma Phys. Control. Fusion* **53**, 125003 (2011).

[53] Y-K.M. Peng, S.K. Borowski and T. Kammash, *Nucl. Fusion* **18**, 1489 (1978).

[54] W.T. Taitano, L. Chacón, A.N. Simakov and K. Molvig, *J. Comput. Phys.* **297**, 357 (2015).

[55] E.S. Yoon and C.S. Chang, *Phys. Plasma* **21**, 032503 (2014).

[56] J.S. Chang and G. Cooper, *J. Comp. Phys.* **6**, 1 (1970).

[57] E. Fijalkow, *Comp. Phys. Comm.* **116**, 319 (1999).

[58] T.D. Arber and R.G.L. Vann, *J. Comp. Phys.* **180**, 339 (2002).

[59] C.B. Laney, *Computational Gasdynamics* (Cambridge University Press, 1998).

[60] R. Fazio and A. Jannelli, *IAENG Int. J. Appl. Math.* **39**, 1 (2009).

[61] W. Hundsdorfer, B. Koren, M. van Loon and J.G. Verwer, *J. Comp. Phys.* **117**, 35 (1995).

[62] R. Courant, K. Friedrichs and H. Lewy, *IBM J. Res. Develop.* **11**, 215 (1967).

[63] J. Crank and P. Nicolson, *Proc. Camb. Phil. Soc.* **43**, 50 (1947).

[64] J. Callen, *Fundamentals of Plasma Physics* (2006) [ebook] Available at: http://homepages.cae.wisc.edu/ callen/book.html [Accessed 26 October 2016].

[65] J. Urban *et al.*, *Nucl. Fusion* **51**, 083050 (2011).

[66] M. Uchida *et al.*, *J. Plasma Fusion Res.* **80**, 83 (2004).

[67] A. Ejiri *et al.*, *Nucl. Fusion* **49**, 065010 (2009).

[68] C.F. Kennel and F. Engelmann (*Phys. Fluids* **9**, 2377 (1966).

[69] E. Kreyszig, *Advenced Engineering Mathematics* (John Wiley and Sons, 2011).

[70] M. Bornatici, R. Cano, O. De Barbieri and F. Engelmann, *Nucl. Fusion* **23**, 1153 (1983).

[71] A.V. Arefiev, E.J. du Toit, A. Köhn, E. Holzhauer, V.F. Shevchenko and R.G.L. Vann, *AIP Conf. Proc.* **1689**, 090003-1 (2015).

[72] A.V. Arefiev, I.Y. Dodin, A. Köhn, E.J. du Toit, E. Holzhauer, V.F. Shevchenko and R.G.L. Vann, *Nucl. Fusion* **57**, 116024 (2017).

[73] C. Finch, *Examples from shocksolution.com.* [ONLINE] Available at: https://github.com/cfinch/Shocksolution_Examples/blob/master/FORTRAN/BilinearInterpolation/interpolation.f90. [Accessed 24 November 2016].

[74] Trebbin, G., *Grant Trebbin* (2012). [ONLINE] Available at: http://www.grant-trebbin.com/2012/04/off-axis-magnetic-field-of-circular.html. [Accessed 31 August 2016].

[75] K. Miyamoto, *Fundamentals of Plasma Physics and Controlled Fusion* (1997).

[76] P. Helander and D.J. Sigmar, *Collisional Transport in Magnetized Plasmas* (Cambridge University Press, 2005).

[77] N.J. Fisch and C.F.F. Karney, *Phys. Fluids* **24**, 27 (1981).

[78] A.H. Stroud, *Approximate Calculation of Multiple Integrals* (Prentice Hall, 1971).

[79] C.T. Kelly, *Iterative Methods for Linear and Nonlinear Equations* (Society for Industrial and Applied Mathematics, 1995).

[80] Y. Saad, *Iterative Methods for Sparse Linear Systems* (Society for Industrial and Applied Mathematics, 2003).

[81] G. Allaire and S.M. Kaber, *Numerical Linear Algebra* (Springer, 2008).